Engineered Bovine Serum Albumin Protein-based Antifouling Coatings for Bioengineering Applications

by

Ziqian Zhao

A thesis submitted in partial fulfillment of the requirements for the degree of

Doctor of Philosophy

in

Materials Engineering

Department of Chemical and Materials Engineering
University of Alberta

Abstract

Bioengineering and biomedical devices are extensively utilized in diagnostics, therapeutics, stomatology, and orthopedics, saving countless lives and experiencing surging demand due to the population aging. Yet, they face great challenges from irreversible biofouling and associated biocorrosion, causing uncontrollable and rapid device dysfunction. Integrating a biocompatible antifouling coating on device surfaces is vital to address these problems, where bovine serum albumin (BSA) protein-based coating with high-efficient biofouling resistance shows promise. However, limited functionalities and surface instability of BSA molecule greatly restrict its application scope and compromise the antifouling performance, respectively. Furthermore, there is no protein-based protective coating tailored to mitigate the severe fouling-accelerated biocorrosion for the widely used metallic implants. This thesis focuses on addressing these critical limitations faced by protein-based coatings through engineering protein with universal anchoring capability on different surfaces and on-demand functionalities, particularly with robust antifouling properties in complex biofluids and enhanced anticorrosion performance, for bioengineering and biomedical applications.

Since the surface anchoring capability of BSA is the prerequisite of constructing coatings on substrates, it is first investigated through direct interfacial interaction measurements. It is found that the self-adaptive interfacial interactions of BSA to different substrates include hydrogen binding, hydrophobic force, electrostatic force, and other interaction forces. These interactions synergistically enable universal anchoring and controllable deposition of BSA proteins by tuning solution chemistry, such as pH, salinity, reactant concentration, and coating time. A methacrylate-conjugation method is developed based on the facile *thiol-ene* click-chemistry-initiated

polymerization to customize the functionalities of engineered proteins (BSA@Polymer) for different working scenarios, such as enhanced antifouling, robust adhesion, and pH-stimuli drug delivery. With the universal anchoring capability and versatile functionalities, we ultimately achieve the construction of BSA-based coatings with on-demand functionalities on organics, inorganics, and metallics for various bioengineering and biomedical applications.

A zwitterion-conjugated BSA protein coating is engineered based on the conjugation method developed in the first work through grafting sulfobetaine methacrylate (SBMA) segments on native BSA protein molecules for surface coating and antifouling applications in complex biological fluids. Unlike traditional synthetic polymers of which the coating operation requires arduous surface pretreatments, the engineered protein BSA@PSBMA (PolySBMA conjugated BSA) can achieve facile and surface-independent coating on various substrates through a simple dipping/spraying method. Interfacial molecular force measurements and adsorption tests demonstrate that the substrate-foulant attraction is significantly suppressed due to strong interfacial hydration and steric repulsion from the bionic structure of BSA@PSBMA, enabling coating surfaces to exhibit superior resistance to biofouling for a broad spectrum of species including proteins, metabolites, cells, and biofluids under complex biological conditions.

To combat the biofouling-accelerated corrosion for metallic implants, especially for magnesium (Mg)-based biomaterials, a tooth-enamel-inspired, highly compact dual protection $NaMgF_3$@BSA inorganic-protein (Inorganic*Pro*) coating is in-situ constructed on Mg surfaces through a BSA protein-facilitated reaction between sodium fluoride (NaF) and Mg substrate. The association of Mg ions and BSA establishes a local hydrophobic domain that lowers the formation enthalpy of $NaMgF_3$ nanoparticles. This innovation generates finer nanoparticles, facilitating

denser packing, consequently reducing voidage within the coatings by over 50% and reinforcing mechanical durability. Moreover, the incorporation of BSA in and on the coatings plays two synergistic roles: (1) sealing residual cracks within coatings, thereby promoting coating compactness and tripling anticorrosion performance, and (2) mitigating fouling-accelerated biocorrosion in complex biosystems with tenfold resistance against bio-foulant attachments, including biofluids, proteins, and metabolites.

In summary, this thesis introduces an innovative approach harnessing native BSA proteins to create engineered proteins with extraordinary and tailored functionalities for biomedical applications, particularly with the robust antifouling and enhanced anticorrosion properties. This research elucidates the interfacial interaction mechanisms underlying BSA universal anchoring and outstanding antifouling phenomena and demonstrates a pioneering design strategy that leveraging proteins to alter inorganic reactions for enhanced performance. These advancements, grounded in fundamental surface science and applied protein-engineering technology, envision a flourishing development of novel protein-based coatings and materials in biomedical, chemical, food, and energy industries and hold potential to shape the trajectory of future nano-, bio-, and eco-technologies, paving the way for a more innovative, sustainable world.

Preface

This thesis is an original work conducted by Ziqian Zhao under the supervision of Dr. Hongbo Zeng, containing published content from peer-reviewed journals.

Chapter 3 of this thesis has been published as Zhao, Z., Pan, M., Yang, W., Huang, C., Qiao, C., Yang, H., Wang, J., Wang, X., Liu, J. and Zeng, H. Bioinspired engineered proteins enable universal anchoring strategy for surface functionalization. *Journal of Colloid and Interface Science*, (2023) 650, 1525-1535. I conceived the research under the supervision of Dr. Hongbo Zeng. I was responsible for the materials synthesis, data collection, and analysis, as well as manuscript composition. Dr. Mingfei Pan and Dr. Wenshuai Yang contributed to the manuscript revision and experiment design. Chenyu Qiao and Haoyu Yang contributed to the material synthesis and data analysis. Charley Huang, Dr. Jianmei Wang, Dr. Xiaogang Wang, and Dr. Jifang Liu contributed to the manuscript revision. Dr. Hongbo Zeng was the corresponding author and was involved in concept formation and manuscript composition.

Chapter 4 of this thesis has been published as Zhao, Z., Pan, M., Qiao, C., Xiang, L., Liu, X., Yang, W., Chen, X.-Z. and Zeng, H. Bionic Engineered Protein Coating Boosting Anti-Biofouling in Complex Biological Fluids. *Advanced Materials*, (2023) 35(6), 2208824. I conducted the research under the supervision of Dr. Hongbo Zeng. I was responsible for the materials synthesis, data collection, and analysis, as well as manuscript composition. Dr. Mingfei Pan, Dr. Li Xiang, and Dr. Wenshuai Yang contributed to the manuscript revision and experiment design. Chenyu Qiao contributed to the data analysis. Dr. Xiong Liu and Dr. Xing-Zhen Chen contributed to the cell antifouling experiment and manuscript revision. Dr. Hongbo Zeng was the corresponding author and was involved in concept formation and manuscript composition.

Chapter 5 of this thesis has been published as Zhao, Z., Yu, W., Yang, W., Zhang, G., Huang, C., Han, J., Narain. R., and Zeng, H. Dual-Protection Inorganic-Protein Coating on Mg-Based Biomaterials through Tooth-Enamel-Inspired Biomineralization. on *Advanced Materials*, (2024), 2313211. I performed the research under the supervision of Dr. Hongbo Zeng. I was responsible for the materials synthesis, data collection, and analysis, as well as manuscript composition. Dr. Wenting Yu, Dr. Wenshuai Yang, Dr. Guohao Zhang, and Dr. Jianmin Han contributed to the manuscript revision and experiment design. Charley Huang contributed to the manuscript revision. Dr. Hongbo Zeng and Dr. Ravin Narain were the corresponding authors and were involved in concept formation and manuscript composition.

Acknowledgments

First and foremost, I would like to express my sincere gratitude to Dr. Hongbo Zeng for his great supervision, unwavering support, and inspiring thoughts during my whole Ph.D. program. Dr. Zeng gave me step-by-step training on SFA and other experimental techniques at the start of my journey at the University of Alberta, helped me in career planning and developing critical thinking and academic writing skills, as well as provided an excellent research experience with a great academic atmosphere and state-of-the-art facilities in surface science. His enthusiasm for research and commitment to excellence have shaped not only my professional skills but also my personal character.

I am truly grateful to all my committee members for providing constructive feedback on my research and this thesis. I would like to thank all my group members for their kindly help, especially Dr. Wenjihao Hu and Dr. Li Xiang for their inspired advice in the early stage of my Ph.D. program, as well as Dr. Mingfei Pan and Dr. Wenshuai Yang for their helpful discussion. Besides, I appreciate all my co-authors and colleagues, Chenyu Qiao, Yongxiang Sun, Dr. Diling Yang, Dr. Xiaohui Mao, Dr. Wenda Wang, Dr. Lu Gong, Dr. Qiongyao Peng, Charley Huang, Haoyu Yang, Lin Yang, Pan Huang, Siyu Li, and Yimei Sun, for their great supports.

My sincere gratitude goes to the China Scholarship Council (CSC), Natural Sciences and Engineering Research Council of Canada (NSERC), the Canada Foundation for Innovation (CFI), the Canada Research Chairs Program, and Alberta Innovates for the financial support.

Finally, I deeply appreciate the love and support from my grandparents, my parents, my brother, my nephew, and all my family members. Special thanks to my girlfriend, Huyan Xiao, whose support, love, and optimism are the highlights of my life in Edmonton.

Table of Contents

List of Figures

Abbreviations and Symbols

BMD	biomedical device
IMD	implantable medical device
BSA	bovine serum albumin
PTFE	polytetrafluoroethylene
PVDF	polyvinylidene fluoride
PEG	polyethylene glycol
PVA	polyvinyl alcohol
E_{ad}	adhesion energy
$S_{contact}$	contact area
$\gamma_{surface}$	interfacial tension
SBMA	sulfobetaine methacrylate
CBMA	carboxybetaine methacrylate
TMAO	trimethylamine N-oxide
Ip	isoelectric point
TCEP	tris(2-carboxyethyl) phosphine
SFA	surface force apparatus
AFM	atomic force microscopy
QCM-D	quartz crystal microbalance with dissipation monitoring
Δf	frequency change of QCM-D sensor
Δm	mass change on QCM-D sensor
O-PTIR	optical photothermal infrared
FTIR	Fourier transform infrared spectrum
SAM	self-assembly monolayer

SI-ATRP	surface-initiated atom transfer radical polymerization
cBSA	crosslinked BSA
re-BSA	reduced BSA
LSCM	laser scanning confocal microscope
APTES	(3-Aminopropyl) triethoxysilane
OTS	trichloro(octadecyl)silane
CR	Congo red
FBS	Fetal bovine serum
ITC	isothermal titration calorimetry
Inorganic*Pro*	Inorganic-protein
Hb	Hemoglobin
Lyso	lysozyme
K_a	association constant
n	reaction stoichiometry
ΔH	enthalpy change
ΔS	entropy change
ΔG	Gibbs free energy change
ΔE	reaction activation energy
EIS	electrochemical impedance spectroscopy
GBR	guided bone regeneration

CHAPTER 1. Introduction

Biofouling poses a global challenge across various industries, such as marine, food, and bioengineering industries, significantly impacting the economy, environment, and safety.[1-11] Fouling refers to the unwanted accumulation of organic matter on surfaces from the surrounding environment. Biofouling, specifically, encompasses organisms and their by-products from biosystems, like plants, animals, proteins, metabolites, cells, small molecules, and extracellular polysaccharides.[2-4] Typical biofouling process involves keen attachment, colonization, and accumulation of bio-foulants on surfaces when surfaces contact a biosystem such as blood, causing severe adverse effects. This ubiquitous biofouling has particularly affected the bioengineering and biomedical industries recently due to the growing demand for biomedical devices such as implants, sensors, and stents with the population aging. Biofouling in these applications results in severe healthcare-associated infections and device dysfunction. According to the World Health Organization (WHO) 2022 report, 7 patients in high-income countries and 15 patients in low-income countries will acquire at least one healthcare-associated infection (HAI), and 1 in every 10 affected patients will die from their HAI.[12]

Efficient anti-biofouling technology is critical to mitigate surface fouling and reduce mortality rate and human suffering. Over the past decades, various surface technologies, including antifouling coatings,[8, 13, 14] slippery surfaces,[15, 16] and non-adhesive surfaces,[5, 6, 17, 18] have emerged to resist biofouling. However, most effective industrial surface technologies lack biocompatibility, hindering their utilization in bioengineering and biomedical applications. For example, the copper-containing materials, widely used in handles, taps, and pipes, demonstrate highly efficient anti-bacterial and anti-virus performance but pose toxicity concerns, potentially causing chronic

diseases such as Alzheimer's Disease (AD) if used in biomedical implants.[19, 20] Developing novel biocompatible antifouling materials is imperative yet challenging due to the complexity of the biofouling process. This process involves sophisticated interactions between bio-foulants and surfaces, such as electrostatic attraction, hydrophobic forces, and specific coordination. Thus, future antifouling strategies rely on utilizing novel materials with excellent biocompatibility and understanding their antifouling mechanisms at interfaces. The advancements in antifouling materials and mechanisms will bring opportunities to achieve efficient anti-biofouling surfaces and pave the way to solve the challenging biofouling issues in bioengineering and biomedical applications.

1.1 Biofouling in bioengineering applications

1.1.1 Biofouling and its hazards

With the population aging, more patients need biomedical devices (BMD) for organ restoration and real-time disease diagnosis, such as implantable chips for vision restoration,[6, 21-23] human-machine interface for communication and diagnosis, knee replacement, dental implants, and artificial blood vessels.[24] However, a primary challenge faced by BMDs is biofouling. The operation of BMDs inevitably involves biological solutions, such as blood, saliva, buffer, and culture medium, containing bio-foulants, such as proteins, metabolites, enzymes, and cells. These bio-foulants irreversibly adhere to the working surfaces during operation, progressively overturning the electrochemical and biological properties of BMDs, consequently causing unpredictable function degradation.[2-8, 25, 26]

BMDs generally fall into two categories: implantable medical devices (IMDs) and non-implantable medical devices (non-IMDs). IMDs, like knee replacement, dental implants, and

artificial blood vessels, restore organ functionality. Non-IMDs, such as virus test kits, blood glucose meters, and on-skin sensors, detect specific signals operating under relatively mild conditions. Reliable detection generally requires specific working buffers that contain bovine serum albumin (BSA), casein protein, Mg ions, and other pH buffering matters to maintain a stable aqueous environment during operation.[27] For instance, DNA-nanostructure-based biosensing platforms detect nucleic acids, proteins, small molecules, and cells in testing solutions for early-stage diagnosis. However, even in such stable and mild conditions, the proteins inside buffer solutions continuously foul working surfaces, blocking signal transmission. The current density of a bare gold electrochemical sensor significantly drops from 20 μA mm^{-2} to near zero after incubation in a buffer with 1% BSA, falling in detection.[28] Similarly, on-skin flexible sensors acquiring biological signals in real-time experience deterioration in the signal-to-noise ratio of electrocardiography (ECG) and electromyography (EMG) due to the epidermal surface lipid fouling.[22] Integrating a commonly used antifouling coating like a poly (ethylene glycol) (PEG)-based coating can effectively mitigate such biofouling issues, ensuring long-term reliable sensing in mild condition.

Compared to non-IMDs, IMDs face a harsher and unstable working environment. IMDs need implantation surgery, potentially causing foreign body reactions,[29, 30] immune rejection,[31, 32] and inflammation.[2-4] They also undergo wear loss and mechanical damage during patient movement. These result in dynamic and complex postoperative recovery conditions (pH, salinity, types of metabolites, foulant concentration, etc.).[33-38] Although surface modification and medical treatments are cooperatively utilized to prevent biofouling, biofouling control on IMDs is still more challenging than that of non-IMDs. For example, patients should take anti-inflammatory drugs to reduce inflammation after implantation surgery, which helps mitigate the biofouling to

some extent. Similarly, implantable chips are more susceptible to in vivo tests than in vitro tests.[5] Moreover, live cells secrete the extracellular polysaccharides (EPS), leading to microscopic biofilm buildup on IMD surfaces, facilitating secondary macro-organism colonization. For example, artificial blood vessels that replace arterial vessels defunctionalized by the fouling of atherosclerotic plaque in coronary heart disease generally suffer from secondary blood coagulation. Such blood coagulation originates from the undesirable biofouling after the implantation, as 5 ng cm^{-2} of fibrinogen adsorption can facilitate further foulant colonization on the newly implanted artificial blood vessel surfaces.[39] As biofouling on IMDs involves comprehensive physical, chemical, and biological processes, it demands innovative antifouling surface design for IMDs.

1.1.2 Biofouling-accelerated biocorrosion

Biofouling-accelerated biocorrosion represents another detrimental consequence.[40-45] General bio-foulants obstructing signal transmission may not harm the device integrity, while biofouling-induced corrosion can cause permanent damage to the integrity of device surfaces, especially to metallic surfaces. Biofouling establishes localized microenvironments on surfaces, creating variations in oxygen levers, pH, and ion concentration that can generate electrochemical gradients, consequently triggering galvanic corrosion on metal surfaces.[43, 45-47] Some highly active metabolites or microorganism-produced acids aggressively attack metallic surfaces, hastening their degradation. Meanwhile, corrosion-resulted surface roughing increases bio-foulants adsorption, in turn, significantly accelerating surface corrosion. Such a reciprocal deterioration of biocorrosion and biofouling greatly accelerates surface degradation.

This biocorrosion commonly affects orthopedic and dental implants. For example, stainless steel-based or titanium-based dental implants are susceptible to biocorrosion.[48] The presence of

saliva, food particles, and bacteria can lead to biofilm formation and subsequent corrosion of the metal surfaces of dental implants. Similarly, metallic stents supporting blood vessels or arteries are also prone to biocorrosion from blood exposure and flow.[49] Another typical example is the surgical instrument that is not properly cleaned and sterilized, resulting in the accumulation of bio-foulants on instrument surfaces and severe corrosion.

1.1.3 Interfacial mechanisms underlying (anti-) biofouling phenomena

Biofouling is a dynamic process that spans several lengths and time scales and involves complex physical, chemical, and biological processes. Typically, biofouling is described as a three-phase process, spanning from atomic to macro scales and from seconds to months.[2-4]

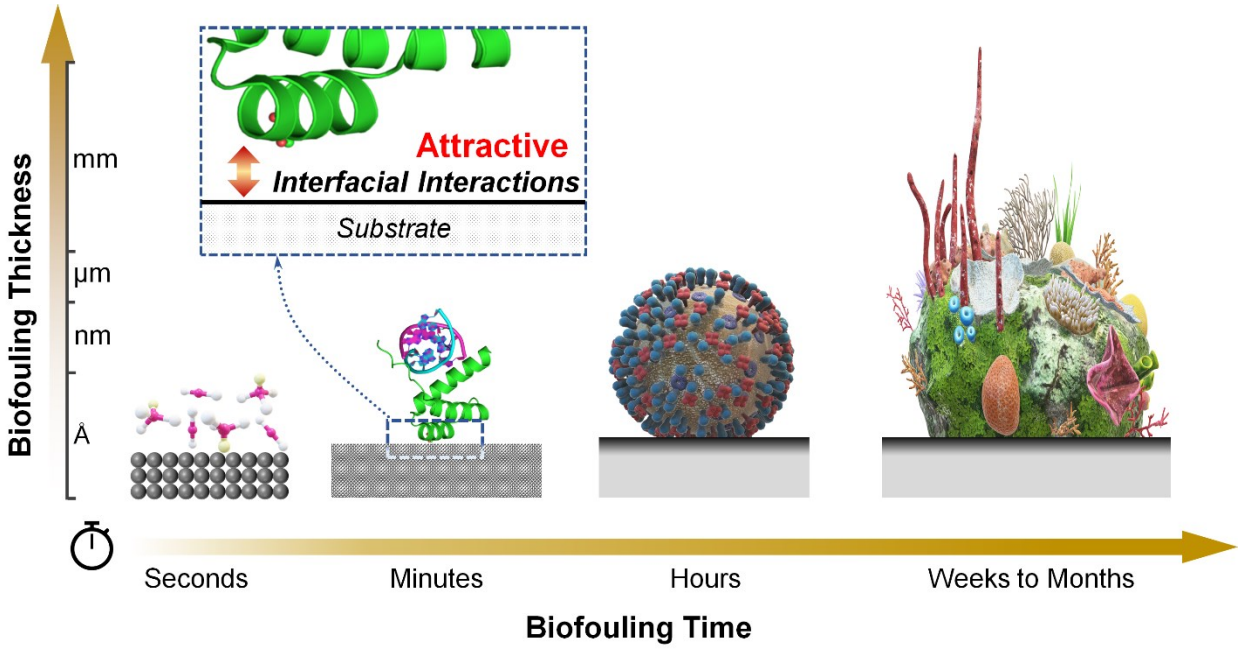

Figure 1.1 Illustration of different phases in the biofouling process.

In the first phase, a conditioning film is formed within seconds or minutes of immersion, where pristine surfaces absorb small molecules and proteins via strong, attractive interfacial interactions. Then, the micro-organisms as primary colonizers will settle on the protein

conditioning layer in the second phase. This colonization is reversible as the micro-organisms, such as cells can detach from surfaces. The micro-organisms produce extracellular polysaccharides (EPS) to form a continuous biofilm, sometimes reaching up to 500 μm in thickness. Finally, in the third phase, macrofouling organisms attach to the biofilm, culminating in a macroscopic fouling community in the following weeks to months. While impeding any of these phases can mitigate biofouling, the most effective strategy is inhibiting the formation of the protein conditioning layer by creating a non-fouling surface.

It can be found that biofouling is fundamentally governed by interfacial interactions between bio-foulants and substrate surfaces, where attractive interactions cause conditioning film and following biofouling phenomena. Therefore, antifouling mechanisms hinge on modulating these interfacial interactions to reduce attractive forces (adhesion) or even generate repulsive forces to prevent fouling on surfaces. Major attractive forces in aqueous environments include the van der Walls force, electrostatic attraction between opposite-charged matters, and hydrophobic forces. Fluoride-based materials, such as Teflon (Polytetrafluoroethylene, PTFE) and polyvinylidene fluoride (PVDF), that exhibit weak interfacial van der Walls force with low surface energy (20-30 mM m^{-1}), have been widely utilized as antifouling materials for decades.[3, 50-52] Generally, tuning electrostatic forces is ineffective, as bio-foulants could be negatively charged or positively charged; even opposite-charged bio-foulants co-exist in complex biofluids; as a result, making surface negatively or positively charged can only reduce the attachment of like-charged bio-foulants but attract more opposite charged bio-foulants. Reducing hydrophobic force via hydrophilic surfaces to resist foulants is also commonly used in aqueous solutions.[9, 53] For example, hydrophilic metal oxides or hydroxides like TiO_2 or $Cu(OH)_2$ surfaces effectively inhibit lipid and other oily foulants attachment, achieving high-efficient and longtime oil-water separation.[54-58]

Improving interfacial repulsions between substrate surfaces and bio-foulants can also mitigate biofouling. Major repulsive forces in aqueous environments include hydration forces, electrostatic repulsion between like-charged matters, and steric forces. Hydration force refers to a monotonically repulsive force raised from the bonded water molecules (hydration layer) at hydrophilic or amphiphilic surfaces, preventing contact between two surfaces.[59] Superhydrophilic zwitterionic polymers, uncharged sugars, and various surfactant monolayers are examples that utilize a hydration layer for antifouling.[9, 53] Steric force is a repulsive osmotic force due to the unfavorable entropy associated with compressing (confining) polymer chains. It is also known as overlap repulsion, as this force arises when two polymer-covered surfaces approach each other and the outer segments begin to overlap, which is crucial in various natural and practical systems.[59] Both synthetic polymers (polyethylene glycol, PEG, polyvinyl alcohol, PVA) and biopolymers (proteins, gelation) are widely used as steric stabilizers against coagulation. For example, polymer additives can lead to steric stabilization of colloids as emulsifiers in cosmetics, pharmaceuticals, and processed food. Surface-grafted Zwitterionic polymer brushes demonstrate repulsion to foulants attachments, showcasing remarkable antifouling performance.[22, 60, 61]

Biofouling, an interfacial phenomenon between bio-foulants and substrates, results from attractive interfacial interactions. The mainstream antifouling strategy is creating a non-fouling surface with reduced attractive interfacial forces. The lower interfacial interactions, the better antifouling performance.

1.1.4 Antifouling strategies

Various techniques have emerged to tackle biofouling issues, falling into three categories: (1) removal of the bio-foulants in solutions by filters or membranes before implementing

biomedical devices; (2) inclusion of antifouling chemicals into bio-solutions to reduce the fouling capacity of bio-foulants; and (3) antifouling surfaces on biomedical devices. Given the working scenarios of biomedical devices that may involve tests in the human body, the third strategy of creating antifouling surfaces on devices seems to be the most feasible alternative to combat the biofouling issues. From an interfacial interaction perspective, the essence of antifouling surfaces is reducing the adhesion of bio-foulants to substrates. No adhesion, no fouling. The interfacial adhesion can be calculated as follows:

$$E_{ad} = S_{contact} \times \gamma_{surface}$$

Where E_{ad} is the interfacial adhesion energy between the foulants and substrates, $S_{contact}$ is their contact area, and $\gamma_{surface}$ is their interfacial tension. Lowering either the contact area or interfacial tension can effectively reduce the adhesion of the foulant-surface, ultimately achieving non-fouling surfaces.

Physical antifouling strategies work by reducing the foulant-surface contact area to minimize foulants attachments. The Lotus effect is one of the most famous examples of physical strategy. Lotus leaves feature lots of microscopic papillae covered with nanoscopic wax tubules, creating a high-roughness surface to inhibit the water droplet wetting, consequently reducing their contact area between droplets.[3, 4, 62, 63] Similarly, sharks possess microscopic topographical skin (or placoid scales) that minimizes the contact of foulants to keep their skin clean. Inspired by the shark skin, various microtopographic patterns have been designed to realize low surface adhesion, seen in commercial products like Sharklet AF™ swimsuit.[3, 4]

Chemical antifouling strategies function by minimizing the foulant-surface interfacial tension to lower bio-foulants' adhesion to surfaces. As summarized in Section 1.1.3, either

decreasing attractive interfacial forces or increasing repulsive forces can effectively lower the interfacial tension between bio-foulants and substrate surfaces. Fluoride or silicon -based surfaces, exhibiting low surface tension, represent the low-attraction antifouling surfaces. The superhydrophilic zwitterionic polymers illustrate the typical high-repulsion antifouling surface via their strong hydration layer in aqueous environments. Hydrophilic materials, possessing superior biocompatibility and posing low health risks, have been widely used in biomedical applications in the last few decades. The commonly used biocompatible, hydrophilic antifouling materials in biomedical applications are displayed in Figure 1.2.

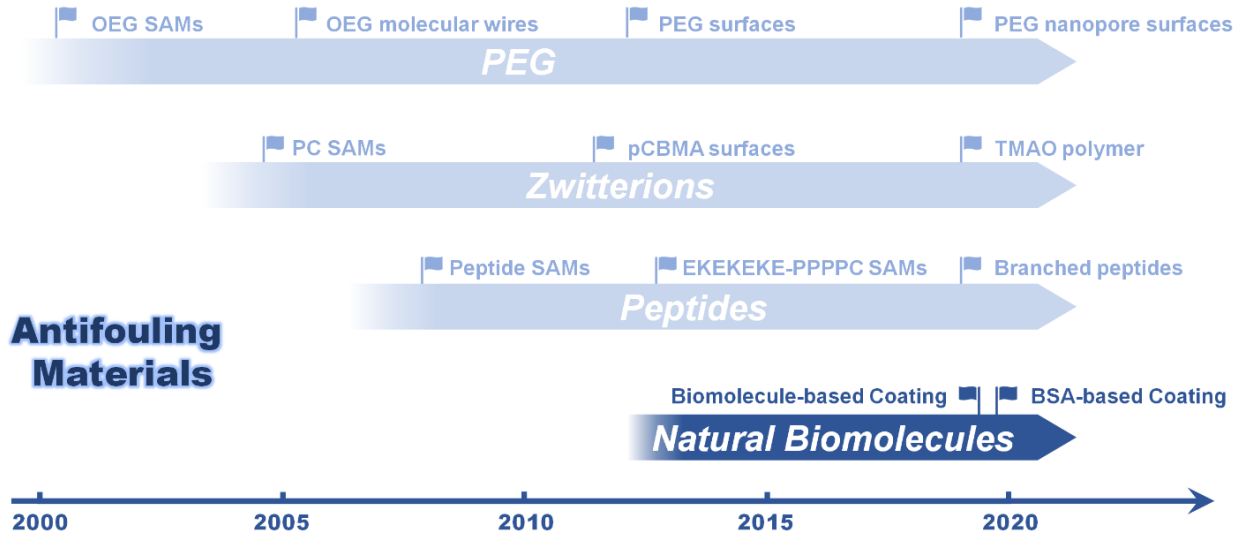

Figure 1.2 Timeline of the emergence of the most commonly used materials in the chemical antifouling approach as well as selected milestones, including PEG and related systems, zwitterionic systems, peptides, and most recent natural biomolecule antifouling materials.[5]

Since the 1970s, polyethylene glycol (PEG; n>10 EG units) and its derivatives oligoethylene glycol (OEG, n ≈ 3-10) have been extensively used in biomedical and biochemical applications, particularly in sensors with PEG-based self-assembled monolayers (SAMs).[5] For instance, CH_3O-PEG-SH or SH-$(EG)_4$-COOH have been grafted on the gold surfaces of sensor

chips to resist biofouling during the detection of human hormones or insulin.[64, 65] The specificity and sensitivity of detection are greatly enhanced with the presence of PEG-antifouling SAMs. However, PEG suffers from oxidation damage and decomposition in the presence of oxygen and transition metal ions, degrading the long-term stability and impeding their prolonged operation in high levels of blood or serum. Zwitterionic materials that feature high oxidative resistance and hydrolytic stability have attracted extensive attraction as promising alternatives to PEG in antifouling applications. Zwitterions are electrically neutral matter that contains both positively charged and negatively charged groups within a single monomer unit, such as sulfobetaine methacrylate (SBMA), carboxybetaine methacrylate (CBMA) and Trimethylamine N-oxide (TMAO). [8, 9, 18, 22, 26, 66, 67] Because of the short intramolecular distance between positively charged and negatively charged groups, the polarity and hydration capacity of zwitterions are dramatically increased, compared with PEG. Therefore, the antifouling performance of zwitterions is boosted and can work under highly challenging conditions. For example, CBMA-based label-free biosensors can sensitively detect insulin in neat serum, which, some years later, still represents a benchmark in the selective label-free electrochemical detection of targets in complex fluids.[68] Regardless of excellent and stable antifouling properties, zwitterions often involve complicated synthesis or high cost other than SBMA and require arduous treatments to be grafted on surfaces. In this decade, peptides emerged as natively biocompatible antifouling materials due to their sequence-tunable physicochemical characteristics. With the inherent, high hydrogen binding ability and zwitterionic charges of the polar functional groups in amino-acids, peptides are usually strongly hydrated and can prevent biofouling.[5, 69] He and co-workers demonstrated that zwitterionic CRERERE peptide SAMs achieved ultralow levels of protein adsorption (1.97-11.79

nm cm^{-2}).[70] Recent study shows that branched peptides offered better antifouling performance than that of linear analogs, likely due to the conformational entropy.[71]

In very recent studies, natural biomolecules such as proteins have been directly employed as antifouling materials.[1, 5-7, 72-75] Protein is an assembly of many peptides. Consequently, protein inherits the characteristics of small peptide molecules, including hydrophilicity, zwitterionic charge, anchor groups, and hydration layer. In addition, proteins demonstrate a self-adaptive conformation, hierarchical structures, and specific metal ion coordination as macromolecules and biological functions as biomolecules.[76-80] Such additional properties may greatly benefit proteins as the antifouling coating. For example, the self-adaptive conformation of proteins can help protein molecules anchor on versatile surfaces without grafting addition chemical anchors like the thiol group. Hierarchical structure and complex conformation of proteins may exert added steric force similar to branched peptides, further enhancing the antifouling performance. With these merits, natural biomolecules emerge as a new class of antifouling materials in biomedical applications. Yang and co-workers demonstrated that amyloid-like reduced BSA protein can be used as the antifouling coating material.[7] Ingber and co-workers reported the generation of a cross-linked BSA-nanowire composite interface with long-term antifouling performance.[6] Werner and co-workers exhibited that cholesterol-containing layers counteract bio-foulants via entropic repulsion and resist the contaminations from complex biofluids.[1] In summary, natural biomolecules demonstrate their antifouling performance as promising antifouling materials in bio-applications.

However, lots of unknowns outstand in this interdisciplinary but emerging filed, including the anchoring and antifouling mechanisms of natural biomolecules, such as proteins, at interfaces, what feasible strategies can introduce advanced functionality in protein-based coatings, and how

to address biofouling-introduced problems such as biocorrosion through protein-based coatings. Our goal in this research is to answer these open questions through employing one commonly used model protein, BSA protein, to explore the interfacial interaction mechanisms and engineering it with advanced introduced functionalities via an innovative approach to achieve superior antifouling performance for bioengineering and biomedical applications and to mitigate the biofouling-accelerated corrosion for metallic biomaterials.

1.2 BSA protein-based coatings

1.2.1 BSA protein and its coatings

Bovine serum albumin (BSA) is a monomeric protein primarily derived from cow blood serum. It is a soluble, globular protein with a molecular weight of 66.5 kDa and an isoelectric point (Ip) at pH 4.8, composed of 583 amino acids residues, 17 intramolecular disulfide bonds, and 3 homologous domains (each domain is broken down into two sub-domain, A and B).[81-83] BSA belongs to the albumin family of proteins, sharing structural and functional similarities with human serum albumin (HSA). It acts as a carrier protein to transport fatty acids, minerals, and hormones, functions as an anticoagulant to extracellular fluids, and serves as a biological buffer to maintain pH levels and osmotic pressure within capillaries. BSA is a small, stable, non-toxic, and non-antigenic protein and is not expected to cause an immune response in humans or other animals. Therefore, it is safely and widely used in research and bio-applications, such as used as a blocker to shield active binding sites on reaction tubes, preventing non-specific adsorption of tested antibodies on those sites, ultimately improving the sensitivity and reliability in immunohistochemistry.[84-86] Ma et al. suggest that the self-adaptive conformation change of BSA

protein may facilitate the deposition of protein on different substrates to block active sites.[87] In this process, BSA molecules may optimize their conformation and orientation to minimize interfacial free energy, resulting in hydrophobic domains in contact with surfaces and hydrophilic parts exposed to the aqueous solution. Additionally, it serves as a nutrient in cell and microbial culture and as a template to synthesize nanostructure and determine the toxicity of metal ions.[82] Thanks to the excellent biocompatibility, blocking performance, ion binding ability, and the capability to prevent non-specific adsorption of BSA protein, research community has attempted to employ BSA as antifouling coating materials for bio-applications in recent years.

Ingber et al. prepared a three-dimensional porous matrix of cross-linked BSA supported by a network of conductive nanomaterials composed of either gold nanowires, gold nanoparticles, or carbon nanotubes for electrodes with antifouling performance.[6] They attribute antifouling properties to the size-exclusive of the porous matrix, repelling bio-foulants. Hu et al. construct an antifouling coating via amyloid-like BSA reduced by tris(2-carboxyethyl) phosphine (TCEP).[7] The anchored BSA layer exerts resistance to protein, serum, cells, and microbes. The origin of the protein antifouling may come from the strong hydration ability of mixed charged groups uniformly distributed at the molecular level, similar to zwitterionic groups.[69]

Nevertheless, a controllable deposition of BSA protein on versatile substrates is still challenging, especially in environments with various pH, different ions, and salinity, notably due to the inadequate understanding in interfacial interactions between BSA protein and substrates. These interfacial interactions enable BSA anchoring and depositing on different substrates,

governing the preparation and stability of BSA-based coatings. Furthermore, it should be taken into consideration that the fluctuations of pH and metal ion concentrations, commonly presented in complex biofluids, may significantly alter the charge status of the functional groups on BSA surfaces, thus seriously weakening interfacial hydration and compromising the antifouling performance of BSA coatings. Therefore, the concept naturally arises that engineering native protein with advanced introduced functionality to boost its inferior antifouling properties.

1.2.2 Engineered protein coatings

Native proteins, such as BSA, exhibit naturally intrinsic functionalities and can be employed in antifouling applications. However, these limited intrinsic functions sometimes cannot fulfill the comprehensive and challenging requirements of biomedical device settings. Fortunately, the diversity of functional groups within proteins offers exciting opportunities to incorporate artificially introduced functions into these native proteins. The modified native protein, enriched with advanced introduced functions, is known as the engineered protein. The design and preparation strategies of engineered proteins encompass conjugation, hybridization, and recombination, as displayed in Figure 1.3.[88]

Conjugation is widely employed in biochemical analytic assays and can be achieved through either non-covalent or covalent connections. The antibody (ligand)-receptor in virus detection assays is a typical conjugation reaction.[89] Moreover, biotin-streptavidin binding, which is commonly utilized in biochemical molecule modification, also belongs to the conjugation method.[90] Another exquisite non-covalent interaction is the host-guest reaction that involves molecular recognition, such as cyclodextrin-based inclusion complexation.[91] Covalent conjugation

provides a much more diverse and stable connection between native proteins and functional chemical moieties. This conjugation can be achieved via typical chemical reactions such as Michael addition,[92, 93] click reaction,[94-96] and NHS/EDC coupling.[97] For example, SBMA monomers have been grafted on BSA through the Michael addition for enhanced antifouling performance. The conjugation method focuses more on introduced functional moieties than on proteins; thereby, native proteins are usually utilized as building blocks.

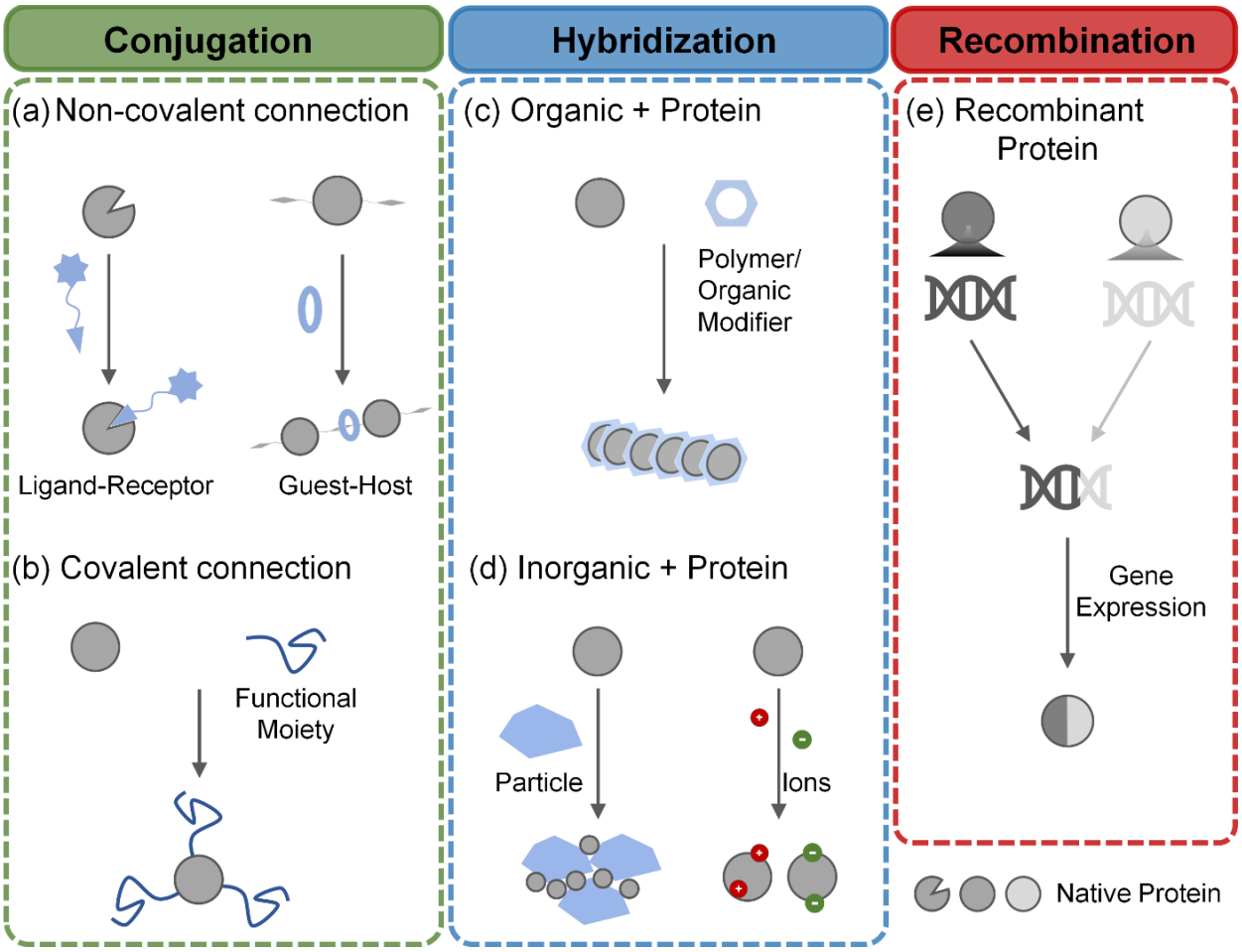

Figure 1.3 Illustration of Engineered Protein and the major design strategies for engineered proteins.

Hybridization refers to simply mixing non-proteinaceous components, organic or inorganic, with native protein to create an engineered protein with unique properties. For example, Poly (amido amine) dendrimers and cricoid proteins are assembled to construct high-ordered dual-enzyme protein nanowires.[98] BSA can aggregate as coating, thin film, or designed pattern through TCEP-induced amyloidization.[7] Protein can also be hybridized with catalysts, which are capable of photoconversion.[99] Biomineralization, seen in the formation of tooth enamel, bone, fish scale, and crab shell, represents a typical process of inorganic-protein hybridization, where proteins associate ions and then convert them to inorganic matter.[100-103] Meanwhile, residual proteins integrate with inorganic matter, creating inorganic-protein hybrids with durable mechanical properties and anticorrosion performance. The hybridization method can facilely achieve desirable properties that are different by only using proteins.

Recombination allows for the production of proteins that may not naturally exist.[104] Recombinant proteins are artificially engineered in the laboratory by inserting a DNA sequence encoding a specific part of protein into a host like bacteria and then expressing the recombinant DNA. For example, Liu et al. reported an engineered protein-based superglue obtained by rationally recombining VPGKG peptides and random coil peptides.[105] This method shows great potential for broad applications, especially in pharmaceutical and healthcare-related industries, but usually necessitates computer-aided design and incurs high-cost.

1.3 Objectives

Bioengineering and biomedical devices save numerous patients and experience growing demand within healthcare systems. However, biofouling poses a great challenge to their long-term and reliable operation, especially for implantable medical devices. Biofouling typically involves a

series of comprehensive phases on device surfaces, causing disastrous consequences like inflammatory, device dysfunction, and biocorrosion-induced degradation. Integrating antifouling materials onto device surfaces can effectively address these issues. While the biocompatible BSA protein shows promise in tacking biofouling issues, they encounter great challenges before practical use in bioengineering and biomedicine. These include the lack of understanding regarding its critical anchoring and deposition mechanisms that govern the coating preparation and stability, limited on-demand functionalities that restrict its application scope, and surface instability in complex biofluids with compromised antifouling performance. Moreover, even though numerous biomaterials are metallic and susceptible to biofouling-accelerated corrosion, there is currently no protein-based protective coating tailored to mitigate this issue.

The main objective of this thesis is to develop engineered BSA protein-based coatings with enhanced antifouling and other tailored functionalities. These coatings are intended to effectively mitigate the biofouling and its derivative biocorrosion for bioengineering and biomedical devices operating in complex biological conditions. Furthermore, this research endeavors to reveal the fundamental anchoring and antifouling interaction mechanisms of BSA-based coatings at interfaces. More specifically, this thesis focuses on the following three areas:

(1) Probe the interfacial interaction forces that govern the anchoring and deposition of BSA protein on surfaces and accordingly achieve controllable BSA-based coating preparation though tuning solution chemistry (BSA concentration, pH, ions, and salinity). Develop a feasible polymer-protein conjugation method to engineer native BSA with on-demand functions and ultimately realize the universally anchoring of a series of tailored engineered BSA proteins for versatile surface functionalization.

(2) Apply the novel polymer-protein conjugation method developed in part one to prepare an engineered BSA protein-based coating with enhanced antifouling performance that can work in complex biological fluids, as well as elucidate the underlying interfacial mechanisms that maintain the exceptional antifouling performance in complex aqueous environments with pH variation and high salinity.

(3) Incorporate new anticorrosion function into the engineered BSA protein-based coating via an inorganic-protein hybridization strategy to mitigate the biofouling-accelerated biocorrosion for metallic implants. This investigation will specifically focus on evaluating the protection of engineered protein-based coating to pure magnesium (Mg), a metallic biomaterial known for its high corrosion propensity.

1.4 Structure of thesis

Chapter 1 introduces the biofouling issues in bioengineering and biomedical applications, as well as antifouling strategies, especially the emerging BSA protein-based antifouling coating. The objectives of this thesis are also included.

Chapter 2 describes the major experimental techniques used to probe interfacial interaction mechanisms and characterize biofouling adsorption.

Chapter 3 reports bioinspired engineered BSA@Polymer proteins enabling universal anchoring and versatile surface functionalization. The universal anchoring mechanisms of BSA at interfaces are revealed by surface force apparatus (SFA) to facilitate the BSA coating preparation and benefit its stability in use. A methacrylate-protein (BSA@Polymer) conjugation method is developed via click-chemistry-initiated polymerization to engineer BSA-based coating with on-demand functionalities.

Chapter 4 demonstrates a bionic engineered protein BSA@PSBMA synthesized through the methacrylate-protein conjugation method, boosting the anti-biofouling performance in complex biological fluids. The underlying interfacial mechanisms that generate exceptional antifouling properties in complex aqueous environments with varying pH and high salinity are also investigated by using SFA.

Chapter 5 presents a tooth-enamel-biomineralization-inspired hybridization strategy to design a $NaMgF_3$@BSA inorganic-protein (InorganicPro) dual protection coating for mitigating the biofouling-accelerated corrosion for Mg-based biomaterials. The thermodynamics and kinetics in $NaMgF_3$@BSA formation are investigated to explore the mechanisms that improve anticorrosion performance of InorganicPro coating. The interfacial interaction of the BSA protein layer to bio-foulants is measured by atomic force microscopy (AFM) to elucidate its antifouling mechanisms.

Chapter 6 concludes the major fundings and original contributions in the thesis and provides perspectives of the further work of protein-based coatings.

CHAPTER 2. Major Experimental Techniques

2.1 Surface forces apparatus (SFA)

Surface forces apparatus (SFA) has been widely employed for the measurement of interaction forces between two surfaces as a function of separation distance in the presence of aqueous and non-aqueous media since 1969.[59] SFA features high sensitivity with a force sensitivity of <1 nN and distance resolution of <0.1 nm and can achieve long-time contact of two surfaces. The state-of-the-art SFA2000 is utilized in this study and its working principle is displayed in Figure 2.1.[28, 105-108] Specifically, back-silvered thin mica sheets (1-5 um) were firstly glued onto two cylindrical silica disks with the same radius, R= 2 cm, and then mounted in the SFA chamber in a crossed-cylinder configuration. The white light that passes through the two mica surfaces will generate multiple bean interferometry (MBI) fringes, which are also known as fringes of equal chromatic order (FECO), as shown in Figure 2.1a. The absolute surface separation (D) can be monitored and measured in situ and in real-time according to the position of FECO. The interfacial interaction forces (F) are quantified based on Hook's law, $F=k\Delta x$, where k is the spring constant of the cantilever and Δx is the spring deflection determined using an equation $\Delta x=D_{actual}-D_{applied}$. The $D_{actural}$ is obtained from the real-time position of FECO and the $D_{applied}$ is determined according to the moving distance of the surfaces driven by a motor. The interaction forces between two mica surfaces are equivalent to a sphere of radius R approaching a flat surface when their separation distance D is much smaller than R based on the 'Derjaguin approximation. In a typical SFA force measurement, two surfaces are first brought to approach each other ('approach') and are kept for a different time (contact time), followed by separation ('separation'). Adhesion (F_{ad}/R) is measured when the two attractive surfaces are separated and jumped apart (so-called 'jump out').

The energy per unit area W_{ad} can be calculated based on the Johnson-Kendall-Roberts (JKR) model $F_{ad}/R = 1.5\pi \cdot W_{ad}$, which is generally applied for soft deformable surfaces with relatively large curvature and interfacial adhesion.[105]

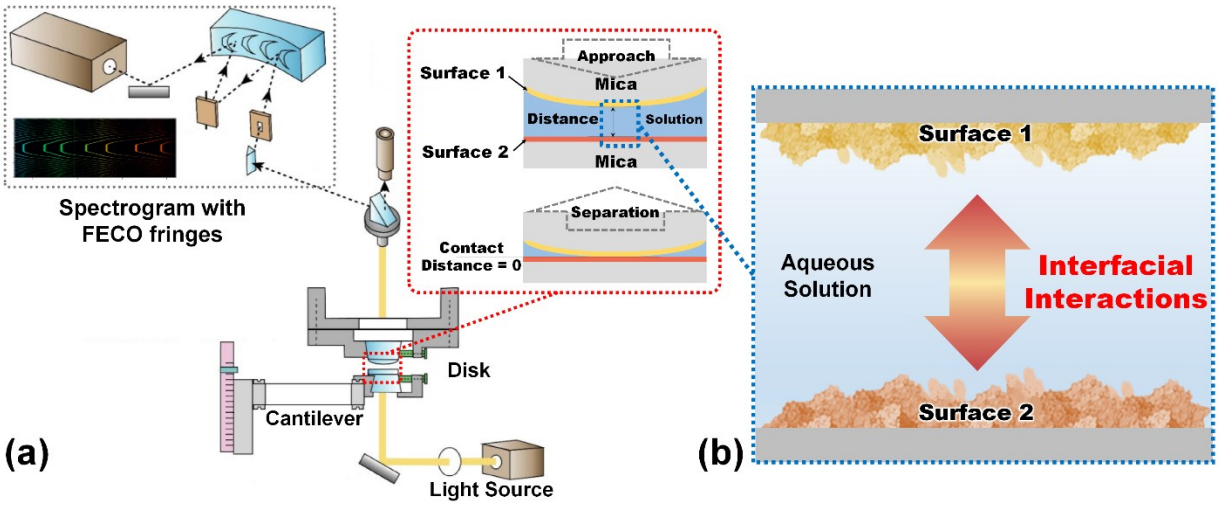

Figure 2.1 Illustration of the setup of interfacial interaction measurements using SFA. (a) Typical light path in SFA and a picture of FECO fringes, corresponding to the contact position of two curved surfaces.[28] (b) Two surface-modified surfaces and their interfacial interactions in the aqueous solution.

2.2 Atomic force microscope (AFM)

AFM nanomechanical study is another direct and quantitative analysis technique for interaction forces between two components, which does not require transparency and molecular smoothness of test surfaces compared to SFA.[109, 110] AFM can determine the separation distance according to the laser deflection on the displacement sensors and measure the interaction forces based on Hook's law, which is similar to the working principle of SFA. In a typical force measurement, the AFM probe will be first brought to approach substrates ('approach') and

followed by separation ('separation'). Adhesion between fouling compounds and substrates will be measured at least 200 times and then statistically analyzed by Gauss distribution to determine the average adhesion forces. In this study, a colloidal probe AFM is employed to measure the interfacial interactions between fouling compounds and Mg-based substrates on Bruker ICON AFM.[111, 112] Specifically, a silica colloidal AFM probe is firstly prepared by gluing a silica microsphere with a diameter of ~ 5 μm onto a tipless cantilever using epoxy glue and then is cleaned by UV/ozone treatment for 10 min before being functionalized by different fouling compounds. Then, the interfacial interaction measurement will be conducted following the standard operation procedure in different aqueous solutions.

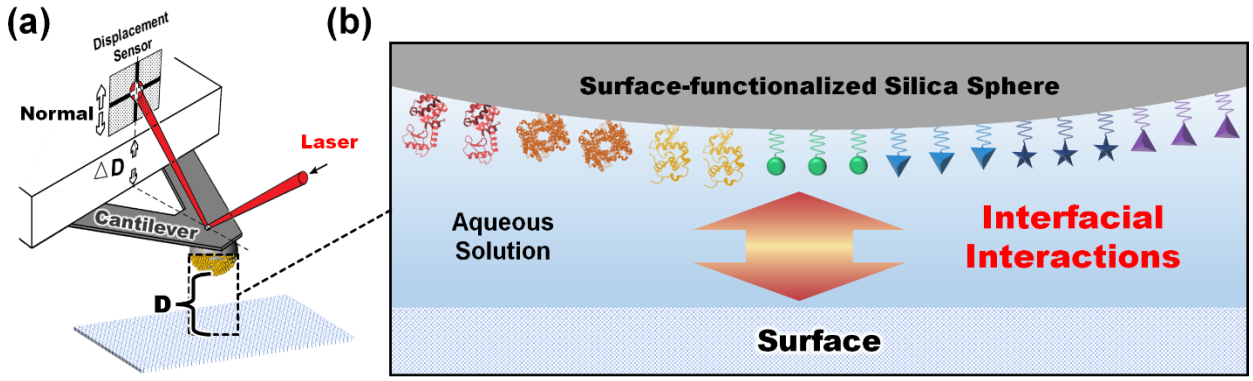

Figure 2.2 (a) Illustration of the setup of interfacial interaction measurements using colloidal probe AFM.[109] (b) Interfacial interactions between surface-functionalized silica sphere and substrates.

2.3 Quartz crystal micro-balance with dissipation (QCM-D)

Quartz Crystal Microbalance with Dissipation monitoring (QCM-D) is a real-time, surface-sensitive technique for analyzing dynamic fouling phenomena via detecting mass changes at the sensor surface with nanoscales resolution (Figure 2.3).[85, 113-116] The resonance frequency of the

QCM-D sensor will shift when foulants are attached, and this change in frequency (Δf) is related to the mass uptake (Δm) at the surfaces based on the Sauerbrey relation:

$$\Delta f = -C \cdot \Delta m$$

Where Δf is the change of the resonance frequency, C is the lumped constant, Δm is the change of mass on the QCM-D sensor. By measuring the frequency change in real-time, we can monitor the dynamic fouling phenomena.

In a typical QCM-D test (Figure 2.3b, Q-Sense E4, Biolin Scientific, Finland), a fouling solution will be introduced to the QCM-D chamber to contact the new surface of the sensor. In this stage, the mass uptake increases rapidly and the frequency decreases with foulant attached to surfaces. After stable frequency was attained, ultrapure water was introduced into the chamber to remove the loosely bonded foulants on sensors, giving rise to an increase in frequency. The adsorption of different foulants will be calculated based on the frequency changes.

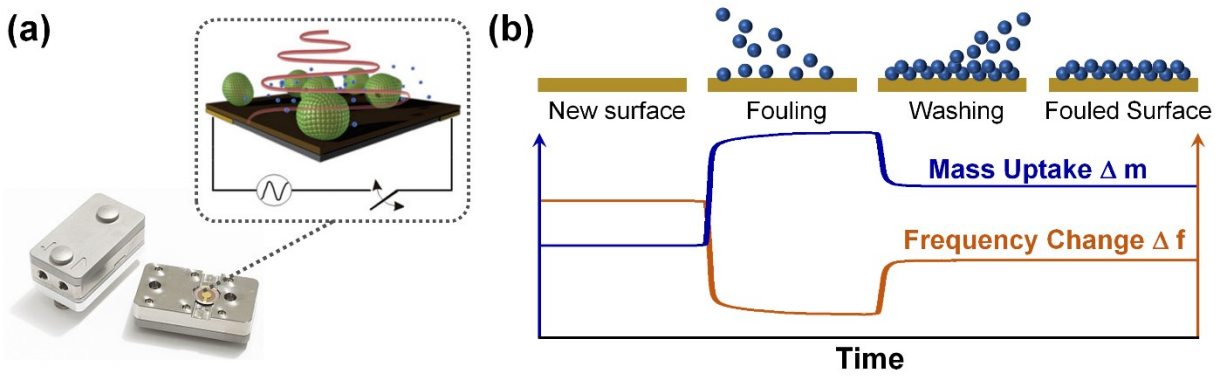

Figure 2.3 (a) QCM-D configuration and illustration of resonance frequency change of QCM-D sensor when foulants attached. (b) Mass and frequency change during the QCM-D test.

2.4 Optical photothermal infrared (O-PTIR) microscope

Characterization of fouling distribution on surfaces is critical for evaluation of the antifouling performance of coatings. The optical photothermal infrared (O-PTIR) microscope offers a non-contact and macroscopic characterization of fouling distribution.[117-120] In a typical O-PTIR characterization (Figure 2.4a), a tunable pulsed mid-infrared (IR) laser induces photothermal effects onto a sample surface, which are measured using a scattered visible probe laser to focus on the sample. The reflection IR spectra recorded by O-PTIR can be correlated to ATR-FTIR spectra. The O-PTIR spectra of bio-foulants will show their corresponding characteristic peaks. Then, using characteristic IR pecks to scan the sample surfaces to map the foulants distributed on the sample surfaces with the high resolution < 250 nm (Figure 2.4b, mIRage, Photothermal Spectroscopy Corp, CA). The O-PTIR mapping overcomes the limitation of EDS characterization, which cannot identify organic groups with the same composition, and the spatial resolution limitation of traditional FTIR microscopy (10-20 microns).

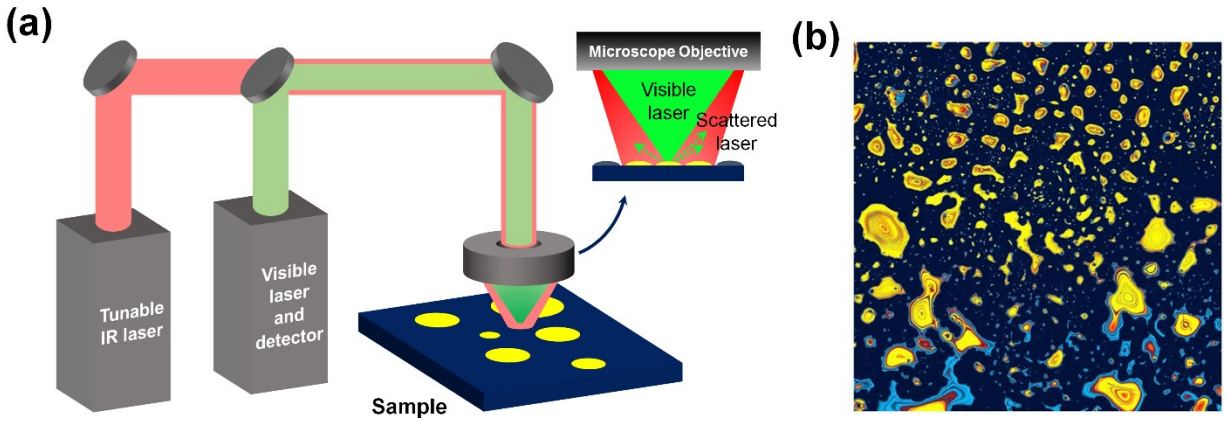

Figure 2.4 (a) Illustration of the setup of O-PTIR. (b) An O-PTIR image.

CHAPTER 3. Bioinspired Engineered BSA Proteins enable a Universal Coating Strategy for Versatile Surface Functionalization

3.1 Introduction

Biomedicine and bioengineering systems save numerous lives via advanced biotechnologies. Most diagnostic and therapeutic devices in these systems for personalized treatments need to satisfy the complicated requirements with their on-demand surface functions. [8, 121-123] For example, implantable medical devices, which help more than 5% of citizens in developed countries with a global market value of $120.5 billion USD, require antifouling surfaces to improve their reliability and avoid inflammation.[3, 124-126] Bioadhesives need rapid and strong interfacial adhesion for visceral hemostasis.[127] These on-demand surface properties are imparted through the immobilization of functional materials on target surfaces via covalent or non-covalent binding.[59] Strong binding is a prerequisite for good performance and durability. Conventionally, covalent binding was employed to connect existing and/or artificially introduced chemical motifs for ultra-thin, robust, and effective functional coatings, such as Au-S bond or R-Si-O-Si bond for self-assembly monolayer (SAM) [128] and functional polymer brush coating prepared via surface-initiated atom transfer radical polymerization (SI-ATRP).[129] However, covalent binding requires surfaces with special chemistry and arduous surface pretreatment, sometimes even involving toxic reagents, greatly limiting their applications in nano- and biosystems. Non-covalent binding overcomes such limitations and is deemed as the future of surface coating technology, thanks to the surface-independent nature of non-covalent interactions, such as electrostatic, hydrogen bonding, hydrophobic, and coordination interactions.[59, 124, 130] However, the relatively low bonding

strength and instability of non-covalent interactions are the Achilles' heel of such a promising strategy, commonly leading to poor durability and unreliable performance of coatings.

Over the past decades, great efforts and considerable attempts have been made to strengthen non-covalent interactions, in which transformative strategies were derived from biological procedures, especially protein-surface interaction protocols.[131-133]. Protein molecules could bind to surrounding substances with multiple molecular interactions and adapt their configurations with different properties of substrate surfaces, maximizing the strength of binding interactions. One notable example is dopamine-assisted co-deposition technology derived from adhesive mussel foot proteins (mfps), where catechol in mfps binds to different substrates with multiple strong and adaptive molecular interactions.[57, 131-142] Via mimicking this process, the small molecule dopamine, which also consists of catechol groups, can adapt its configuration to maximize multiple interactions with different surfaces, facilitating the universal and strong anchoring, even comparable to covalent binding in strength.[57, 131-142] These findings raise a question: In addition to protein-derived small molecules, why not use whole proteins as surface anchors? Compared with small molecules, whole proteins contain not only anchoring fragments but also boosting fragments that facilitate the reorientation and redistribution of anchoring fragments to strengthen the binding further.[87, 143, 144] For example, native bovine serum albumin (BSA) protein is well-known for its 'stickiness' that non-specifically binds to almost any surface with multiple molecular interactions, such as hydrogen bonding, hydrophobic and electrostatic attractions. The BSA protein could alter its secondary structure and orientation to adapt to substrate surface properties, achieving rapid and robust anchoring on different substrates. Therefore, it is widely used as the blocking agent in immunoassays.[7, 87, 143, 144] Natural proteins can only impart surfaces with their intrinsic functions,[6, 7, 88, 145] while small biomolecules like dopamine can

covalently connect diverse chemical motifs with artificially introduced properties, yielding on-demand surface functionalization while anchoring to substrates. As a result, it is critical to develop a practical approach to engineering proteins with diverse introduced functions for on-demand properties of protein-based coatings.

Herein, we reported an innovative strategy to furnish BSA proteins with a broad selection of polyacrylates for desired functions in accordance with the 'root-leaf' structure of grass (Figure 3.1a), realizing versatile functionalized surfaces and achieving universal anchoring on virtually any substrate. Specifically, polyacrylates as functional 'leaves' were grafted on native BSA proteins to produce engineered proteins, BSA@Polymer, through the *thiol-ene* click reaction.[88, 96, 124] The sticky BSA part in the engineered proteins serves as a 'root' for surface-independent anchoring on target substrates via various molecular interactions (Figure 3.1b). The conjugated polyacrylates part acts as 'leaves' to access virtually unlimited functionalities with their versatile functional groups, such as zwitterionic, charged, and stimuli-responsive groups.[142] Such bioinspired engineered proteins can facilely bind to various substrates through a facile dip/spraying method with excellent stability in harsh conditions, thanks to the strong and adaptive adhesion of BSA molecules to substrate surfaces. The underlying molecular mechanisms for the versatile adhesion and robust anchoring were elucidated by directly measuring the forces between the BSA protein layer and substrates using a surface forces apparatus (SFA). Conjugated polyacrylates with desired functional groups can customize the physicochemical properties of protein coatings, realizing the tailored surface functions for various biomedical applications. This work provides a straightforward route of using engineered proteins as universal anchors to impart new functionalities to different surfaces and developing versatile protein-based biomaterials for a variety of medical and biological engineering applications.

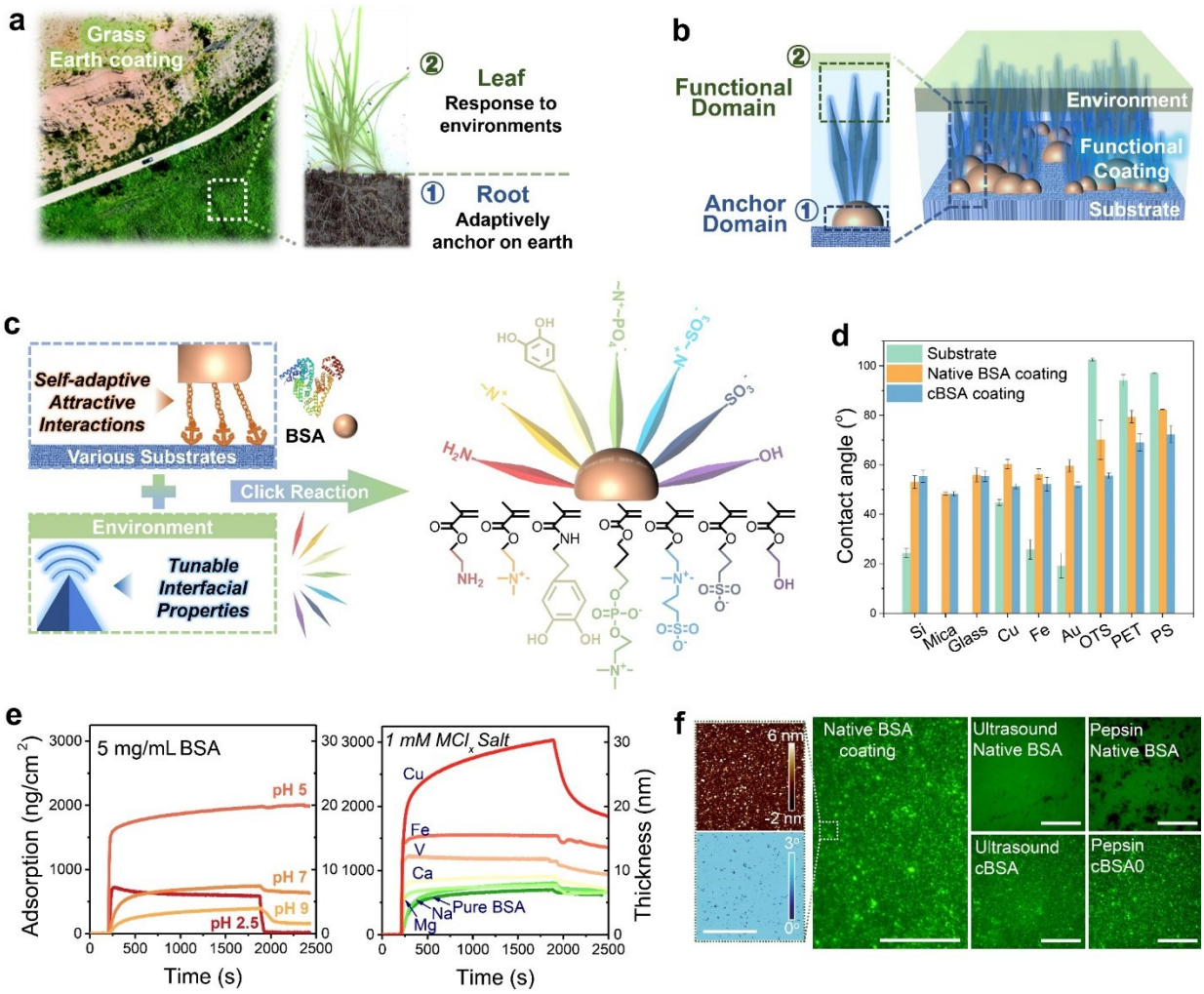

Figure 3.1 A bioinspired engineered protein for universal anchoring and versatile surface functions. a, Grass in the desert area and its 'leaf-root' structure. b, Schematic showing the dual function-anchor layers of desired functional coatings. c, Versatile functional coatings prepared based on BSA protein. d, Static water contact angle on bare substrates and substrates coated with native BSA protein and the crosslinked BSA protein (cBSA). e, Tuning the coating thickness via changing solution pH value and salinity, measured by QCM-D. f, Protein coatings treated in harsh conditions. Scale bars in (f) are 40 μm. Values in (d) represent the mean and the standard deviation (n≥3).

3.2 Experimental Methods

3.2.1. Materials

Bovine serum albumin (BSA), Glutaraldehyde solution (GA, 25 wt% in water), 2-Aminoethyl methacrylate hydrochloride (AMA), [2-(Methacryloyloxy)ethyl]trimethylammonium chloride solution (MTAC), 2-Methacryloyloxyethyl phosphorylcholine (MPC), [2-(Methacryloyloxy) ethyl]dimethyl-(3-sulfopropyl) ammonium hydroxide (known as Sulfobetaine Methacrylate, SBMA), 3-Sulfopropyl methacrylate potassium salt (SPAK), 2-Hydroxyethyl methacrylate (HEMA), Sodium acrylate (SA), Tris buffer (Tris(hydroxymethyl)aminomethane), MES buffer, Ethylenediaminetetraacetic acid (EDTA), L-Cysteine, Trichloro(octadecyl)silane (OTS), NaCl, KCl, $CaCl_2$, $MgCl_2$, $CuCl_2$, $FeCl_3$, VCl_3 powders, polystyrene, polyethylene terephthalate plastic plates, Fluorescein isothiocyanate isomer I (FITC), Pepsin, Tween 80, Dimethyl sulfoxide (DMSO), Methacryloyl chloride, dopamine chloride, sodium borate, sodium carbonate anhydrous, (3-Aminopropyl)triethoxysilane (APTES), N-(3-Dimethylaminopropyl)-N'-ethylcarbodiimide hydrochloride (EDC), Reagent Alcohol (anhydrous), Congo Red, silica sphere powder were purchased from Sigma-Aldrich. Sodium borohydride ($NaBH_4$, >99.0%) was purchased from Fisher Scientific. Cellulose nanocrystal solution (6 wt% solutions in water) and cellulose nanofiber solution (0.9 wt% in water) were purchased from Cellulose lab, Canada. Au, Cu, and Fe substrates were obtained by Electron-Beam evaporation (Gomez, Kurt J. Lesker, CA) of corresponding metal on Si wafer (Substrata, Thin film solutions, CA). Fetal bovine serum (FBS), milk, and Canola oil (lipid) were from the local grocery. Ultrapure water in the experiments was from Milli-Q Advantage A10 (Millipore, USA). PVDF membranes were purchased from Millipore Co. Ltd.

3.2.2. Preparation of BSA and BSA@Polymer coatings

Native BSA and engineered protein BSA@Polymer coatings could be prepared via spraying or dip coating. Specifically, substrates were immersed in 5 mg mL^{-1} native BSA or engineered BSA@Polymer for 4 h, rinsed with ultrapure water and then dried by nitrogen. For spraying coating, as shown in Figure S3.1, 5 mg mL^{-1} protein solution was sprayed on the surface and stored in a humid environment for 30 min to 1 h to form the coating. The as-prepared BSA coatings enhanced by glutaraldehyde crosslinking (2.5% GA for 1 h at room temperature, denoted as cBSA coatings, Figure S3.6) were incubated under different harsh environments for 2 h (aqueous solution with pH 1 and pH 12, 1% pepsin solution, DMSO, and 2% Tween 80 solution) to the robustness of the as-prepared protein coatings. The coatings were subjected to ultrasonic treatment for 1 h. The coverage of the coating on the substrate was calculated based on laser scanning confocal microscope (LSCM) images (labeled by FITC).

3.2.3. Synthesis of engineered protein BSA@Polymer

A broad selection of functions for the protein-based coatings could be imparted through grafting polyacrylates with desired functional groups on BSA molecules via a facile radical-mediated *thiol-ene* click reaction under mild conditions. For example, synthesizing BSA@PSBMA based on BSA and sulfobetaine methacrylate (SBMA) started with the reduction of disulfide bonds in BSA molecules (5 mg mL^{-1}) by $NaBH_4$ (200 mM) for 1h (denote reduced BSA as re-BSA) to produce free thiol groups (-SH). Afterward, the re-BSA solution was mixed with SBMA monomers (200 mM) to initiate the rapid click reaction between free thiol radicals and carbon-carbon double bonds in SBMA. Finally, keep the polymerization at ambient conditions for 30 h. The resultant biopolymer was dialyzed and freeze-dried.

3.2.4. Interfacial interaction forces measurements by surface force apparatus (SFA)

In SFA measurement. One of the mica surfaces was immersed in 50 mM APTES in reagent alcohol (anhydrous) solution for 30 min, then washed with reagent alcohol and dried with nitrogen. The APTES functionalized mica was immersed in the 10 mg mL^{-1} BSA solution with 20 mM EDC for 15 min to prepare the protein-functionalized mica surface. The OTS-coated surface was prepared via immersing the mica surface in 50 mM OTS in the reagent alcohol (anhydrous) solution for 30 min. The Au-coated surface was prepared through the e-Beam method with an ultralow deposition rate (0.1 Å s^{-1}). Then, the BSA-coated surface and mica/OTS/Au surface were mounted in the SFA chamber in a crossed-cylinder configuration. Adhesion (F_{ad}/R) was measured when the two attractive protein-coated mica surfaces were separated and jumped apart (so-called 'jump out'). The normal force was measured based on Hooke's law. The aqueous solution between two surfaces is 1 mM NaCl if not otherwise specified. For the aqueous solutions with different salts, 10 mM NaCl, KCl, $CaCl_2$, $MgCl_2$, $CuCl_2$, and $FeCl_3$ salts were added into ultrapure water, respectively.

3.2.5. In vitro biofouling test

Substrates were incubated in bovine serum, milk, and lipid for 48 h at 37 °C to evaluate the fouling resistance of coatings. Bio-foulants on the surfaces were characterized using O-PTIR (mIRage, Photothermal Spectroscopy Corp, CA). The O-PTIR spectra of bio-foulants in milk, lipid, and serum (Figure S3.19) showed their corresponding characteristic peaks. Then, using IR at 1650 cm^{-1} (milk as an example) to scan the sample surfaces with the resolution of 500 nm to map the milk foulants distributed on the sample surfaces.

3.2.6. Catch-release test

Catch-release test was employed to characterize the pH-responsive performance of coatings. Specifically, the BSA@PAMA coated PVDF and bare PVDF (as the control group) were immersed in 2 mg mL^{-1} Congo Red (CR) solution to catch CR for 5 min and then rinsed with pure water and dried with nitrogen. The CR-dyed membranes were immersed in an aqueous solution with pH 7 and 9.5 to release CR. After releasing CR for a certain time, the solution will be sampled and diluted 10 times before characterization by the UV-Vis spectrum. The absorbances at 510 nm were recorded for Congo red samples.

The release data were fitted using the Korsmeyer-Peppas equation:

$$M^t/M^\infty = kt^n$$

Where M^t/M^∞ is the cumulative release fraction, k is the release constant, n indicates the transport mechanism of the delivery system.

3.2.7. Other Characterization

Controllable preparation of protein coatings could be in-situ monitored by using quartz crystal microbalance with dissipation monitoring (QCM-D, Biolin Scientific, Finland**)**. 5/10/50 mg mL^{-1} BSA solution (pH=7) was introduced into the QCM-D chamber for ~ 30 min and then rinsed with ultrapure water to remove the loosely bonded BSA molecules on Au sensors as shown in Figure S3.2. Similarly, the solution pH was adjusted from pH 2.5 to pH 9, and adding various salts to solution before the coating process. The affinity of 1 mM $CaCl_2$ and 0.36 mM BSA was directly measured by isothermal titration calorimetry (ITC, NanoITC, TA, USA), where the reaction stoichiometry (n), and the change in enthalpy (ΔH), and other thermodynamic parameters could be accurately determined. In a test, 5 μL salt solution was injected into 950 μL BSA 50

injections. The reaction heat was corrected by subtracting the heat of titrant to buffer, buffer to titrand, and analyzed by the different models on the software NanoAnalyze. The stability of the coatings was evaluated by the reciprocating ball-on-disk friction test by NTR^3 nano tribometer (Anton Paar, Austria). Specifically, a nylon ball with a diameter of 2 mm as a counter-facing ball was contacted with the coating in water with applying loading force ranging from 1 mN to 40 mN with a sliding velocity of 1 mm s^{-1} and amplitude 1 mm. X-ray photoelectron spectroscopy (XPS) was obtained from Kratos AXIS Ultra, UK. The binding energy was calibrated by C_{1s} peak at 284.6 eV. Scanning electron microscopy (SEM) and energy dispersive spectrometer (EDS) characterizations were performed on Sigma GEMINI FE-SEM, ZESSI, Germany. Atomic force microscopy imaging was obtained on ICON, Bruker, Germany, using the tapping mode. Static water contact angle in the air of various substrates was measured with a 3 μL ultrapure water droplet.

3.3. Results and discussions

3.3.1 Surface-independent and robust anchoring of BSA protein

The surface-independent, controllable, and robust anchoring of engineered proteins arises from the BSA-substrate interactions in the protein coating process. The sticky BSA (5 mg mL^{-1} dip-coating for 30 min) was coated on various substrates, including inorganics, organics, and metallics (Figure S3.3-S3.4), with a typical thickness of ~14.5 nm (Figure S3.5). After coating, the static water contact angle of substrates all changed from their initial contact angles (~0° to ~105°) to ~60° (Figure 3.1d). The prepared protein coatings could be further stabilized via glutaraldehyde crosslinking (denoted as cBSA), resulting in a slightly decreased contact angle. Besides the universal anchoring, BSA exhibited a controllable coating behavior, which was monitored in real-time using a quartz crystal microbalance with dissipation monitoring (QCM-D). As shown in

Figure 3.1e, fast adsorption of BSA on the Au sensor was observed upon introducing BSA solutions into the QCM-D chamber. After stable adsorption was attained (~1800 s), deionized water was introduced into the chamber to remove the loosely bonded BSA. The QCM-D results in Figure S3.2 indicated that a higher concentration of BSA in the solution would lead to faster protein adsorption and a thicker coating. Solution pH also remarkably influenced the coating process (Figure 3.1e). The adsorption rate was highest at pH near the isoelectric point (Ip, pH 4.8 for BSA), where the electrostatic repulsion among protein molecules was minimal.[59, 124, 146] Salinity also greatly altered the coating behavior of the proteins (Figure 3.1e). It was found that 1 mM of multivalent salt ions could significantly increase the adsorption of proteins on substrates. For example, the BSA adsorption capability in an aqueous solution with Cu^{2+} ions was 4 times higher than that in the pure BSA solution, as displayed in Figure 3.1e. The salt ions could neutralize the surface charges of proteins to decrease the electrostatic repulsion[59, 146] or change the protein secondary structures to enhance the attraction between substrates and protein molecules,[87, 144, 147, 148] accelerating the protein coating process. After being coated on substrates, the proteins could robustly anchor on the substrates even in harsh conditions, including ultrasound, varying pH, surfactant attack, and enzymatic digestion treatments. The atomic force microscope (AFM) and laser scanning confocal microscope (LSCM) images in Figure 3.1f displayed the BSA proteins were uniformly coated on silicon surfaces. Although some proteins detached from the substrates during the harsh environment treatments, the coating coverage remained higher than 85%. After crosslinking with glutaraldehyde, the cBSA coatings could stably anchor on substrates and maintain similar surface coverage and wettability as that before treatments (Figure S3.7-3.10). The crosslinked BSA proteins were more stable in harsh environments.[6, 7] The universal anchoring and robustness of protein coating most likely stemmed from the strong and adaptive interactions

between BSA molecules and substrates,[7, 124] of which the strength could be tuned by solution chemistry, such as pH and salinity, resulting in a controllable coating process.[124, 145, 149] Therefore, such protein-substrate interactions would be directly and experimentally quantified by molecular force measurements.

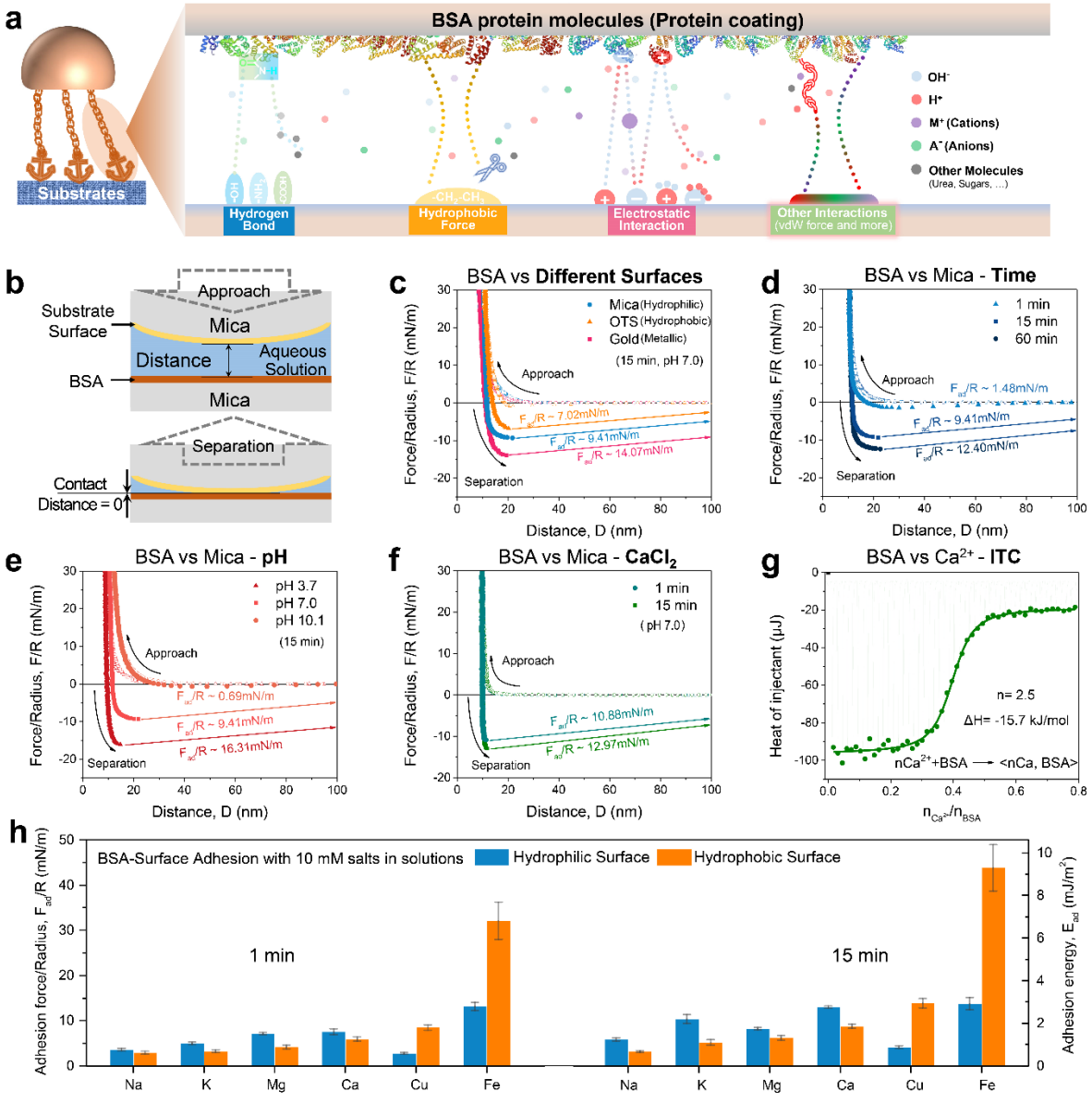

Figure 3.2 Molecular interactions between protein coatings and substrates. a, Schematic showing major interfacial molecular interactions enabling BSA anchoring. b, Typical experimental configurations in SFA force measurements. Interfacial interaction force profiles (normalized force-

distance, F/R-D) of protein coating to different substrate surfaces (c) and to mica surfaces with different contact time (d) in 1 mM NaCl solutions at various pH (e). f, Interfacial interaction force profiles between protein-coating and mica surface in 10 mM $CaCl_2$ solution. g, ITC test between Ca^{2+} ions and BSA protein. h, Normalized adhesion force (F_{ad}/R) and adhesion energy (E_{ad}) of protein coatings and mica (hydrophilic surface) or OTS (hydrophobic surface) determined in aqueous solutions with the addition of various salts. Values represent the mean and the standard deviation ($n \geq 3$).

It is well-acknowledged that the interfacial molecular interactions between substrate surfaces and BSA proteins fundamentally govern the anchoring strength of coatings. Stronger interactions resulted in more robust anchoring. Therefore, directly measuring the interactions between BSA and target substrate surfaces is critical to elucidate the underlying anchoring mechanisms and advance the development of a non-covalent coating strategy. The major non-covalent interactions in the aqueous solution include hydrogen bonding, hydrophobic force, electrostatic interactions, and other interactions (e.g., van der Waals force, cation-π, and anion-π interactions), as indicated in Figure 3.2a.[59, 124, 146, 150] An interfacial binding usually hybridizes several different interactions under a specific condition. The interfacial interaction forces between BSA and substrates in aqueous solutions were measured using a surface forces apparatus (SFA) (Figure 3.2b). For all SFA experiments, 1 mM NaCl was used as a background aqueous solution [151] and other salts were also introduced into the background solution to evaluate their impact on the interfacial molecular interactions. In the SFA measurements, normalized force-distance (F/R-D) profiles and adhesion (anchoring forces) of BSA and to different model substrate surfaces were displayed in Figure 3.2c. It was found that BSA-substrate interaction strengths were substrate-specific. Specifically, BSA demonstrated comparable anchoring strength to the hydrophilic mica

surface (9.41 mN m^{-1}) and to the hydrophobic trichloro(octadecyl)silane (OTS) surface (7.02 mN m^{-1}) and higher adhesion to the metallic gold surface. The adhesion of BSA to mica increased with longer contact time as shown in Figure 3.2d. The enhanced adhesion (7.93 mN m^{-1}) with time between BSA and hydrophilic mica could be mainly due to the strengthened hydrogen bonding.[59, 105, 150] Hydrophobic interaction played an important role in the interactions of BSA with hydrophobic OTS surfaces.[152] Figure 3.2e displayed that the adhesion of BSA to mica surfaces decreased with increasing the solution pH. Such decrease resulted from the increased electrostatic repulsion under the alkaline environment, agreeing with the lower adsorption of BSA shown in Figure 3.1f. In the presence of 10 mM Ca^{2+} ions, the BSA-mica adhesion increased from 9.41 mN m^{-1} to 12.97 mN m^{-1} (Figure 3.2f). Protein-substrate interactions can be complex in the presence of salt ions.[143, 144, 147, 148, 153-157] For example, Ca^{2+} ions could weaken hydrogen bonding between BSA and mica,[59, 124, 146] as suggested by the increase in adhesion when the contact time increased from 1 min to 15 min, which was only 2.09 mN m^{-1} (Figure 3.2f), in contrast to the increased adhesion for the case without Ca^{2+} ions, which was 7.93 mN m^{-1} in Figure 3.2d. Ca^{2+} ions could also reduce electrostatic repulsion between BSA and mica via adsorbing on surfaces to neutralize the surface charge of both mica and BSA (Figure 3.2g).[146] The reduced electrostatic repulsion compensated for the weakened hydrogen binding, leading to an increased adhesion between BSA and mica surfaces in the presence of Ca^{2+} ions. The other ions in the aqueous solutions also influenced the BSA-substrate adhesion, as displayed in Figure 3.2h, S11, and S12. For example, the adhesion of BSA to the hydrophilic mica surface increased from 9.41 mN m^{-1} to 13.75 mN m^{-1} in the presence of 10 mM Fe^{3+} ions; and the adhesion forces to the hydrophobic OTS surface (43.8 mN m^{-1}) in 10 mM Fe^{3+} solution improved to 625% of the solution without Fe^{3+} ions (7.02 mN m^{-1}). Generally, electrostatic attraction increased with the presence of ions (adhesion of

contact for 1 min, Figure 3.2h) due to the charge neutralization of protein surfaces,[59, 146, 147, 157] whereas the ions weakened the hydrogen binding at a different level. As a result, the adhesion forces at 15 min of contact were ion-specific, as indicated in Figure 3.2h. The overall effects of multivalent ions on BSA adhesion are quite complex and might involve ion-protein affinity (following one of the Hofmeister Lyotropic series),[59, 150, 153-156] ion-protein reactions,[147] and ion-induced protein structure changes.[148, 149] Nevertheless, the results of interfacial molecular force measurements demonstrated that the strong anchoring capability of BSA protein originated from multiple molecular interactions, and the strength of these interactions could adaptively change with the target surface properties and the chemistry of the surrounding aqueous solution, such as pH and salinity.

3.3.2 Synthesis of versatile BSA@Polymers for surface functionalization

A series of BSA@Polymer engineered proteins have been developed in this work, as shown in Figure 3.3a.[88, 96, 124] For example, starting with the reduction of disulfide bonds in BSA molecules to produce free thiol groups (-SH) as detected using UV-vis spectrum (Figure 3.3b) and X-ray photoelectron spectra (XPS) (Figure 3.3c).[158]. Then, the re-BSA solution was mixed with SBMA to initiate the rapid click reaction between free thiol radicals and carbon-carbon double bonds in SBMA, during which most of the free thiol groups reacted with carbon-carbon double bonds as suggested in Figure 3.3d. Fourier transform infrared spectra (FTIR, Figure 3.3e and S13), XPS scan (Figure 3.3f and S3.14), and energy dispersive spectra (EDS, Figure S3.16) confirmed that the as-synthesized BSA@Polymer contained both the characteristic peak of polyacrylates and BSA, indicating the successful preparation of eight BSA@Polymers. For example, the FTIR spectrum of BSA@PSBMA included amide peaks of BSA and -C=O and -SO_3 groups of SBMA monomer (Figure 3.3e); XPS (Figure 3.3f) and EDS (Figure S3.16) double-confirmed the presence

of -SO_3 in engineered protein.[124] FTIR spectra of BSA@PSPAK (SPAK, 3-Sulfopropyl methacrylate potassium, Figure S3.17) showed that the carbon-carbon double bond (980 and 1275 cm^{-2}) in SPAK monomer was broken after polymerization and the presence of SPAK (-C=O group, 1726 cm^{-2} and -SO_3, 1040 cm^{-2}) and BSA (Amide I and Amide II) in the final product. The synthesized BSA@Polymers could easily dip/spray coated on substrates to perform diverse functions for versatile scenarios.

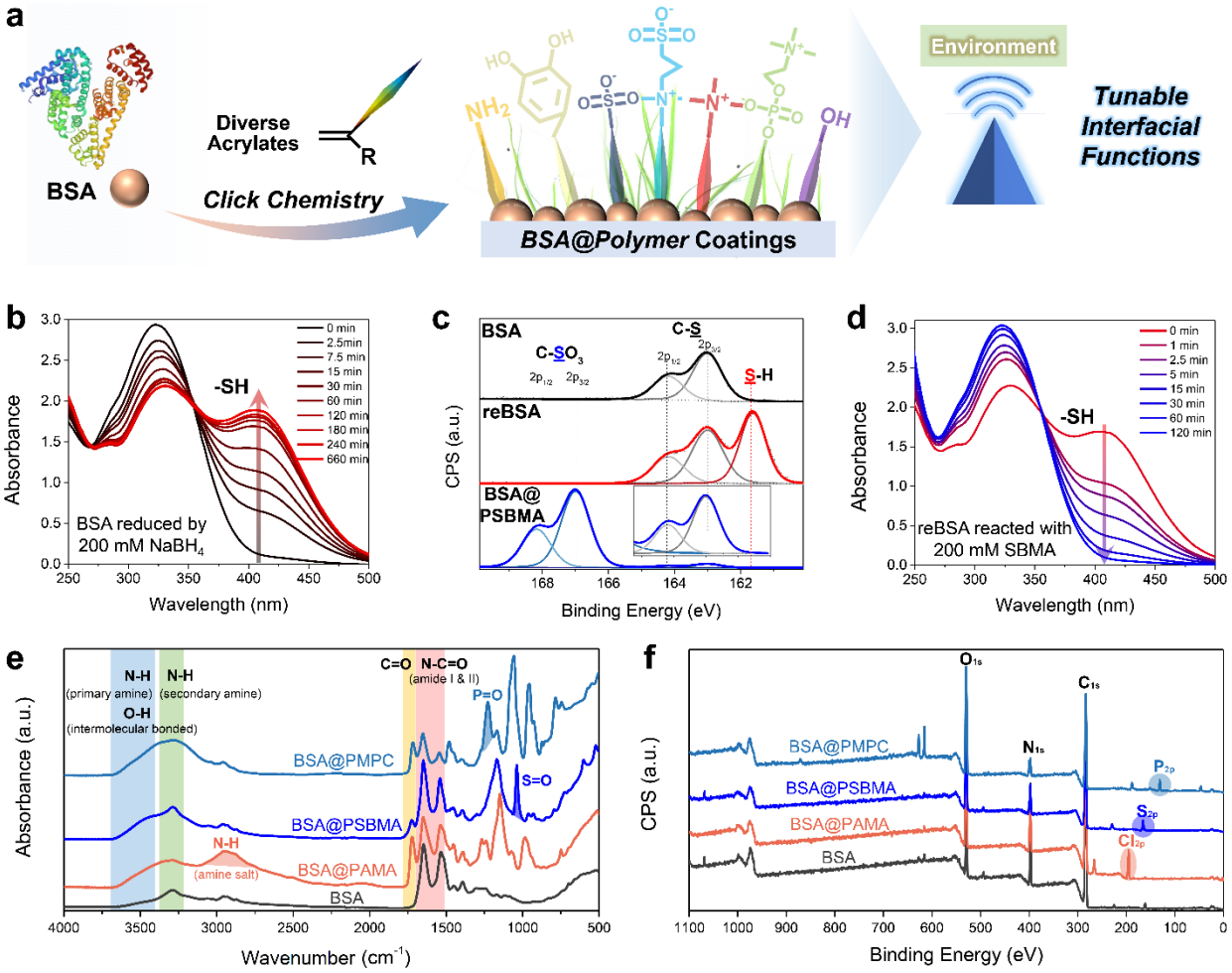

Figure 3.3 Synthesis of engineered protein BSA@Polymer with diverse functional groups via click chemistry. a, Schematic showing the process of synthesizing BSA@Polymer via thiol-ene click chemistry, where R is -CH_3 or -H. b, UV-Vis spectra of Ellman's reagent to detect

the free thiol groups in protein solution during the reduction by $NaBH_4$. c, XPS high-resolution S deconvolved spectra of BSA, re-BSA, and BSA@PSBMA. d, VU-Vis spectra of Ellman's reagent to detect the free thiol groups during reBSA reacted with SBMA monomers. FTIR spectra (e) and XPS survey scan (f) of several typical synthesized BSA@Polymers.

3.3.3 Antifouling properties of BSA@PSBMA engineered protein coating

The diversity of engineered protein BSA@Polymer could impart substrate surfaces with tunable and versatile physicochemical properties for various applications, such as non-adhesion antifouling surface,[3, 7, 121, 124, 159] pH-responsive coating for catch-release property,[160, 161] and adhesive interfacial glue, [105, 145] as indicated in Figure 3.4a. The interactions of BSA@PSBMA (blue) and BSA@PMTAC (red) to mica surfaces were displayed in Figure 3.4a and S3.17, where BSA@PSBMA demonstrated near zero adhesion to substrates while BSA@PMTAC exhibited a strong adhesion. The area between adhesion and non-adhesion was the transition domain with tunable interfacial interaction. BSA@PSBMA as an antifouling coating was demonstrated in this work. Specifically, gold substrates were first dip-coated in 5 mg mL^{-1} BSA@PSBMA solution for 4 h. Then, the protein coating was patterned as indicated in Figure 3.4b. Finally, incubating the patterned protein-coated substrate in milk at 37 °C for 48 h before characterizing the foulant distribution by optical photothermal infrared (O-PTIR) (Figure S3.19). Figure 3.4c clearly showed that non-coated parts of substrates were contaminated by the foulants from milk, while in BSA@PSBMA-coated areas, no foulant was founded. The antifouling coatings also demonstrated excellent fouling resistance to other biological fluids, such as lipid (Canola oil) and fetal bovine serum, and the corresponding foulants distribution was displayed in Figure 3.4d and S3.19. The coverage of foulants on substrate surfaces was quantified by setting foulants coverage on bare substrate surfaces as 100% in Figure 3.4e. It was found that bare substrate surfaces were all covered

with a large number of foulants, while BSA@PSBMA coatings resisted over 99% of foulants from all complex biofluids. This superior antifouling property of BSA@PSBMA most likely originated from its bionic structure with strong interfacial hydration and steric repulsion, hindering the initial attachment of foulants on surfaces.[3, 7, 8, 59, 121, 124, 159]

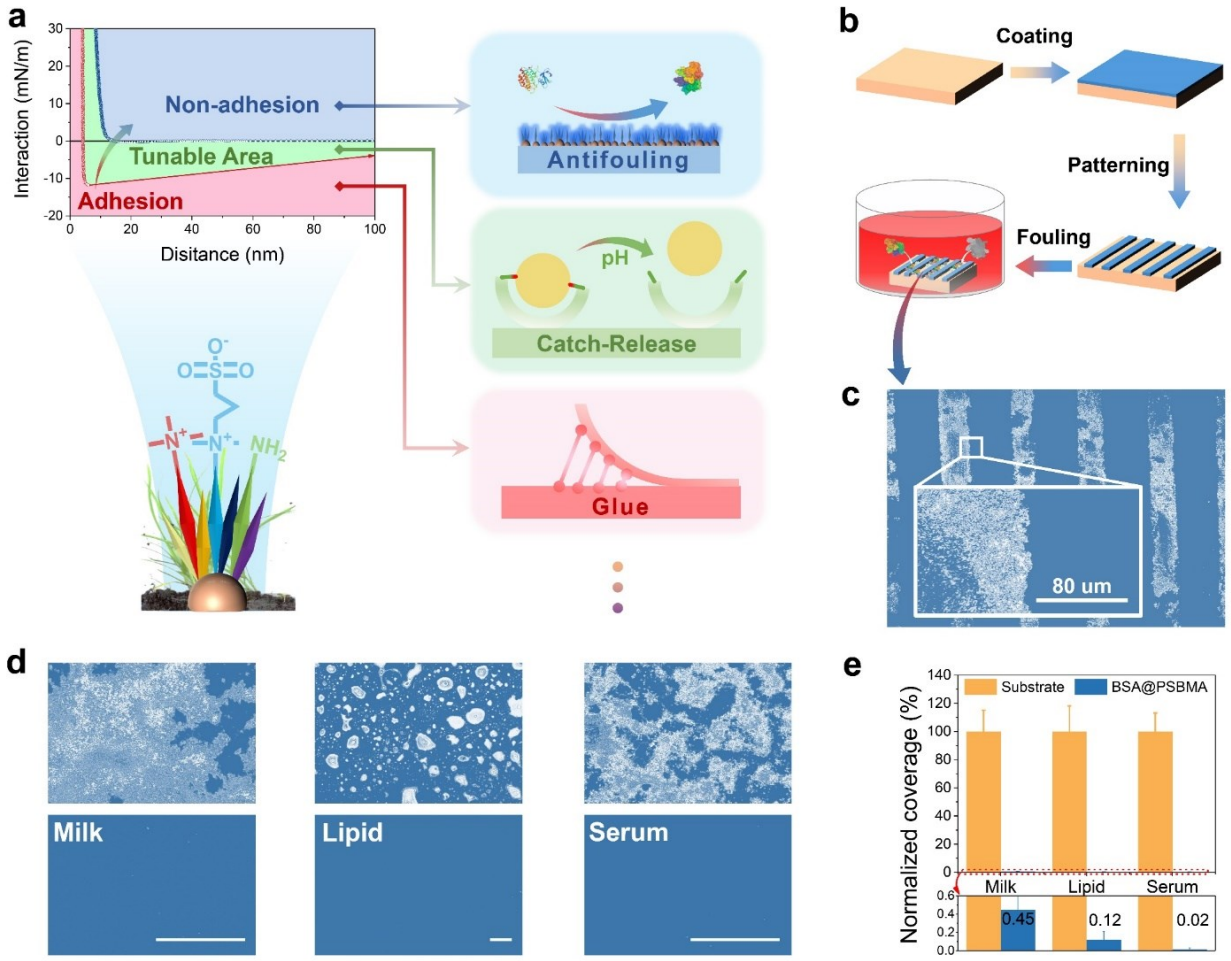

Figure 3.4 Multifunctional BSA@Polymer coatings and BSA@PSBMA antifouling coating. a, Interfacial interactions of different BSA@Polymer coatings to substances from the surrounding environment and potential applications. b, Preparation of BSA@PSBMA antifouling coating, fouling test, and corresponding foulants distribution mapped by O-PTIR (c). d, O-PTIR mappings of foulants on the bare substrate surfaces and BSA@PSBMA coated surfaces, and

corresponding fouling coverage in milk, lipid, and bovine serum solutions (e). Scale bars in (d) are 500 μm. Values in (e) represent the mean and the standard deviation (n≥3).

3.3.4 pH-responsive properties of BSA@PAMA engineered protein coating

Tunable or smart surfaces that exhibit stimuli-responsive functions are essential for targeted therapy, controllable drug release, water treatment, waste removal, and interventional imaging, which could be achieved via coupling stimuli-responsive polyacrylates with native proteins.[160-163] For example, AMA (2-Aminoethyl methacrylate hydrochloride) with the pH-responsive amino groups (-NH_2) was grafted on BSA to produce the engineered protein BSA@PAMA. The as-prepared BSA@PAMA coating exhibited pH-responsive behavior and was employed as a carrier for the controllable catch-release, as indicated in Figure 3.5a. At pH 7, the amino groups in BSA@PAMA will be protonated, and therefore BSA@PAMA will be positively charged, leading to electrostatic attraction and catching the negatively charged model contamination CR. At pH 9.5, the carboxyl groups on BSA will be deprotonated, and therefore BSA@PAMA will be negatively charged, leading to electrostatic repulsion and releasing the CR (Figure 3.5a and 3.5b). Based on this tunable performance, BSA@PAMA coated polyvinylidene fluoride (PVDF) membrane could be contaminated at pH 7 and then release contamination at pH 9.5, as indicated in Figure 3.5c, S3.20-S3.21. The catch-release behavior of the BSA@PAMA coated PVDF and bare PVDF membrane was quantified using UV-Vis spectra (Figure 3.5d and S3.22). It was found that almost no CR was released from BSA@PAMA-coated PVDF at pH 7, while at pH 9.5, the CR was released from BSA@PAMA-coated surfaces rapidly. The cumulative release of CR was displayed in Figure 3.5e and Figure 3.5f, indicating that the release rate of CR from BSA@PAMA-coated PVDF membrane at pH 9.5 was 8.5 times higher than that at pH 7. BSA@PAMA coating is an example of stimuli-responsive coating. Other BSA@Polymer coatings

with tunable functions for customized applications could also be prepared based on the strategy in this work.

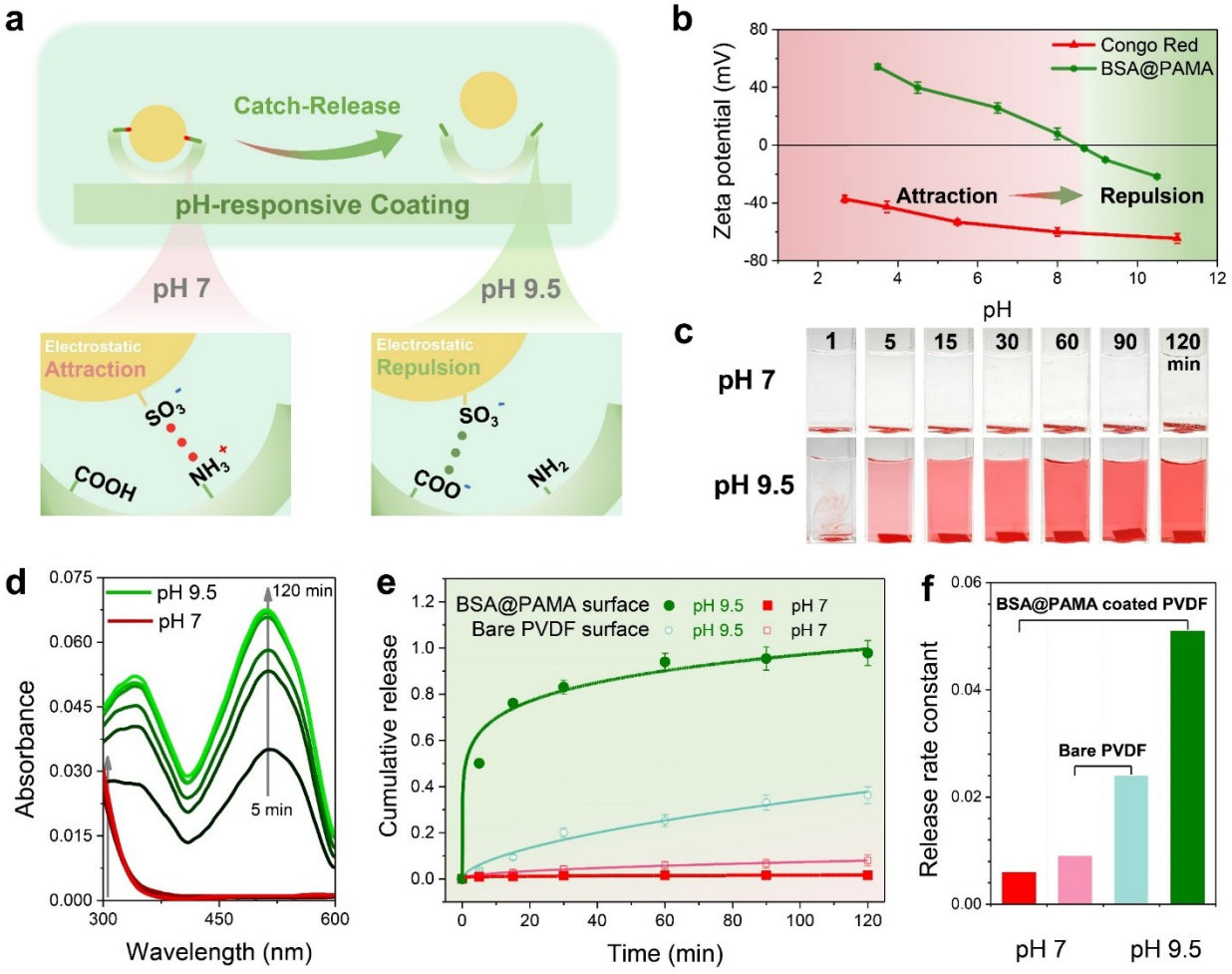

Figure 3.5 BSA@PAMA pH-responsive coating as cargo for catch-release. a, Interfacial interactions of BSA@PAMA coatings with model dye (Congo Red) at different pH. b, Zeta potential of BSA@PAMA and CR. c, optical image: BSA@PAMA-coated PVDF membranes release CR at different time. d, UV-Vis spectra of the solutions with the released CR in Figure 3.5c. e, Cumulative release of CR of different surfaces and their release rate constant (f). Values in (e) represent the mean and the standard deviation (n≥3)

3.3.5 Adhesive properties of BSA@PMTAC engineered protein coating

Immobilizing nanomaterials on therapeutic sensors is commonly needed for bioengineering applications, and therefore an interfacial binder that could 'glue' various nanomaterials has been developed based on the engineered protein BSA@PMTAC, as it showed strong attraction to the negatively charged surfaces (Figure 3.4a). MTAC is the methacrylate with quaternary ammonium group that maintains positively charged to attract negatively charged nanomaterials, such as the rigid and hydrophilic cellulose nanocrystal (CNC), silica spheres, and cellulose nanofibers (Figure 3.6a) on its surface. Figure 3.6a clearly showed that the CNC could not be immobilized on the substrate without the BSA@PMTAC coating. The reciprocating ball-on-disk friction test evaluated the stability of the immobilized CNC on BSA@PMTAC coating.[164] The typical friction curves - friction force versus sliding distance under a certain normal loading force - were shown in Figure 3.6b. The CNC/BSA@PMTAC coating was undergone over 1000 cycles of friction, in which the normal force increased from 5 mN to 40 mN in the initial stage and then decreased from 40 mN to 1 mN, then gradually increased back to 25 mN. The friction coefficient between the ball and CNC/BSA@PMTAC coating under 10 mN of loading force was 0.46 during the 100-150 cycles of friction and remained almost unchanged after 950 cycles (Figure 3.6c). It suggested that CNC/BSA@PMTAC coating maintained its structural integrity during the friction test, and CNC was firmly glued on the adhesive BSA@PMTAC surfaces. These three applications offered practical paradigms for introducing on-demand functions to engineered proteins, such as BSA@Polymer, and then facilely applying these engineered proteins as coatings to enable versatile surface functions, ranging from adhesion to antifouling and beyond.

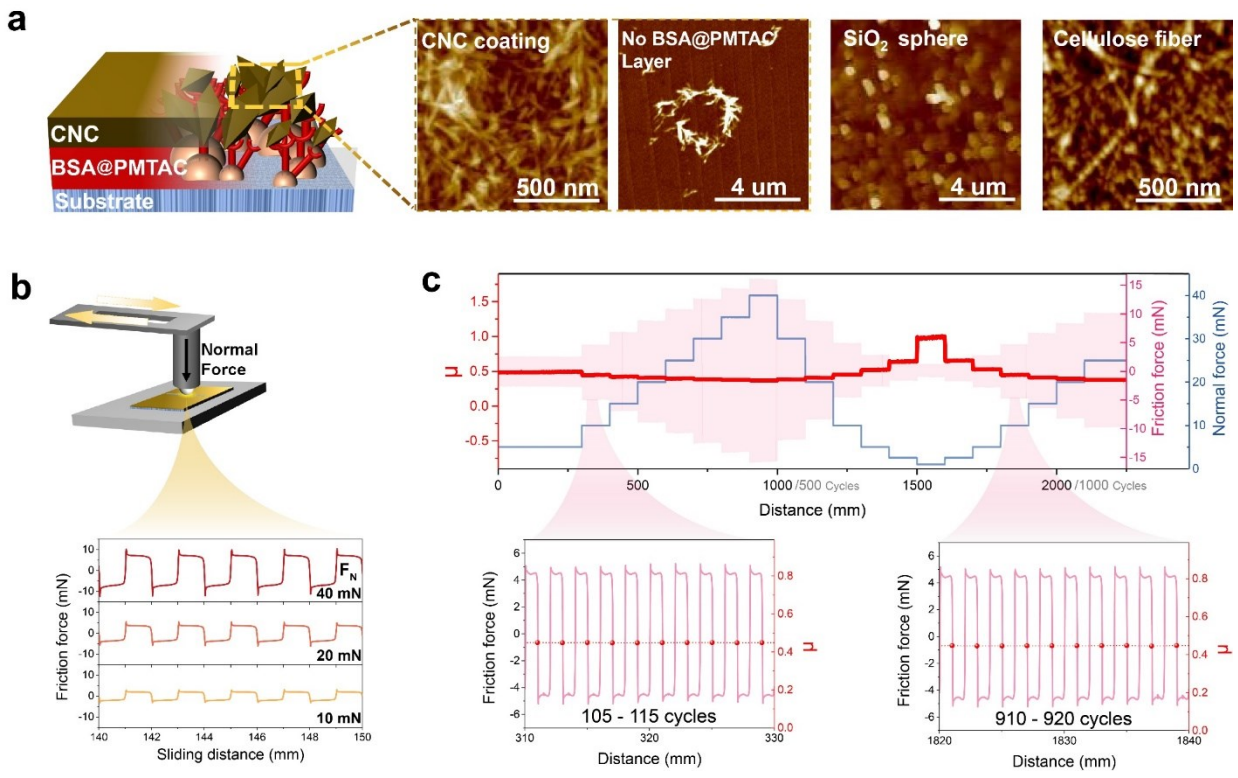

Figure 3.6 BSA@PMTAC adhesive coatings as the interfacial binder. a, CNC, silica sphere, and cellulose fiber integrated on the BSA@PMTAC coating. b, the experimental setup of nanotribometer for reciprocating ball-on-disk friction test and typical friction forces with the normal loading force of 10, 20, and 40 mN. c, Friction coefficient change under different loading forces during >1000 friction cycles.

3.4. Conclusions

In summary, we have developed a series of engineered protein BSA@Polymers that can universally anchor on diverse substrate surfaces and impart surfaces with various on-demand functionalities. The engineered proteins were prepared by grafting polyacrylates with a broad selection of physicochemical properties on BSA molecules via facile *thiol-ene* click chemistry in accordance with a bionic 'root-leaf' design. The as-prepared engineered proteins not only

preserved the intrinsic stickiness of native BSA proteins, enabling robust anchoring on metallic, inorganic, and organic surfaces even under harsh conditions, including ultrasound, varying pH, surfactants attacks, and enzymatic digestion treatment, but also integrated the artificially introduced functions of polyacrylates for versatile and tailored surface functionalization. Molecular force measurements revealed that the stickiness of BSA stemmed from its multiple adaptive molecular interactions with target substrate surfaces, which could be tuned by the solution chemistry, such as pH and salinity. Eight polyacrylate-conjugated proteins were successfully developed in this work and could be facilely applied to surfaces via a simple dip or spray coating method. We demonstrated three potential applications of those engineered protein coatings. BSA@PSBMA, as an antifouling coating, can effectively resist over 99% of foulants in complex biological fluids. BSA@PAMA coating can catch and release CR in a controllable manner via changing the solution pH. BSA@PMTAC coating served as an interfacial binder, robustly immobilizing various nanomaterials for non-implantable medical devices. Compared with previous work in engineering proteins for a specific application such as antifouling or adhesion, [6, 7, 124] This study showcases the efficacy of engineering the native protein BSA as a versatile backbone with multiple functions, applicable across a diverse range of scenarios and applications. This work further demonstrates the versatility of BSA-based materials, illustrating their universal anchoring capabilities and ability to accommodate diverse surface functionalization for nano- and bio-applications. The method in this work can be readily extended to engineer other native proteins with desired functional chemical motifs, boosting the development of new biomaterials and protein-based coatings for bioengineering applications and nanotechnologies, such as self-assembly, point-of-care diagnostics, chemical sensing, and molecular sieve-assisted phase separation.

Supporting Information

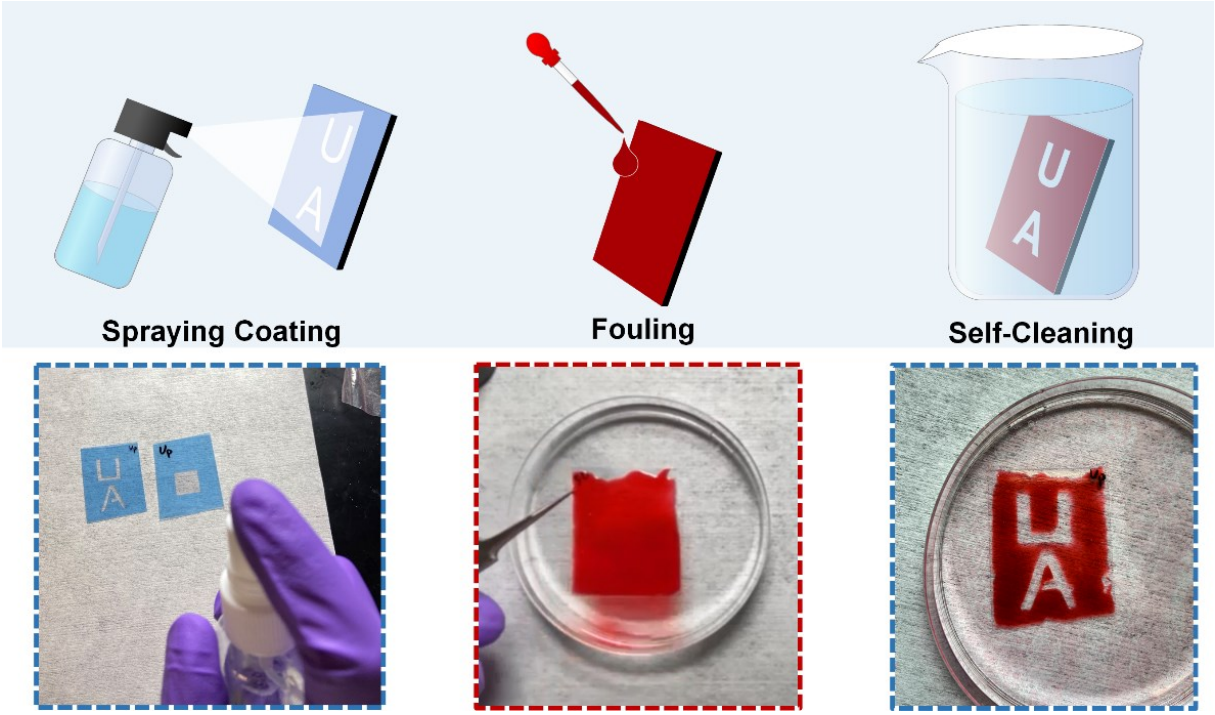

Figure S3.1 Preparation of BSA@PSBMA coating by spraying method and self-cleaning test.

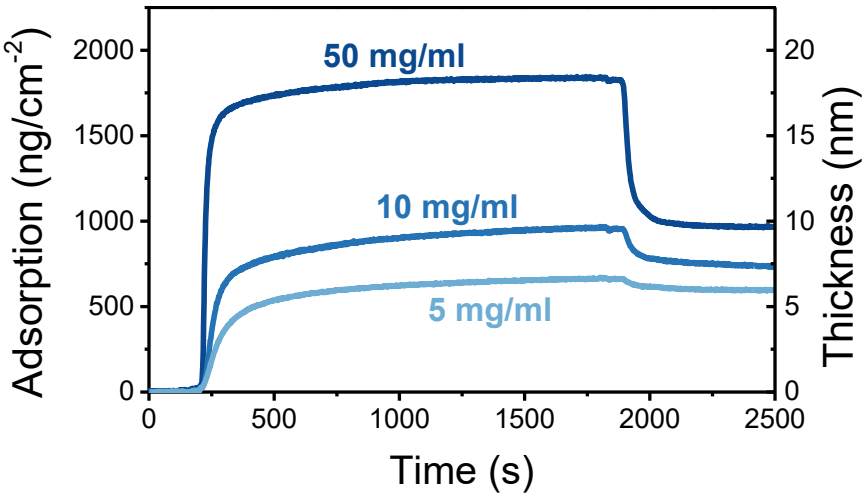

Figure S3.2 QCM-D curves: the change in resonance frequency associated with BSA adsorption in the solution with different BSA concentrations.

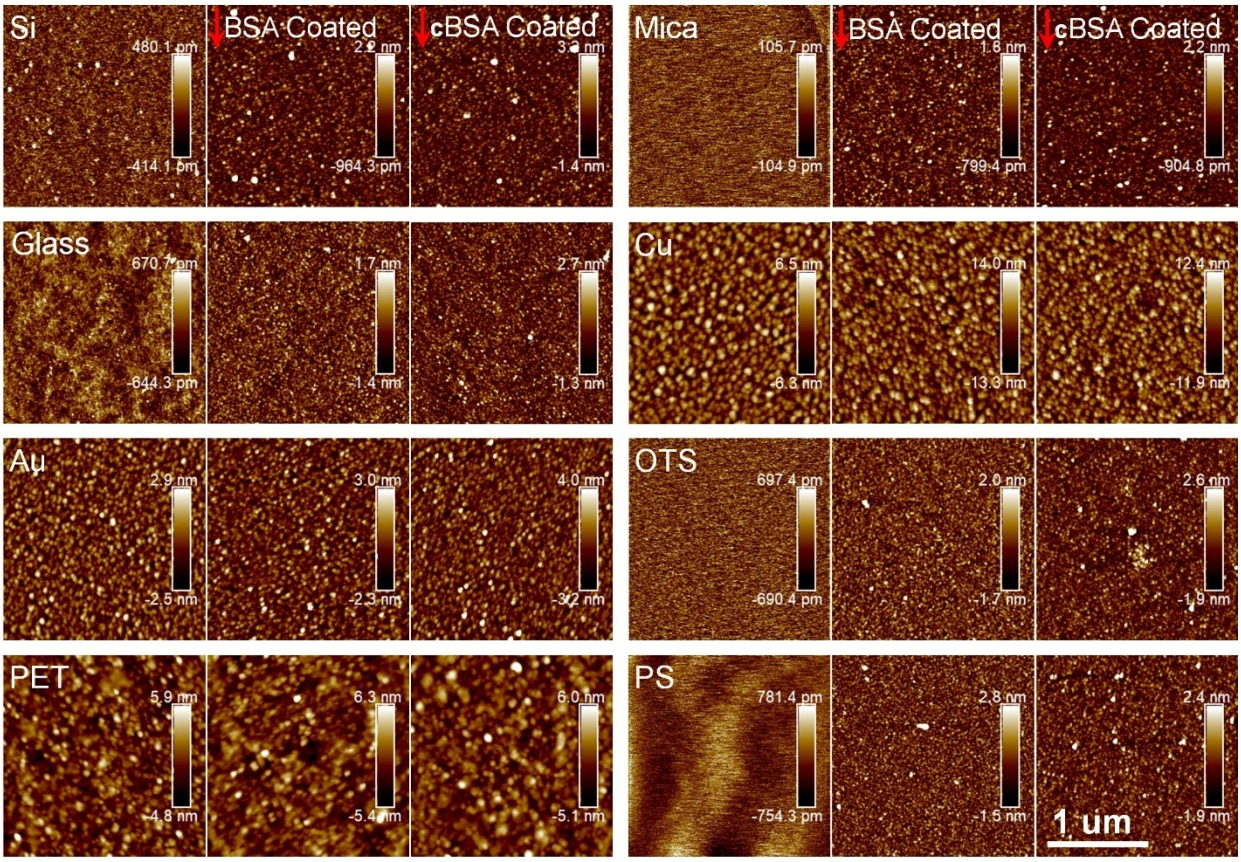

Figure S3.3 AFM images (2x2 μm^2): Morphology of bare substrate surfaces and the surfaces coated with native BSA and cBSA

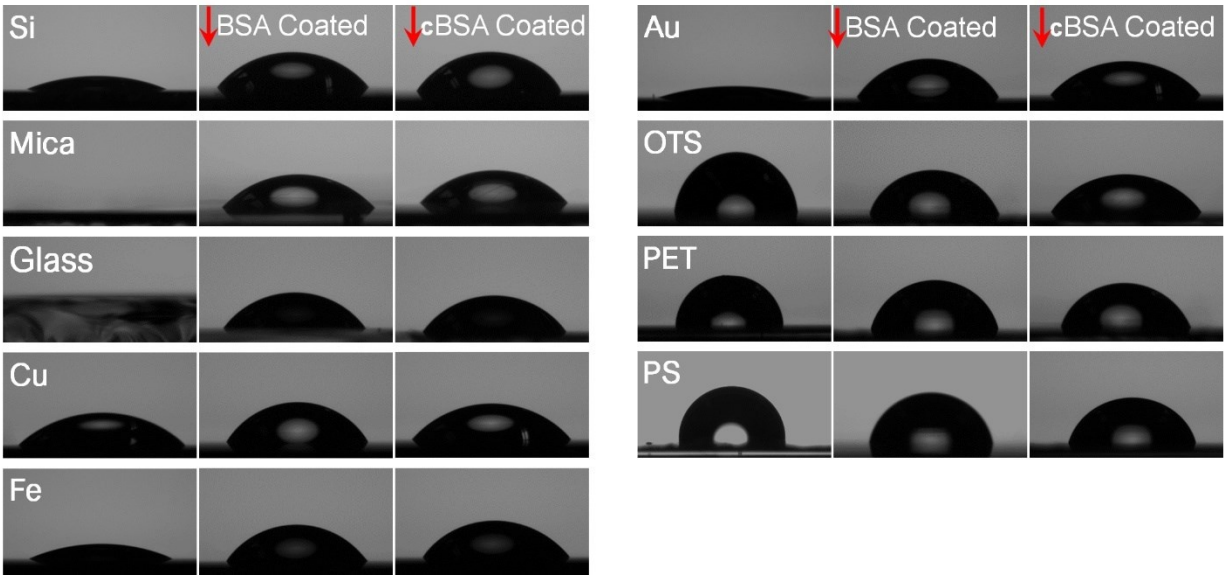

Figure S3.4 Static water contact angle in the air of various surfaces

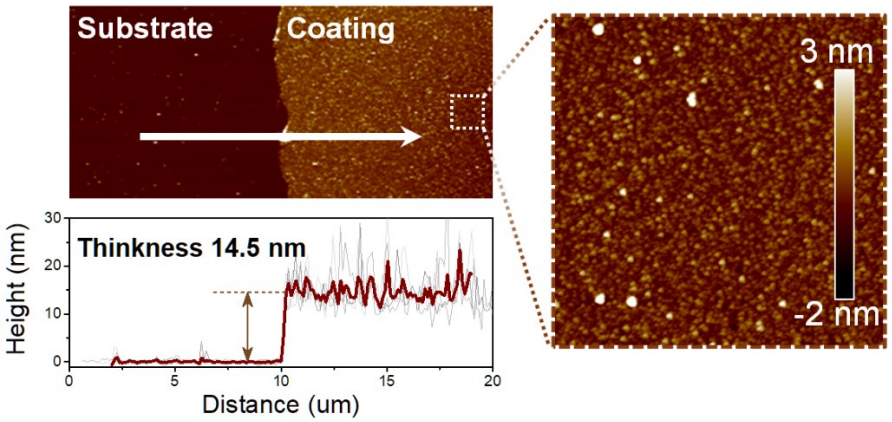

Figure S3.5 Thickness of the coating after dip-coating in 5 mg mL^{-1} BSA solution for 30 min.

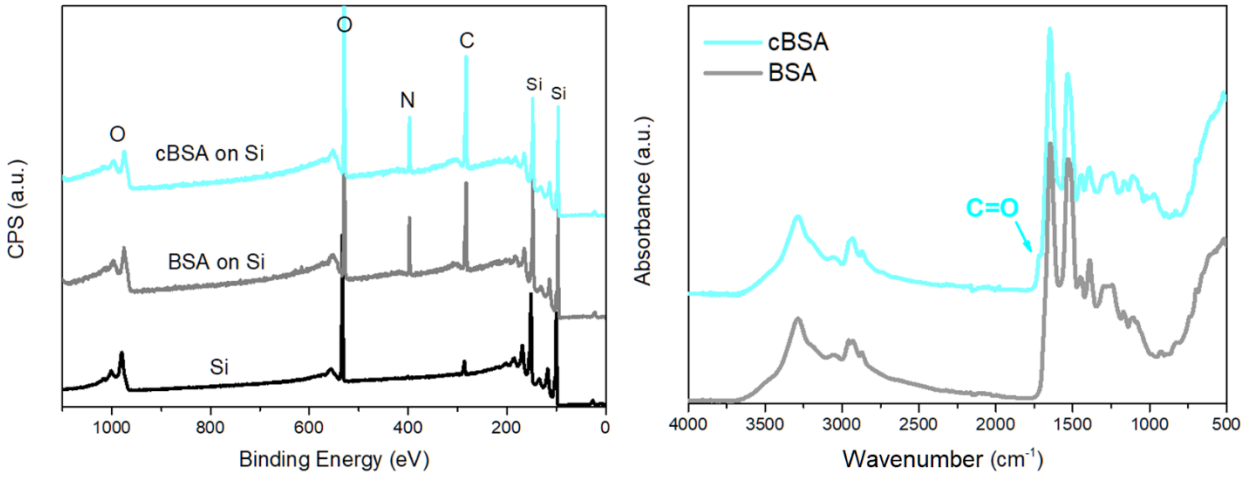

Figure S3.6 cBSA and BSA coating on Si wafer characterized by XPS and FTIR.

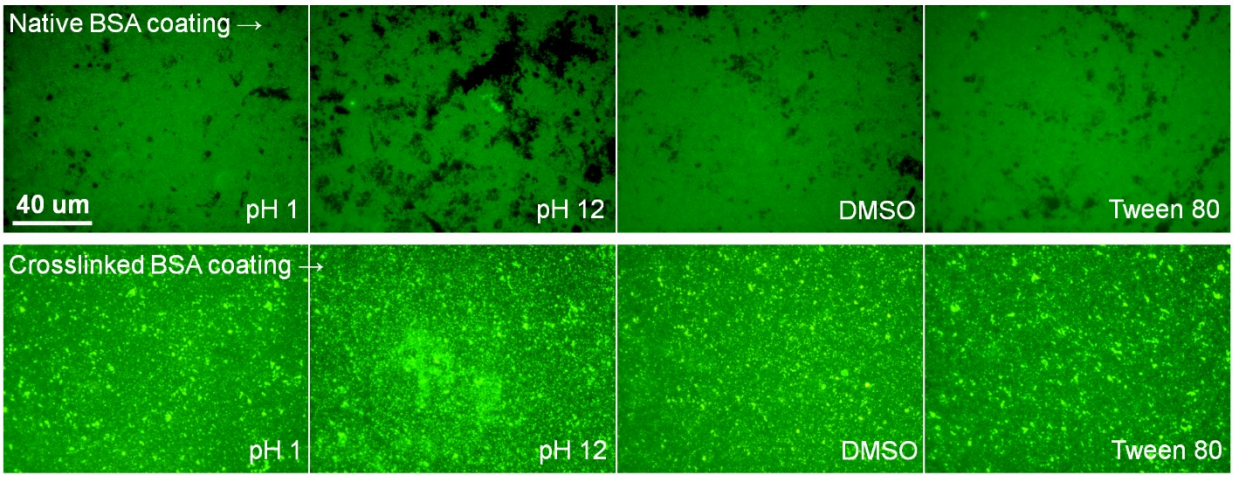

Figure S3.7 LSCM images of protein coatings after treatments in harsh conditions

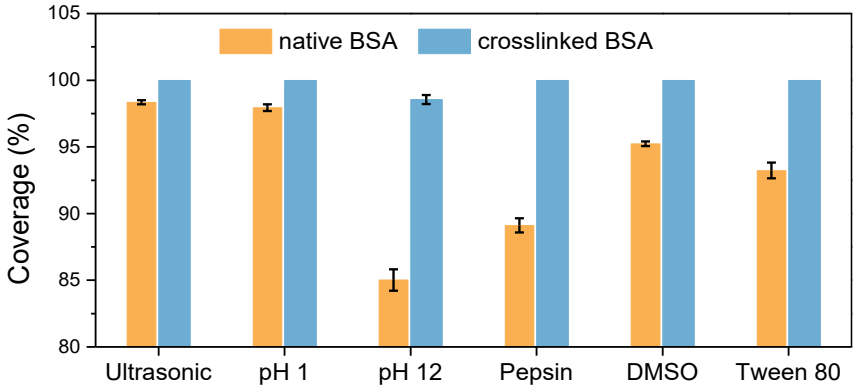

Figure S3.8. Protein coating coverage before and after harsh conditions treatments

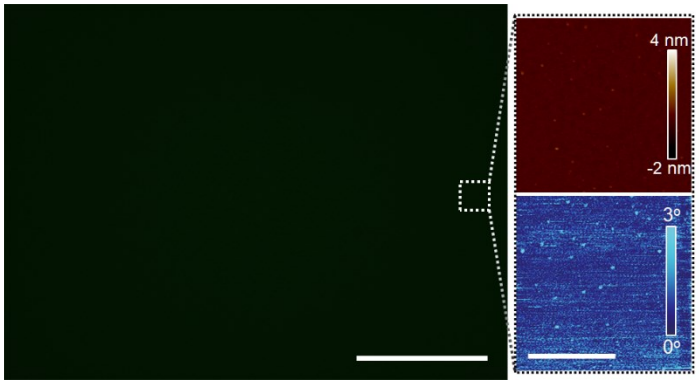

Figure S3.9 LSCM image of bare silicon surface and corresponding AFM morphology (upper right) and phase image (bottom right). Scale bar in LSCM image is 40 μm in AFM image is 1 μm.

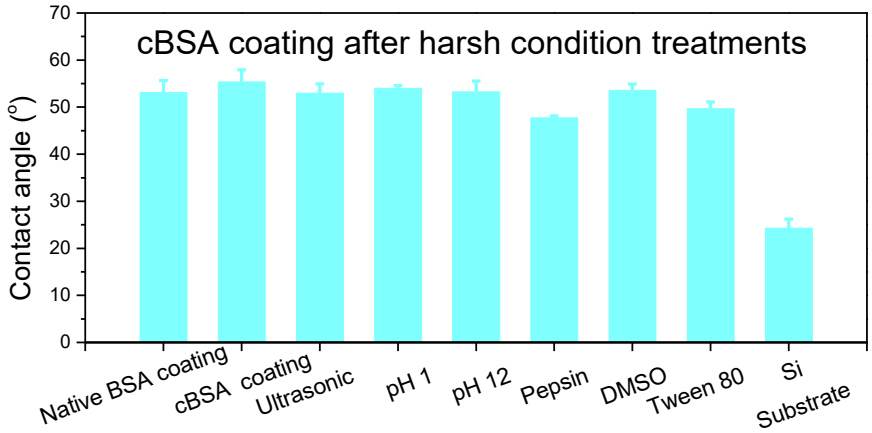

Figure S3.10 Static water contact angle of protein coatings after treatments in harsh conditions

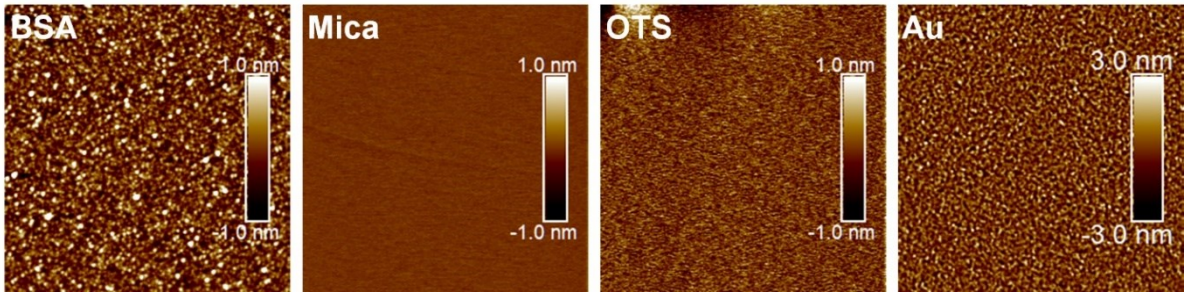

Figure S3.11 AFM images (2x2 μm^2): Morphology of mica and the surfaces coated with BSA, OTS, and Au for SFA measurements.

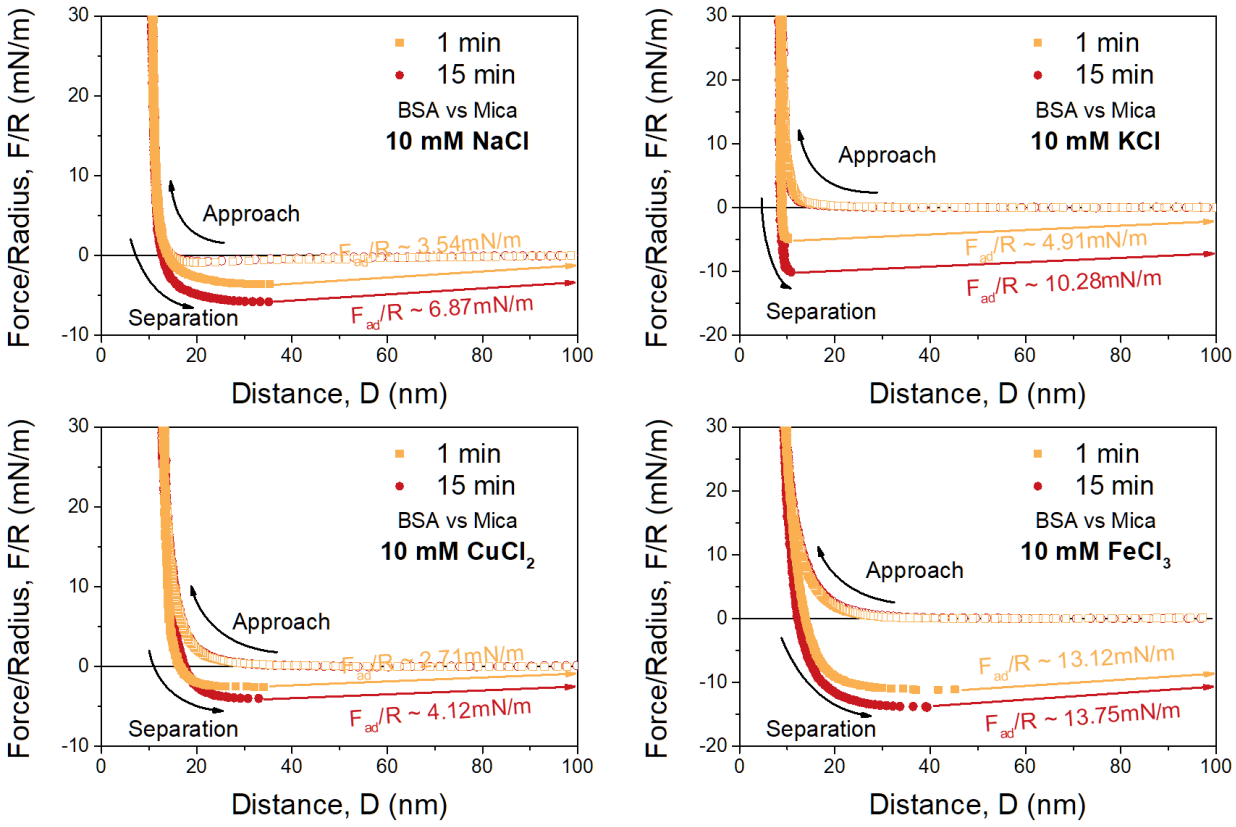

Figure S3.12. Force-distance profiles between native BSA and mica surface in solutions with different salinity

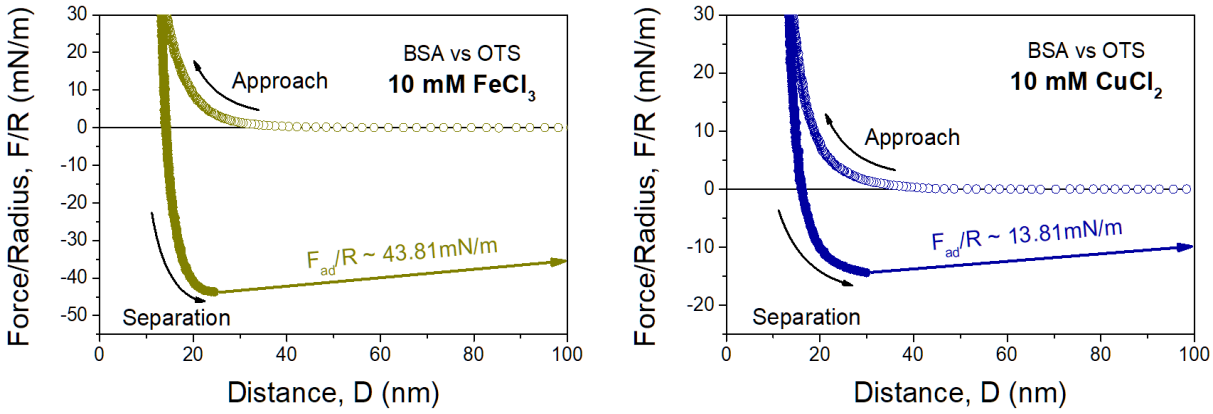

Figure S3.13 Force-distance profiles between native BSA and OTS surface in solutions with $FeCl_3$ or $CuCl_2$.

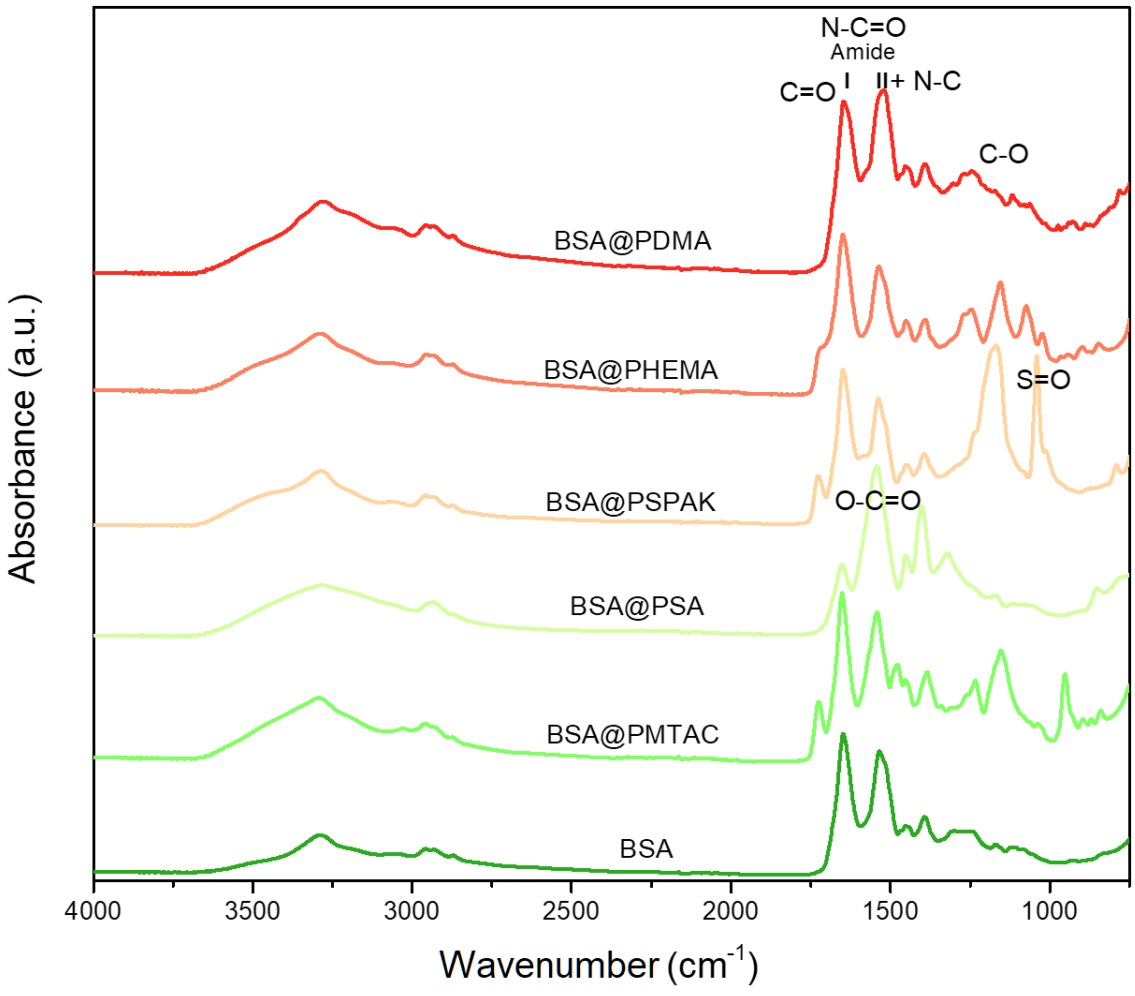

Figure S3.14 FITR spectra of synthesized BSA@Polymer

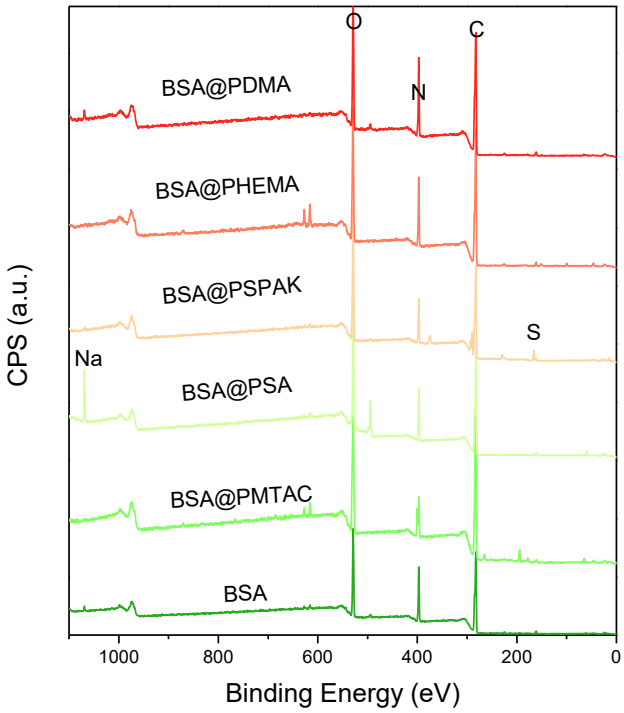

Figure S3.15 XPS survey scan of synthesized BSA@Polymer

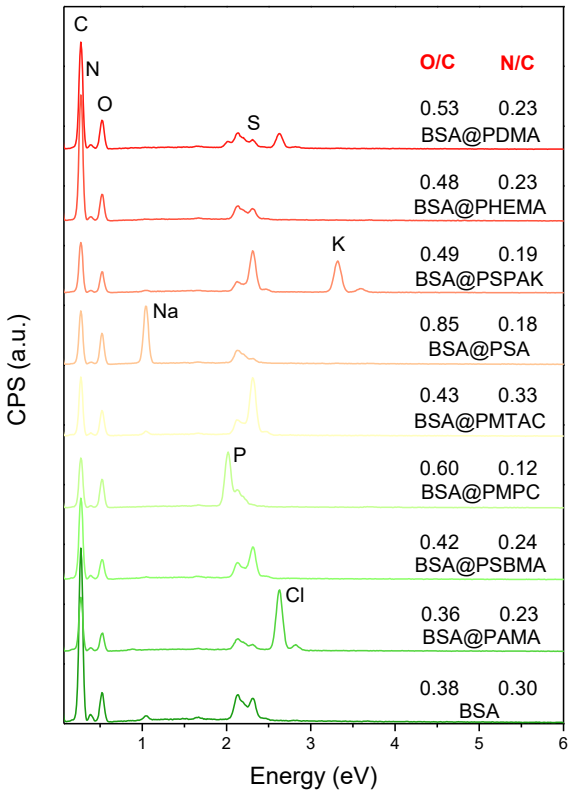

Figure S3.16 EDS spectra of synthesized BSA@Polymer

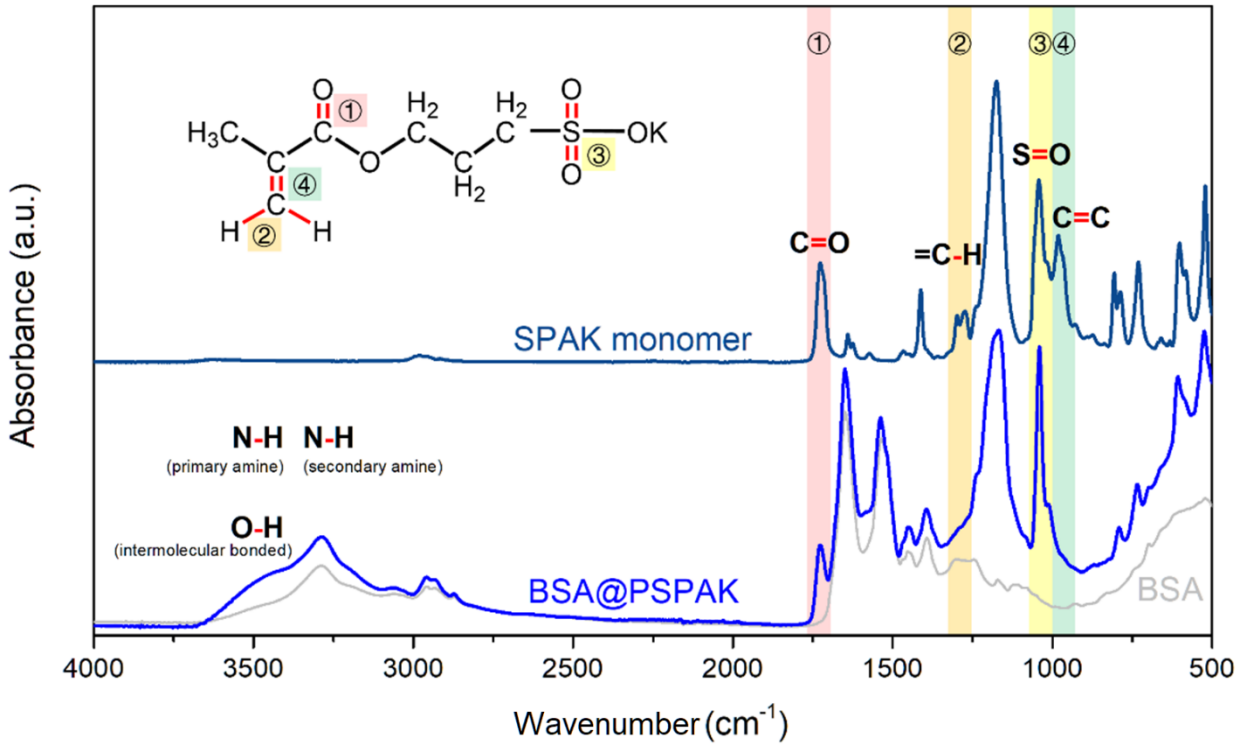

Figure S3.17 FITR spectra of native BSA, SPAK monomer, and as-synthesized BSA@PSPAK. The FITR spectrum of BSA@SPAK combined the characteristic peaks of BSA and SPAK except for the double carbon bond in SPAK.

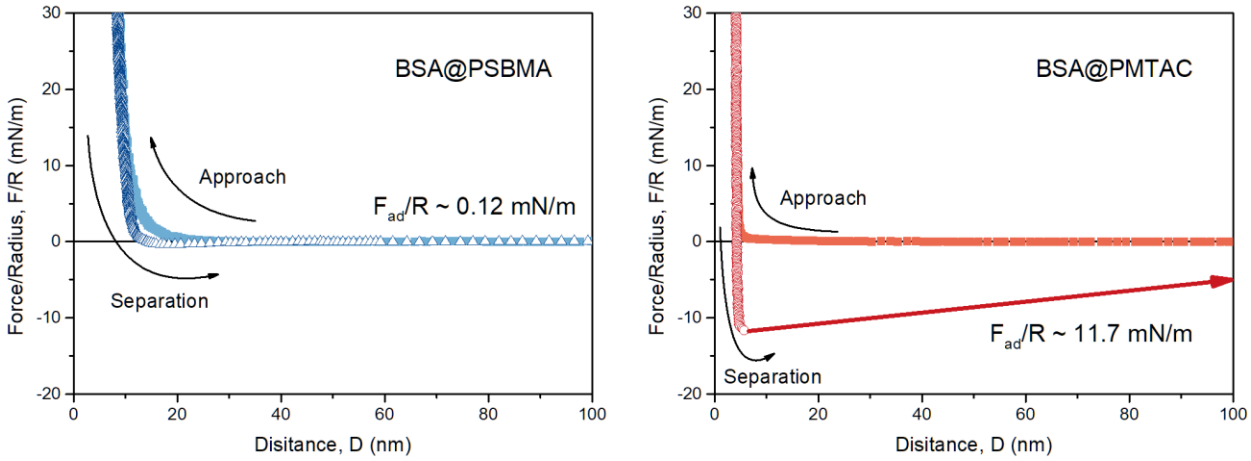

Figure S3.18 Interfacial interactions (normalized force-distance, F/R-D, profiles) between mica surfaces and BSA@PSBMA / BSA@PMTAC

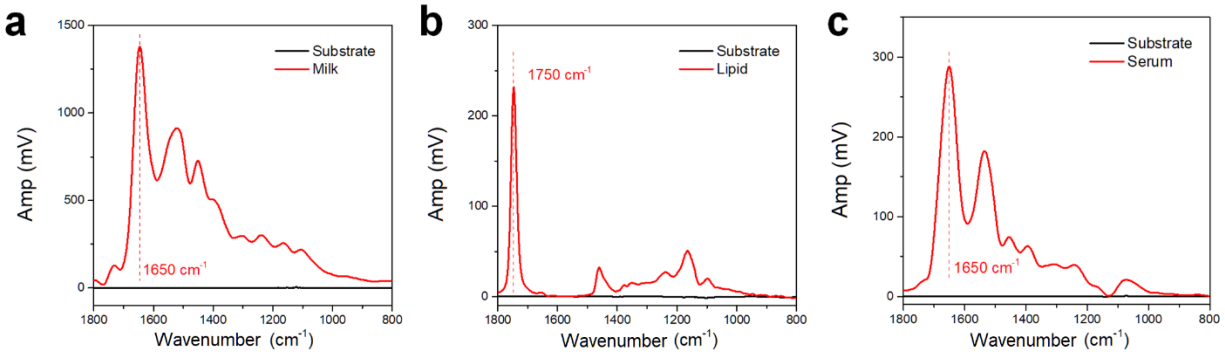

Figure S3.19 O-PTIR spectra of Milk, lipid, and serum (marked wavelength used as the characteristic peck for mapping)

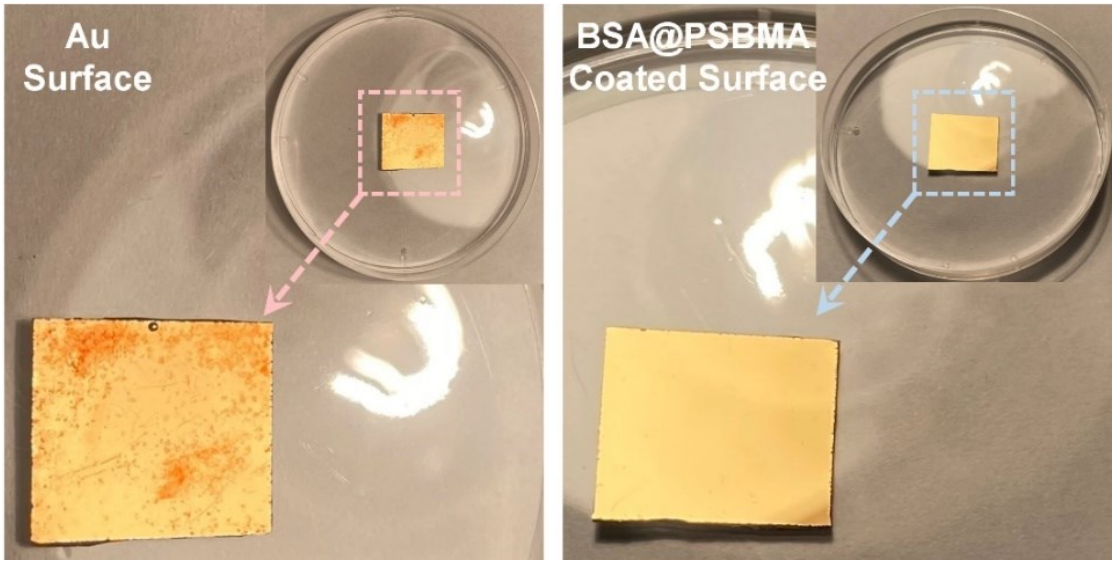

Figure S3.20 Gold wafer surface and the BSA@PSBMA coated surface immersed in fetal bovine serum for 48 h

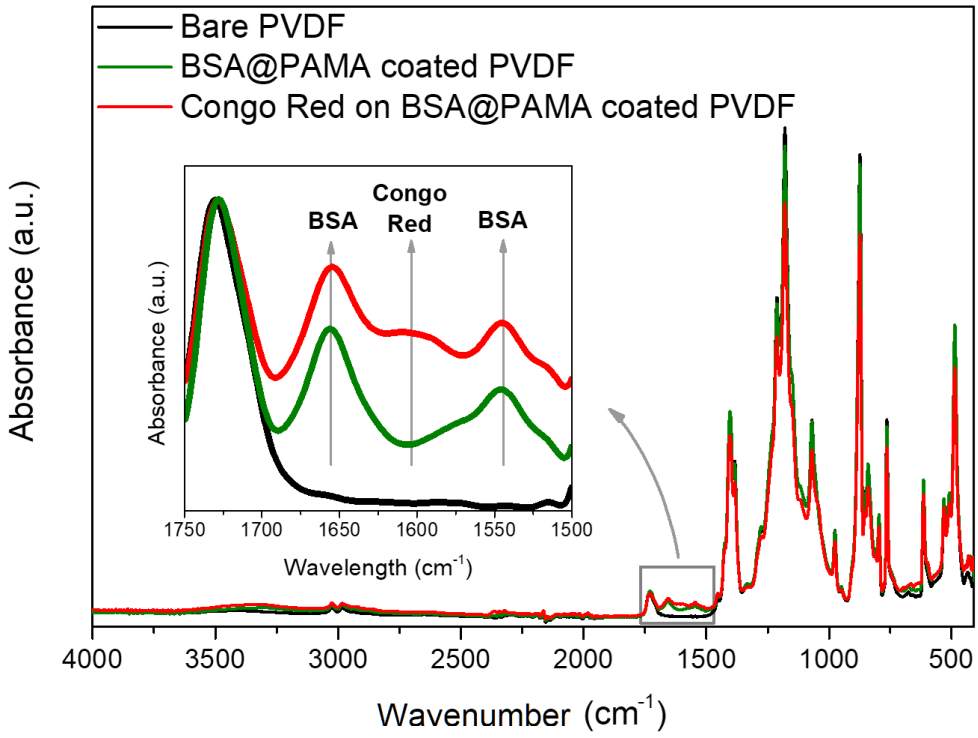

Figure S3.21 FTIR spectra of bare PVDF membrane, BSA@PAMA coated PVDF, and Congo Red absorbed on BSA@PAMA coated PVDF

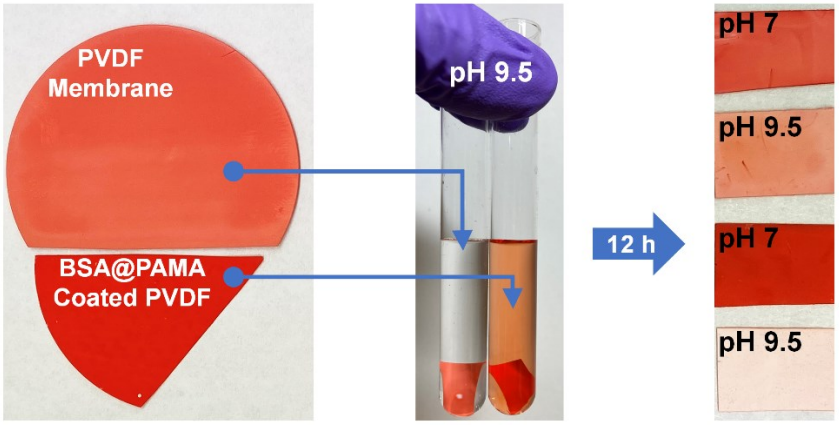

Figure S3.22 Catch-release test procedure. (1) absorbing model drug (Conge Red, CR) on surfaces, (2) releasing drug in solution with different pH, and (3) optical image: after releasing drug for 12 h

CHAPTER 4. Bionic Engineered Protein BSA@PSBMA Coating Boosting Anti-Biofouling in Complex Biological Fluids

4.1 Introduction

Implantable medical devices (IMDs), such as implantable sensors for chronic disease diagnosis,[6, 21-23] knee replacements, and artificial blood vessels,[24] save countless lives for organ restoration and have a huge global market valued at USD 120.5 Billion in 2021.[165] More than 5% of citizens in developed countries currently need IMDs for essential clinic use.[166-168] However, the foulants including proteins, enzymes, and metabolites from surrounding biofluids would irreversibly adhere to the working surfaces of IMDs during their long-lasting operation and incrementally overturn the electrochemical and biological properties of IMDs, causing unpredictable device dysfunction and serious infections that result in millions of infection-related deaths annually.[2-8, 25, 26] Constructing antifouling coatings on devices is considered as the most straightforward and effective approach to addressing biofouling issues.[7, 8, 16, 136, 164, 169-171] Traditional synthetic polymer coatings, such as poly(ethylene glycol) (PEG) and zwitterionic polymer coatings, can grant IMD surfaces antifouling capacity in biofluids through their strong hydration layer on substrate surfaces.[172-174] However, the fabrication of these polymeric coatings commonly suffers from time-consuming and arduous pretreatment for different substrates or involves toxic reagents in synthesis, resulting in inferior biocompatibility and limiting their biomedical applications.[5, 8, 9, 26, 53, 175-178]

Native proteins remove the limitations of synthetic polymers as coating materials with their naturally good biocompatibility and surface-independent anchoring capability. Recent progress in protein-based materials implies that some proteins might simultaneously demonstrate surface-

independent anchoring capability and antifouling property.[5-7, 179] For instance, native BSA protein can anchor on plastics, metals, and glass surfaces as the blocking agent in immunoassays [7, 180, 181] and is also well-known to prevent the non-specific adsorption of other proteins on BSA-modified surfaces.[182-184] Such bifunctionality of native proteins comes from their amphiphilicity.[185, 186] Hydrophilic parts in proteins would bind with surrounding water molecules and form a hydration layer to hinder the attachments of biomolecules through steric repulsion.[5-7, 9, 26] Other parts facilitate the surface-independent anchoring on various target substrates via multiple molecular interactions, including van der Waals, hydrophobic, hydrogen bonding interactions, and other attractive interactions.[105, 187, 188] Although with natural advantages in surface-independent anchoring capability and antifouling property, an intrinsic limitation of native protein coatings is that they cannot maintain a reliable and high-efficient antifouling performance under complex biological fluid conditions. Under the most common complex biological condition - high salinity and varying pH that occur after surgery, injury, or in an unhealthy body,[35-38] the charge property of native BSA coating surface will be inevitably influenced, significantly weakening the interfacial hydration and resulting in the failure of its antifouling function in practical applications.[26, 189, 190]

Herein, inspired by the 'thorn on vine' structure of climbing vines to defend against predators, we have designed a zwitterion-conjugated protein in accordance with this bionic structure and synthesized it via grafting zwitterionic sulfobetaine methacrylate (SBMA) segments on native BSA molecules through facile *thiol-ene* click chemistry[88, 174, 191, 192] (Figure 4.1a) to enhance the physicochemical stability of protein coating surfaces and strengthen their antifouling performance in complex biological environments. SBMA is a typical zwitterion with a more robust hydration layer than commercial PEG materials to resist biofouling. Moreover, zwitterions are generally more inert to pH and salinity changes in aqueous solutions than the charged functional

groups, such as $-COO^-$ and $-NH_3^+$ groups, on native BSA protein surfaces.[8, 60, 66, 177, 193]. The bionic design of the BSA@PSBMA protein integrates the natural function of native BSA in surface-independent anchoring on diverse target substrates with the artificially modified function of SBMA to prevent biofouling with strong interfacial hydration. The synthesized BSA@PSBMA material could be facilely and uniformly coated on various substrates, including metals, minerals, and plastics, through a one-step dipping or spraying method without the need of surface pretreatment. The as-prepared BSA@PSBMA coating demonstrated very weak attraction and superior resistance to proteins, enzymes, metabolites, cells, and biofluids and excellent reliability under diverse pH and salinity conditions. This work has offered an energetic and innovative paradigm of using native proteins to generate engineered proteins with tunable interfacial properties as antifouling coatings in bioengineering applications, which extends the lifespan and reduces infection incidents of IMDs.

4.2 Experimental Methods

4.2.1. Materials

Bovine serum albumin (BSA), [2-(Methacryloyloxy)ethyl]dimethyl-(3-sulfopropyl) ammonium hydroxide (known as Sulfobetaine Methacrylate, SBMA), Tris buffer (Tris(hydroxymethyl)aminomethane), MES buffer, Ethylenediaminetetraacetic acid (EDTA), L-Cysteine, lysozyme (Lyso), concanavalin A (Con A), collagenase, Mucin from porcine stomach, sucrose, fructose, humic acid, dopamine hydrochloride, L-lysine, and L-Alanine, Trichloro(octadecyl)silane (OTS), NaCl, KCl, $CaCl_2$, $MgCl_2$ powders, polystyrene, polyethylene terephthalate, polypropylene plastic plates were purchase from Sigma-Aldrich. Sodium borohydride ($NaBH_4$) and medical tube (Saint-Gobain Tygon) were purchased from Fisher scientific. Au, Cu, Fe substrates were obtained by Electron-Beam evaporation (Gomez, Kurt J.

Lesker, CA) of corresponding metal on Si wafer (Substrata, Thin film solutions, CA). Fetal bovine serum (FBS), milk, and Canola oil (lipid) were from the local grocery. Ultrapure water in the experiments was from Milli-Q Advantage A10 (Millipore, USA). The new substrates before use would be cleaned by UV-Ozone cleaner for 30 min, followed by copious rinsing with ethanol and ultrapure water. Au sensors (QSX301) for QCM-D was from Biolon Scientifc.

4.2.2. Synthesis of engineered BSA@PSBMA protein

Mix BSA solution (8 mg mL^{-1}) and $NaBH_4$ solution (100 mM) at a volume ratio of 1:1 for 30 min to obtain reduced-BSA (re-BSA). Then, the *thiol-ene* click chemistry[191, 192] of re-BSA and 400 mM SBMA monomer was initiated by ultraviolet (UV) crosslinker (UPV crosslinker, Analytikjena, USA) for 30 min and followed by reacting for 30 h at room temperature to synthesize BSA@PSBMA biopolymer. The synthesis of engineered BSA@PSBMA proteins was characterized via UV-Vis spectrum (Evolution 300, Thermo Scientific, USA), X-ray photoelectron spectroscopy (XPS, Kratos AXIS Ultra, UK), and Attenuated Total Reflection-Fourier-transform infrared spectroscopy (ATR-FTIR, Nicolet iS50, Thermo Scientific, USA).

First, UV-Vis standard calibration curves of BSA protein solutions (TE buffer, 50 mM Tris-HCl + 1mM EDTA, 7.5 pH) were established in Figure S4.1. The free thiol group in a solution is detected by using the well-known Cysteine-Ellman reaction.[194] Specifically, 50 ul of 4 mg mL^{-1} Ellman's reagent solution and 2.5 mL samples are mixed and incubated at room temperature for 15 mins before recording UV-Vis spectra. $NaBH_4$ residual in re-BSA solution was completely depleted by HCl solution prior to reacting with Ellman's reagent to avoid the interfering reaction between $NaBH_4$ and Ellman's reagent in the quantitative analysis. As demonstrated in Figure S4.2,

by keeping the re-BSA solution at room temperature for 15 min or quenched with HCl solution, there would be no $NaBH_4$ residual to interfere thiol-Ellman reaction.

Second, BSA reduced by 50 mM $NaBH_4$ for different time has been characterized and summarized in Figure S4.3, which suggests that $NaBH_4$ reduced BSA rapidly and the reduction would finish within 10 min. A new -SH peak in XPS spectra of re-BSA (Figure 4.1c) further confirmed the successful reduction of the disulfide bond to the free thiol group.[195, 196] Therefore, BSA will be reduced by 50 mM NaBH4 for 15 min before reacting with the SBMA monomer.

Third, re-BSA was conjugated with SBMA monomers via *thiol-ene* click chemistry. Specifically, 4mg mL^{-1} re-BSA and 400 mM SBMA monomer were mixed and reacted for different duration at room temperature and in the air; corresponding UV-Vis spectra were shown in Figure S4.4. The rapid decrease of free thiol group intensity indicated an intensive reaction, and most of the thiol groups had been reacted with carbon-carbon double bond in SBMA within 100 min. Prolonging the reaction time may help the chain propagation of poly-SBMA. The increased intensity of the characteristic O=C-O-C peak of SBMA in XPS spectra (Figure S4.5) also supported the hybridization of BSA and SBMA. After polymerization, the BSA@PSBMA solution was dialyzed for 5 days using the 14-16 KDa dialysis bag and then freeze-dried to obtain the BSA@PSBMA material.

Finally, the composition of the synthesized BSA@PSBMA material was quantified by thermogravimetric analysis (TGA, TGA Q500, TA, USA), energy dispersive spectrometer (EDS, Sigma GEMINI FE-SEM, ZESSI, Germany), and FTIR. Additional DTA peck of BSA@PSBMA at 440^{o}C in differential thermal analysis (DTA, Figure S4.6a) and the higher S content and lower N content of BSA@PSBMA measured by EDS (Figure S4.6b) compared with BSA indicated the

successful conjugation of BSA and SBMA. Figure S4.7a displayed the FTIR spectra of SBMA monomer and BSA mixtures, in which SBMA monomer and BSA protein were mixed and dissolved into Milli-Q water with different mass ratios (7/3.5/1.4/0.7/0.35/0.07) followed by freeze-drying. The characteristic peak of SBMA monomer is at 1035 nm, assigned for -SO_3 group, and that of BSA is at 1538 nm, which is for the -NH- group of peptides in the BSA protein. A standard calibration curve regarding the characteristic absorbance ratio of SBMA/BSA and their mass ratio has been established, as shown in Figure S4.7b, based on the Beer-Lambert law. The characteristic absorbance ratio of SBMA/BSA for the engineered BSA@PSBMA protein was 1.023. Thus the mass ratio of SBMA/BSA is 0.6778, calculated by the standard calibration curve. Moreover, the absorbance of the characteristic peak for BSA@PSBMA was between the spectra of SBMA/BSA mixture with a mass ratio of 0.35 and 0.7 as indicated in Figure S4.7c, which double confirmed the mass ratio of BSA and SBMA in engineered BSA@PSBMA. Herein, the molar ratio of SBMA over BSA was 1068.

4.2.3. Preparation of BSA@PSBMA coatings

The BSA@PSBMA coating could be prepared via spraying or dip coating as shown in Figure S4.8a. Specifically, 4 mg mL^{-1} BSA@PSBMA solution was sprayed on the surface and stored in a humid environment for 30 min to 1 h to form the coating. A '**UA**' pattern has been prepared via the spraying method as displayed in Figure S4.8b. In the dip coating, substrates were immersed in the BSA@PSBMA solution (4mg mL^{-1} BSA@PSBMA in TE buffer, pH=5) for 4 h. This method is suitable for various substrates, especially with porous and shaped materials.

4.2.4. Quartz crystal microbalance with dissipation monitoring (QCM-D) test

20% dilution of biofluids and 10mg mL^{-1} protein and other water-soluble substances were used in this test. For the lipid (Canola oil, a highly viscous oil, employed as a model lipid), it was

dissolved in ethanol with a concentration of 10 mg mL^{-1} and dispersed via ultrasonic for 30 min, then the lipid/ethanol mixture was dispersed in water via a homogenizer (T18 digital ULTRA TURRAX, IKA, Germany, speed 20,000 rpm, 15 min). The pH of the fetal bovine serum was adjusted by NaOH and HCl solution before QCM-D tests. The salinity of fetal bovine serum was adjusted by NaCl, KCl, $CaCl_2$, and $MgCl_2$. The Au sensors were immersed in 4mg mL^{-1} native BSA or BSA@PSBMA solution at room temperature for 4 h to obtain the native BSA-coated Au or BSA@PSBMA-coated Au sensors. QCM-D tests were conducted on Q-Sense E4 (Biolin Scientific, Finland) and the data analysis follows the extended viscoelastic model on QTools software (Biolin Scientific, Finland).The adsorption value was averaged by 3 measurements.

4.2.5. Bulk fouling tests

To evaluate the fouling resistance of BSA@PSBMA coatings, the bare substrates, native BSA-coated substrates, and BSA@PSBMA-coated substrates were incubated in bovine serum, milk, and lipid for 48 h at 37°C. After fouling for 48 h, the substrates were copiously rinsed with ultrapure water before characterization. Si substrates were used for the lipid fouling test. (Si and Au substrates are from Angstrom Engineering, CA). In the cell attachment test, the Chinese hamster ovary (CHO) cells were used as a model to evaluate the cell attachment property of as-prepared substrates (Bare silicon substrate, native BSA-coated silicon substrate, and BSA@PSBMA-coated silicon substrate). The CHO cells were firstly cultured in Dulbecco's Modified Eagle Medium/Nutrient Mixture F-12 (DMEM/F-12) supplemented with L-glutamine, 10% fetal bovine serum, and penicillin-streptomycin. The bare silicon wafers and the silicon wafers coated by native BSA and BSA@PSBMA were placed in a 24-well cell culture plate and sterilized by exposure to UV light for 1 h. The CHO cells were then seeded on the surface of

substrates at the density of 1×10^5 cells and incubated for 48 h at 37°C. After incubation, the substrates were washed with PBS buffer to remove nonadherent cells before characterizations.

4.2.6. Biofouling distribution characterized by Optical Photo Thermal InfraRed (O-PTIR)

Bio-foulants on the surfaces in the above fouling tests have been characterized using O-PTIR, a non-contact submicron visible probe infrared spectroscopy (mIRage, Photothermal Spectroscopy Corp, CA). In O-PTIR characterization (Figure 4.3b), a tunable pulsed mid-infrared (IR) laser induces photothermal effects onto a sample surface, which are measured using a scattered visible probe laser to focus on the sample. The reflection IR spectra recorded by O-PTIR can be correlated to ATR-FTIR spectra. The O-PTIR spectra of bio-foulants in milk (Figure 4.3b), lipid, cell, and serum (Figure S4.16) showed their corresponding characteristic peaks. Then, using IR at 1650 cm^{-1} (milk as an example) to scan the sample surfaces with the resolution of 500 nm to map the milk foulants distributed on the sample surfaces (Figure 4.3c). The O-PTIR mapping overcomes the limitation of EDS characterization, which cannot identify organic groups with the same composition, and the spatial resolution limitation of traditional FTIR microscopy (10-20 microns). The coverage of foulants on surfaces was measured on two samples with 3 different areas.

4.2.7. Interfacial interaction measurements by using a surface forces apparatus (SFA)

The interfacial interaction forces between the protein-based coating and model bio-foulants (Figure 4.5, Figure S4.19) were measured by using the surface forces apparatus (SFA, SFA 2000, Surforcellc, USA) in aqueous environments with different pH and salinity. 4mg mL^{-1} native BSA or BSA@PSBMA with different pH was dip-coated on the mica surfaces for different incubation time. The thickness of the coating could also be quantified due to the high spatial resolution (<0.1

nm) of SFA. The coating thickness D_T could be determined via the shift of FECO wavelength before and after coating (Figure 4.1f and Figure S4.14).

For interaction forces between protein-based coatings and bio-foulants, one of the mica surfaces was functionalized with native BSA or BSA@PSBMA by dip coating (0.5 mg mL^{-1}), and the counter one was modified by chemicals with respective properties of the foulants (bare mica for the hydrophilic bio-foulants, OTS for hydrophobic bio-foulants) (Figure 4.5b). OTS coating was prepared by immersing the mica surface into 100 mM OTS solution (solvent: anhydrous ethanol) for 30 min and followed dried by nitrogen. In a typical SFA force measurement, two surfaces were first brought to approach each other ('approach') and were kept for a different time (contact time), followed by separation ('separation') (Figure 4.5b and Figure 4.5c). Adhesion (F_{ad}/R) was measured when the two attractive protein-coated mica surfaces were separated and jumped apart (so-called 'jump out'). The normal force was measured based on Hooke's law. The adhesion force was measured on 3 different contact areas in each SFA measurement.

4.2.8. Isothermal titration calorimetry measurement (ITC)

The ion-biomolecule binding was directly measured by ITC (NanoITC, TA, USA), in which the association constant (K_a), reaction stoichiometry (n), and the change in enthalpy (ΔH), entropy change (ΔS), and Gibbs free energy (ΔG) could be accurately determined. The affinity of Ca^{2+}-BSA and Ca^{2+}-BSA@PSBMA have been analyzed by ITC in Figure S4.20, in which Ca ion dissolved in MES buffer (pH 6) was titrated into BSA or BSA@PSBMA solution (MES buffer, pH 6). In a test, 5 μL 1 mM Ca ion solution was injected into 950 μL 0.36 mM BSA or 50 mM Ca solution to 0.04 mM BSA@PSBMA for 50 injections. The reaction heat was corrected by subtracting the heat of titrant to buffer, buffer to titrand, and analyzed by the independent model.

The ITC results should the association constant of Ca-BSA is 10,000 greater than that of Ca-BSA@PSBMA (Figure S4.20e), suggesting a much high affinity between Ca ion and BSA than that of Ca-BSA@PSBMA. Lower heat release and Gibbs free energy of the reaction of Ca-BSA@PSBMA further confirmed that BSA@PSBMA has a lower affinity to Ca ion, which accounted for unfailing low interactions between BSA@PSBMA coating and surfaces in various salinity.

4.2.9. In-vitro blood flow test

In-vitro blood flow test consisted of 1) serum circulation system and 2) blood flow rate meter (Figure 4.6b). In the serum circulation system, undiluted fetal bovine serum (FBS) was continuously pumped to pass through a medical tube at 37°C for the different duration (upper subfigure in Figure 4.6b). During the circulation, the bio-foulants inside FBS would incrementally attach and accumulate on the inner surface of the medical tube. After fouling for a certain time, the inner medical tubing will be gently cleaned with ultrapure water and set up into the blood flow rate measurement system (bottom subfigure in Figure 4.6b). A constant pressure (1000 Pa, the same as human blood pressure) pressed the FBS to flow through the fouled tubes, and the mass of the passed FBS with time was recorded. The density of the FBS is ~1.06 g cm^{-3} and the inner diameter of the medical tubing is 0.79 mm. Then the flowing rate of blood in medical tubes could be calculated at different operation time. The flowing rate was measured by 3 different tubes.

4.2.10. Self-cleaning test and induction timer test

The '**UA**' template obtained by the spraying method in Figure S4.8 was immersed in Canola oil (labeled by oil red) for 1 min and then rinsed into ultrapure water (Figure 4.6h). The oil on the BSA@PSBMA-coated part was detached within 15 s. To further understand the self-

cleaning phenomenon, the interaction between an oil droplet and the functionalized surface has been characterized by an induction timer (IT). In the characterization (Figure S4.22), an oil droplet created at the end of a capillary tube approaches the surface of Au substrates. After initial contact, the droplet continuously approaches a litter bit to keep the contact and holds for 3 s. Then the droplet retracts from the surface, and finally, the droplet is detached from the surface, leaving residuals behind if applicable. Compared with pure Au surface and native BSA-coated surface, there was no residual oil left on the BSA@PSBMA-coated surface, suggesting the lower adhesion between oil and BSA@PSBMA coating, which responded to the excellent self-cleaning properties in Figure 4.6h.

4.2.11. Other Characterizations

X-ray photoelectron spectroscopy (XPS) was obtained from Kratos AXIS Ultra, UK. The binding energy was calibrated by C1s peak at 284.6 eV. Scanning electron microscopy (SEM) and energy dispersive spectrometer (EDS) characterizations were performed on Sigma GEMINI FE-SEM, ZESSI, Germany. For EDS mapping of medical tubes, the tubes were cut along the tangent line of the inner surface to make the contaminated surface and tube wall at the same plane as much as possible, avoiding sample height inference on elements mapping (Figure 4.6e). Thermogravimetric analysis (TGA) was conducted on TGA Q500, TA, USA, with a heat-up rate of 15°C min^{-1} and temperature varied from room temperature to 600°C. Atomic force microscopy imaging was obtained on ICON, Bruker, Germany using the tapping mode. Zeta potential measurements were carried out on a Zetasizer Nano ZSP system (Malvern Panalytical, UK), in which a 0.5 mg mL^{-1} protein sponge was dissolved in Milli-Q water with different pH values and homogenized with ultrasonic before the tests. Static water contact angle in the air of various substrates was measured with a 3 μL ultrapure water droplet. The ions in fetal bovine serum and

milk were measured by inductively coupled plasma-optical emission spectroscopy (ICP-OES, Thermo iCAP6300 Duo, Thermo Fisher, UK) after filtering by 5 μm filters.

4.3 Results and discussions

4.3.1. Preparation of BSA@PSBMA engineered protein

The engineered protein BSA@PSBMA could be high-efficiently synthesized via a facile radical-mediated *thiol-ene* click reaction (Figure 4.1a) under mild conditions without side products.[191, 192, 197] Specifically, disulfide bonds in BSA molecules (4 mg mL^{-1}, pH 7.5) were reduced to free thiol groups by $NaBH_4$ (50 mM) (denote reduced BSA as re-BSA).[198] Free thiol group (-SH) was detected using the X-ray photoelectron spectra (XPS) of re-BSA in Figure 4.1c and UV-vis spectrum in Figure S4.3 after reduction.[196] Then, the re-BSA solution was mixed with SBMA monomer (400 mM, pH 7.5) to initiate the rapid click reaction between free thiol radicals and carbon-carbon double bonds of SBMA (Figure 4.1a and S4.5), and finally keeping the polymerization at ambient conditions for 30 h.[95, 96, 199-201] The resultant biopolymer was dialyzed and freeze-dried. The XPS characteristic peaks of BSA (O=C-NH-C) and SBMA ($-N^+$ and $-SO_3^-$) in Figure 4.1c and the thermogravimetric analysis (Figure S4.6a) of the resultant biopolymer indicated a successful conjugation of BSA and SBMA.[195-197, 202, 203] Fourier transform infrared (FTIR, Figure 4.1d) spectra of BSA@PSBMA further confirmed that the carbon-carbon double bond (1324 cm^{-2}) in SBMA was broken after polymerization and the presence of SBMA (aldehyde group, $-N^+$ and $-SO_3$) and BSA (Amide I and Amide II) in the final product.[7, 204] An average of 1068 SBMA units was grafted on one BSA molecule as estimated from the FTIR spectra (Figure S4.7) and energy dispersive spectroscopy (EDS, Figure S4.6b).

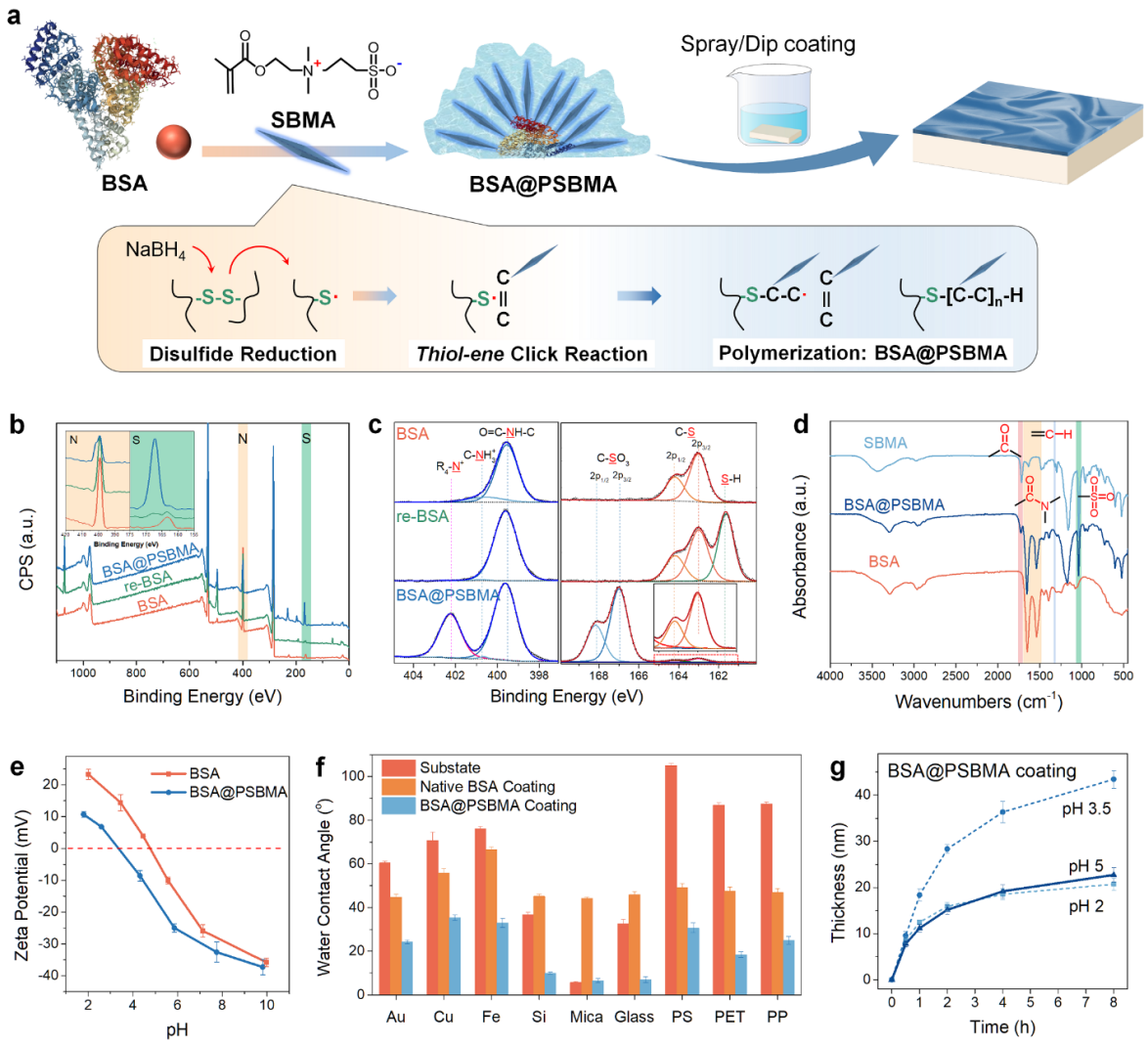

Figure 4.1 Preparation of the engineered protein coating. (a) Schematic diagram showing the process of synthesizing BSA@PSBMA via *thiol-ene* click chemistry. (b) XPS wide scan spectra of BSA, re-BSA, and BSA@PSBMA and (c) corresponding high-resolution N and S deconvolution spectra. (d) FTIR spectra of BSA, SBMA, and BSA@PSBMA. (e) Zeta potential. (f) Static water contact angle on various surfaces. (g) Thickness change of BSA@PSBMA coating over coating time under different pH conditions measured using a surface forces apparatus (SFA). Values in (e, f, g) represent the mean and the standard deviation (n=3).

The zeta potential results in Figure 4.1e showed that the isoelectric point (Ip) of BSA@PSBMA was at pH 3.3, lower than that of native BSA at pH 4.8, due to the conjugation of SBMA.[61] To test its anchoring capability, BSA@PSBMA was deposited on metallic, inorganic, and organic substrates by either spraying or dipping methods (Figure 4.1f, S4.8, S4.9, and S4.10). The lower static water contact angles on BSA@PSBMA-coated surfaces than on native BSA-coated surfaces (Figure 4.1f and S4.11) resulted from the higher hydrophilicity of BSA@PSBMA. The coating thickness can be regulated by tuning solution pH, reactant concentrations, and coating time. The thickness of BSA@PSBMA coating on mica surfaces under different pH conditions was measured using a surface forces apparatus (SFA, Figure S4.12). Figure 4.1g showed that the thickness of BSA@PSBMA coating at pH 3 steadily rose to ~36 nm in 4 h, and further prolonging the coating time would not significantly increase the coating thickness (Figure S4.13). At pH 5, the thickness was only ~18 nm after 4 h. Such different coating behaviors most likely stem from the increased adsorption rate of proteins at pH near Ip, where the electrostatic repulsion among molecules is minimal.[59, 146] With a longer coating time, the coverage of proteins on surfaces could increase and surface roughness would decrease (Figure S4.14), benefiting the antifouling performance. The successful synthesis and facile preparation of BSA@PSBMA coatings enable the following antifouling performance tests at micro and macro scales.

4.3.2. Antifouling performance of engineered protein BSA@PSBMA

Fouling is a spontaneous process in biosystems associated with the dynamic adsorption and accumulation of biomolecules on surfaces, which could be directly monitored in real-time using a quartz crystal microbalance with dissipation monitoring (QCM-D) (Figure 4.2a).[7, 135, 205, 206] The antifouling performance of BSA@PSBMA-coated surfaces against various model foulants

from biosystems was screened using a QCM-D, where the bare Au sensor and native BSA-coated Au sensor were used as the control group.

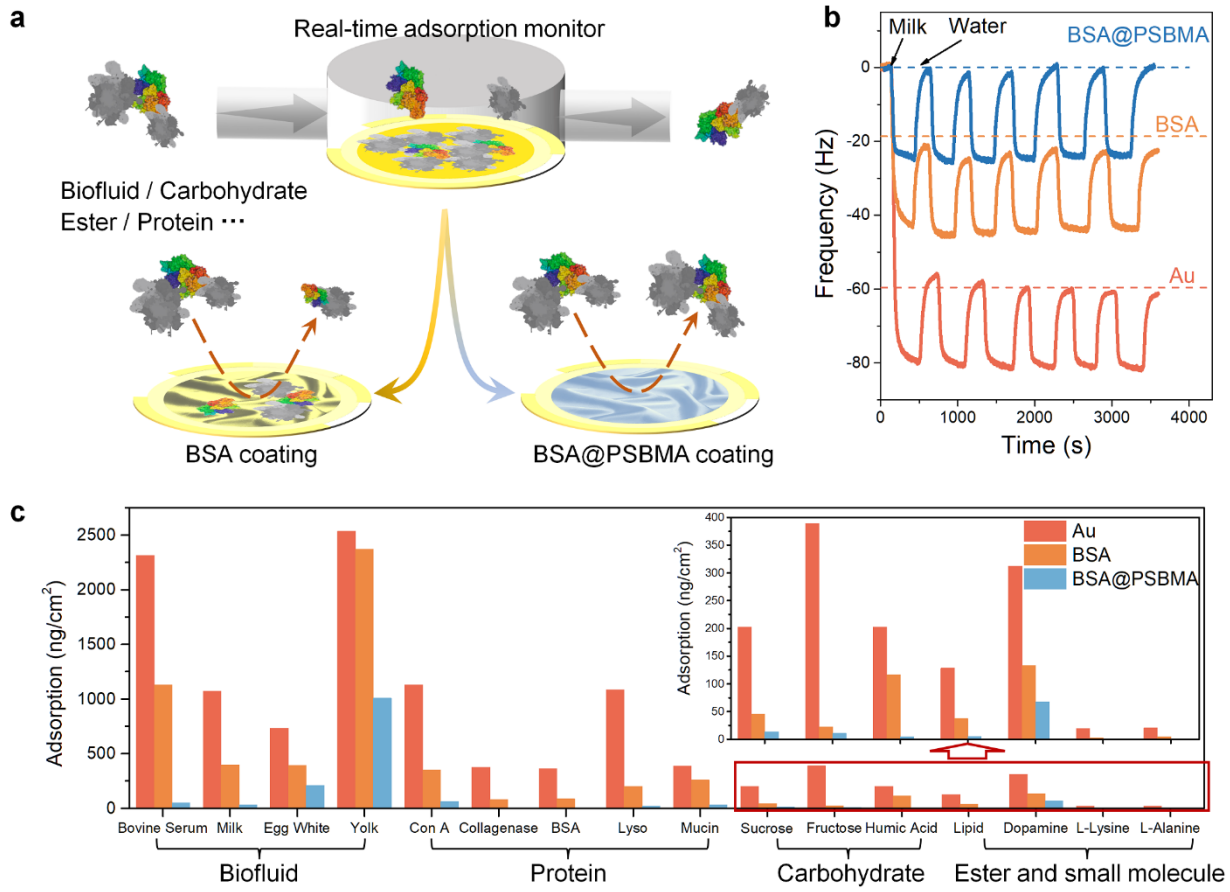

Figure 4.2 Dynamic adsorption of bio-foulants on QCM-D sensors. (a) Schematic diagram illustrating dynamic adsorption of foulants on the bare Au sensors and Au sensors coated by native BSA and BSA@PSBMA sensors. (b) Change in resonance frequency associated with the adsorption of milk on different sensors during the alternative rinsing with milk and water. (c) Adsorption of biofluids, proteins, carbohydrates, and small molecules on different sensors after rinsing with water.

As shown in Figure 4.2b, a strong negative frequency shift was observed for all test sensors upon the introduction of milk into the QCM-D chamber, indicating the adsorption of foulants from milk on all tested surfaces. After stable frequency was attained, ultrapure water was introduced into the chamber to remove the loosely bonded foulants on sensors, giving rise to an increase in frequency. This milk-water alternative rinsing was continuously conducted six times. The almost complete reversible adsorption-desorption of milk on the BSA@PSBMA-coated sensor demonstrated excellent antifouling performance of BSA@PSBMA coatings. BSA@PSBMA-coated sensors also exhibited high-efficiency antifouling capability to a broad spectrum of bio-foulants, including biofluids (e.g., bovine serum, egg white, and yolk), common proteins (concanavalin A (Con A), collagenase, BSA, lysozyme (Lyso), mucin from porcine stomach), carbohydrate in body fluids (sucrose, fructose, humic acid), and small biological signaling molecules like dopamine (Figure 4.2c and S4.15). For instance, the remnant bovine serum on the BSA@PSBMA-coated sensor after rinsing with water was ~50.3 ng cm^{-2}, while those on the native BSA-coated sensor and bare Au sensor were as high as ~1131 ng cm^{-2} and ~2313 ng cm^{-2}, respectively.

Long-term operation in macroscale bulk tests with real biological fluids (Figure 4.3a) is of practical importance to evaluate the antifouling capability of coatings, in addition to short-period dynamic adsorption of biomacromolecules at the nanoscale by QCM-D in biological buffers. In macroscale tests, the tested surfaces would undergo more complicated chemical and biological processes, such as the formation of biofilms and the colonization of microorganisms on surfaces, which primarily cause irreversible dysfunction of devices and healthcare-associated infection.[3, 4, 11, 207] In these tests, bare substrate surfaces and surfaces coated with native BSA and BSA@PSBMA were incubated in representative biofluids at 37°C for 48 h (Figure 4.3a), including

milk, lipid (Canola oil), Chinese hamster ovary (CHO) cells nutrient mixture, and fetal bovine serum (FBS). All tested surfaces were rinsed with ultrapure water before the characterizations by optical photothermal infrared (O-PTIR), which is a non-contact technique that couples a visible laser with an infrared laser to precisely position foulants based on their characteristic infrared (IR) peaks, as shown in Figure 4.3b.[118-120, 208]

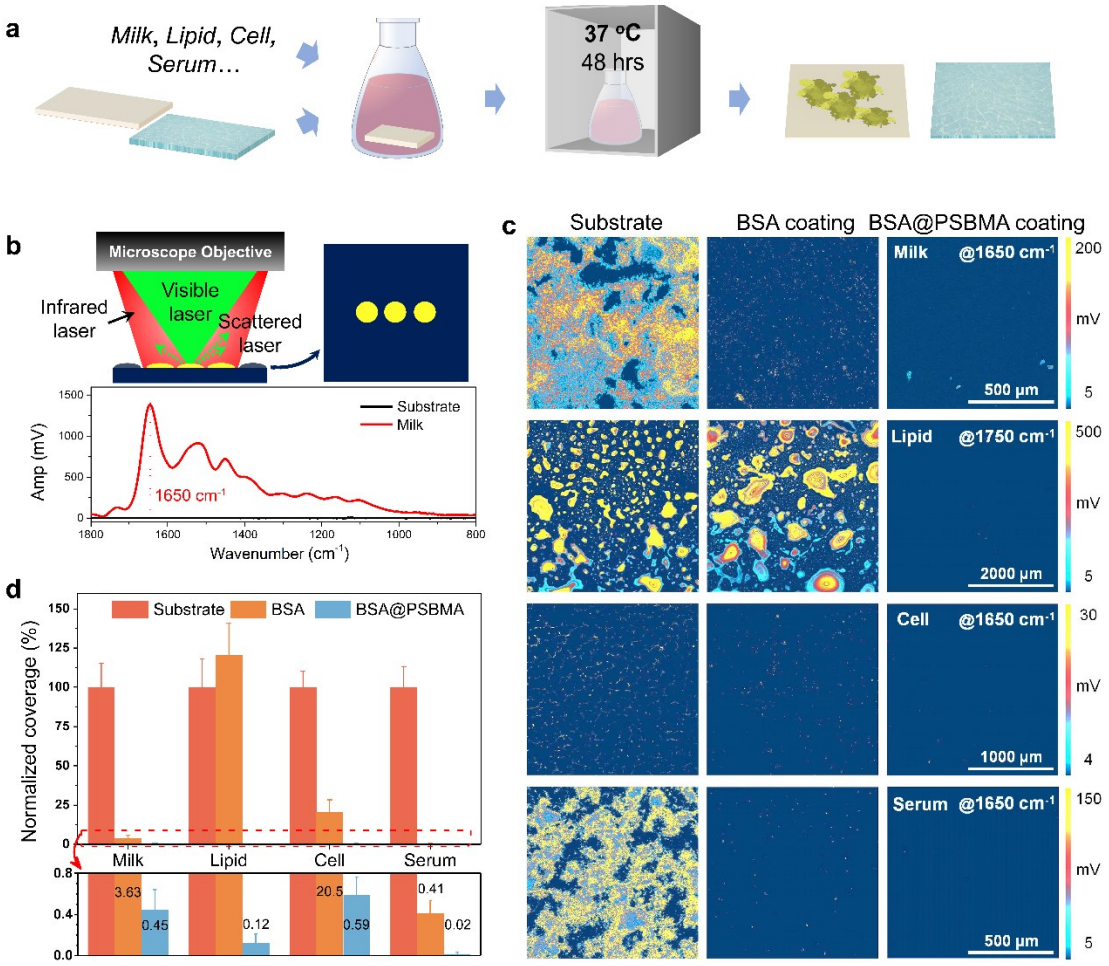

Figure 4.3 Coating antifouling performance in bulk fouling tests. (a) Diagram illustrating the processes of macroscale bulk tests. (b) Working principle of O-PTIR and O-PTIR spectra of Au substrate and foulants in milk. (c) O-PTIR mappings of foulants on the bare substrate surfaces and surfaces coated by native BSA and BSA@PSBMA and (d) corresponding fouling coverage in milk, lipid, CHO cells, and bovine serum solutions. Values in (d) represent the mean and the standard deviation (n=6).

Bio-foulants on the surfaces incubated in milk were mapped in Figure 4.3c, based on its characteristic IR peak at 1650 cm^{-1} (bottom spectra in Figure 4.3b). Likewise, surfaces fouled in the lipid, CHO cells, and bovine serum were also characterized in Figure 4.3c according to their individual characteristic IR peaks (Figure S4.16). Figure 4.3c indicated that a large number of foulants adhered on all bare substrate surfaces, less on native BSA-coated surfaces except for the lipid, and nearly zero fouling on BSA@PSBMA-coated surfaces in all biofluids. The coverage of bio-foulants on surfaces was quantified in Figure 4.3d by setting bio-foulants coverage on bare substrate surfaces as 100%. The results in bulk fouling tests are consistent with the nanoscale adsorption tests, both demonstrating remarkably reduced biofouling on BSA@PSBMA-coated surfaces. This superior antifouling property most likely originated from the bionic hierarchical structure of BSA@PSBMA that provides strong interfacial hydration and steric repulsion to hinder the initial attachment of foulants on surfaces.

4.3.3. Antifouling performance in biological fluids with complex conditions

The antifouling capability of BSA@PSBMA coatings was further examined in more complex biological fluids with diverse pH and salinity conditions which could greatly compromise the antifouling performance in practice. Such complex biological conditions inevitably occur after the medical device implantation or during clinic testing, which leads the surrounding environment of the antifouling coatings extremely complex. In the following bulk tests, protein-coated surfaces were incubated in fetal bovine serum (FBS) under various pH and salinity conditions. Specifically, bare Au surfaces and Au surfaces coated with native BSA and BSA@PSBMA were incubated in FBS at pH 3.6, 6.8, 7.4, and 9.8 or with various salinity (250 mM for KCl and NaCl, 10 mM for $CaCl_2$ and $MgCl_2$) for 48 h at 37°C. The coverage of bio-foulants on different surfaces was summarized in Figure 4.4a and 4.4b, and the corresponding distribution of foulants on surfaces

was displayed in Figure 4.4c and 4.4d. It was found that BSA@PSBMA-coated surfaces exhibited high-efficient resistance to over 99.9% of the adsorption of biomacromolecules in FBS under high salinity and various pH conditions, over 10-fold superior to native BSA-coated surfaces in antifouling capability. Such extraordinary antifouling performance of BSA@PSBMA could be attributed to its bionic 'vine-thorn' design. The hydrophilic SBMA part endowed the coating with a strong interfacial hydration layer and additional steric repulsions that greatly hindered the initial attachment of foulants on surfaces, while the bare BSA coating failed to resist biofouling under complex biological conditions. The less biofouling on Au surfaces at higher pH conditions (Figure 4.4a) could be attributed to the lower settling rate of foulants due to the higher electrostatic repulsion between foulants and substrates. High salinity resulted in worse biofouling on surfaces, as suggested in Figure 4.4b and 4.4d. The same trend was also observed in the dynamic adsorption of FBS (Figure 4.4e and S4.17) on protein-coated surfaces. The adsorption of FBS at different pH and salinity (Figure 4.4f and 4.4g) clearly showed the superior antifouling performance of BSA@PSBMA coating. With higher salt concentration (Figure 4.4g), the adsorption amount of bio-foulants decreased on both native BSA and BSA@PSBMA coatings, which was fundamentally determined by the comprehensive intermolecular interactions between foulants and the coating surfaces. Specifically, the increased ionic strength at high salinity could suppress the electrostatic repulsion between negatively charged foulants and BSA molecules at coating surfaces, increasing attraction between foulants and surfaces.[146] In contrast, the high concentration of salt ions might weaken attractive intermolecular interactions like the hydrogen bonding between foulants and BSA proteins, decreasing attraction between foulants and surfaces.[59] The interfacial interaction forces between the protein-coated surfaces and foulants from biofluids will be investigated by direct interaction force measurements.

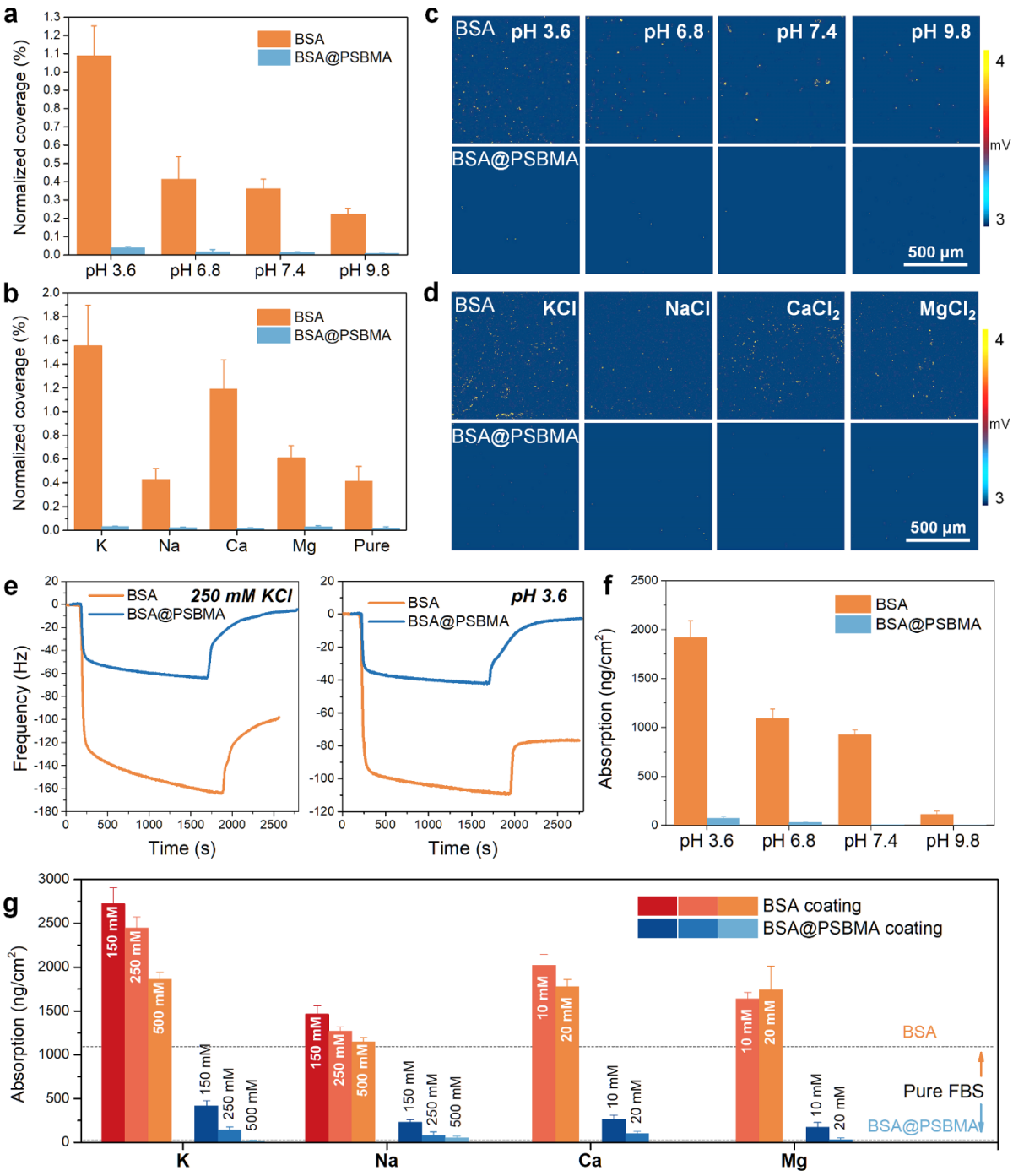

Figure 4.4 Coating antifouling performance in environments with diverse pH and salinity. Normalized coverage of bio-foulants on native BSA-coated and BSA@PSBMA-coated surfaces and corresponding O-PTIR mappings incubated in fetal bovine serum (FBS) with diverse (a)(c) pH and (b)(d) salinity. (e) Dynamic adsorption of FBS with 250 mM KCl or pH 3.6 on BSA-coated

and BSA@PSBMA-coated sensors and corresponding adsorption amount of FBS with diverse (f) pH and (g) salinity measured by QCM-D. (Dash line indicates the amount of adsorption of pure FBS on different surfaces). Values represent the mean and the standard deviation (n=3).

4.3.4. Interfacial interactions between BSA@PSBMA and model foulants

It is well-acknowledged that the biofouling process in different lengths and time scales is fundamentally governed by intermolecular interactions between substrate surfaces and foulants. Attractive interactions would lead to fouling, while repulsive ones result in non-fouling, as indicated in Figure 4.5a. In this work, a mica surface was modeled as a hydrophilic foulant substrate, and trichloro(octadecyl)silane (OTS) composed of a long-chain alkyl group was set as the hydrophobic case. The interfacial interactions between protein-coated surfaces and hydrophilic mica surface or hydrophobic OTS surface in aqueous solutions at different contact time were measured using a SFA (Figure 4.5b). In SFA measurements, normalized force-distance (F/R-D) profiles and adhesions between protein-coated surfaces and different model foulants were displayed in Figure 4.5c and 4.5d. It was found that adhesion (F_{ad}/R) between BSA@PSBMA-coated surface and mica surface was only ~0.95 mN m^{-1} after 45 min of contact (Figure 4.5c), 5-fold lower than that between native BSA-coated surface and mica surface ~4.11 mN m^{-1}. Such low adhesion could be attributed to the steric repulsion of the 'thorn' part on BSA@PSBMA that significantly counteracted attractive interfacial interactions, such as van der Waals (vdW) force, time-dependent hydrogen bonding, and other interactions (electrostatic force, cation-π interaction and ion bridging).[59, 105, 209-211] Likewise, the bionic structure induced steric repulsion granted zero adhesion between BSA@PSBMA coating and OTS, whereas the adhesion between native BSA coating and OTS reached up to ~3.39 mN m^{-1} (Figure 4.5d). Such weak interfacial attraction between the BSA@PSBMA coating and model foulants well accounted for the excellent resistance

to biofouling in both nanoscale dynamic adsorptions (Figure 4.2c) and macroscale bulk tests (Figure 4.3d).

Interaction forces between protein-coated surfaces and model foulant surfaces in aqueous solutions with different pH and salinity were then systematically measured to investigate the underlying antifouling mechanisms of BSA@PSBMA in complex biological conditions. Figure 4.5e and 4.5f presented the interaction forces between a hydrophilic mica surface and protein-coated surfaces in aqueous solutions with various pH values. It was found that the adhesion of the mica surface to the BSA@PSBMA-coated surface was as low as 0.45-0.98 mN m^{-1} in a wide range of pH values (Figure 4.5e); however, the adhesion between native BSA-coated surface and mica surprisingly reached up to 8.06 mN m^{-1} at pH 3.6 (Figure 4.5f), which may be resulted from the strong electrostatic attraction under low pH conditions. Figure 4.5f also shows that the adhesion between the BSA and mica surfaces decreased with increasing the solution pH due to the increased electostic repulsion under alkaline pH condition. Figure 4.5g displayed the interaction forces of mica surfaces with protein-coated surfaces in a solution with the presence of 10 mM $CaCl_2$, and it clearly showed a zero adhesion and long-range steric repulsion between BSA@PSBMA-coated surface and mica surface, whereas a dramatical high adhesion (~12.71 mN m^{-1}) between native BSA-coated surface and mica surface. Likewise, increased interfacial interactions between native BSA-coated surfaces and mica surfaces were found in all the tested solutions with the presence of salts (7-17.3 mM m^{-1}, 10 mM and 15 min) as summarized in Figure 4.5h and S4.19, which were over 10-fold higher than the adhesion between BSA@PSBMA-coated surfaces and mica surfaces (Figure 4.5i). Those results demonstrated very weak interfacial attraction between the BSA@PSBMA-coated surfaces and mica surfaces. More importantly, such low interfacial attraction would not increase in the solutions with the presence of salts and in a wide range of pH

values, implying the robust antifouling performance in practical complex biological conditions. Such retained low interfacial interaction energy of engineered BSA@PSBMA material arose from the hydrophilic zwitterionic PSBMA part on BSA, which exhibited a self-adapting anti-electrolyte property and shifted from a compressed conformation to a relatively loose conformation in salt solutions,[212-214] introducing long-range and strong steric respulsion to reduce the adhesion (Figure 4.5g). Furthermore, the association constant, K_a, between native BSA molecule and Ca^{2+} ions was as high as 1.02×10^6 in isothermal titration assays (ITC, Figure S4.20). As a result, a large amount of Ca^{2+} ions were adsorbed on the native BSA coating surface from the surrounding environments, decreasing its surface charge density and weakening its binding with interfacial water molecules, causing dehydration on the surface of native BSA coating, as indicated in Figure 4.5a. The lower surface charge density reduced the electrostatic repulsion and dehydration lowered repulsive steric hydration force, resulting in significantly increased adhesion between native BSA-coated surfaces and foulants surfaces. Fortunately, our engineered BSA@PSBMA could effectively address such salinity-induced unstable interfacial hydration issue because of the low K_a of Ca^{2+} with BSA@PSBMA (~160.3), rendering an unfailing low interfacial interaction and less fouling under complex biological conditions. The antifouling properties of native protein coatings could be weakened with the presence of different ions due to multiple interactions between the ions and proteins, including the protein affinity with ions (generally following the Hofmeister Lyotropic series[153-156, 215], where Ca^{2+} ions demonstrated higher affinity to proteins that Mg^{2+} ions.), ionic valence, ion-condensation, and ion-correlation interactions.[59] Nevertheless, our bionic design of BSA@PSBMA demonstrated its unfailing low interfacial interaction energy with other surfaces and high-efficient fouling resistance to biomacromolecules in complex biological fluids/buffers, paving the way for practical applications.

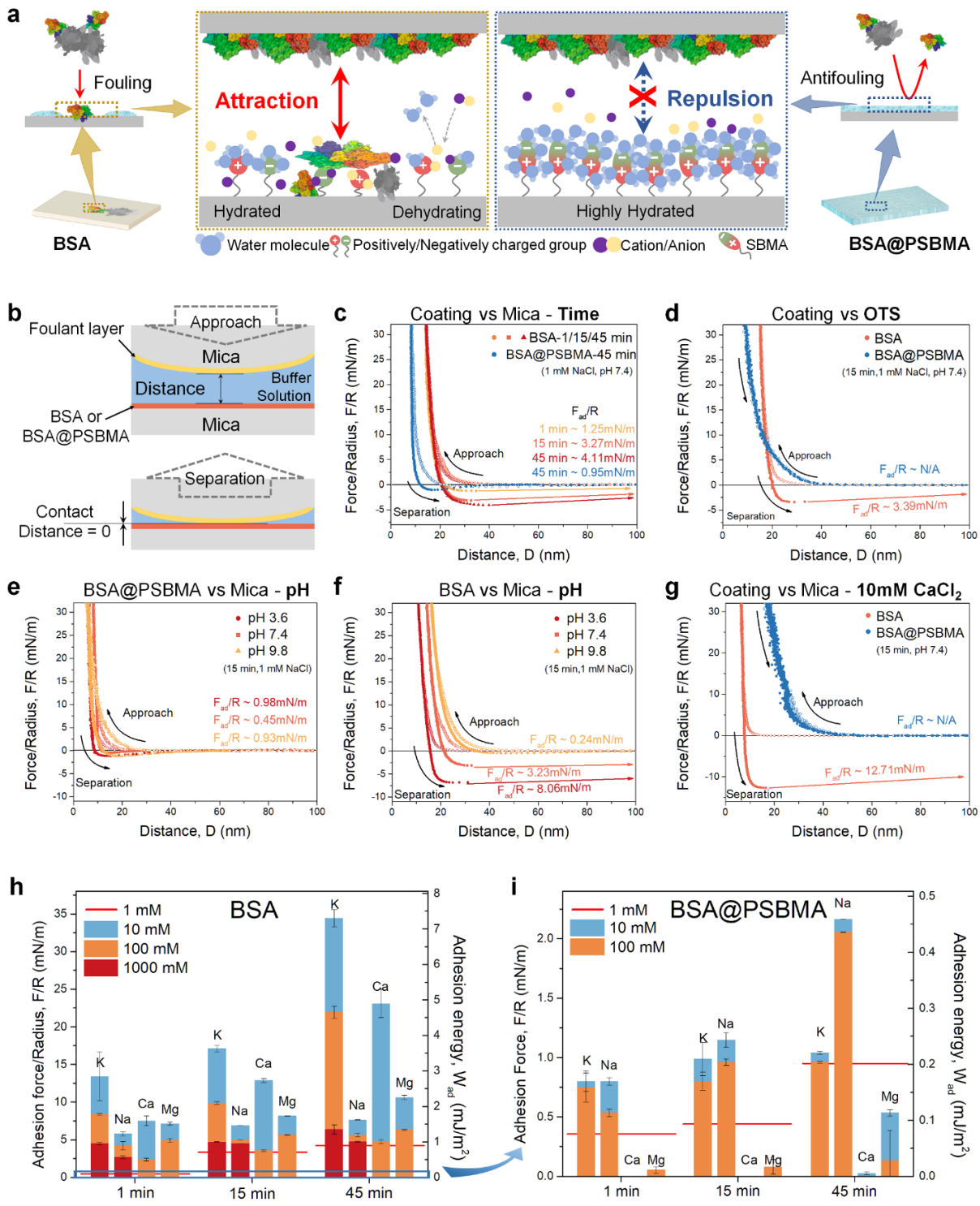

Figure 4.5 Interfacial interactions between foulants and coating surfaces measured by SFA force measurements. (a) Schematic diagram showing fouling/antifouling phenomena. (b) Experimental configurations in SFA force measurements. Interfacial interactions (normalized

force-distance, F/R-D, profiles) between protein-coated surfaces and (c) hydrophilic mica surfaces or (d) hydrophobic OTS surfaces. Interactions between mica surfaces and (e) BSA@PSBMA-coated or (f) native BSA-coated surfaces in solutions with different pH. (g) Interactions between protein-coated surfaces and mica surfaces in a solution with 10 mM $CaCl_2$. Adhesion force and energy between mica surfaces and (h) native BSA-coated or (i) BSA@PSBMA-coated surfaces in solutions with various salinity at different contact time. Values in (h, i) represent the mean and the standard deviation (n=3).

The BSA@PSBMA coating with excellent antifouling properties holds great potential to be used in biomedical applications, such as on-skin biosensors, implanted microsensors, and artificial substitutes, as indicated in Figure 4.6a. One of the most commonly used artificial substitutes is the artificial blood vessels that replace arterial vessels defunctionalized by the fouling of atherosclerotic plaque in coronary heart disease.[4, 216, 217] Such undesirable biofouling should be absolutely avoided after the implantation of new artificial vessels because 5 ng cm^{-2} of fibrinogen adsorption[39] can cause blood coagulation on the newly implanted artificial blood vessel surfaces. Here, we demonstrated a BSA@PSBMA-coated low-fouling artificial blood vessel, allowing stable operation in a long-term *in-vitro* blood circulation test (Figure 4.6b). After operation for 16 days, the flowing rate of blood in the BSA@PSBMA-coated medical tube was 8.98 cm s^{-1}, which was 92.0% of the original flowing rate. That of the native BSA-coated tube was 7.09 cm s^{-1}, 73.3% of the initial rate, and for the pristine tube, it rapidly dropped down to 4.37 cm s^{-1}, 49.11% of the initial (Figure 4.6c). The decrease in blood flowing rate resulted from the in-stent restenosis in which the inner tube narrowed down with the accumulation of bio-foulants on the inner surfaces. Figure 4.6d and S4.21 displayed the surface morphology of the inner wall of the medical tubes after operation for 16 days.

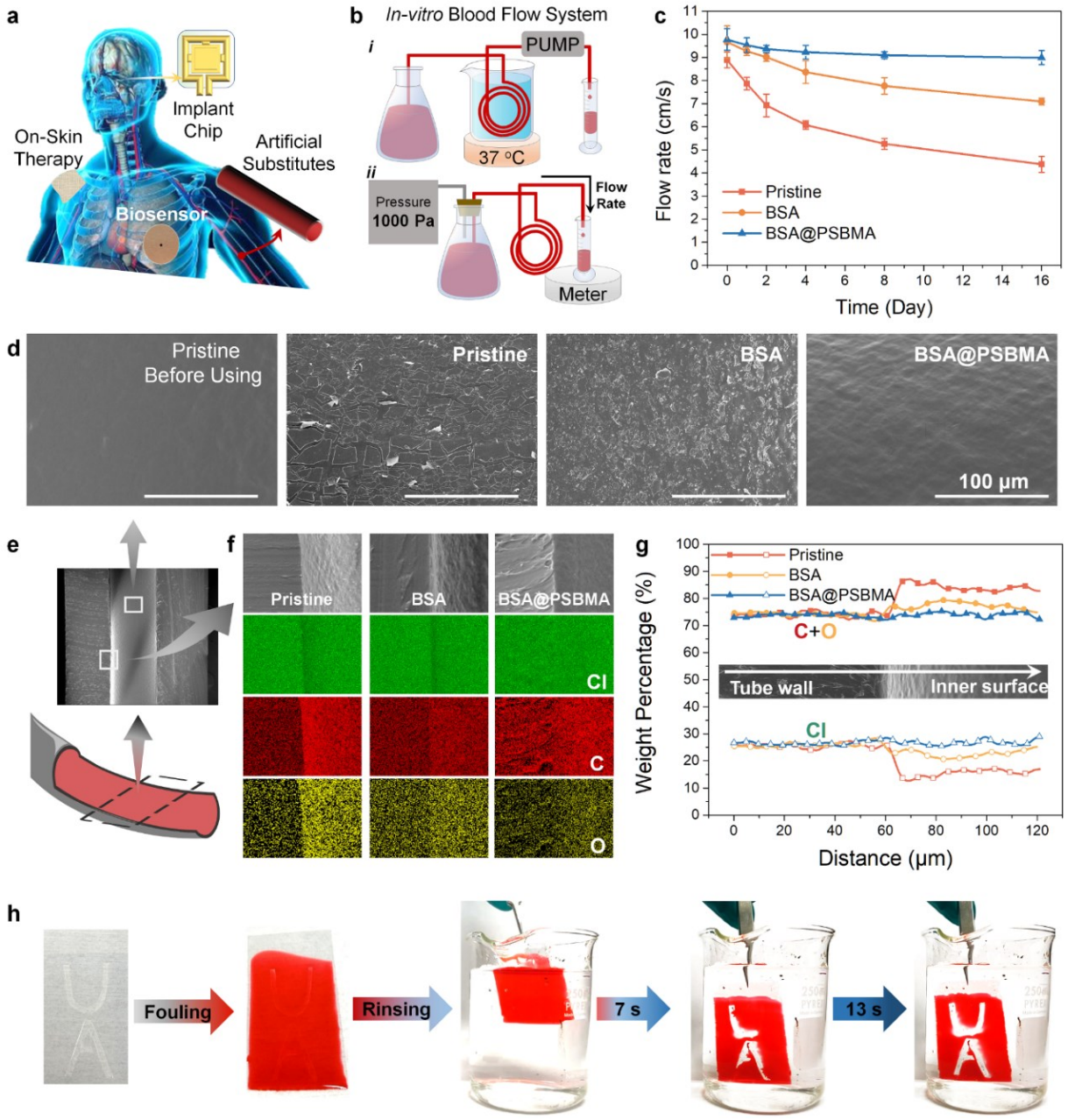

Figure 4.6 Demonstration of using BSA@PSBMA coating for biofouling resistance in artificial blood vessels. (a) Antifouling applications for biomedical needs. (b) In-*vitro* blood flow system. (c) Blood flowing rate for pristine, BSA-coated, and BSA@PSBMA-coated medical tubes over operation time. (d) SEM images: the morphology for the inner surfaces of different tubes after 16 days of blood flowing. (e) Intersection of a medical tube. (f) EDS mapping and (g) linescan showing the compositions change from the tube wall to the inner surface of different medical tubes.

(h) Self-cleaning tests for a BSA@PSBMA coating surface with '**UA**' pattern. Values in (c) represent the mean and the standard deviation (n=3).

It can be seen that large foulant debris fully covered the inner surface of the pristine tube, smaller and sporadic foulants on the native BSA-coated inner surface, and no obvious biofouling on the BSA@PSBMA-coated inner surface. As a result, more carbon and oxygen, the main composition of bio-foulants, were found on inner surfaces as displayed in EDS mapping (Figure 4.6f) and linescan (Figure 4.6g) of C+O elements. Besides, the fouling release property of the BSA@PSBMA-coated surface was demonstrated in a self-cleaning test (Figure 4.6h). In the test, the '**UA**' pattern prepared in Figure S4.8b by spraying method was first contaminated by viscous oil, then immersed in pure water, and finally, oil detached from the BSA@PSBMA-coated surface within 13 s. Such fouling release property of BSA@PSBMA coating was further supported by the induction timer test (Figure S4.22),[218] in which a viscous oil droplet was brought to the surface and then retraced from the surfaces without any oil residual left behind on the BSA@PSBMA-coated surface. The combination of excellent resistance to foulants attachment and fouling release performance in an aqueous environment implied the potential of the engineered BSA@PSBMA protein material in clinical utility.

4.4 Conclusions

In summary, we have developed an engineered BSA@PSBMA protein as antifouling coatings which overcome the intrinsic weakness of native protein coatings and achieve high-efficient and robust antifouling performance in complex biological fluids/buffers. Zwitterionic SBMA was grafted on BSA molecules via a simple *thiol-ene* click reaction in accordance with a bionic 'vine-thorn' design. The as-prepared engineered protein BSA@PSBMA preserved the intrinsically natural function of native BSA in surface-independent anchoring on various substrates,

such as metallic, inorganic, and organic substrates, and introduced the advanced function of SBMA on extraordinary resistance to a wide spectrum of potential bio-foulants, including proteins, CHO cells, and biofluids. The surface-independent anchoring capability is contributed by the amphiphilic segments of BSA that generate multiple attractive interactions with target substrate surfaces. The robust antifouling capability of BSA@PSBMA coating in complex biological environments mainly originates from the zwitterionic SBMA segments grafted on BSA molecules, enabling a bionic 'thorn-on vine' structure to induce the defensive interfacial hydration layer and additional steric repulsion between the coatings and foulants, which was confirmed via direct molecular force measurements. We have also demonstrated the potential application of this engineered protein with an artificial blood vessel that exhibits low-fouling properties and long-term stability in an in-*vitro* blood circulation test. The engineered BSA@PSBMA protein has great potential applications in many industrial and biomedical areas, considering its simplicity for manufacturing at a large scale and low cost of raw materials. The method in this work can be readily extended to engineering other native proteins via conjugation with functional nonproteinaceous motifs, providing an innovative paradigm of developing protein-based antifouling materials for various medical and non-medical applications, such as molecule/virus detection, point-of-care diagnostics, environmental toxin sensing, and microfluidic systems.

Supporting Information

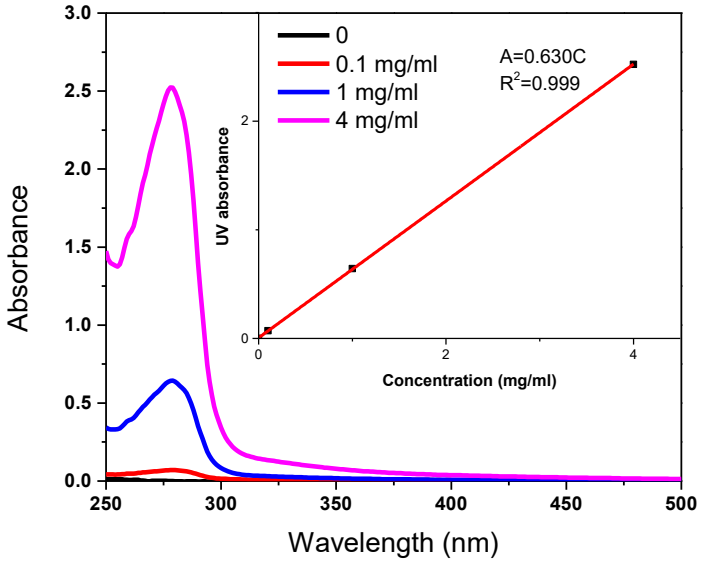

Figure S4.1 UV-Vis standard calibration curve of native BSA protein

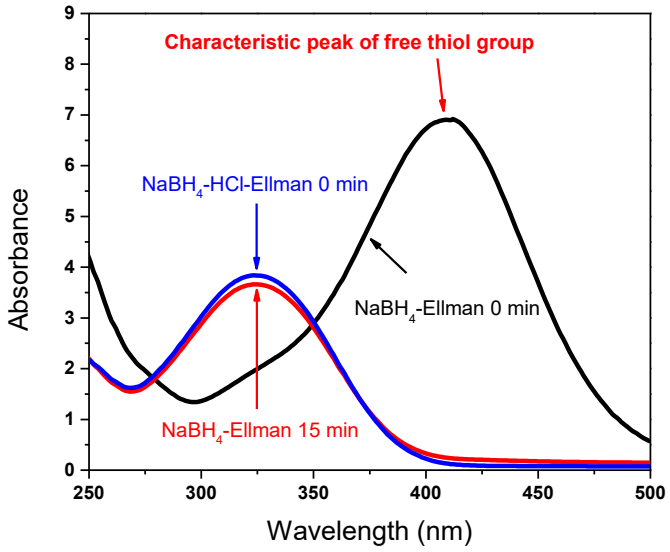

Figure S4.2 UV-Vis spectra: $NaBH_4$-Ellman reaction in different solutions

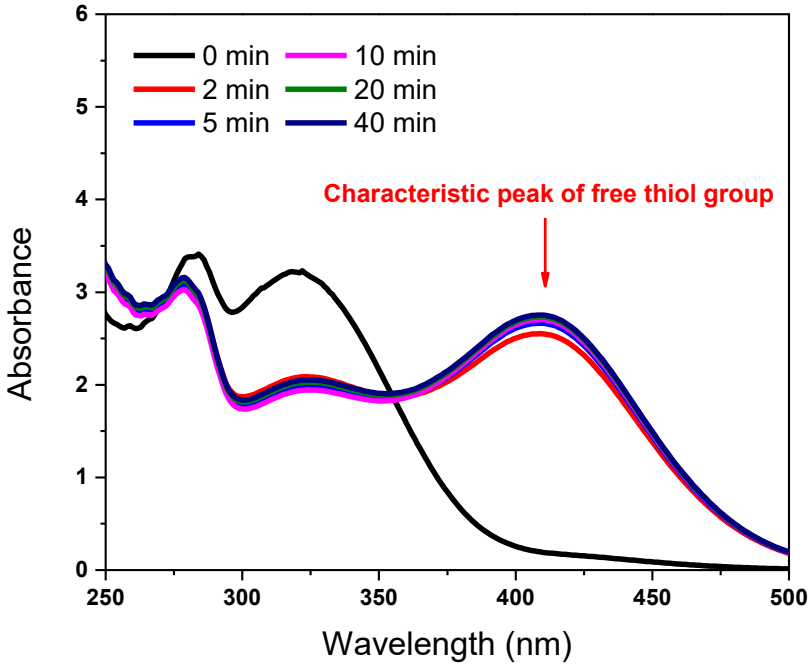

Figure S4.3 UV-Vis spectra: BSA reduced by $NaBH_4$ with different time

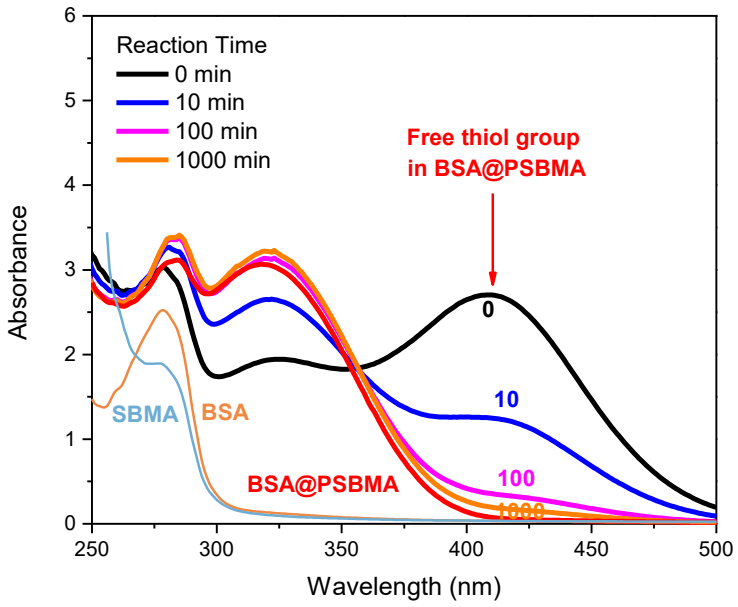

Figure S4.4 UV-Vis spectra: re-BSA/SBMA thiol-ene click chemistry for different time

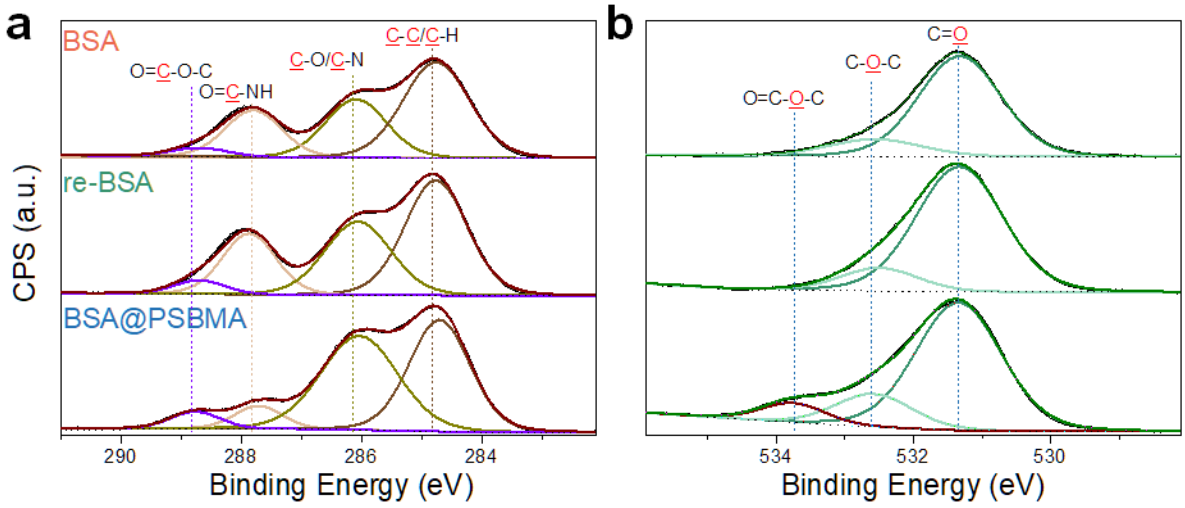

Figure S4.5 High-resolution XPS spectra of BSA, re-BSA, and BSA@PSBMA. (a) C spectra; (b) O spectra

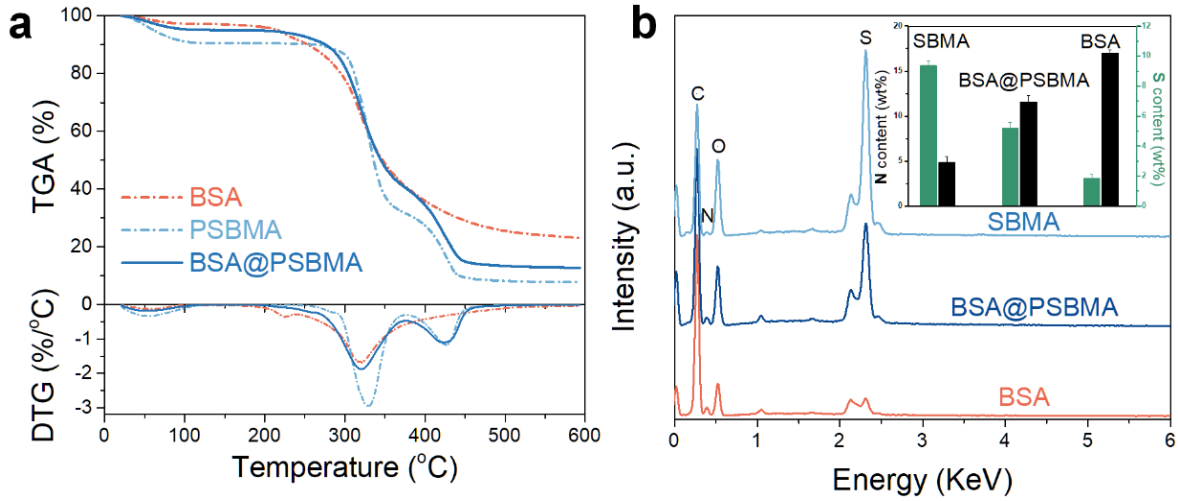

Figure S4.6 TGA and EDS characterization of engineered BSA@PSBMA proteins

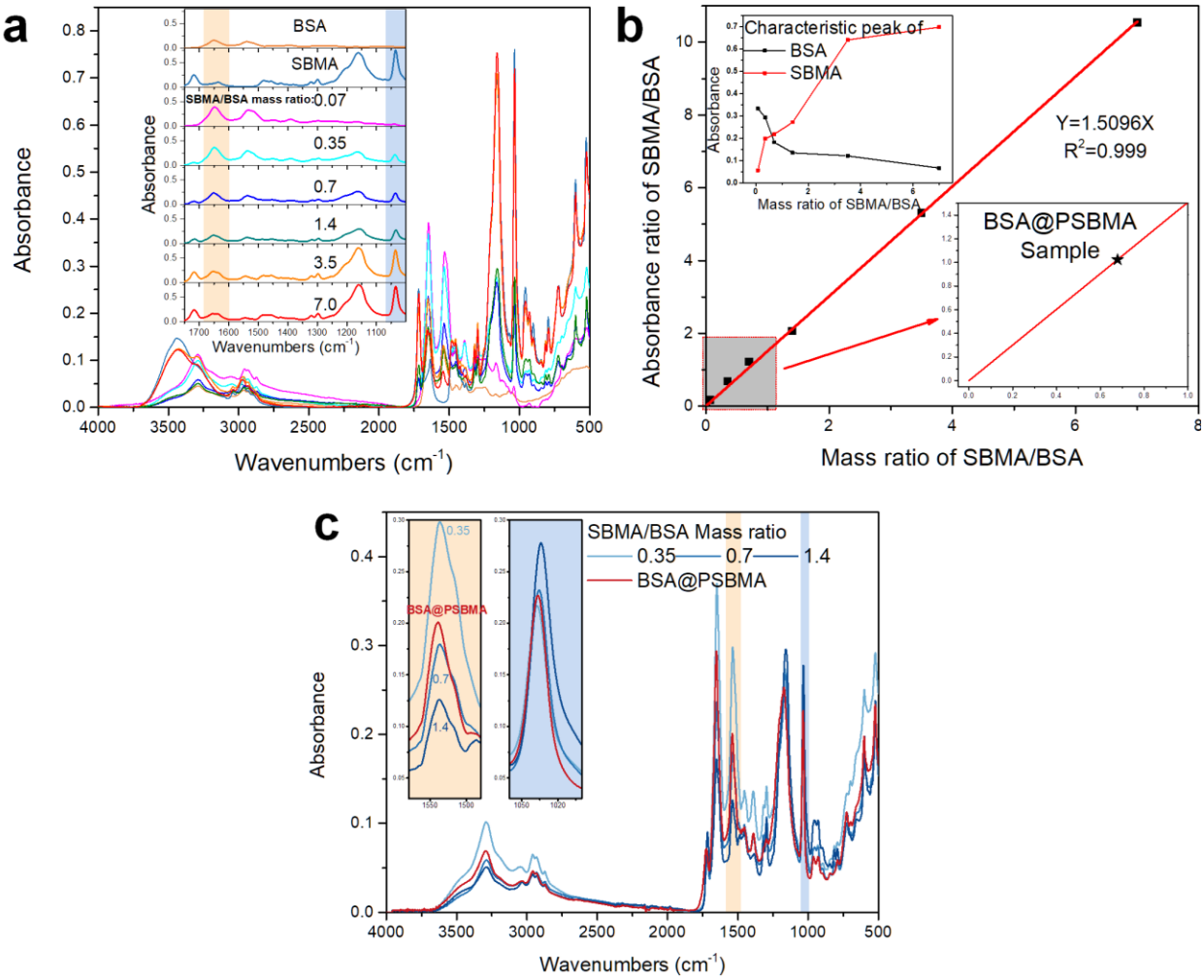

Figure S4.7 (a) FTIR spectra of SBMA monomer and BSA protein mixture with series of mass ratios; (b) Standard calibration curve for SBMA/BSA mass ratio; (c) FTIR spectra of engineered BSA@PSBMA protein

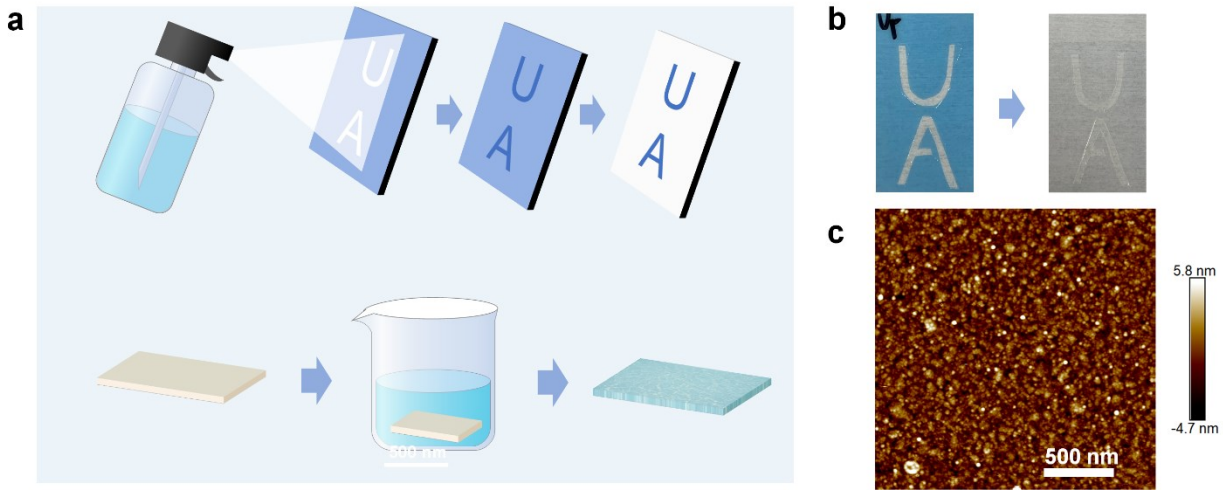

Figure S4.8 (a) Preparation of BSA@PSBMA coating by spraying and dipping method; (b) Spraying coating with specific pattern '**UA**'; (c) AFM image of BSA@PSBMA-coated Au surface by dip coating.

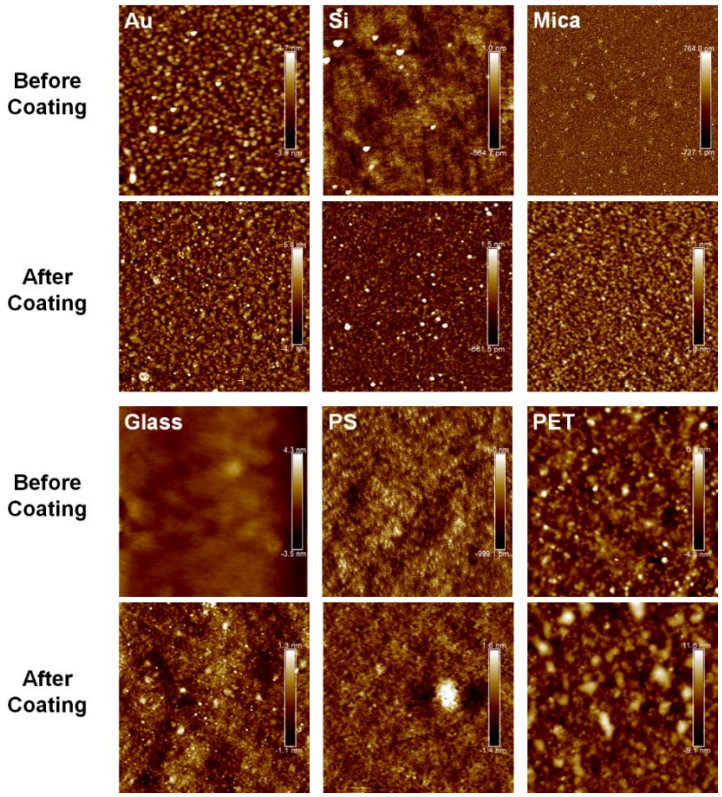

Figure S4.9 AFM images (2x2 μm^2): morphology change before and after coating (4 h) by engineered BSA@PSBMA protein

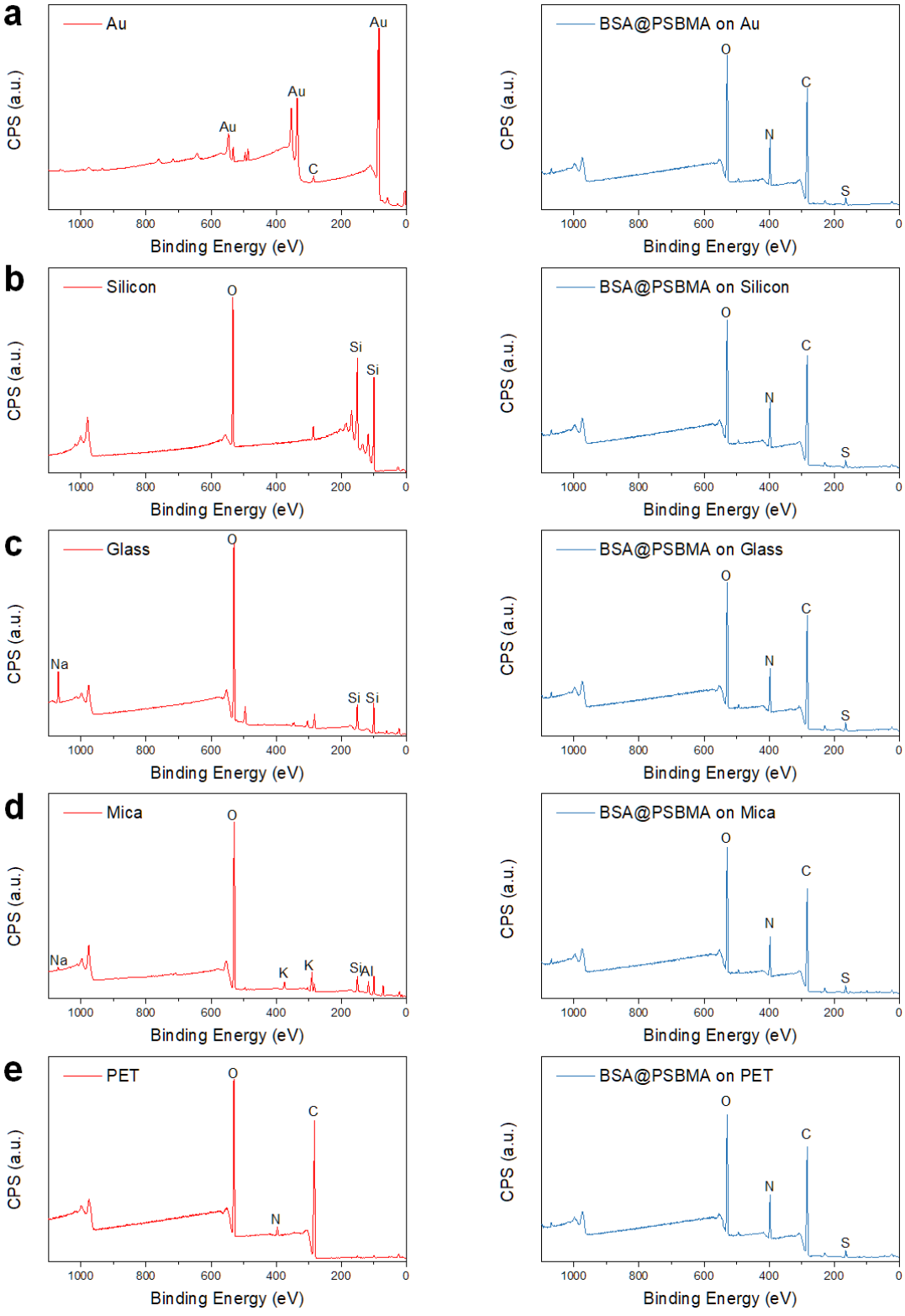

Figure S4.10 XPS spectra of surfaces before and after coating of BSA@PSBMA

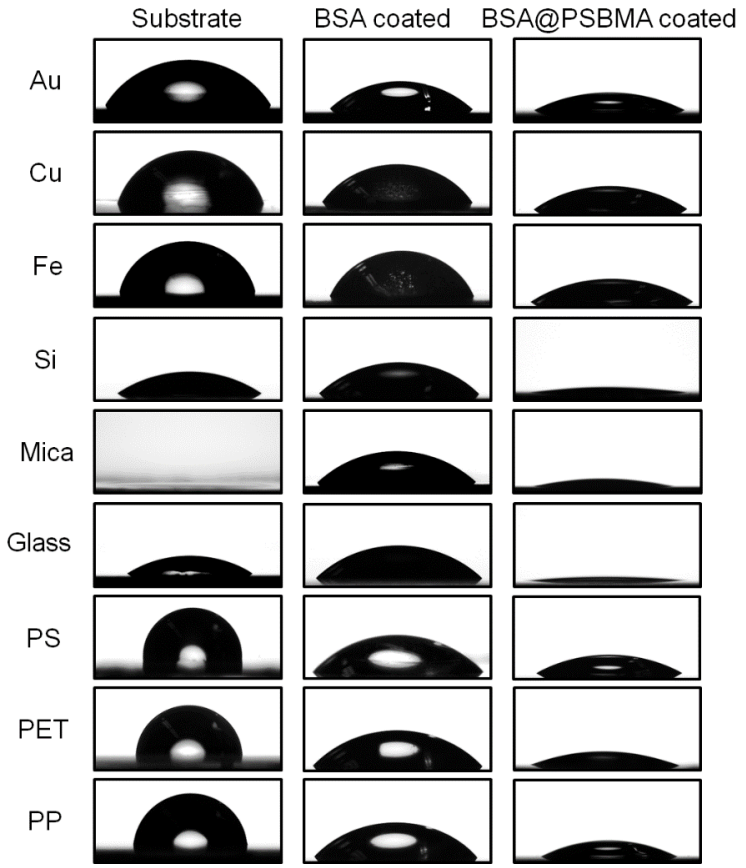

Figure S4.11 Static water contact angle in the air of various substrates

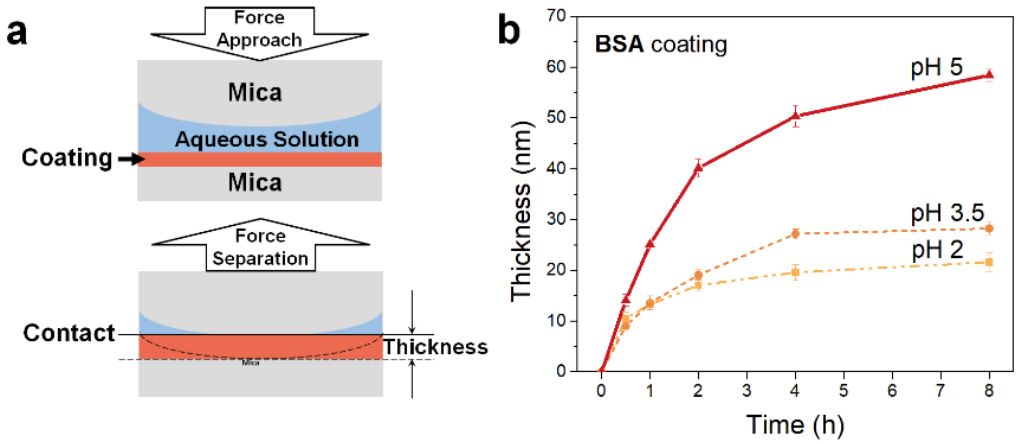

Figure S4.12 Coating thickness measurement by SFA (a) and coating thickness of BSA coating with different coating time and pH (b).

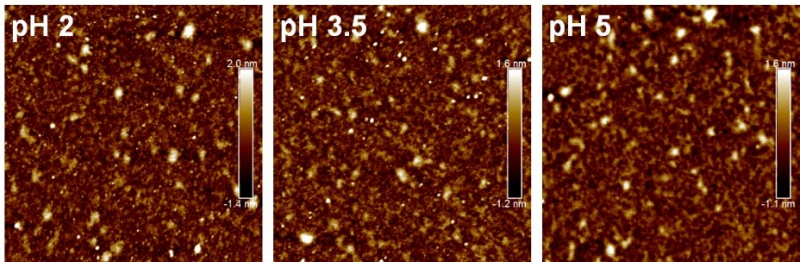

Figure S4.13 AFM images (2x2 μm^2): morphology of BSA@PSBMA coatings on Si wafer for 4 h at different pH.

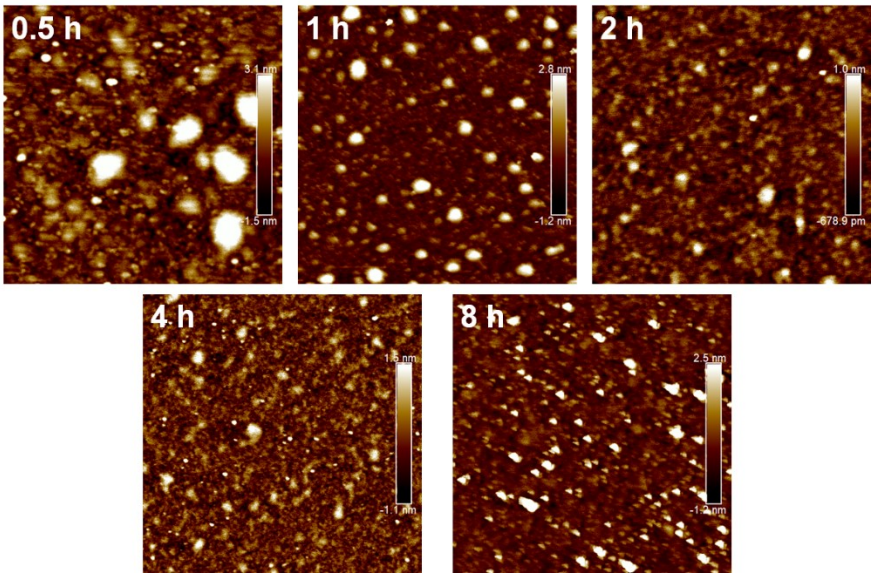

Figure S4.14 AFM images (2x2 μm^2): morphology of BSA@PSBMA coatings on Si wafer for different time (pH=5)

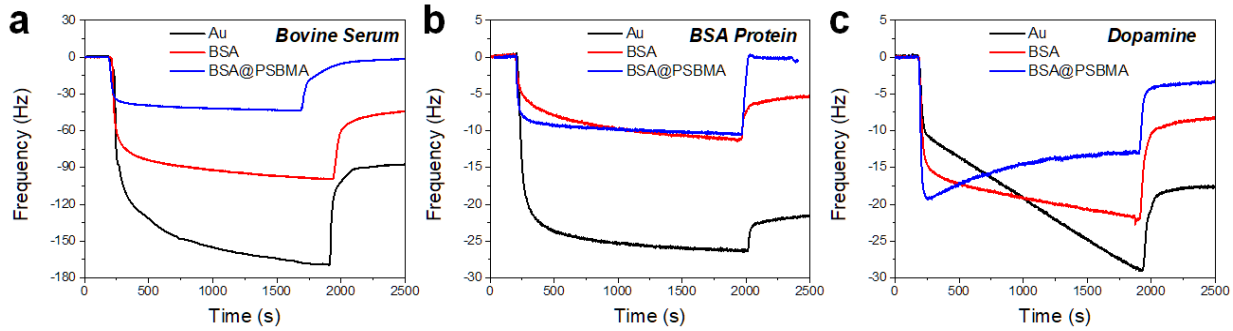

Figure S4.15. QCM-D curves: the change in resonance frequency associated with different foulants adsorption

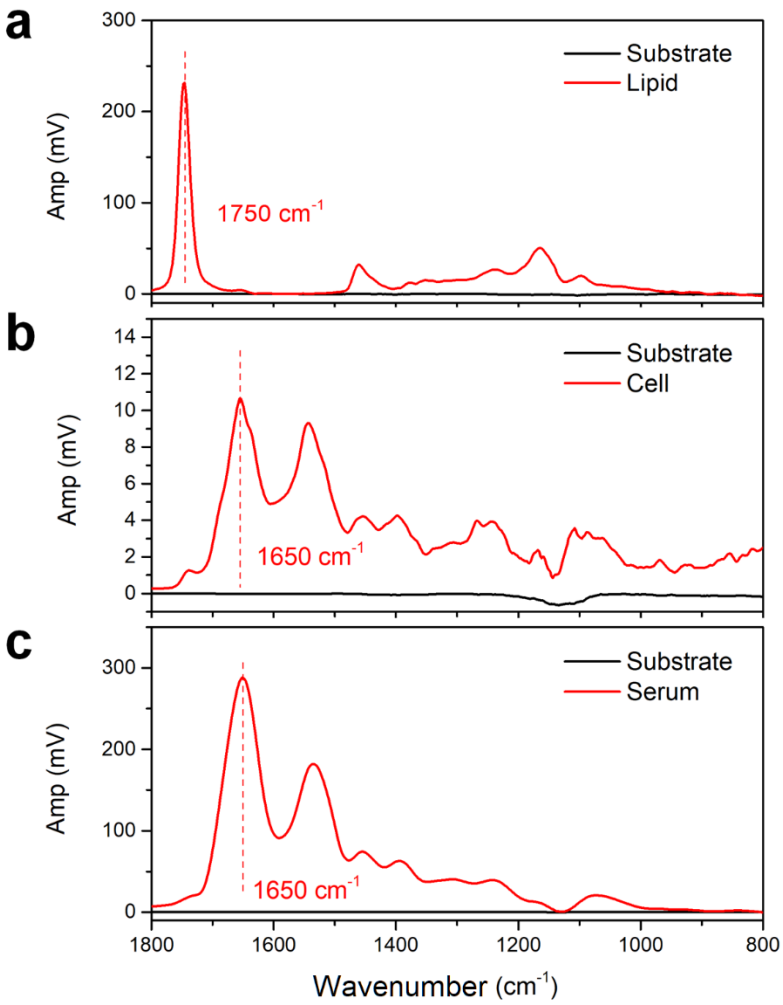

Figure S4.16 O-PTIR spectra of lipid, cell, and serum (marked wavelength used as the characteristic peck for mapping)

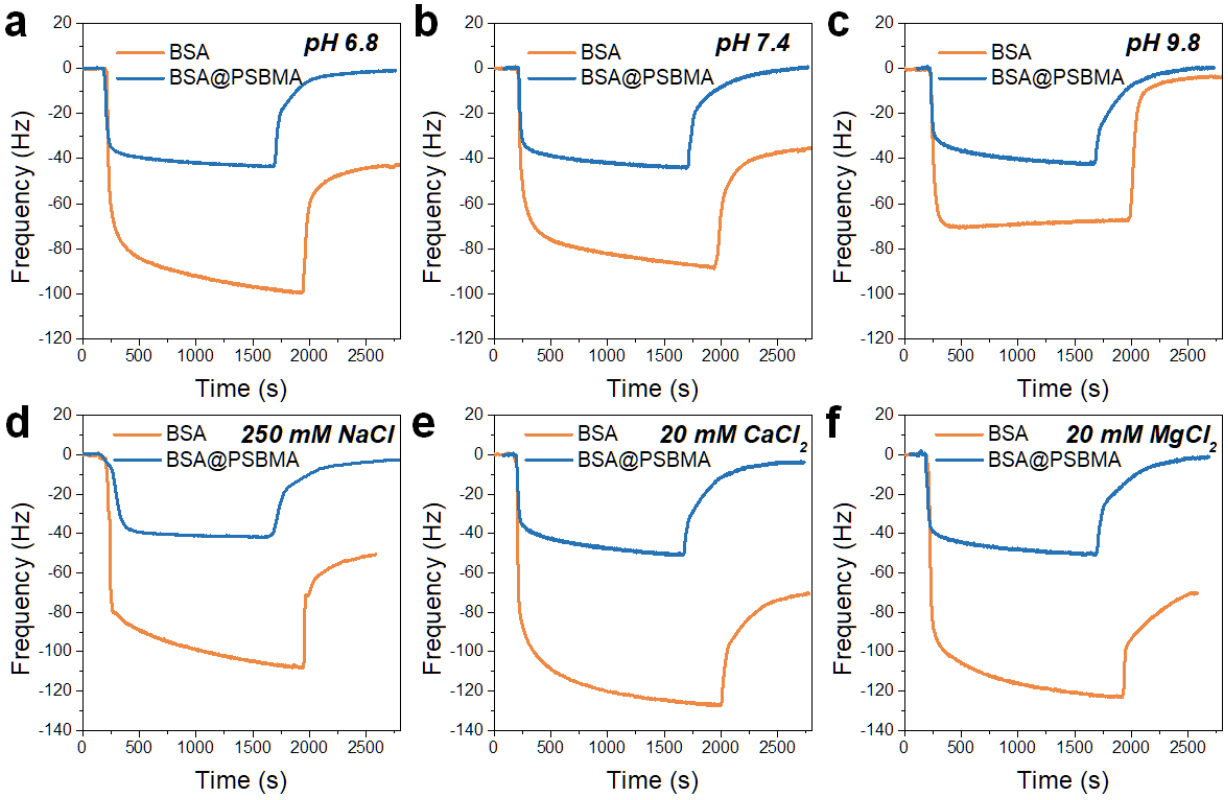

Figure S4.17 QCM-D curves: the change in resonance frequency caused by diluted FBS attached to sensors at different pH and salinity

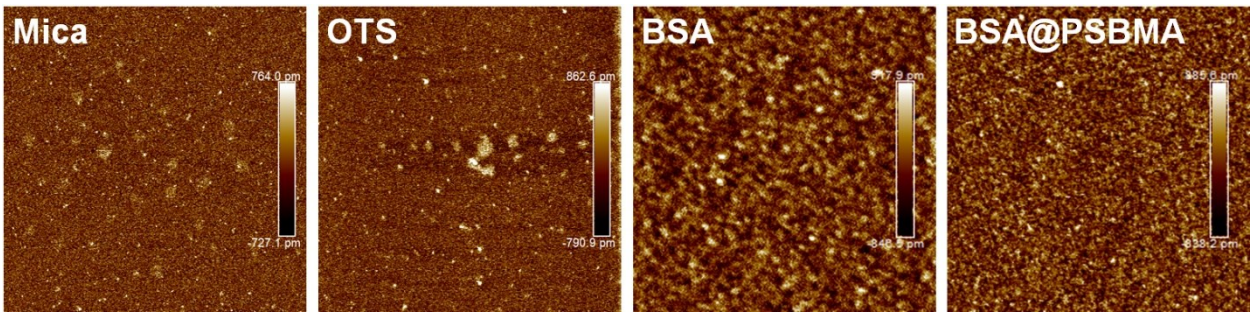

Figure S4.18 AFM images (2x2 μm^2): bare mica and functionalized mica surfaces used in SFA force measurements

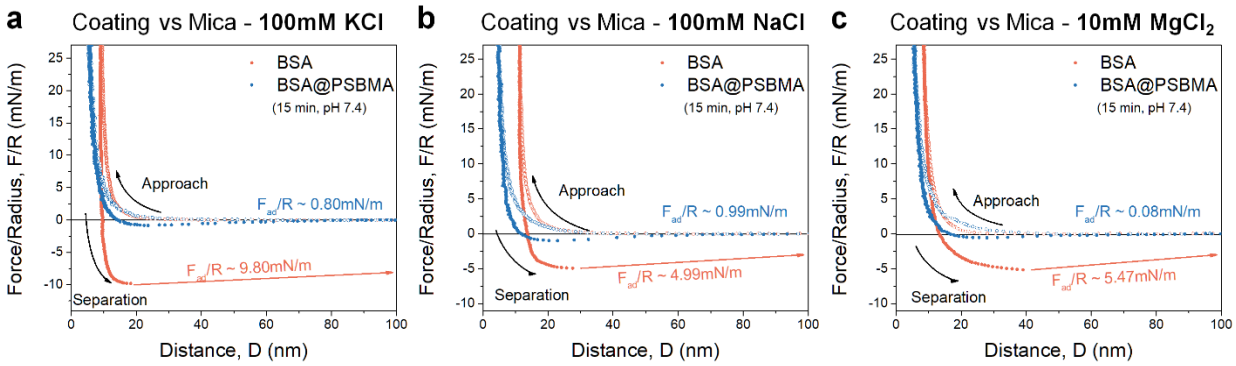

Figure S4.19 Force-distance profiles between native BSA or BSA@PSBMA coatings and mica surface in solutions with various salinity

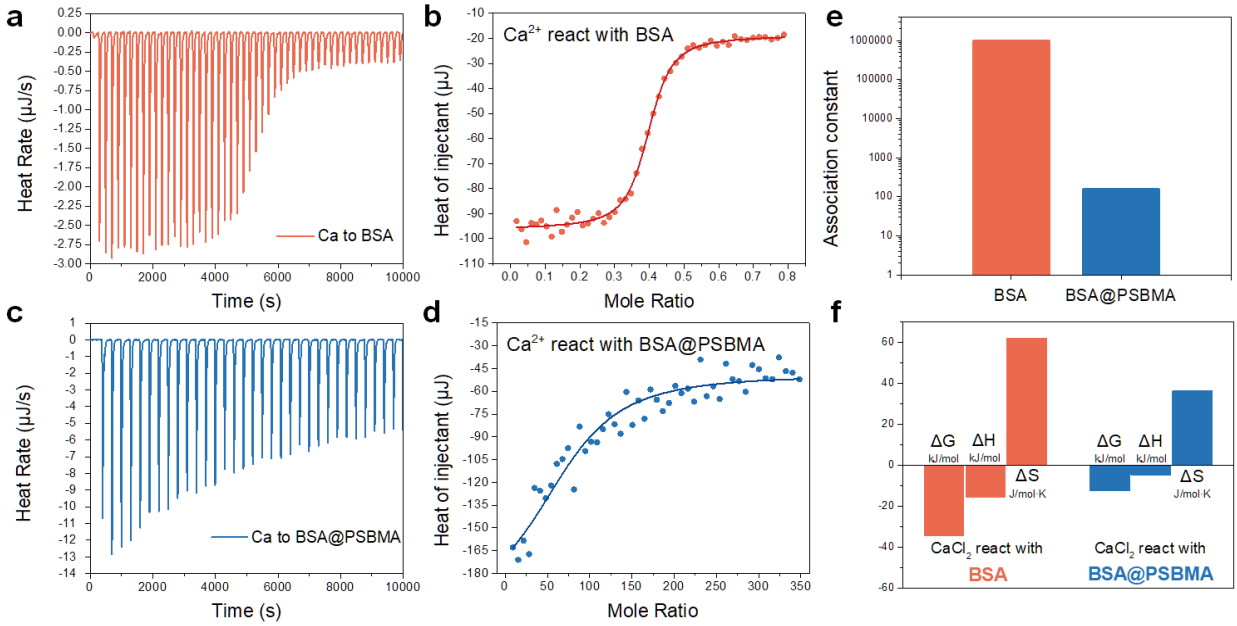

Figure S4.20 ITC characterizations: thermograms of Ca-BSA and Ca-BSA@PSBMA (a,c) and corresponding fitting models (b,d); thermodynamic parameters of the reactions (e,f)

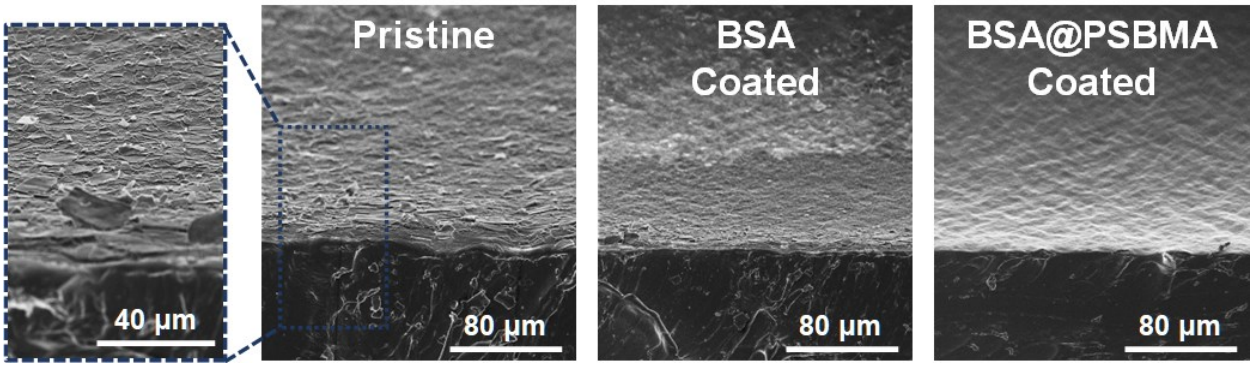

Figure S4.21 SEM images: morphology of intersection of different medical tubes after 16 days of working in an in-vitro blood circulation system (bottom black part: the intersection of tubing; bright upper part: the inner surface of tubing)

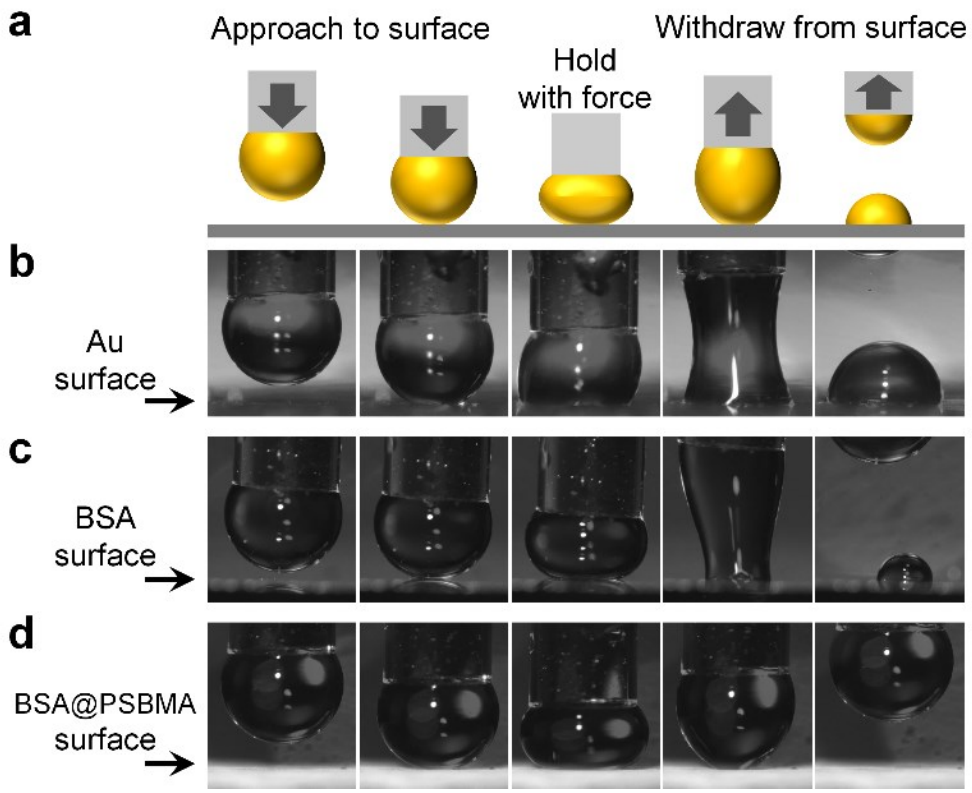

Figure S4.22 Induction timer working principle and the interactions between viscous an oil droplet and various surfaces

CHAPTER 5. Biomimic Engineered $NaMgF_3$@BSA Inorganic-Protein Coating enables Dual Protection for Mg-biomaterials

5.1 Introduction

Dental and orthopedic biomaterials, such as fixation plates for broken bone healing and barrier membranes for dental implantation, have benefited countless patients and represent a substantial $80 Billion USD global market in 2022.[219-223] Commercial biomaterials used in dentistry and orthopedics,[48] such as stainless steel, titanium alloys, ultrahigh molecular weight polyethylene, and polycaprolactone polymers, have shown increasing limitations. Hard metallic biomaterials could induce stress-shielding effects, leading to peri-implant bone loss and necessitating additional removal surgery. Soft polymeric biomaterials cannot function as load-bearing replacements and also raise clinical toxicity concerns when degraded. Magnesium (Mg)-based biomaterials overcome such limitations and have been under extensive investigation for decades due to their bone-like mechanical properties and biodegradability.[63, 224-228] This degradability (corrosion) avoids the secondary surgery for implant removal, and More importantly, Mg ions released from Mg biomaterials promote bone regeneration and accelerate new bone tissue formation.[48, 229-231] However, despite these merits, the rapid degradation induced by biocorrosion poses a great challenge to their clinical applications. The rapid corrosion can deteriorate structural integrity, reduce mechanical strength, and cause health risks like subcutaneous emphysema. Constructing an anticorrosion coating appears to be a more feasible and safer alternative to address these issues, compared with traditional microalloying strategies that involve accelerated degradation and toxic elements.[225, 226, 228, 232] However, directly constructing a coating on Mg substrates is incredibly challenging due to the high reactivity of Mg surfaces, which causes surface

alkalinization (pH ~10.5) to degrade the coatings and generates numerous H_2 bubbles, resulting in porous coatings or coating delamination.[229, 233, 234]

Traditional used organic coatings are highly compact but suffer from insufficient mechanical durability and low interfacial adhesion to Mg substrates, resulting in uncontrollable damage and delamination.[235, 236] Integrating organic anticorrosion coatings atop inorganic-coated Mg substrates may improve the interfacial adhesion, but this approach typically involves time-consuming and arduous operations.[237] As a result, inorganic coatings are more desirable due to their stronger adhesion to Mg substrates, better mechanical durability, and facile preparation. Chromate conversion coating is the most frequently utilized inorganic anticorrosion coating but faces regulatory restrictions because of environmental concerns.[238, 239] Eco- and bio-friendly phosphate-based,[233] fluoride-based,[240-242] or rare-earth-based[243] conversion coatings have been developed but are vulnerable and intrinsically have low compactness due to their large particles. The large particles result from a mineralization process, where dissolved Mg ions are converted into inorganic minerals on Mg surfaces. They cannot densely pack on a substrate, causing mismatch-induced cracks as electrolyte pathways that enable corrosion. Moreover, conventional inorganic coatings lack antifouling properties and exhibit increased susceptibility to accelerated and complex biocorrosion after implantation. Biocorrosion involves a reciprocal deterioration of corrosion and fouling, where randomly distributed bio-foulants on the surface significantly hastening corrosion.[40, 244] Consequently, the design of the next-generation coating for Mg surfaces requires dual protection: advanced anticorrosion function involving finer particles and sealing agents to compact coatings, as well as additional antifouling function to mitigate fouling-accelerated biocorrosion.

Tooth enamel is the hardest part of our body, renowned for its highly compact structure with fine hydroxyapatite (HAP) particles.[245] It is an inorganic-organic composite, functioning as the protective armor of the tooth against wear and corrosion. This function is aligned with the functions of protective coatings, inspiring us to construct a similar inorganic-organic composite coated on Mg substrates as 'enamel' via mimicking the formation of tooth enamel. More importantly, tooth enamel formation is a typical mineralization process, like the inorganic coating formation. In tooth enamel formation, enamel proteins, including amelogenin and non-amelogenin proteins, play a pivotal role in transforming Ca-Na-PO_4-F ions into enamel (Figure 5.1a).[102, 246, 247] Enamel proteins modulate the kinetics and thermodynamics of Ca-Na-PO_4-F biomineralization via protein-ions association, aligning the inorganic hydroxyapatite (HAP) crystallites and reducing their size to form a densely packed coating (Figure 5.1a).[248-254] Following this tooth-enamel-formation-inspired concept, we can potentially develop a desirable, compact protective coating with fine inorganic particles on Mg surfaces. Moreover, the proteins embedded in the enamel can seal the residual internal cracks within the coating, establishing a 'brick-and-mortar' structure along with HAP particles, further promoting the compactness of the coating to protect the tooth.[255]

Herein, inspired by tooth enamel formation, we introduce a natural protein, bovine serum albumin (BSA), as the 'enamel protein' to facilitate the formation of an inorganic-protein (inorganicPro) coating as 'enamel' packed on Mg substrates. This innovation upgrades a general mineralization to biomineralization that converts ions into finer coating particles (Figure 5.1b). Specifically, such inorganicPro coating is prepared by immersing Mg surfaces into a solution with sodium fluoride (NaF) and BSA proteins. NaF, a biocompatible additive in toothpaste, will mineralize with the surface-released Mg ions, forming nanoparticles deposited on Mg substrates as an anticorrosion coating.

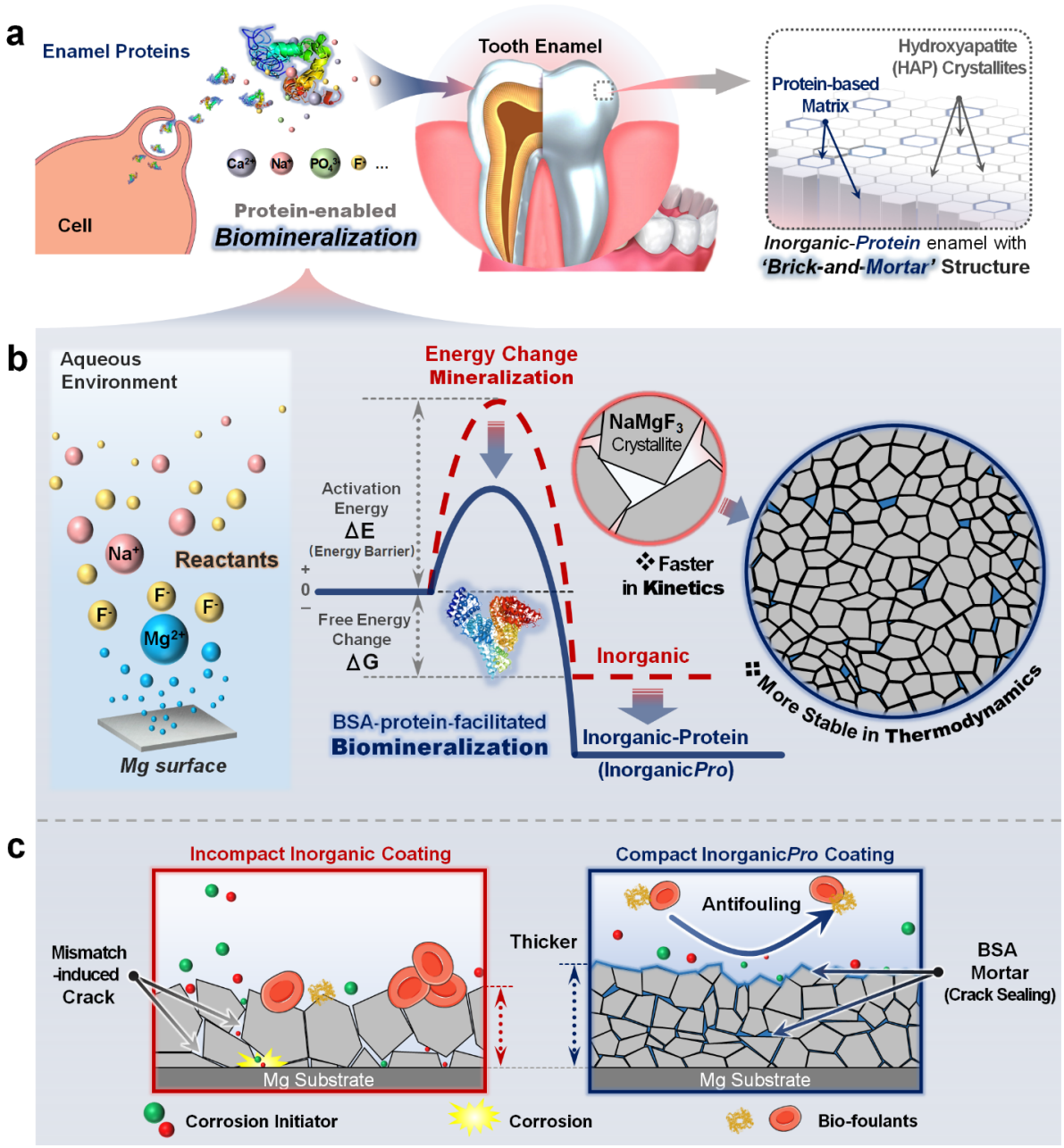

Figure 5.1 Illustration of Inorganic-protein (inorganic*Pro*) coating Strategy inspired by biomineralization of tooth enamel formation. a, Tooth enamel formation based on protein-involved biomineralization and its 'brick-and-mortar' structure. b, Schematic diagram showing the comparison of energy change in the formation of conventional inorganic coatings and the new biomimetic InorganicPro coatings in this work. c, Schematic diagram showing the incorporation of BSA in and on the coatings achieves two synergistic functions: 'mortar' to seal residual cracks within the coatings to promote compactness, and mitigating biofouling issues.

BSA, an abundant protein in plasma with high binding affinity to various ions,[256] can affect the formation kinetics and thermodynamics of nanoparticles through biomineralization. BSA proteins boost the kinetics of the Na-Mg-F mineralization, refine the deposited nanoparticles, and enhance the compactness of in-situ formed coatings - akin to the role of the enamel protein during tooth enamel formation. Meanwhile, the BSA macromolecules embedded inside inorganicPro coating act as 'mortar' to seal the corrosion pathways, further reinforcing the coatings. Besides, BSA is well recognized for its ability to inhibit biofouling and can anchor atop inorganic coatings, functioning as an antifouling layer.[6, 7, 124] This anticorrosion and antifouling dual protection synergistically mitigates fouling-accelerated biocorrosion in complex biological conditions, offering three times higher corrosion resistance and tenfold better antifouling performance than its conventional inorganic counterpart. This work has demonstrated an innovative strategy using proteins to alter the reaction kinetics to achieve a dual-protection inorganic-protein coating for Mg-based biomaterials, potentially paving the way for the application of Mg-based biomaterials and the development of advanced biomedical surface designs.

5.2 Experimental Methods

5.2.1. Materials

Bovine serum albumin (BSA), MES buffer, PBS buffer, Trichloro(octadecyl)silane (OTS), $AgNO_3$, NaCl, $MgCl_2$, $CuCl_2$, CrO_3 powders, glutaraldehyde, 16-mercaptohexadecanoic acid, 8-mercapto-1-octanol, (3-Aminopropyl) triethoxysilane (APTES), Reagent Alcohol (anhydrous), Calmagite, silica sphere powder, Whey, Hemoglobin (Hb), lysozyme (Lyso), Glucose, humic acid (HA), dopamine hydrochloride, L-lysine, artificial saliva, and L-Alanine were purchased from Sigma-Aldrich. NaF and RPMI 1640 medium were purchased from Fisher Scientific. Fetal bovine blood, milk, and Canola oil (lipid) were from the local grocery store. Ultrapure water in the

experiments was from Milli-Q Advantage A10 (Millipore, USA). Mg sheet (0.2 mm in thickness) was purchased for Xintong Metals, China. The raw Mg sheet was annealed at 300℃ for 3 h before polishing and using in this work. Si sensors (QSX301) for QCM-D were from Biolon Scientific.

5.2.2. Measurement of the Mg ion concentration in solution via UV-Vis spectroscopy

The reaction rate could be estimated by monitoring the Mg ion concentration change during the reaction between $MgCl_2$ (12 mM) and NaF (500 mM) at 30℃. The concentration of Mg ion could be measured by Calmagite solution (0.25 mM Calmagite in 3 mM $Na_2B_4O_7$ buffer, pH 9.25).[257, 258] 10 μL Mg ion solution was injected into 1 mL Calmagite solution and then, after 1.5 min, tested by UV-Vis spectrum on Evolution 300, Thermo Scientific, USA. The standard calibration curves and the Mg ion concentration change during the reaction with/without BSA are shown in Figure S5.17, S5.18, and Figure 5.4b.

5.2.3. Isothermal titration calorimetry measurement (ITC)

The ion-ion and ion-BSA binding was directly measured by ITC (NanoITC, TA, USA), in which the association constant (K_a), reaction stoichiometry (n), and the change in enthalpy (ΔH), entropy change (ΔS), and Gibbs free energy (ΔG) could be accurately determined.[157, 259, 260] The affinity of Mg-Na-F with/without the presence of 10 mg mL^{-1} BSA protein has been measured by ITC in Figure 5.3d and S5.20, in which $MgCl_2$ salt solution (200 mM in 10 mM MES buffer, pH 6) was titrated into NaF solution (100 mM in 10 mM MES buffer, pH 6). In Mg-BSA affinity measurement, $MgCl_2$ salt solution (2 mM in 10 mM MES buffer, pH 6) was titrated into BSA solution (0.36 mM in 10 mM MES buffer, pH 6). In each measurement, 5 μL titrant solution was injected into 950 μL titrand solution with 50 injections. The reaction heat was corrected by subtracting the heat of titrant to buffer, buffer to titrand, and analyzed by the different models on

the software NanoAnalyze by 1 independent onesite model. The enthalpy (ΔH) and reaction stoichiometry (n) for each reaction were listed in corresponding figures.

5.2.4. Measurement of mechanical properties and density of coatings

The mechanical properties of the coatings, such as the hardness and friction behavior, are essential for the long-term operation of implants, which are measured on the NHT nano indenter NTR^3 nano tribometer (Figure 5.3a-c, Anton Paar, Austria). In the nanoindentation test, the Berkovich indenter measured the hardness with 2.5 mN of normal loading force. At least 30 different points were tested and the averaged curves were plotted in Figure 5.3a. The nanoindentation curves were analyzed by using Oliver-Pharr theory to calculate the surface hardness. In the reciprocating ball-on-disk friction test, a nylon ball with a diameter of 2 mm as a counter-facing ball was contacted with the coating in a NaF (100 mM) aqueous solution with 30 mN of loading force. The ball reciprocally slid on the surfaces with a velocity of 1 mm s^{-1} and sliding amplitude 1 mm for different cycles. Typical shear force and friction coefficient versus sliding distance/cycle were displayed in Figure 5.3b, and wear depth during the friction was shown in Figure 5.3c.

The density of the coatings was determined by the weight and volume change before and after coating removal by a CrO_3 solution for 10 min, following the American Society of Testing Materials (ASTM) standard method (ASTM B659-90 R2014). Specifically, the weight and volume of the coated sample were measured using an analytic balance and Archimedes' principle, respectively. After removing the coatings, the weight and volume of the sample were re-measured. The change in weight and volume of the sample was then considered as the weight and volume of the coating. The density of the coatings could be calculated by their weight and volume accordingly.

5.2.5. Cytotoxicity

Human gingival fibroblasts (HGF, ScienCell, American) were used to evaluate cell biocompatibility in vitro and incubated in complete medium including Dulbecco's modified Eagle's medium (DMEM), 10% fetal bovine serum (FBS), and 100 IU mL^{-1} penicillin and 100 IU mL^{-1} streptomycin (Gibco, American). Before the cell test, all samples (pure Mg, inorganic-coated Mg, and inorganicPro-coated Mg) were irradiated with ultraviolet light for two hours for sterilization. The sterilized samples were immersed in the medium at 37°C for 24 h to obtain the extracts and the ratio of the surface area of the sample to the volume of the medium was 3 cm^2 mL^{-1}. Then, the HGF cells were seeded in a 96-well plate with a density of 2,000 cells per well and cultured in a humidified incubator with 5% CO_2 at 37°C for 24 h. The culture medium was then changed to the sample extracts and cultured for 1, 2, and 3 days with the complete medium as the control group, respectively. The 10 μL CCK-8 (Cell Counting Kit-8, Bestbio, China) solution was added to each well and further cultured in a cell incubator for 2 h. Then the absorbance at 450 nm was determined by a microplate spectrophotometer (SpectraMax paradigm, Molecular Devices, USA).

The HGF cells were seeded in 96-well plate with a density of 3,000 cells per well and cultured in a humidified incubator at 37°C for 24 h. The culture medium was then changed to the sample extracts and cultured for 1, 2, and 3 days with the complete medium as the control group, respectively. Then, the samples were washed with phosphate buffered solution (PBS, pH 7.4) and stained with Calcein-AM/EthD-1 (Invitrogen, American) for 30 min at 37°C. After staining, the samples were rinsed with PBS and the live/dead cells on the sample surface were observed with an inverted fluorescence microscope (Olympus, Japan).

5.2.6. Corrosion test and weight loss measurements

A series of pure Mg and coated Mg was corroded in different bioflouids, including 1× PBS buffer cell culture-medium (RPMI 1640 Medium) supplemented with 10% FBS (Fetal Bovine Serum), artificial saliva at pH 6.8 and 7.9, and 20% diluted blood for different durations. The lost Mg will be dissolved into the corrosion solution or form corrosion products on the surface. Such weight loss of Mg was measured by the golden standard method – using CrO_3 (200 g L^{-1}) + $AgNO_3$ (10 g L^{-1}) to remove the corrosion products on Mg surfaces. Specifically, corroded Mg was immersed in CrO_3 solution for 20 min. Then, the clean Mg was rinsed with water and dried before measuring the weight change. The weight loss will be normalized by surface area for different samples. An accelerated corrosion solution (5 wt% NaCl + 2 mM $CuCl_2$) was used to examine the corrosion rate of different Mg surfaces, as shown in Video S1.

5.2.7. In vitro biofouling test

The inorganic/inorganicPro-coated Mg were incubated in bovine blood and milk for 24 h and 48 h, respectively, to evaluate the fouling resistance of coatings. After fouling, the surfaces were copiously rinsed with ultrapure water before characterization. Bio-foulants on the surfaces in the tests have been characterized using O-PTIR, a non-contact submicron visible probe infrared spectroscopy (mIRage, Photothermal Spectroscopy Corp, CA). In O-PTIR characterization, a tunable pulsed mid-infrared (IR) laser induces photothermal effects onto a sample surface, which are measured using a scattered visible probe laser to focus on the sample. The reflection IR spectra recorded by O-PTIR can be correlated to ATR-FTIR spectra. The O-PTIR spectra of bio-foulants in blood and milk (Figure S5.21) showed their corresponding characteristic peaks. Then, using IR at 1540 cm^{-1} (blood as an example) to scan the sample surfaces with the resolution of 500 nm to map the milk foulants distributed on the sample surfaces (Figure 5.5a). The O-PTIR mapping

overcomes the limitation of EDS characterization, which cannot identify organic groups with the same composition, and the spatial resolution limitation of traditional FTIR microscopy (10-20 μm). The coverage of foulants on surfaces was measured on two samples with 3 different areas. The results from the biofouling test demonstrated the excellent antifouling properties of inorganicPro coating.

5.2.8. Quartz crystal microbalance with dissipation monitoring (QCM-D) test

20% dilution of biofluids and protein (5 mg mL^{-1}) and other water-soluble metabolites were used in this test. For the lipid (Canola oil, a highly viscous oil employed as a model lipid), it was dissolved in ethanol with a concentration of 20 mg mL^{-1} and dispersed via ultrasonic for 30 min, and then the lipid/ethanol mixture was dispersed in water via a homogenizer (T18 digital ULTRA TURRAX, IKA, Germany, speed 20,000 rpm, 15 min). The inorganic and inorganicPro surfaces were obtained by the dip-drying method, in which inorganic/inorganicPro particles were dispersed in ultrapure water and then dipped on the APTES-functionalized Si sensors and dried for 1 h. The coated sensor was rinsed with ultrapure water to remove the loosely bonded particles before QCM-D tests on Q-Sense E4 (Biolin Scientific, Finland). The data analysis follows the extended viscoelastic model on QTools software (Biolin Scientific, Finland). The adsorption value was averaged by 3 measurements.

5.2.9. Interfacial interaction forces measurements by colloidal probe atomic force microscopy (AFM)

AFM nanomechanical study is a direct and quantitative analysis technique for interaction forces between two components [109, 110]. This work measured the interaction forces between the foulant-coated AFM probe and inorganic/inorganicPro coatings. Protein (Whey, Hb, Lyso) -coated

AFM probe was prepared via the dip-coating method, in which a silica colloidal AFM probe was firstly prepared by gluing a silica microsphere with a diameter of ~ 5 μm onto a tipless cantilever using epoxy glue and then was immersed in protein solution (0.5 mg mL^{-1} protein) and incubated for 1 h, followed by thorough rinsing with Milli-Q water and drying by nitrogen. -NH_2 and -CH_3 functional group coated AFM probe was prepared via immersing silica probe in APTES (20 mM in anhydrous reagent alcohol) and OTS (20 mM in anhydrous reagent alcohol), respectively, for 2h, followed by thorough rinsing with reagent alcohol and drying by nitrogen. -COOH and -OH coated AFM probe was prepared via immersing gold-coated probe in 16-mercaptohexadecanoic acid (10 mM in anhydrous reagent alcohol) and 8-mercapto-1-octanol (10 mM in anhydrous reagent alcohol) for 12 h, followed by thorough rinsing with reagent alcohol and drying by nitrogen.

AFM force measurements between foulant-coated AFM probe and inorganic/inorganicPro coatings were carried on Bruker ICON AFM in 1× PBS buffer at pH 7.4. To ensure the accuracy of force measurements, force mapping was performed on various coatings in an area of 10 × 10 μm^2 to acquire a two-dimensional array of force-separation profiles with 15 × 15 points in at least three different regions of the coatings and at least two independently prepared samples of the same batch. The Gaussian method statistically analyzed the measured interfacial interaction forces, as shown in Figure 5.6b and S5.22.

5.2.10. In vitro Mg-Blood corrosion test

The Mg-based devices will be under bio-corrosion after implantation, where the blood continuously fouls and corrodes the surface of Mg-implants, resulting in rapid degradation of surface integrity and mechanical properties. The surface morphology and mechanical strength of Mg-implants during bio-corrosion were characterized by an in-vitro Mg-Blood corrosion test, as

shown in Figure 5.7a. The pure Mg barrier membrane materials were incubated in blood at 37°C for several days. After bio-corrosion, the tensile strength of Mg-membrane materials was measured and their fracture morphology was analyzed by scanning electron microscopy (SEM), as indicated in Figure 5.7.

5.2.11. Other Characterizations

Glancing Incidence X-ray Diffraction (GI-XRD) of coatings on Mg substrates was conducted on Rigaku XRD Ultima IV, Rigaku, Japan, with a glancing angle of 0.5°. Power XRD measurements were performed on D8 Discover, Bruker, Germany. X-ray photoelectron spectroscopy (XPS) was from Kratos AXIS Ultra, UK. The binding energy was calibrated by C_{1s} peak at 284.6 eV. Attenuated Total Reflection-Fourier-transform infrared spectroscopy (FTIR) was performed on Nicolet iS50, Thermo Scientific, USA. Static water contact angle (CA) in the air of various substrates was measured with a 3 μL of ultrapure water droplet. Scanning electron microscopy (SEM) and energy dispersive spectrometer (EDS) characterizations were performed on Sigma GEMINI FE-SEM, ZESSI, Germany. Scanning transmission electron microscopy - energy dispersive spectrometer (STEM-EDS) characterization was performed on JEM-ARM200CF, JEOL, Japan. Particle size measurements were carried out on a Zetasizer Nano ZSP system, Malvern Panalytical, UK. Electrochemical Impedance Spectroscopy (EIS) and potentiodynamic polarization tests were performed on the electrochemical workstation, CH Instruments, USA. Tensile tests were conducted on AGS-X universal tensile testing machine, Shimadzu, Japan, with the tensile speed 1 mm min^{-1}.

5.3 Results and discussions

5.3.1. Preparation of InorganicPro coating

The inorganicPro coating could be facilely prepared via immersing pure Mg surface into an aqueous solution containing NaF (500 mM) and BSA (10 mg mL^{-1} in 10 mM MES buffer, pH = 6) for 48 h at room temperature, as shown in Figure 5.2a. Released Mg ions from Mg surfaces interact with Na and F ions to form the $NaMgF_3$ coating with the assistance of BSA, as indicated by X-ray diffraction (XRD) profiles. Notably, there is no peak position shift between the inorganic coating and inorganicPro coating, confirming that the 'brick' part in the inorganicPro coating is $NaMgF_3$ crystallite alone. To further stabilize the inorganicPro coating, it is dipped in a 10% glutaraldehyde solution for 10 min to cross-link BSA proteins embedded in the coatings.

The characteristic peak of BSA at 1540 cm^{-1} in Fourier transform infrared (FTIR, Figure 5.1b and S5.4) spectra of the coatings and a significant presence of carbon observed in energy dispersive spectroscopy (EDS, Figure S5.1 and S5.3) indicate that the abundant embedding of BSA molecules within the inorganicPro coating. A distinct N peak in X-ray photoelectron (XPS, Figure 5.1c) spectra, notable intensity of optical photothermal infrared (O-PTIR, Figure 5.1d) image at 1540 cm^{-1}, and higher contact angle (Figure S5.5) of inorganicPro coating show that lots of BSA molecules anchor on the surface of inorganicPro coating. The scanning transmission electron microscopy (STEM) and corresponding EDS images of inorganicPro coating in Figure S5.2 clearly demonstrate its 'brick-mortar' structure. The experimentally observed distribution of BSA aligns with the illustration in Figure 5.1c, demonstrating that BSA both embeds within and anchors on the surface of the coating.

The morphology of coatings is displayed in Figure 5.1f and 5.1g. The average size of nanoparticles in inorganicPro coating is 503 nm in diameter, finer than that in bare inorganic coating deposited in the absence of BSA (652 nm). The inorganicPro coating is also thicker than that of its inorganic counterpart. To quantify the compactness of the prepared coatings, we measure the density of the coatings based on an American Society of Testing Materials (ASTM) standard method (ASTM B659-90 R2014). The estimated density of the inorganicPro coating is 2.71 g cm^{-3} and denser than that of the inorganic coating of 2.30 g cm^{-3} (Figure 5.2e). As the density of pure solidified $NaMgF_3$ crystal is 3.03 g cm^{-3}, the calculated compactness of inorganic coating is ~75.9%, with the volume of mismatch-induced cracks inside the inorganic coating being ~ 24.09 vol%. In contrast, the compactness of the inorganicPro coating is as high as 89.4%, with only 10.56 vol% of cracks inside the coating, suggesting that finer nanoparticles reduce cracks in coatings by 56.16 vol%, contributing to a denser and more compact inorganicPro coating, as proposed in Figure 5.1. This denser and more compact coating is anticipated to enhance the mechanical and anticorrosion performance to protect Mg surfaces.

The biocompatibility of coated Mg samples is evaluated by CCK-8 assay (Figure S5.6) through culturing human gingival fibroblasts (HGF) in sample extracts for 1, 2, and 3 days. It can be found that the Mg-based biomaterials, including pure Mg and coated Mg samples, exhibit excellent biocompatibility with cell viability higher than 96% after 3 days of cell proliferation (Figure S5.6). The fluorescent images of live/dead staining of cells in Figure 5.2h and S5.7 show the increase in the number of living cells during the culture. This test demonstrates the good biocompatibility of the coated-Mg samples in this work.

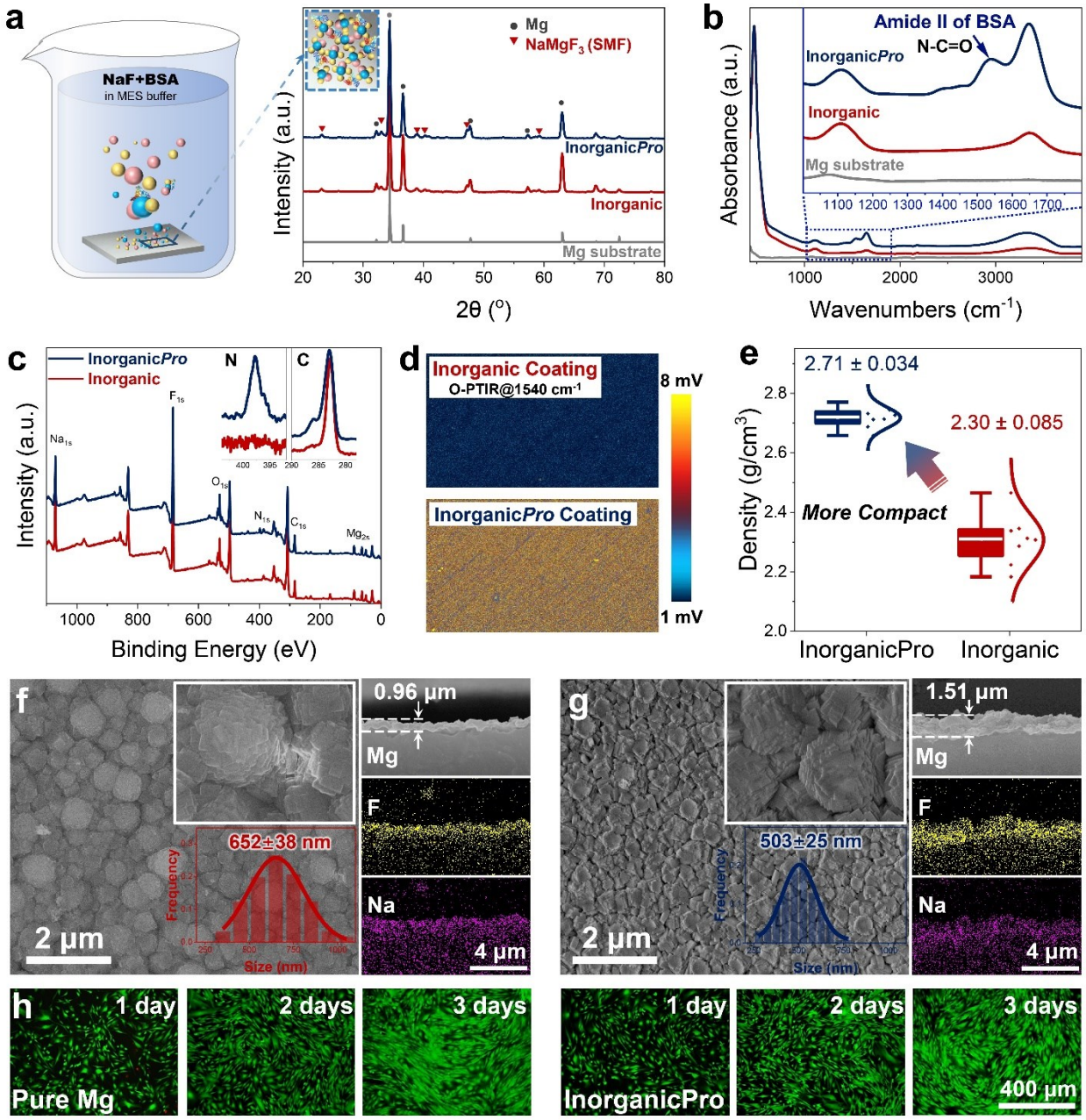

Figure 5.2 Preparation of Inorganic*Pro* coating. a, Facile one-pot preparation of $NaMgF_3$-BSA coating on Mg surfaces and corresponding XRD profiles. b, c, and d, FTIR spectra, XPS spectra, and O-PTIR images of inorganic-coated and inorganicPro-coated Mg surfaces. e, Density of the coatings. f and g, Morphology and thickness of inorganic and inorganicPro coatings. h, Fluorescent images of live/dead (green/red) staining of cells after culturing in extracts for for different time.

5.3.2. Anticorrosion performance of InorganicPro coating

Mechanical durability is critical in practical operation and tested in this work. Nanoindentation in Figure 5.3a indicates that inorganicPro exhibits higher hardness (807 MPa) than the conventional inorganic coating (700 MPa), likely attributed to its higher density. A nylon ball that represents the average mechanical properties of contact surfaces in dental applications is employed for friction with the coatings. The finer and evenly distributed nanoparticles in inorganicPro coating make the surface smoother with a lower friction coefficient (Figure 5.3b). Consequently, the wear depth of inorganicPro coating is much lower and there is no friction-induced surface damage after long-term friction (Figure 5.3c). The more compact nature of inorganicPro coating will also demonstrate better anti-corrosion performance. During the corrosion test in PBS buffer (Figure 5.3d), dissolved Mg will convert to black corrosion products and accumulate on surfaces. The corrosion rate of Mg samples in PBS buffer is measured by the golden standard weight loss method, as summarized in Figure 5.3e. It is found that the pure Mg surface rapidly develops a black and porous surface morphology with the fastest corrosion rate. The corrosion pits are observed on pure Mg surfaces after immersion in PBS for 20 min (Figure S5.10) and corrosion products rapidly populate entire surfaces within 1 h of corrosion. The corrosion products are composed of high P and O elements (Figure S5.11) and could be a mixture of $Mg(OH)_2$, $Mg_3(PO_4)_2$, and other products (Figure S5.13 and S5.14). The corrosion layer breaks into lots of separated fragments with obvious cracks on day 5 of corrosion. Consequently, the new Mg surface exposed in the crack area will experience further corrosion, producing a thicker corrosion layer. While inorganic coating partially reduced this rapid corrosion, lots of pitting corrosion can be found on the bare inorganic-coated Mg surfaces. In contrast, the inorganicPro notably decreases the corrosion rate of Mg samples, maintaining a clean and shining surface after

two days of corrosion. After 5 days of corrosion, inorganicPro-coated Mg undergoes small, localized corrosion (Figure S5.10). This localized corrosion demonstrates a similar morphology to the corrosion pits of pure Mg surface and is composed of high P and O elements. In the following 10 days of corrosion, the corrosion area increases slowly compared with pure Mg and bare inorganic-coated Mg surfaces. In an accelerated corrosion solution, abundant H_2 bubbles rapidly generate on the pure Mg surface, fewer bubbles on the inorganic-coated Mg surface, and no apparent bubbles are found on the inorganicPro-coated Mg surface, illustrating the exceptional corrosion resistance of inorganicPro coatings. The anticorrosion performance of coatings was further investigated via electrochemical measurement in PBS buffer. Electrochemical impedance spectroscopy (EIS) data of different samples are analyzed using the equivalent circuit model in Figure S5.8. As seen in the Nyquist plots (Figure 5.3f), the inorganicPro-coated surface possesses the largest diameter of the capacitive semicircle compared with the pure Mg and bare inorganic-coated Mg surfaces. In the corresponding Bode diagram (Figure S5.9), the inorganicPro coating features a low-frequency impedance modulus (|Z| 0.1 Hz) of 1.81×10^4 Ω cm^{-2}, nearly 4 times higher than that of the inorganic coating (5.21×10^3 Ω cm^{-2}) and 14 times of the pure Mg surfaces (1.36×10^3 Ω cm^{-2}). The potentiodynamic polarization results in Figure 5.3g showcase that inorganicPro-coated surfaces demonstrate the highest corrosion potential (E_{corr}, -1.61 V) and lowest corrosion current density (i_{corr}, 2.46 μA cm^{-2}). In comparison, the E_{corr} and i_{corr} of inorganic-coated are -1.73 V and 7.58 μA cm^{-2}, respectively. These findings indicate that the compact inorganicPro coating elevates the interfacial impedance, consequently slowing the corrosion of Mg in PBS buffer. In PBS buffer (Figure S5.15), the corrosion potential of pure Mg surface first increases from -1.82 mV (0 h) to -1.65 mV (1 day) and then decreases to -1.68 mV (5 days). The increase in corrosion potential could be attributed to the formation of a P-containing corrosion

layer on the Mg surface against the corrosion from PBS buffer. The corrosion layers break into small fragments after 1 day of corrosion due to the volume mismatch between corrosion products and Mg (Figure S5.10), allowing new Mg surfaces to be exposed to PBS buffer for further corrosion, causing a decrease in overall corrosion potential. The corrosion current density continuously decreases during the 5 days of corrosion due to more corrosion products generated on the Mg surface blocking electron transfer. In contrast, the corrosion potential of the inorganicPro-coated surface remains stably high and corrosion current density maintains a low value (Figure S5.15), implying a lower corrosion rate. This low corrosion rate enables a longer time for P-containing corrosion layer formation in the small broken area of inorganicPro coating (Figure S5.12) to mitigate further corrosion. The corrosion behavior of Mg samples is also examined in different biofluids, including cell culture medium, artificial saliva, and blood, as shown in Figure 5.3h and S5.16. The corrosion behavior of Mg samples is also examined in diluted blood, as shown in Figure 5.3h. Compared with PBS buffer, various bio-foulants, such as proteins, metabolites, and cells, significantly accelerate the biocorrosion process. It can be found that the corrosion ability varies among different biofluids, with blood > artificial saliva > cell culture medium ≈ PBS buffer. This ranking is attributed to the complexity of blood, which contains hundreds of proteins, metabolites, and various cells. After 10 days of corrosion, the weight loss of pure Mg in blood is 1176 μg cm^{-2}, which is almost 3 times that in PBS buffer (431 μg cm-2). For the inorganic-coated surface, the weight loss is 635 μg cm^{-2} in blood and twice as high as in PBS buffer (351 μg cm^{-2}). Surprisingly, the inorganicPro-coated surface exhibits a weight loss of only 265 μg cm^{-2} in blood, slightly higher in the PBS buffer (227 μg cm^{-2}). This outstanding anticorrosion performance could be attributed to the more compact surface, mitigating the fouling-accelerated corrosion on the inorganicPro-coated Mg surface. These results highlight that the

enhanced mechanical properties and superior anticorrosion performance of inorganicPro coating stem from the finer nanoparticles generated during BSA-involved biomineralization. Therefore, it is critical to understand the underlying mechanisms of particle refinement in the presence of BSA molecules.

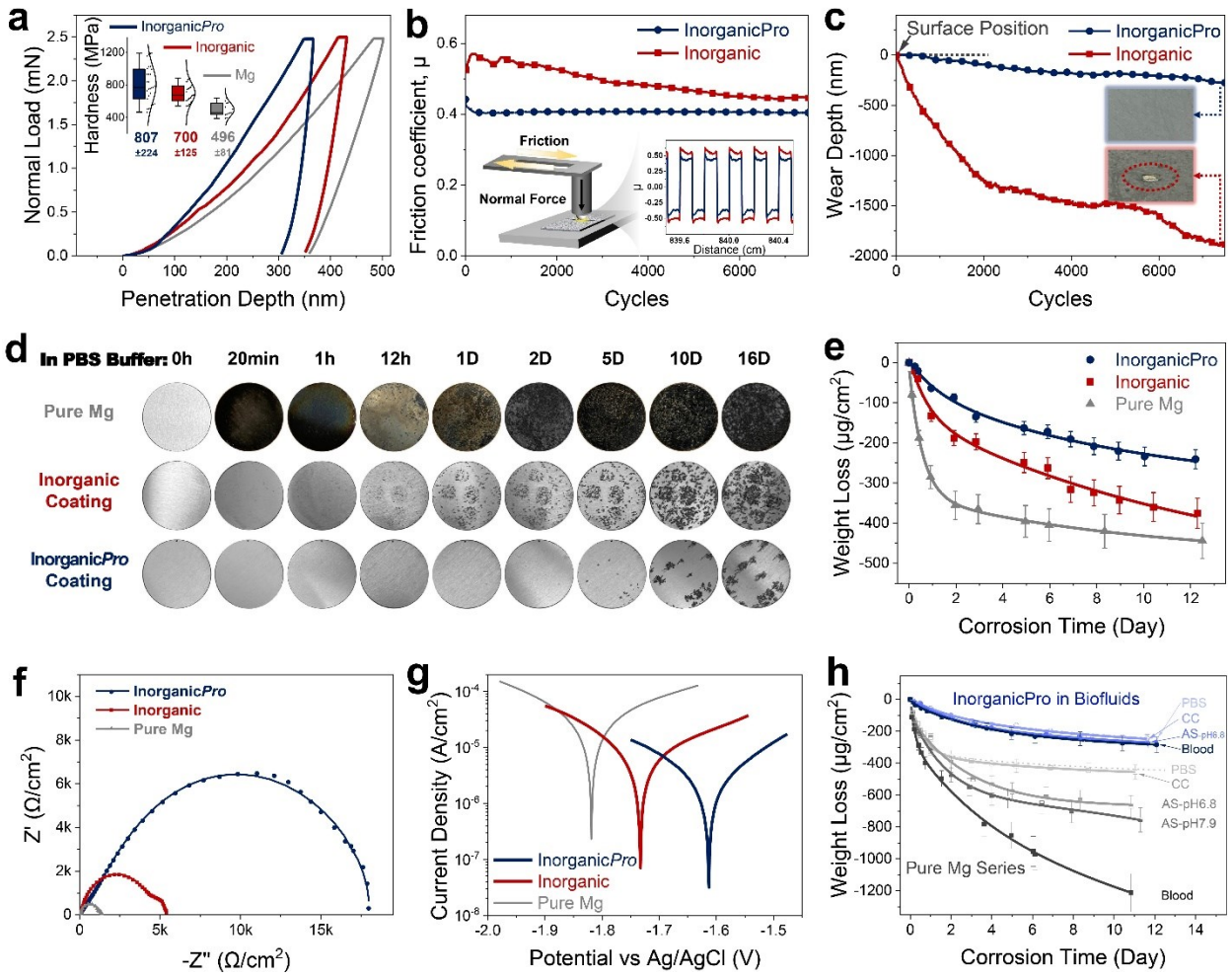

Figure 5.3 Mechanical and anticorrosion properties of inorganicPro-coated Mg surfaces. a, Hardness of prepared coatings measured by nanoindentation. b, Friction coefficient and c, wear depth change during the friction test. d, Surface morphology and e, weight loss of pure Mg and coated-Mg immersed in PBS buffer for different durations. f, Nyquist and g, potentiodynamic polarization curves of pure Mg and prepared coated-Mg in PBS buffer. h, Weight loss of pure Mg and coated Mg in different biofluids.

Thanks to the finer and more densely packed nanoparticles on surfaces, the inorganicPro coating exhibits exceptional anticorrosion performance. It is essential to figure out the underlying mechanism of nanoparticle refinement. As illustrated in Figure 5.4a, BSA molecules may enzymatically boost the nucleation of $NaMgF_3$ to generate more and smaller nanoparticles with lower reaction activation energy *(ΔE*), which could be estimated based on the reaction kinetics and thermodynamics. In the reaction kinetics test, the change in Mg ion concentration is monitored after injecting $MgCl_2$ (12 mM) into a NaF (500 mM) solution with and without the presence of BSA molecules at 30℃ (Figure 5.4b, S5.17, and S5.18).[257, 258] It is evident that Mg ions rapidly react in the initial stage and reach a final plateau after 100 min. Na-Mg-F reaction is faster in the presence of BSA, as shown in the insert subfigure of Figure 5.4b. The faster reaction suggests the activation energy with the presence of BSA is lower than that without BSA *($\Delta E_1 < \Delta E_2$)*.[261, 262]With boosted reaction kinetics, more $NaMgF_3$ nanoparticles nucleate within 1 h, and consequently, the average diameter of nanoparticles with the assistance of BSA is reduced to 289 nm, much smaller than that without BSA (474 nm in Figure 5.4c). The thermodynamic parameters of the Na-Mg-F reaction are measured by the isothermal titration assays (ITC, Figure 5.4d). It is considered that Na-Mg-F formation is a two-step reaction: in the first step, six coordinated water molecules dissociate from Mg ions with significant heat absorption to produce bare Mg^{2+} ions;[263-265] in the second step, the Mg^{2+} reacts with F^- and Na^+, forming $NaMgF_3$ nanocrystals (Figure S5.19). Due to a large amount of heat absorbed during the Mg-H_2O decoordination, the overall reaction is endothermic with an enthalpy change (ΔH_2) of 12.0 kJ mol^{-1}, as displayed in Figure 5.4d. When BSA molecules are present in Na-Mg-F solution, the Mg ions will react with BSA before with F^- ions, as Gibbs free energy of BSA-Mg reaction *($\Delta G_{BSA\text{-}Mg}$* = -29.28 kJ mol^{-1}, Figure S5.20) is much lower than that of Na-Mg-F reaction (ΔG_2 = -12.02 kJ mol^{-1}). Once Mg and BSA bond, the more hydrophobic β sheet structure will form in the BSA-Mg association (Figure 5.4e).

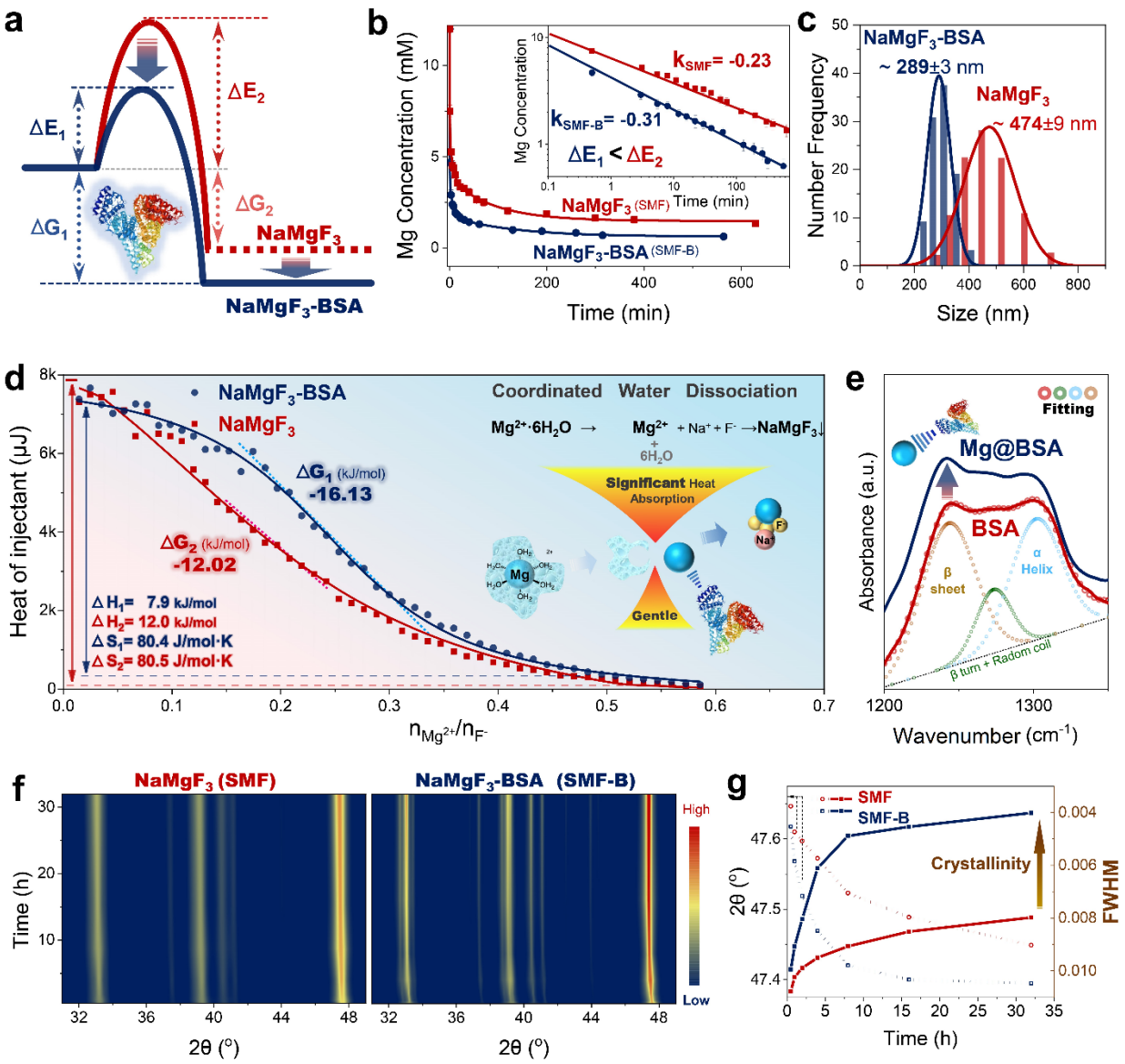

Figure 5.4 Kinetics and thermodynamics in the formation of $NaMgF_3$-BSA composite. a, Reaction activation energy (*ΔE*) and Gibbs free energy (*ΔG*) change in the formation of $NaMgF_3$ and $NaMgF_3$-BSA. b, Mg ion concentration change in $MgCl_2$-NaF reactions at 30°C with and without the presence of BSA molecules. c, Average diameter of $NaMgF_3$ and $NaMgF_3$-BSA particles. d, ITC curves showing the energy change of reactions. e, FTIR spectra showing the secondary structure of BSA protein. f, XRD profile for $NaMgF_3$ and $NaMgF_3$-BSA particles and (g) their characteristic peck position and crystallinity with different preparation duration.

This association creating a local hydrophobic domain will facilitate the decoordiation of Mg-H_2O and reduce the reaction enthalpy from ΔH_2 = 12.0 kJ mol^{-1} to ΔH_1 = 7.9 kJ mol^{-1}. By reducing the reaction barrier posed by H_2O molecules, the reaction between Mg and F will become more kinetically favorable and faster. The BSA-boosted Na-Mg-F reaction also facilitates the formation of $NaMgF_3$ crystals. The higher crystallinity of $NaMgF_3$ nanoparticles (Figure 5.4f and 5.4g) and lower Gibbs free energy (Figure 5.4d) in the presence of BSA suggests that $NaMgF_3$-BSA is more stable. The Mg-BSA association enables Mg ions as active anchor sites for BSA molecules to glue the inorganic $NaMgF_3$ particles, strengthening the hardness and contributing to a better wear resistance of inorganicPro coating, as indicated in Figure 5.3a-5.3c. In the novel coating design, involving BSA in biomineralization not only reinforces the coating compactness to improve the anticorrosion performance but also grants coatings antifouling properties to mitigate the fouling-accelerated biocorrosion, as suggested in Figure 5.3h.

5.3.3. Antifouling performance of InorganicPro coating

In biocorrosion, bio-fouling can accelerate surface corrosion, while corrosion-induced surface roughing leads to more bio-foulants adsorption, triggering a reciprocal deterioration, as shown in Figure 5.1c and 5.3h. Therefore, it is necessary to study the biofouling status on different coatings and investigate the role of surface-anchored BSA in antifouling performance. Figure 5.5a displays the bio-foulant distribution on inorganic and inorganicPro coatings after incubation in blood and milk for different durations. The O-PTIR images reveal that after fouling 48 h in blood, around 16.4% of the surface area on the inorganic coating is occupied by foulants. In contrast, only 1.5% of the surface area is contaminated on the inorganicPro coating, indicating around 10 times better fouling resistance. Similarly, the inorganicPro coating also exhibits outstanding fouling resistance in milk solution, with only 6.2 % surface fouled after 48 h.

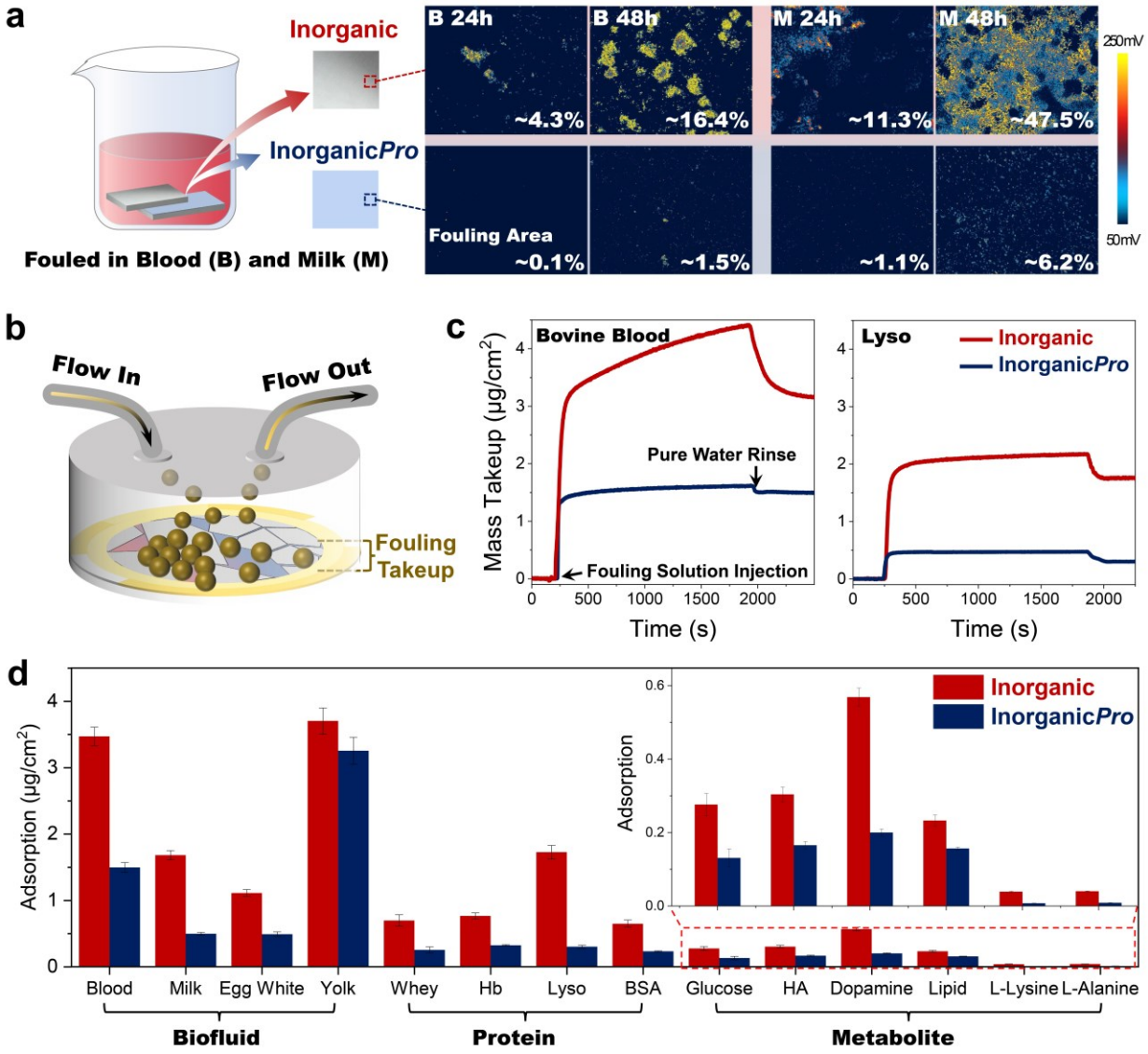

Figure 5.5 Antifouling performance of inorganicPro-coated Mg surface. a, Foulant distribution on inorganic and inorganicPro-coated Mg after immersed in blood and milk for 24 h and 48 h, measured by O-PTIR mapping. b, Monitoring dynamic adsorption of fouling on surfaces via QCM-D. c, Dynamic adsorption of blood and lysozyme on surfaces. d, Absorption/fouling amount of different bio-foulants on surfaces.

To further examine the antifouling capability of inorganicPro coatings against typical bio-foulants in biosystems, such as biofluids, proteins, and metabolites, the dynamic adsorption of

biomolecules on coatings is directly monitored in real-time using a quartz crystal microbalance with dissipation monitoring (QCM-D, Figure 5.5b). As shown in Figure 5.5c, a strong mass takeup is observed upon the introduction of blood into the QCM-D chamber, indicating the adsorption of foulants from blood on both inorganic and inorganicPro surfaces. After 30 min, ultrapure water was introduced into the chamber to remove the loosely bonded foulants on coatings, decreasing mass takeup. It is found that the fouling from the blood or Lyso protein solution on the inorganicPro coating is considerably lower than that on the bare inorganic coating. InorganicPro coating also exhibited high-efficiency fouling resistance to a broad spectrum of bio-foulants, as summarized in Figure 5.5d. For instance, the remnant bovine blood on the inorganicPro coating after rinsing with water is ~1.49 μg cm^{-2}, while those on the inorganic coating are as high as 3.47 μg cm^{-2}. The remnant Lysozyme protein on the inorganicPro coating is only ~0.30 μg cm^{-2}, while those on the inorganic coating are as high as 1.72 μg cm^{-2}. This superior antifouling property most likely originates from the surface-anchor BSA that provides interfacial hydration and steric repulsion to hinder the initial attachment of foulants on surfaces.[59, 124] Such interfacial interactions between the coatings and typical foulants could be quantified by direct interaction force measurements.

It is well acknowledged that the biofouling process is fundamentally governed by interfacial intermolecular interactions between surfaces and foulants, where attractive interactions would lead to more fouling. Therefore, directly measuring the interfacial interaction forces between coatings and foulants is critical to understand the underlying antifouling mechanisms. In this work, interaction forces of general bio-foulants and typical bio-related functional groups with inorganic and inorganicPro coatings are investigated by employing the colloidal probe atomic force microscopy (AFM).[109, 111, 164]

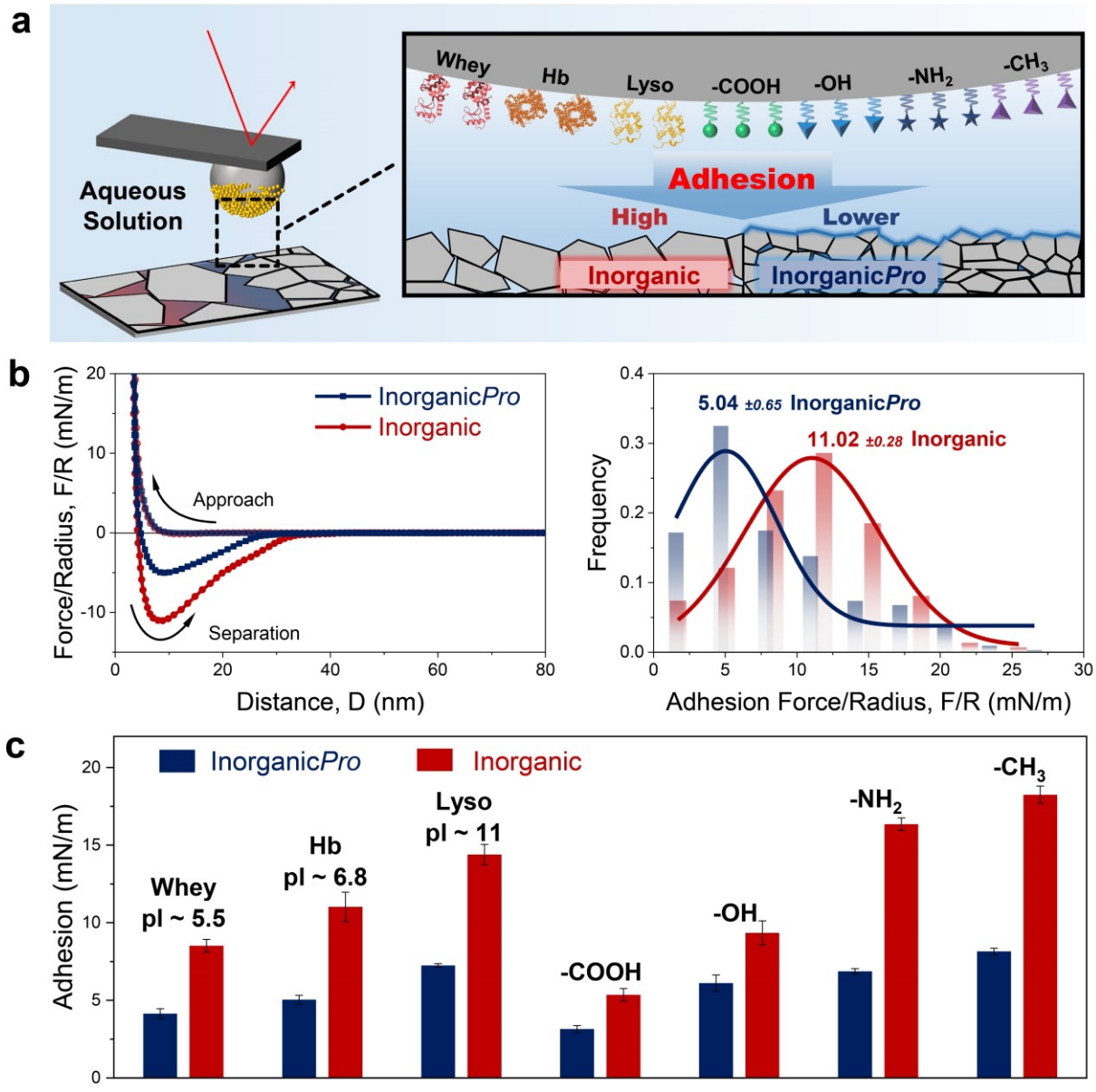

Figure 5.6 Interfacial interactions between bio-foulants and inorganic/inorganicPro coatings measured by colloidal probe AFM. a, Schematic diagram showing experiment configuration in AFM force measurement and the interactions of typical foulants and functional groups with inorganic/inorganicPro coatings. b, Interfacial interactions (normalized force-distance, F/R-D, profiles) between Hb protein-coated surfaces and inorganic/inorganicPro coatings. c, Adhesion between different foulants and coatings.

The experimental setup of AFM force measurements is illustrated in Figure 5.6a, where adhesion between protective coatings and surfaces covered with Whey, Hb, and Lyso proteins as well as -COOH, -OH, $-NH_2$, and $-CH_3$ functional groups are measured in PBS buffer. The normalized force-distance (F/R-D) profiles in Figure 5.5b show that the adhesion (F_{ad}/R) of Hb protein to inorganic coating is 11.02 mN m^{-1}, twice as strong as that to inorganicPro coating at 5.04 mN m^{-1}, suggesting that surface-anchored BSA weakens the interfacial interactions between bio-foulants and inorganicPro surfaces. Likewise, the adhesion of a series of bio-foulants to inorganicPro coatings is only 40-50% of their adhesion to inorganic coatings (Figure 5.6c). For example, the adhesion of Lyso protein to inorganicPro coating is 50% of that to inorganic coating, and the adhesion of amino-coated surface to inorganicPro coating is 42% of that to inorganic coating (Figure S5.22). Such weak interfacial attraction accounted for the high resistance to biofouling in Figure 5.5. As reported in previous research, these weak interfacial interactions may stem from the interfacial hydration and steric repulsion from BSA molecules. The developed inorganicPro coating demonstrates excellent dual protection - anticorrosion and antifouling - paving the way for potential practical applications.

The inorganicPro coating with dual protection holds great potential applications in implant dentistry, notably used as the Mg-based barrier membrane for guided bone regeneration (GBR) in dental regeneration surgery.[223, 266] GBR utilizes a barrier membrane to occlude soft-tissue cells, allowing slower-growing bone cells to repopulate the defect and regenerate bone, as shown in Figure 5.7a. However, biocorrosion poses a significant challenge, causing a severe deterioration in the mechanical properties of Mg-membranes, leading to the failure to encapsulate and support dental bone grafts.

The developed inorganic and inorganicPro coatings are employed to protect the Mg-membrane against biocorrosion. We use the most corrosive biofluids tested in this work, blood, to challenge the protective performance of the coatings in an in vitro bio-corrosion test. Specifically, all the Mg samples are incubated in an in-vitro Mg-Blood corrosion system that simulates the post-implantation conditions. After 1 day, a porous corrosion layer appears on the pure Mg surface (Figure S5.23). After 2 days, pitting corrosion is found on the inorganic-coated surface. After 4 days of corrosion, some sparsely distributed corrosion is found on the inorganicPro surface; in contrast, continuous and thick corrosion products already cover the entire pure Mg surface.

The mechanical properties of Mg samples are tested and summarized in Figure 5.7b and 5.7c. After 30 days of corrosion, the tensile strength of pure Mg is only 85.1 MPa, 47.1% of the original one, and that of bare inorganic-coated Mg is 131.2 MPa, 72.7% of the original value. In contrast, the tensile strength of inorganicPro-coated Mg is twice as high as that of pure Mg, demonstrating a high strength of 159.2 MPa, 88.5% of the original value. The fracture morphology in Figure 5.7d shows that the pure Mg without corrosion is a quasi-cleavage and intergranular fracture and then transfers to cleavage and transgranular fracture after corrosion, which may result from the released hydrogen diffusion inside the grains of Mg samples. The inorganicPro-coated sample exhibits hydrogen embrittlement but demonstrates quasi-cleavage patterns similar to Mg without corrosion. The dual protection coating reduces the corrosion rate in blood and helps keep the desirable mechanical properties of Mg-based biomaterials, benefiting their potential applications in clinical utility.

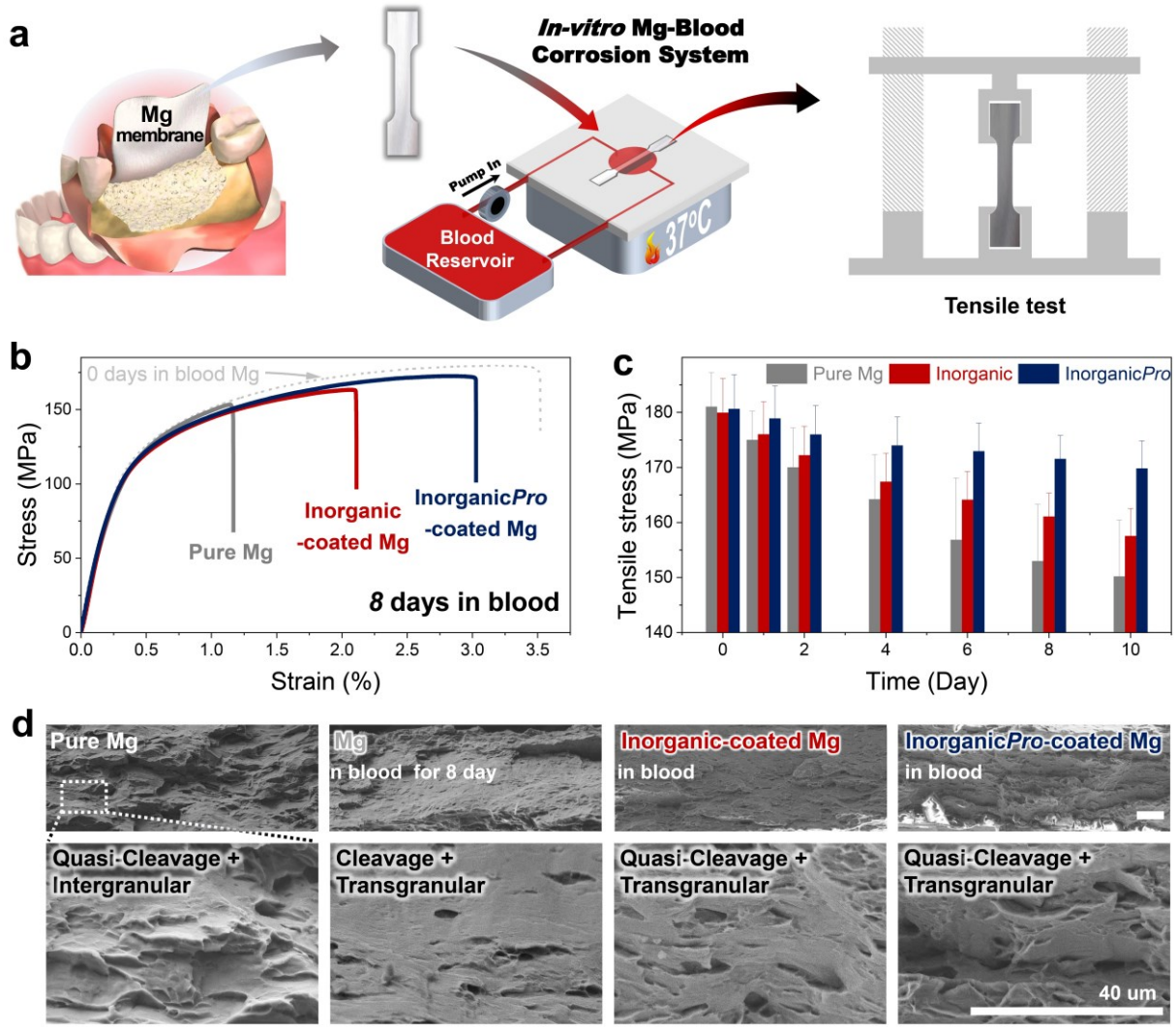

Figure 5.7 Application of inorganicPro coating on Mg-based barrier membrane. a, In-vitro Mg-Blood corrosion system. b, Tensile curve of pure Mg and coated Mg-membrane materials after testing for 8 days. c, Tensile strength of Mg-membrane materials with different testing duration. d, Fracture morphology of tested Mg-membrane materials.

5.4 Conclusions

In summary, inspired by the formation of tooth enamel, we have developed a novel in-situ inorganic-protein coating strategy for Mg-based biomaterials by simply immersing Mg surfaces

into a NaF solution in the presence of BSA proteins. The introduced BSA molecules enhance coating compactness by boosting Na-Mg-F biomineralization kinetics to generate more and finer $NaMgF_3$ nanoparticles. The finer inorganic nanoparticle 'bricks' densely pack on Mg surfaces, reducing mismatch-induced internal cracks by 56% and reinforcing the mechanical durability of coatings, consequently tripling anticorrosion performance. The underlying kinetics boosting mechanism is elucidated: in the BSA-involved biomineralization, BSA molecules associate with Mg ions to generate a locally hydrophobic domain, facilitating the decoordination between Mg ions and H_2O molecules. This, in turn, lowers the enthalpy of Na-Mg-F reaction from ΔH_2 = 12.0 kJ mol^{-1} to ΔH_1 = 7.9 kJ mol^{-1} and kinetically boosts the nucleation of $NaMgF_3$ nanoparticles, reducing their average size from 652 nm to 503 nm. Moreover, the BSA macromolecules embedded inside inorganicPro coatings act as 'mortar' to seal mismatch-induced cracks between nanoparticles, forming a 'brick-and-mortar' structure of inorganicPro coating to further reinforce coating compactness and increase the interfacial electrochemical impedance fourfold. The surface-anchored BSA molecules create an antifouling layer atop coatings to reduce adhesion between coatings and bio-foulants, enabling resistance to a broad spectrum of potential bio-foulants attachment, including metabolites, proteins, and biofluids. Synergizing with antifouling performance, the inorganicPro coating effectively mitigates the fouling-accelerated biocorrosion and successfully secures exceptional anticorrosion properties in complex biological conditions. This work showcases a facile and effective preparation of a dual-protection coating on Mg-based biomaterials via employing proteins to alter the reaction kinetics, as well as incorporating the intrinsic antifouling functions of proteins into new coatings, potentially paving the way for the application of Mg-based biomaterials.

Supporting Information

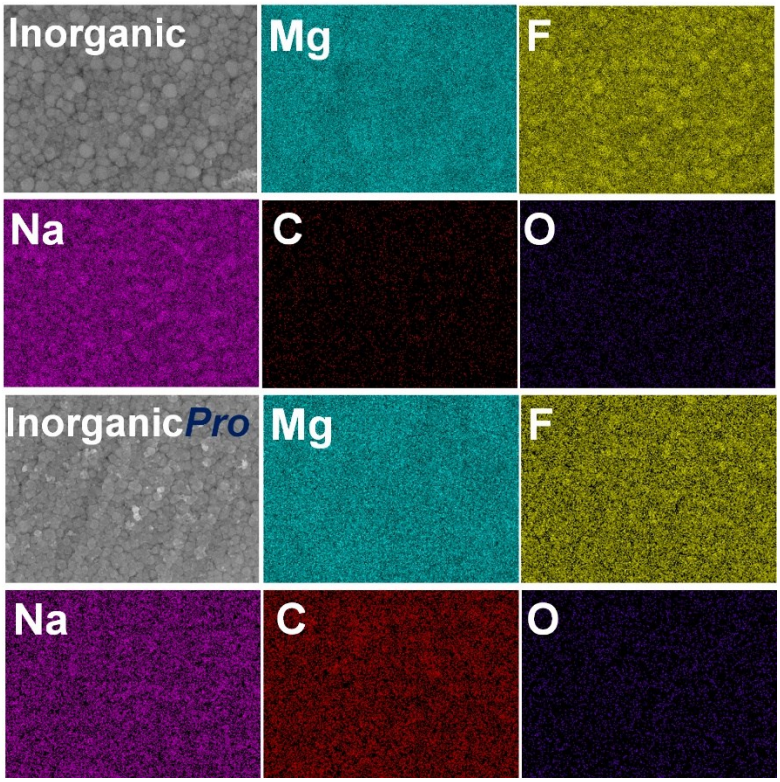

Figure S5.1. Morphology and surface composition of inorganic / inorganicPro-coated Mg sheets

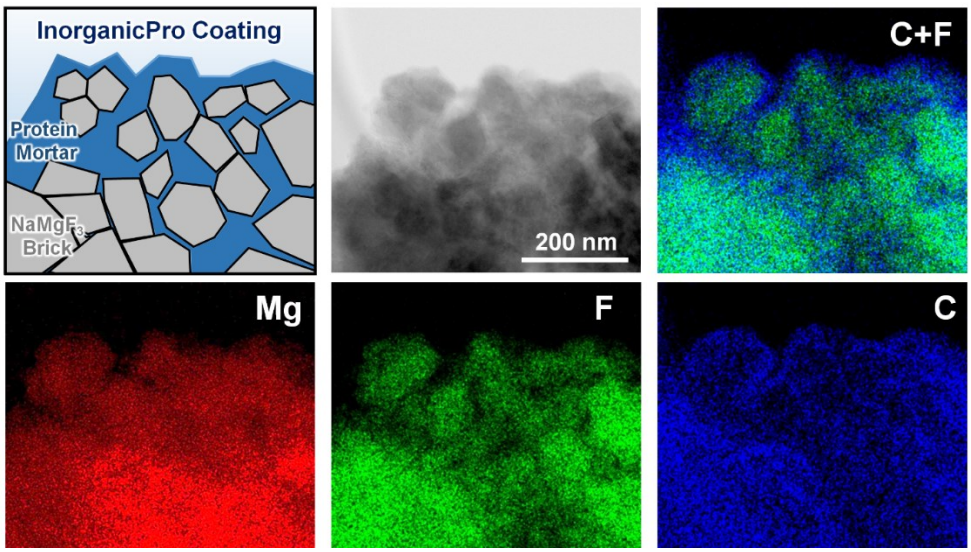

Figure S5.2. Illustration of 'Brick-Mortar' structure of inorganicPro coating as well as STEM image and element distribution of developed inorganicPro coating.

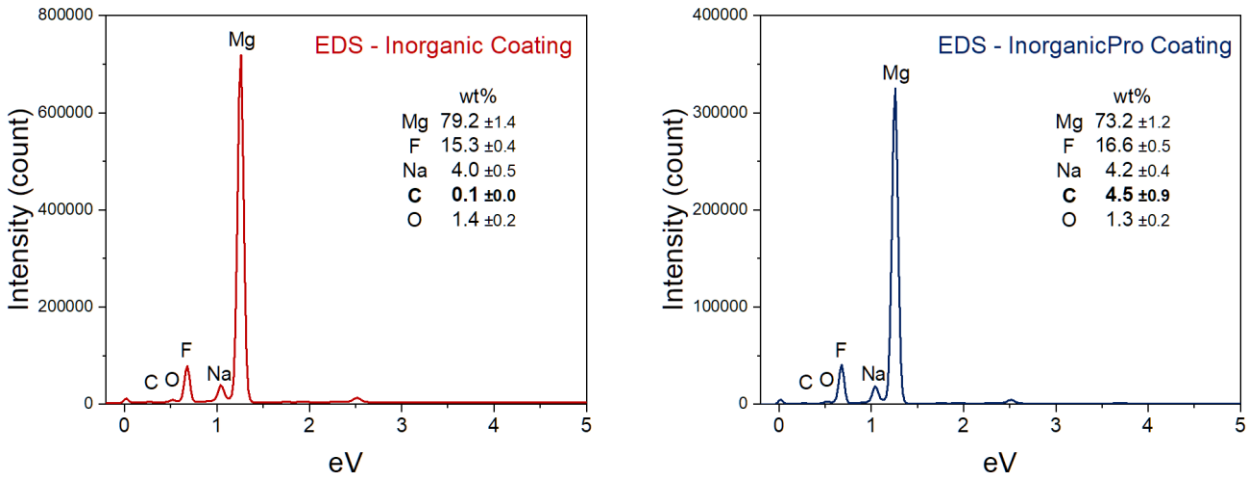

Figure S5.3. EDS spectra and element contents of inorganic / inorganicPro-coated Mg sheets

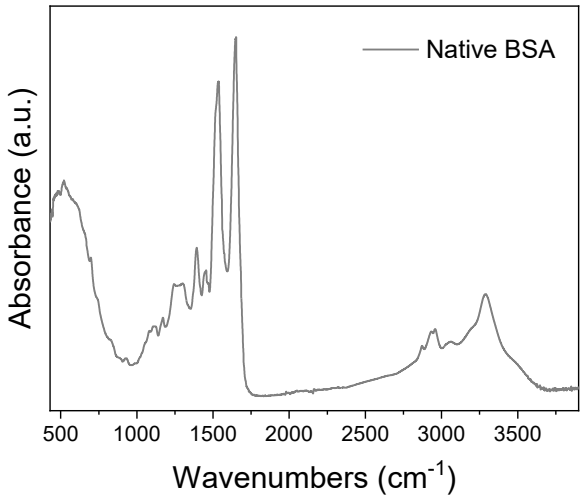

Figure S5.4. FTIR spectrum of native BSA protein

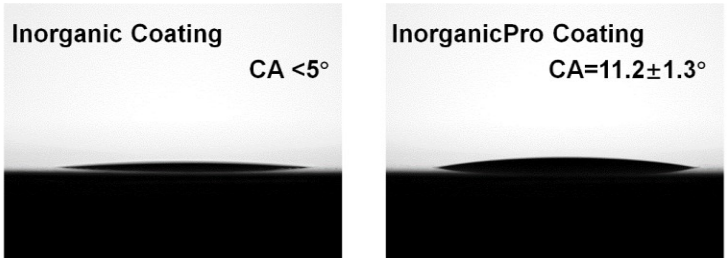

Figure S5.5. Static water contact angle (CA) of inorganic / inorganicPro-coated Mg sheets

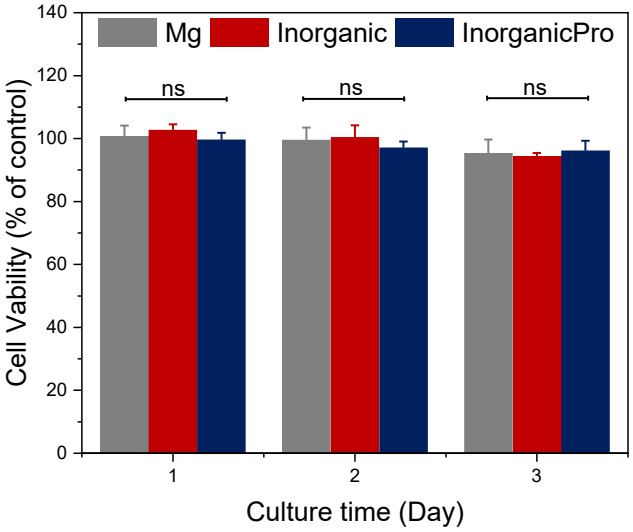

Figure S5.6. Cell viability in the different extracts.

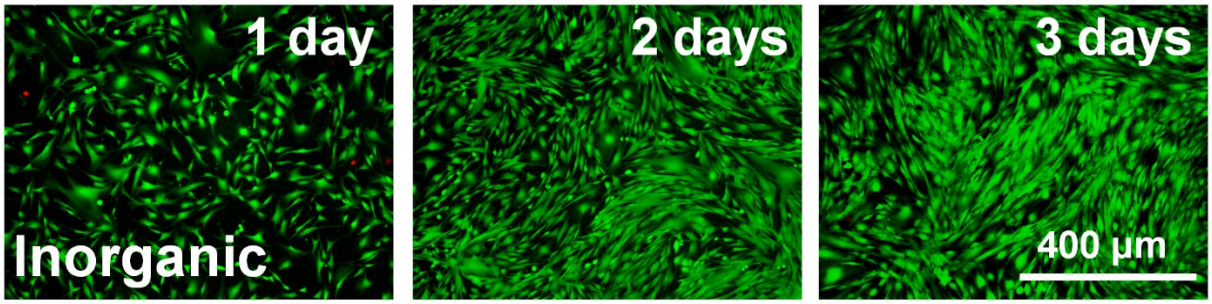

Figure S5.7. Fluorescent images of live/dead (green/red) staining of cells after culturing in inorganic-coated Mg extracts for different time.

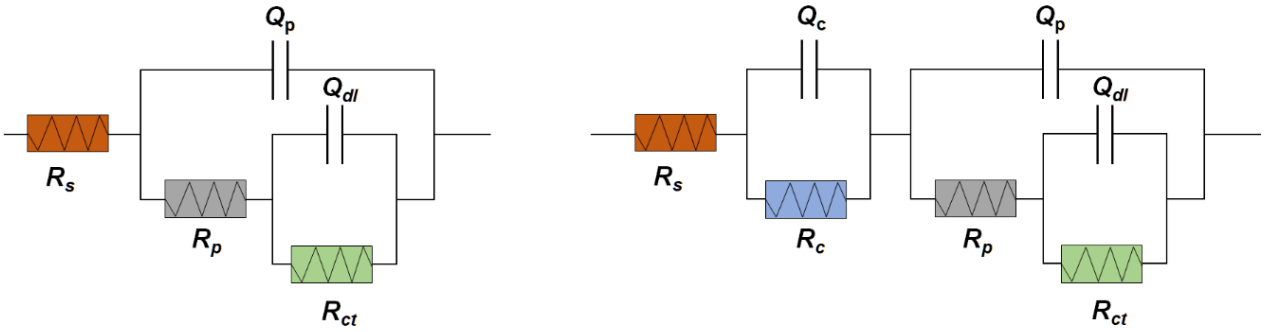

Figure S5.8. The proposed models for the equivalent electrical circuits, where R_S represents solution resistance, R_{ct} is charge transfer resistance, R_p is the resistance of the porous Mg-Oxide surface formed in air, and R_c corresponds to the coating resistance

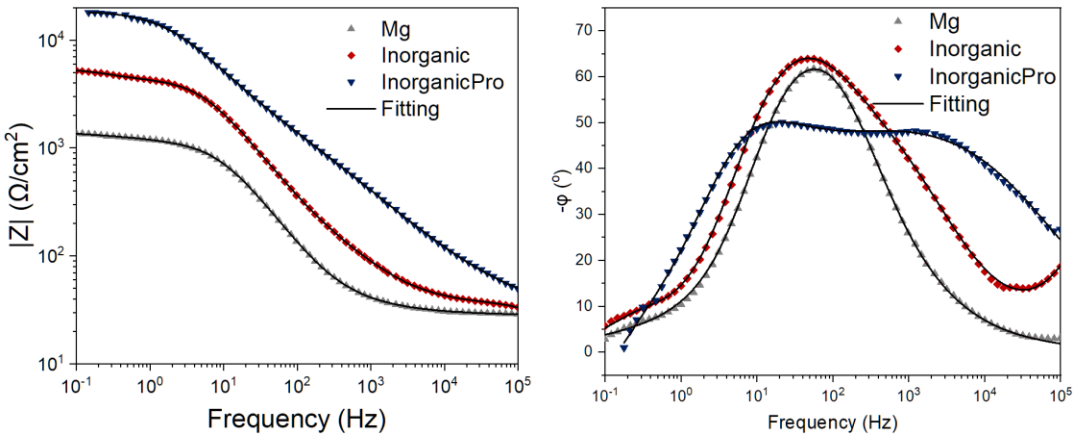

Figure S5.9. Bode plots of the pure Mg and coated-Mg surfaces fitted by proposed equivalent electrical circuit models

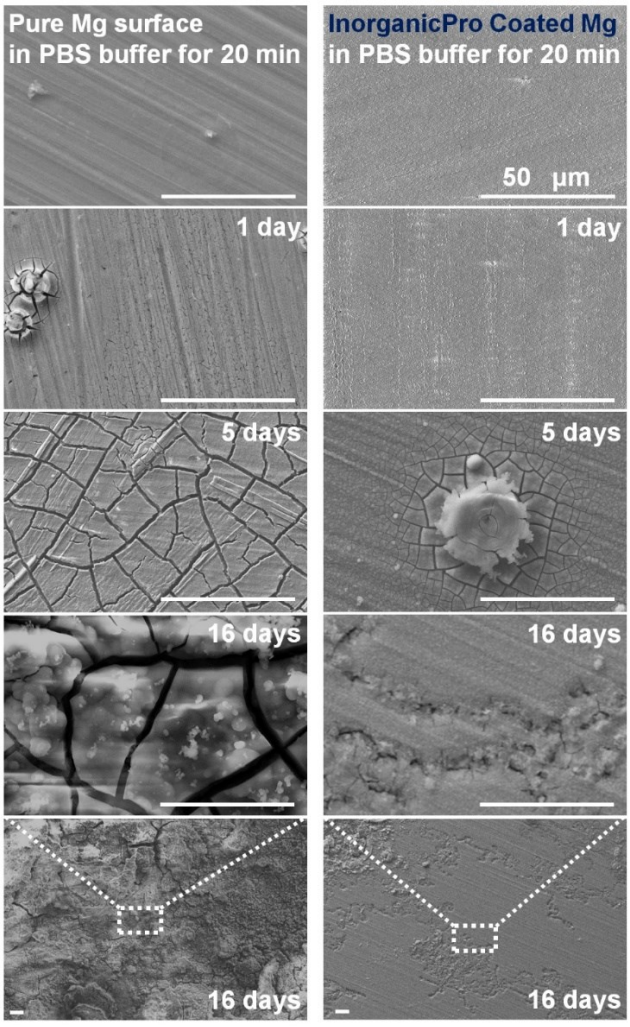

Figure S5.10. SEM images showing the morphology of pure Mg and inorganicPro-coated Mg during the corrosion in PBS buffer.

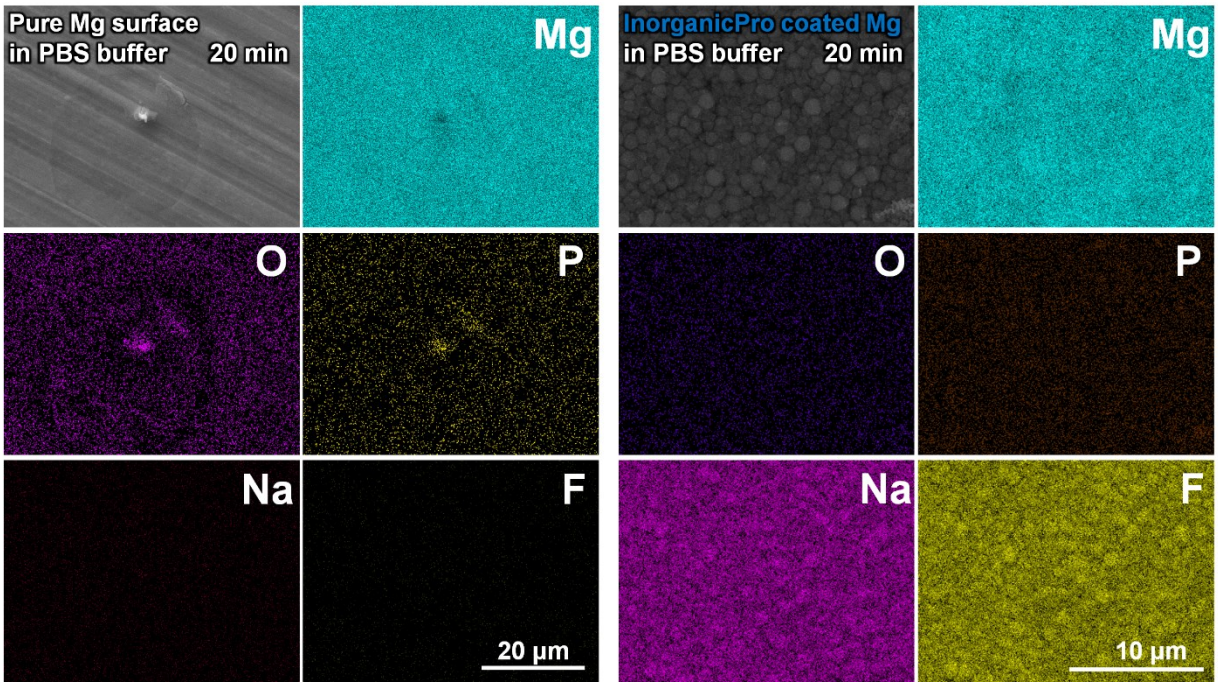

Figure S5.11. EDS result of surface composition of pure Mg and inorganicPro-coated Mg after immersion in PBS for 20 min.

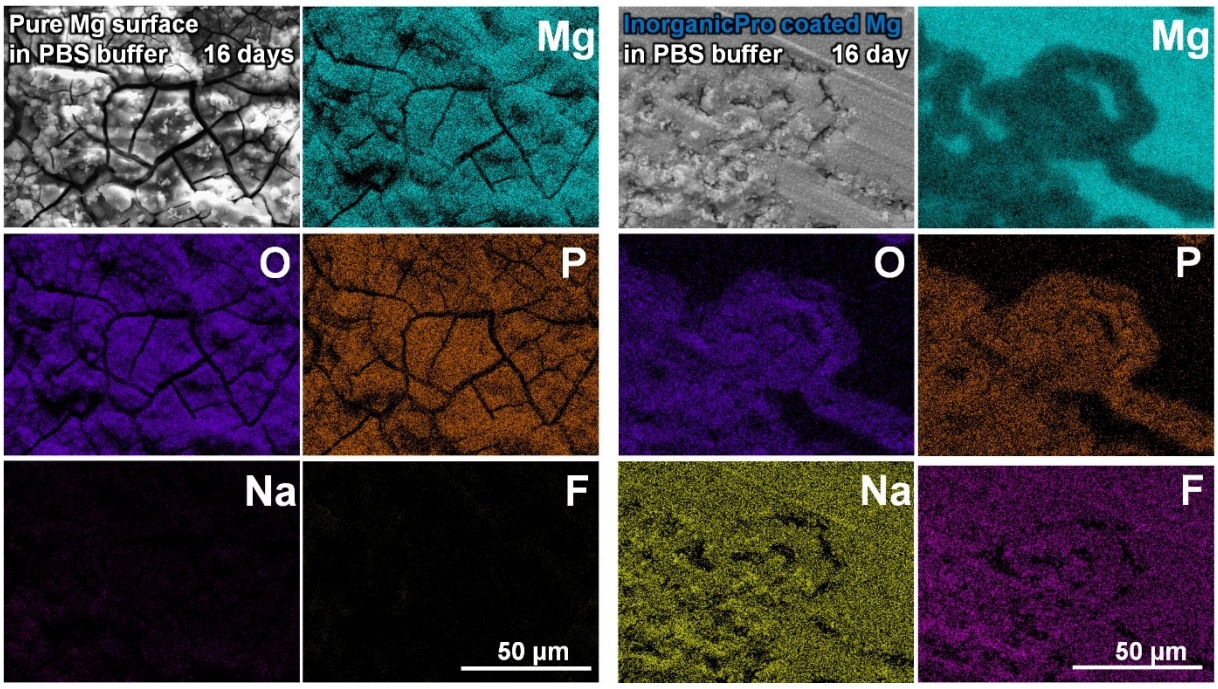

Figure S5.12. EDS result of surface composition of pure Mg and inorganicPro-coated Mg after immersion in PBS for 16 days.

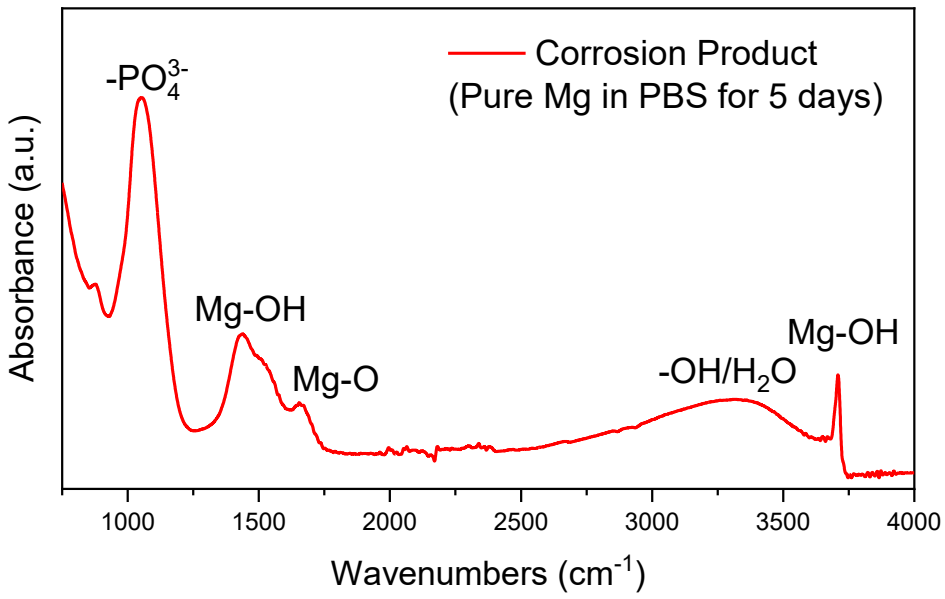

Figure S5.13. FTIR result of corrosion product of pure Mg after immersion in PBS for 16 days.

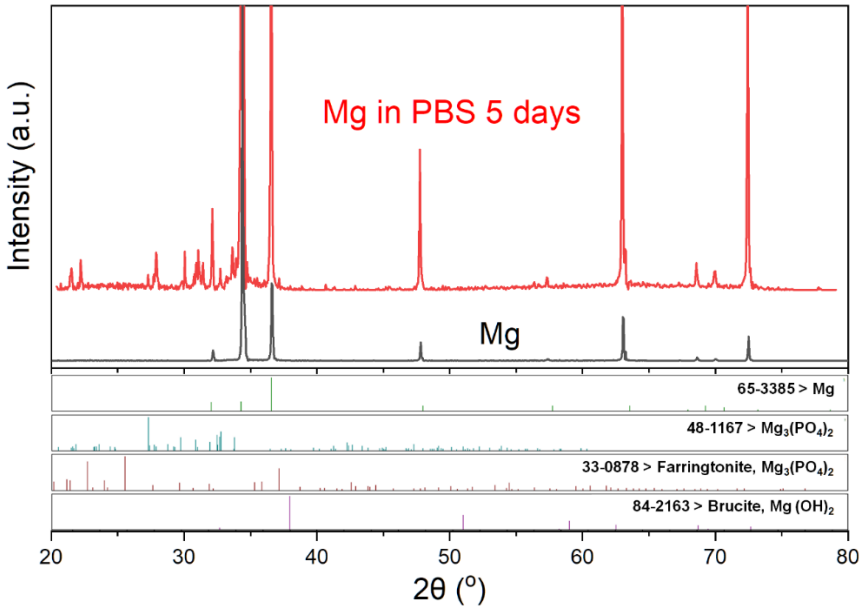

Figure S5.14. XRD result of corrosion product of pure Mg after immersion in PBS for 16 days.

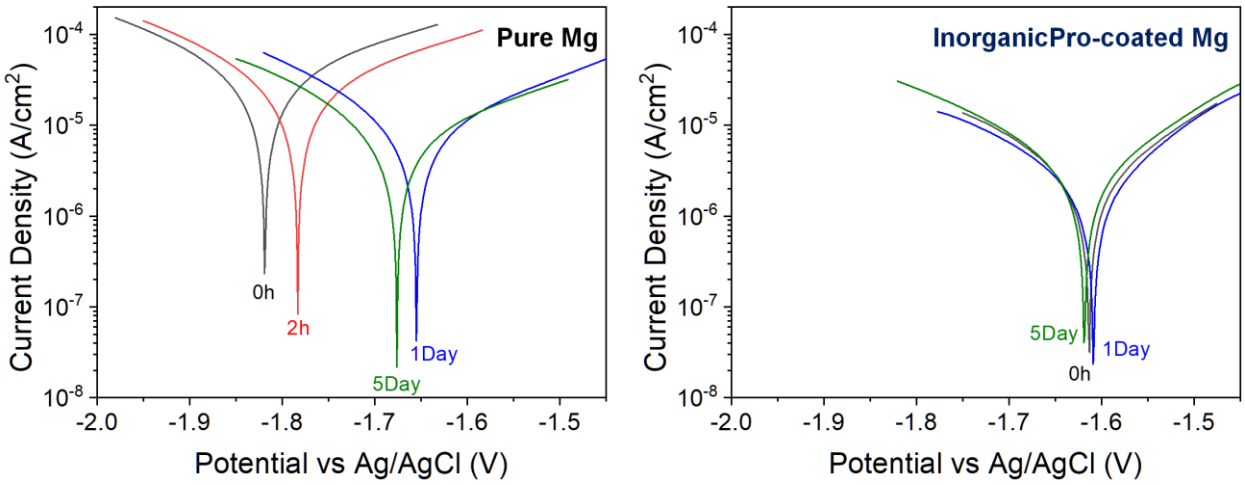

Figure S5.15. Potentiodynamic polarization curves of pure Mg and inorganicPro-coated Mg in PBS buffer for different duration.

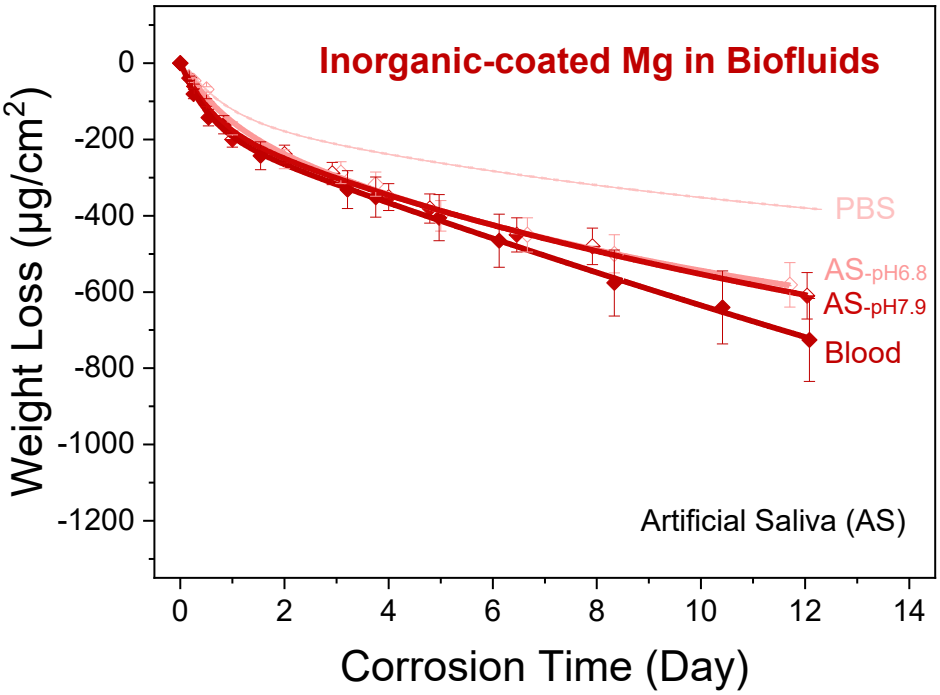

Figure S5.16. Weight loss of inorganic-coated Mg in different biofluids.

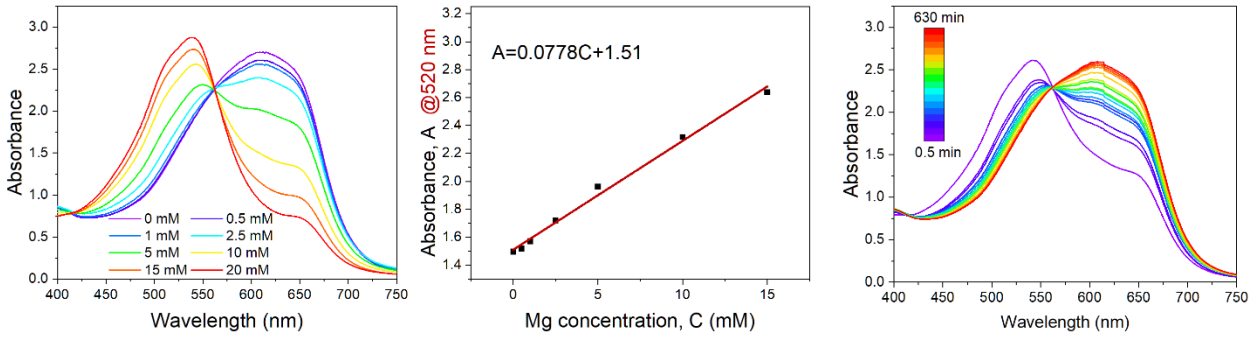

Figure S5.17. Standard UV-Vis calibration curve of Mg-Calmagite solution with different Mg concentration and Mg concentration change during $MgCl_2$-NaF reaction

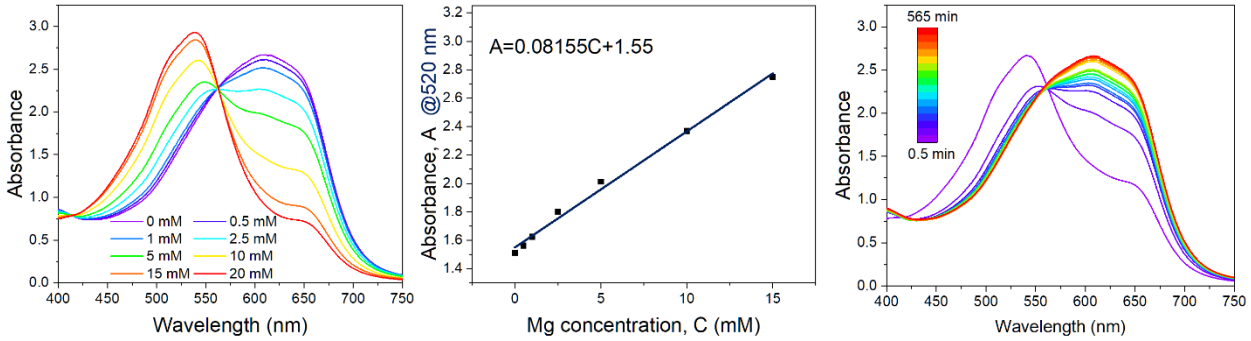

Figure S5.18. Standard UV-Vis calibration curve of Mg(BSA)-Calmagite solution with different Mg concentration and Mg concentration change during $MgCl_2$-NaF-BSA reaction

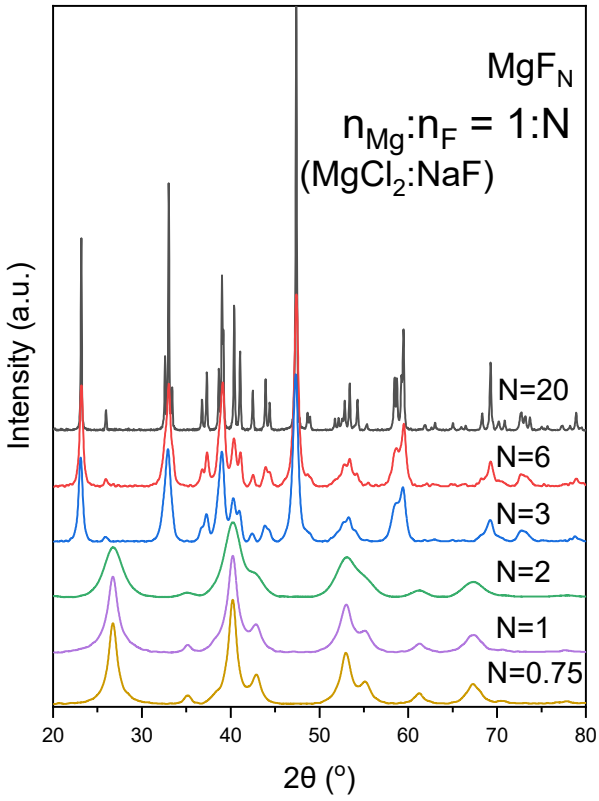

Figure S5.19. XRD profiles of synthesized <Mg, Na, F> inorganics with different ratios of reactants

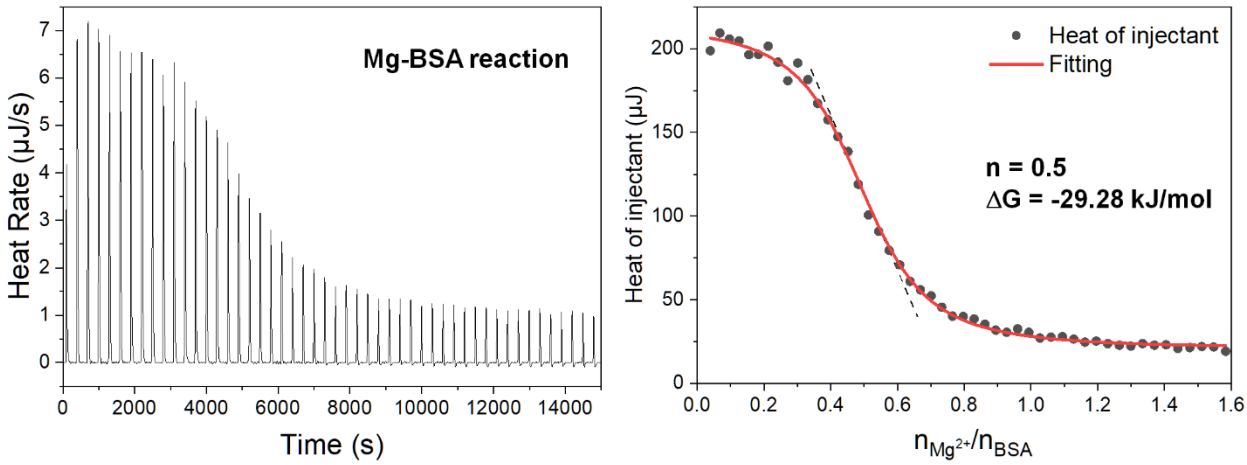

Figure S5.20. ITC measurement of the affinity between Mg ion and BSA protein

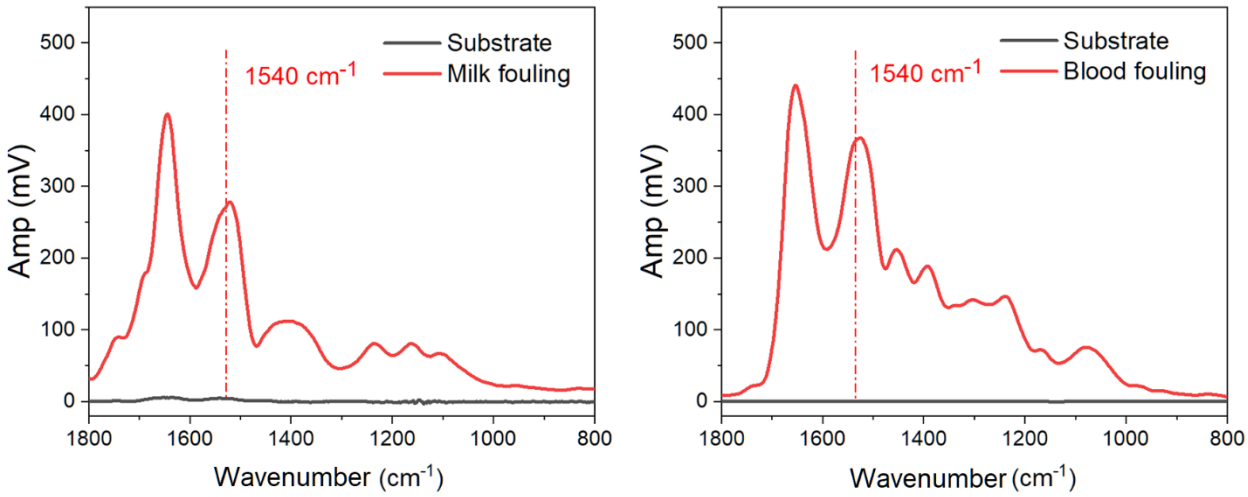

Figure S5.21. O-PTIR spectra of Milk and Blood (marked wavelength used as the characteristic peck for mapping)

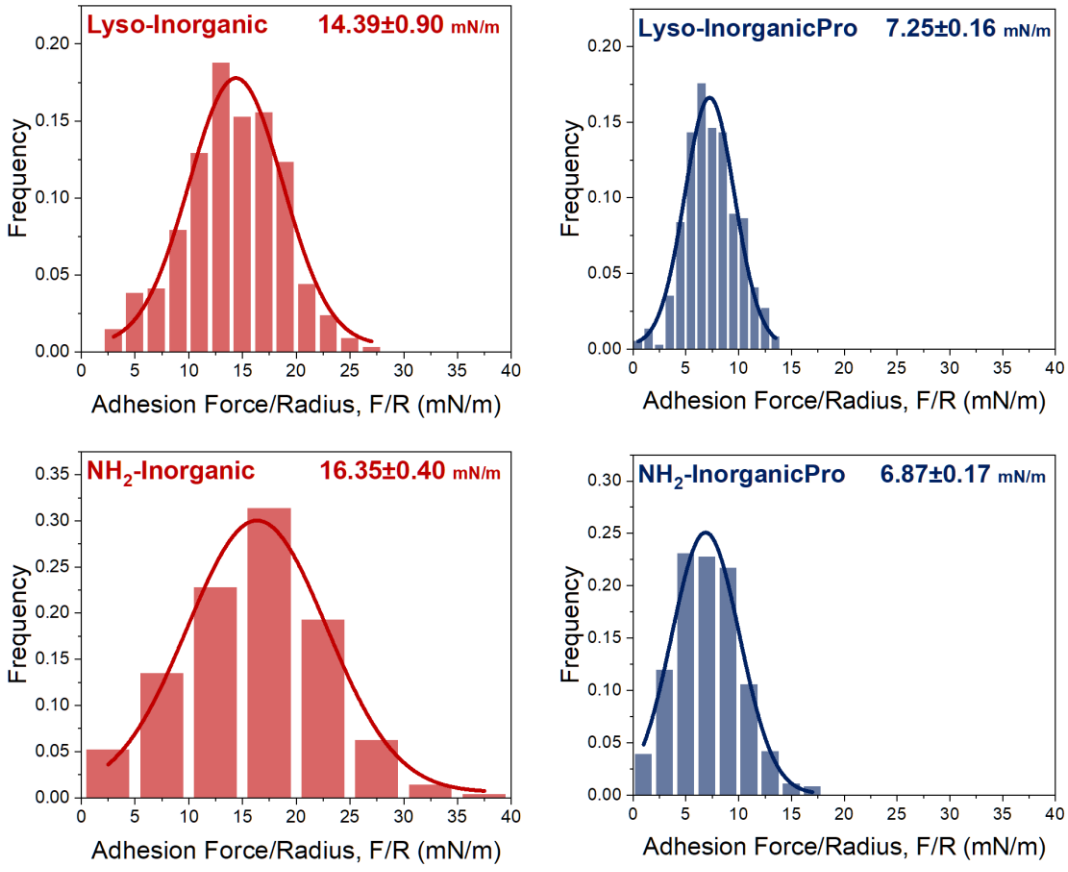

Figure S5.22. Histogram of typical foulant-surface interaction forces and their fitted Gaussian distribution

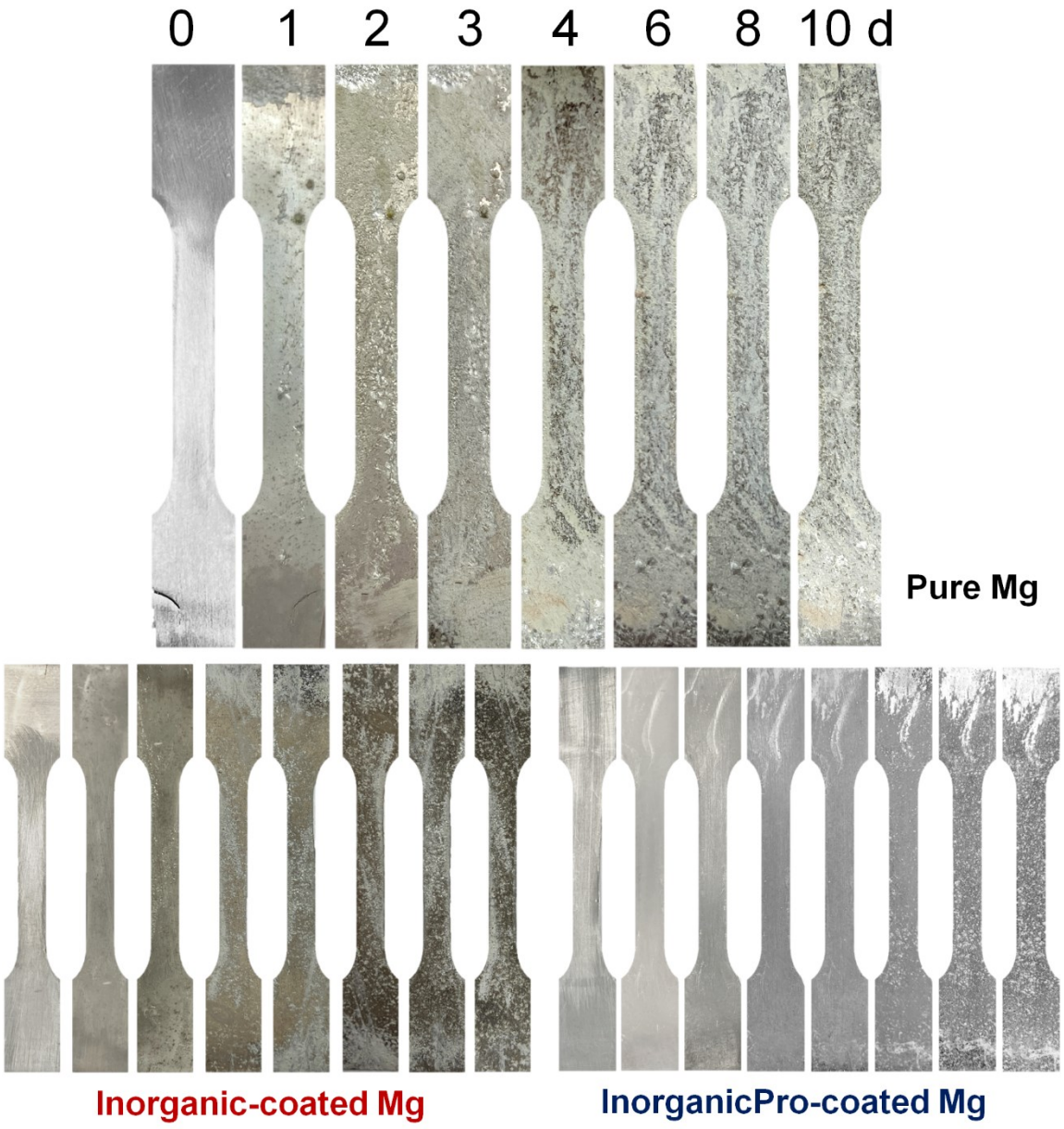

Figure S5.23. Morphology of pure Mg, inorganic, and inorganic-coated Mg-membrane materials tested in blood for different durations

CHAPTER 6. Conclusions and Perspectives

This thesis endeavors to develop protective coatings with the aim of mitigating biofouling and biocorrosion issues, with a special focus on BSA-protein-based coatings. Despite of the great challenges, including inadequate understanding in anchoring and deposition mechanisms that govern the preparation and stability of BSA coatings, limited on-demand functionalities, unstable surface of protein molecule that compromises antifouling performance in complex biofluids, as well as the absence of tailored protein-based coating to combat biocorrosion for metallic implants, we successfully design and prepare novel BSA-based coatings with excellent antifouling and robust anticorrosion properties in accordance with innovative protein-engineering and advanced understanding in fouling/antifouling processes. Specifically, these innovation in this thesis encompasses the elucidated interfacial interaction mechanisms underlying BSA anchoring and antifouling phenomena and the engineered native BSA protein with advanced introduced functions via conjugation and hybridization strategies.

6.1 Major conclusions and contributions

The first work probed the interfacial interaction forces governing anchoring and deposition of BSA protein on surfaces and developed a feasible polymethacrylate-protein conjugation method to engineer native BSA with on-demand functions. Specifically, a series of engineered protein BSA@Polymers that can universally anchor on diverse substrate surfaces and impart surfaces with various on-demand functionalities were prepared by grafting polyacrylates on BSA molecules via facile *thiol-ene* click chemistry in accordance with a bionic 'root-leaf' design. The as-prepared engineered proteins preserved the intrinsic stickiness of native BSA molecules, enabling robust anchoring on metallic, inorganic, and organic surfaces even under harsh conditions. Molecular

force measurements revealed that the stickiness of BSA stemmed from its multiple adaptive molecular interactions with target substrate surfaces, which could be tuned by the solution chemistry, such as pH and salinity. Eight polyacrylate-conjugated proteins were successfully developed in this work and could be facilely applied to surfaces via a simple dip or spray coating method. These engineered protein BSA@Polymer successfully imparted coatings with versatile on-demand functionalities, such as pH-responsive performance and robust adhesion with various nanomaterials. The method in this work can be readily extended to engineer other native proteins with desired functional motifs, boosting the development of new biomaterials and protein-based coatings for bioengineering applications and nanotechnologies, such as self-assembly, point-of-care diagnostics, chemical sensing, and molecular sieve-assisted phase separation.

The second work applied the conjugation strategy developed in the first work to synthesize an engineered BSA@PSBMA protein as antifouling coatings which overcome the intrinsic weakness of native protein coatings and achieve high-efficient and robust antifouling performance in complex biological fluids. The as-prepared engineered protein BSA@PSBMA preserved the intrinsically natural function of native BSA in surface-independent anchoring on various substrates, such as metallic, inorganic, and organic substrates, and introduced the advanced function of SBMA on extraordinary resistance to a wide spectrum of potential bio-foulants, including proteins, CHO cells, and biofluids. The robust antifouling capability of BSA@PSBMA coating in complex biological environments mainly originates from the zwitterionic SBMA segments grafted on BSA molecules, enabling a bionic ‘thorn-on vine’ structure to induce the defensive interfacial hydration layer and additional steric repulsion between the coatings and foulants. The engineered BSA@PSBMA protein has great potential applications in many industrial and biomedical areas, considering its simplicity for manufacturing at a large scale and low cost of raw materials.

The third work incorporated new anticorrosion function into BSA protein-based inorganic-protein coating via hybridization strategy to mitigate the biofouling-accelerated corrosion for Mg-based biomaterials. Specifically, we have developed a novel in-situ inorganic-protein coating strategy by simply immersing Mg surfaces into a NaF solution in the presence of BSA proteins. The introduced BSA molecules enhanced coating compactness through boosting Na-Mg-F biomineralization kinetics to generate more and finer $NaMgF_3$ nanoparticles. These finer inorganic nanoparticle 'bricks' densely packed on Mg surfaces, tripling anticorrosion performance. The underlying kinetics boosting mechanism was elucidated: in the BSA-involved biomineralization, BSA molecules associated with Mg ions to generate a locally hydrophobic domain, facilitating the decoordination of Mg ions and H_2O molecules. This, in turn, lowered the enthalpy of Na-Mg-F reaction and kinetically boosts the nucleation of $NaMgF_3$ nanoparticles. Moreover, the incorporation of BSA in and on the coatings plays two synergistic roles: (1) acting as 'mortar' to seal residual cracks within coatings, thereby promoting coating compactness and tripling anticorrosion performance, and (2) mitigating fouling-accelerated biocorrosion in complex biosystems with tenfold resistance against bio-foulant attachments, including biofluids, proteins, and metabolites. This work showcases a facile and effective preparation of a dual-protection coating on Mg-based biomaterials via employing proteins to alter the reaction kinetics, as well as incorporating the intrinsic antifouling functions of proteins into new coatings, potentially paving the way for the application of Mg-based biomaterials.

This thesis presents original contributions in Material, Method, and Mechanism (3M). Specifically, it introduces BSA protein as a novel, biocompatible materials for antifouling coatings and develops feasible protein engineering methods (*Conjugation* and *Hybridization*), enabling BSA protein-based coatings with improved protection (antifouling and anticorrosion) for

bioengineering applications. Unveiled interfacial interactions underlying BSA anchoring and antifouling phenomena, as well as discovered protein-inorganic interactions that alter reaction thermodynamics and kinetics have significant implications for future designs of novel protein-based coatings and materials demanded in nano-, bio-, and eco-applications.

6.2 Perspectives

This research advanced the development of protein-based functional coatings, deepened our understanding in protein-surface interfacial interactions, and offered pioneering protein-engineering models to constructing protein-based coatings for bioengineering and biomedical applications. The diversity, modifiability, and sustainability of protein envision a promising, flourishing future of protein-based materials, particularly in the next-generation nano-, bio-, and eco-technology. This unexplored virgin field offers vast opportunities, across materials, mechanisms, and manufacturing (future 3M).

(1) Materials. The appropriate selection of protein is pivotal in designing novel coating with enhanced performance. Different types of proteins offer distinctive properties. Globular proteins, including BSA, Hb, or Whey proteins, may be good candidates for antifouling applications, while fibrous proteins may be good at adhesion. Cassie protein can specifically bind with Ca ions and thereby may improve the performance of Ca-related materials. Squid ring teeth protein with higher hydrophobic β sheet structure may achieve underwater adhesion. If a protein that cannot associate with Mg ions was employed in the third work, the refinement of $NaMgF_3$ particle could not be achieved for higher compactness. We need to comprehensively consider the native properties, structure, and binding capabilities of proteins for optimal selection.

(2) Mechanisms. Protein is a complex macromolecule with hierarchical structure and sophisticated chemical, physical, and biological properties. It is well acknowledged that a better understanding of mechanisms underlying protein behaviors will allow us to create materials with superior performance, however, our understanding is still quite limited. For instance, BSA anchoring behavior is related to the conformation change, but no direct experimental or modelling research reveals the conformation change associated with anchoring. A clear understanding of this process not only helps the development of BSA-based coatings, but also benefits advancements in other materials with conformation changes, such as block copolymer self-assembly. The antifouling mechanism of BSA protein has been attributed to the mixed charged groups at molecular scale, however, every type of protein consists of mixed charged groups on its surface, but not all of them demonstrate antifouling properties. The antifouling mechanisms may stem from the special structure that performs steric repulsion. However, no related research is performed.

(3) Manufacturing. Using proteins as raw materials for high value-added products involves protein engineering and manufacturing techniques. For example, we can employ the low-cost whey protein as 3D printing ink to produce eco-friendly stuff. This challenging, interdisciplinary field promises significant near-term impact in the world and substantial rewards.

Bibliography

1. Friedrichs, J.; Helbig, R.; Hilsenbeck, J.; Pandey, P. R.; Sommer, J.-U.; Renner, L. D.; Pompe, T.; Werner, C., Entropic repulsion of cholesterol-containing layers counteracts bioadhesion. *Nature* **2023,** *618* (7966), 733-739.
2. Jin, H.; Tian, L.; Bing, W.; Zhao, J.; Ren, L., Bioinspired marine antifouling coatings: Status, prospects, and future. *Progress in Materials Science* **2022,** *124*.
3. Kirschner, C. M.; Brennan, A. B., Bio-Inspired Antifouling Strategies. *Annual Review of Materials Research* **2012,** *42* (1), 211-229.
4. Magin, C. M.; Cooper, S. P.; Brennan, A. B., Non-toxic antifouling strategies. *Materials today* **2010,** *13* (4), 36-44.
5. Jiang, C.; Wang, G.; Hein, R.; Liu, N.; Luo, X.; Davis, J. J., Antifouling Strategies for Selective In Vitro and In Vivo Sensing. *Chem Rev* **2020,** *120* (8), 3852-3889.
6. Sabate Del Rio, J.; Henry, O. Y. F.; Jolly, P.; Ingber, D. E., An antifouling coating that enables affinity-based electrochemical biosensing in complex biological fluids. *Nat Nanotechnol* **2019,** *14* (12), 1143-1149.
7. Hu, X.; Tian, J.; Li, C.; Su, H.; Qin, R.; Wang, Y.; Cao, X.; Yang, P., Amyloid-Like Protein Aggregates: A New Class of Bioinspired Materials Merging an Interfacial Anchor with Antifouling. *Adv Mater* **2020,** *32* (23), e2000128.
8. Jiang, S.; Cao, Z., Ultralow-fouling, functionalizable, and hydrolyzable zwitterionic materials and their derivatives for biological applications. *Adv Mater* **2010,** *22* (9), 920-32.
9. Li, B.; Jain, P.; Ma, J.; Smith, J. K.; Yuan, Z.; Hung, H.-C.; He, Y.; Lin, X.; Wu, K.; Pfaendtner, J.; Shaoyi, J., Trimethylamine N-oxide–derived zwitterionic polymers: A new class of ultralow fouling bioinspired materials. *Science advances* **2019,** *5* (6), eaaw9562.

10. Zhang, P.; Ratner, B. D.; Hoffman, A. S.; Jiang, S., Nonfouling Surfaces. In *Biomaterials Science*, 2020; pp 507-513.

11. Melo, L.; Bott, T. R.; Bernardo, C. A., *Fouling science and technology*. Springer Science & Business Media: 2012; Vol. 145.

12. Cloutman-Green, E., Infection Prevention and Control: Healthcare-associated Infection. *Hugo and Russell's Pharmaceutical Microbiology* **2023**.

13. Xie, Y.; Tang, C.; Wang, Z.; Xu, Y.; Zhao, W.; Sun, S.; Zhao, C., Co-deposition towards mussel-inspired antifouling and antibacterial membranes by using zwitterionic polymers and silver nanoparticles. *J Mater Chem B* **2017,** *5* (34), 7186-7193.

14. Chen, S.; Xie, Y.; Xiao, T.; Zhao, W.; Li, J.; Zhao, C., Tannic acid-inspiration and post-crosslinking of zwitterionic polymer as a universal approach towards antifouling surface. *Chemical Engineering Journal* **2018,** *337*, 122-132.

15. Yang, C.; He, G.; Zhang, A.; Wu, Q.; Zhou, L.; Hang, T.; Liu, D.; Xiao, S.; Chen, H. J.; Liu, F.; Li, L.; Wang, J.; Xie, X., Injectable Slippery Lubricant-Coated Spiky Microparticles with Persistent and Exceptional Biofouling-Resistance. *ACS Cent Sci* **2019,** *5* (2), 250-258.

16. Niu, W.; Chen, G. Y.; Xu, H.; Liu, X.; Sun, J., Highly Transparent and Self-Healable Solar Thermal Anti-Deicing Surfaces: When Ultrathin MXene Multilayers Marry a Solid Slippery Self-Cleaning Coating. *Advanced Materials* **2022,** *34* (10), 2108232.

17. Liu, S.; Guo, W., Anti-Biofouling and Healable Materials: Preparation, Mechanisms, and Biomedical Applications. *Advanced Functional Materials* **2018,** *28* (41).

18. Xie, X.; Doloff, J. C.; Yesilyurt, V.; Sadraei, A.; McGarrigle, J. J.; Omami, M.; Veiseh, O.; Farah, S.; Isa, D.; Ghani, S.; Joshi, I.; Vegas, A.; Li, J.; Wang, W.; Bader, A.;

Tam, H. H.; Tao, J.; Chen, H. J.; Yang, B.; Williamson, K. A.; Oberholzer, J.; Langer, R.; Anderson, D. G., Reduction of measurement noise in a continuous glucose monitor by coating the sensor with a zwitterionic polymer. *Nat Biomed Eng* **2018,** *2* (12), 894-906.

19. Srinivasan, M.; Swain, G. W., Managing the use of copper-based antifouling paints. *Environmental Management* **2007,** *39*, 423-441.

20. Tegoni, M.; Valensin, D.; Toso, L.; Remelli, M., Copper chelators: chemical properties and bio-medical applications. *Current medicinal chemistry* **2014,** *21* (33), 3785-3818.

21. Wu, H.; Yang, G.; Zhu, K.; Liu, S.; Guo, W.; Jiang, Z.; Li, Z., Materials, devices, and systems of on skin electrodes for electrophysiological monitoring and human-machine interfaces. *Advanced Science* **2021,** *8* (2), 2001938.

22. He, K.; Liu, Z.; Wan, C.; Jiang, Y.; Wang, T.; Wang, M.; Zhang, F.; Liu, Y.; Pan, L.; Xiao, M.; Yang, H.; Chen, X., An On-Skin Electrode with Anti-Epidermal-Surface-Lipid Function Based on a Zwitterionic Polymer Brush. *Adv Mater* **2020,** *32* (24), e2001130.

23. Palanker, D.; Le Mer, Y.; Mohand-Said, S.; Sahel, J.-A., Simultaneous perception of prosthetic and natural vision in AMD patients. *Nature Communications* **2022,** *13* (1), 1-6.

24. Wang, D.; Xu, Y.; Li, Q.; Turng, L.-S., Artificial small-diameter blood vessels: materials, fabrication, surface modification, mechanical properties, and bioactive functionalities. *Journal of Materials Chemistry B* **2020,** *8* (9), 1801-1822.

25. Callow, J. A.; Callow, M. E., Trends in the development of environmentally friendly fouling-resistant marine coatings. *Nat Commun* **2011,** *2*, 244.

26. Huang, H.; Zhang, C.; Crisci, R.; Lu, T.; Hung, H. C.; Sajib, M. S. J.; Sarker, P.; Ma, J.; Wei, T.; Jiang, S.; Chen, Z., Strong Surface Hydration and Salt Resistant Mechanism

of a New Nonfouling Zwitterionic Polymer Based on Protein Stabilizer TMAO. *J Am Chem Soc* **2021,** *143* (40), 16786-16795.

27. Lin, M.; Song, P.; Zhou, G.; Zuo, X.; Aldalbahi, A.; Lou, X.; Shi, J.; Fan, C., Electrochemical detection of nucleic acids, proteins, small molecules and cells using a DNA-nanostructure-based universal biosensing platform. *Nat Protoc* **2016,** *11* (7), 1244-63.

28. Israelachvili, J.; Min, Y.; Akbulut, M.; Alig, A.; Carver, G.; Greene, W.; Kristiansen, K.; Meyer, E.; Pesika, N.; Rosenberg, K.; Zeng, H., Recent advances in the surface forces apparatus (SFA) technique. *Reports on Progress in Physics* **2010,** *73* (3).

29. Anderson, J. M.; Rodriguez, A.; Chang, D. T. In *Foreign body reaction to biomaterials*, Seminars in immunology, Elsevier: 2008; pp 86-100.

30. Zhang, D.; Chen, Q.; Shi, C.; Chen, M.; Ma, K.; Wan, J.; Liu, R., Dealing with the foreign-body response to implanted biomaterials: strategies and applications of new materials. *Advanced Functional Materials* **2021,** *31* (6), 2007226.

31. Colton, C. K., Implantable biohybrid artificial organs. *Cell transplantation* **1995,** *4* (4), 415-436.

32. Li, C.; Guo, C.; Fitzpatrick, V.; Ibrahim, A.; Zwierstra, M. J.; Hanna, P.; Lechtig, A.; Nazarian, A.; Lin, S. J.; Kaplan, D. L., Design of biodegradable, implantable devices towards clinical translation. *Nature Reviews Materials* **2020,** *5* (1), 61-81.

33. Elliott, K.; Jasper, H., Physiological salt solutions for brain surgery: studies of local pH and pial vessel reactions to buffered and unbuffered isotonic solutions. *Journal of Neurosurgery* **1949,** *6* (2), 140-152.

34. Papsin, B.; McTavish, A., Saline nasal irrigation: Its role as an adjunct treatment. *Canadian Family Physician* **2003,** *49* (2), 168-173.

35. Campbell, I.; Baxter, J.; Tweedie, I.; Taylor, G.; Keens, S., IV fluids during surgery. *BJA: British Journal of Anaesthesia* **1990,** *65* (5), 726-729.

36. Duerr, F. M.; Twedt, D. C.; Monnet, E., Changes in pH of peritoneal fluid associated with carbon dioxide insufflation during laparoscopic surgery in dogs. *American journal of veterinary research* **2008,** *69* (2), 298-301.

37. Lobo, D. N.; Bostock, K. A.; Neal, K. R.; Perkins, A. C.; Rowlands, B. J.; Allison, S. P., Effect of salt and water balance on recovery of gastrointestinal function after elective colonic resection: a randomised controlled trial. *The Lancet* **2002,** *359* (9320), 1812-1818.

38. Simmen, H.-P.; Blaser, J. r., Analysis of pH and pO2 in abscesses, peritoneal fluid, and drainage fluid in the presence or absence of bacterial infection during and after abdominal surgery. *The American journal of surgery* **1993,** *166* (1), 24-27.

39. Unsworth, L. D.; Sheardown, H.; Brash, J. L., Polyethylene oxide surfaces of variable chain density by chemisorption of PEO-thiol on gold: adsorption of proteins from plasma studied by radiolabelling and immunoblotting. *Biomaterials* **2005,** *26* (30), 5927-5933.

40. Zhao, L.; Liu, Q.; Gao, R.; Wang, J.; Yang, W.; Liu, L., One-step method for the fabrication of superhydrophobic surface on magnesium alloy and its corrosion protection, antifouling performance. *Corrosion Science* **2014,** *80*, 177-183.

41. Yan, S.; Song, G.-L.; Li, Z.; Wang, H.; Zheng, D.; Cao, F.; Horynova, M.; Dargusch, M. S.; Zhou, L., A state-of-the-art review on passivation and biofouling of Ti and its alloys in marine environments. *Journal of materials science & technology* **2018,** *34* (3), 421-435.

42. Li, Y.; Ning, C., Latest research progress of marine microbiological corrosion and bio-fouling, and new approaches of marine anti-corrosion and anti-fouling. *Bioactive materials* **2019,** *4*, 189-195.

43. Dexter, S. C., Role of microfouling organisms in marine corrosion. *Biofouling* **1993,** *7* (2), 97-127.

44. Bixler, G. D.; Bhushan, B., Biofouling: lessons from nature. *Philosophical Transactions of the Royal Society A: Mathematical, Physical and Engineering Sciences* **2012,** *370* (1967), 2381-2417.

45. Beech, I.; Sunner, J.; Arciola, C.; Cristiani, P., Microbially-influenced corrosion: damage to prostheses, delight for bacteria. *The International journal of artificial organs* **2006,** *29* (4), 443-452.

46. Vigneron, A.; Head, I. M.; Tsesmetzis, N., Damage to offshore production facilities by corrosive microbial biofilms. *Applied microbiology and biotechnology* **2018,** *102*, 2525-2533.

47. Saravanan, K. G.; Kirubaharan, A. K.; Vishwakarma, V., Characterization of Surface Coatings. In *Polymetallic Coatings to Control Biofouling in Pipelines: Challenges and Potential*, CRC Press: 2021; pp 77-96.

48. Wang, J. L.; Xu, J. K.; Hopkins, C.; Chow, D. H.; Qin, L., Biodegradable Magnesium-Based Implants in Orthopedics-A General Review and Perspectives. *Adv Sci (Weinh)* **2020,** *7* (8), 1902443.

49. Bekmurzayeva, A.; Duncanson, W. J.; Azevedo, H. S.; Kanayeva, D., Surface modification of stainless steel for biomedical applications: Revisiting a century-old material. *Materials Science and Engineering: C* **2018,** *93*, 1073-1089.

50. Yang, L.; Adam, C.; Nichol, G. S.; Cockroft, S. L., How much do van der Waals dispersion forces contribute to molecular recognition in solution? *Nature chemistry* **2013,** *5* (12), 1006-1010.

51. Berger, R.; Resnati, G.; Metrangolo, P.; Weber, E.; Hulliger, J. r., Organic fluorine compounds: a great opportunity for enhanced materials properties. *Chemical Society Reviews* **2011,** *40* (7), 3496-3508.

52. Hof, F.; Scofield, D. M.; Schweizer, W. B.; Diederich, F. o., A weak attractive interaction between organic fluorine and an amide group. *Angewandte Chemie* **2004,** *116* (38), 5166-5169.

53. Zhang, Z.; Chen, S.; Jiang, S., Dual-functional biomimetic materials: nonfouling poly (carboxybetaine) with active functional groups for protein immobilization. *Biomacromolecules* **2006,** *7* (12), 3311-3315.

54. Mao, C.; Wang, X.; Zhang, W.; Hu, B.; Deng, H., Super-hydrophilic TiO2-based coating of anion exchange membranes with improved antifouling performance. *Colloids and Surfaces A: Physicochemical and Engineering Aspects* **2021,** *614*, 126136.

55. Deng, W.; Long, M.; Miao, X.; Wen, N.; Deng, W., Eco-friendly preparation of robust superhydrophobic $Cu(OH)_2$ coating for self-cleaning, oil-water separation and oil sorption. *Surface and Coatings Technology* **2017,** *325*, 14-21.

56. He, H.; Jiang, H.; Chen, C.; Ouyang, L.; Jiang, W.; Yuan, S., Efficient Oil/Water Separation by Zwitterionic Poly(sulfobetaine methacrylate)@$Cu(OH)_2$ Nanoneedle Array-Coated Copper Meshes with Superwetting and Antifouling Properties. *ACS Sustainable Chemistry & Engineering* **2019,** *7* (16), 13815-13826.

57. He, W.; Tao, B.; Yang, Z.; Yang, G.; Guo, X.; Liu, P.-J.; Yan, Q.-L., Mussel-inspired polydopamine-directed crystal growth of core-shell n-Al@PDA@CuO metastable intermixed composites. *Chemical Engineering Journal* **2019,** *369*, 1093-1101.

58. He, Z.; Zhang, Z.; He, J., CuO/Cu based superhydrophobic and self-cleaning surfaces. *Scripta Materialia* **2016,** *118*, 60-64.

59. Israelachvili, J. N., *Intermolecular and surface forces*. Elsevier: London, UK, 2011.

60. Xia, Y.; Adibnia, V.; Huang, R.; Murschel, F.; Faivre, J.; Xie, G.; Olszewski, M.; De Crescenzo, G.; Qi, W.; He, Z.; Su, R.; Matyjaszewski, K.; Banquy, X., Biomimetic Bottlebrush Polymer Coatings for Fabrication of Ultralow Fouling Surfaces. *Angew Chem Int Ed Engl* **2019,** *58* (5), 1308-1314.

61. Guo, S.; Janczewski, D.; Zhu, X.; Quintana, R.; He, T.; Neoh, K. G., Surface charge control for zwitterionic polymer brushes: Tailoring surface properties to antifouling applications. *J Colloid Interface Sci* **2015,** *452*, 43-53.

62. Zhao, Y.; Yu, C.; Lan, H.; Cao, M.; Jiang, L., Improved Interfacial Floatability of Superhydrophobic/Superhydrophilic Janus Sheet Inspired by Lotus Leaf. *Advanced Functional Materials* **2017,** *27* (27).

63. Zang, D.; Zhu, R.; Zhang, W.; Yu, X.; Lin, L.; Guo, X.; Liu, M.; Jiang, L., Corrosion-resistant superhydrophobic coatings on Mg alloy surfaces inspired by lotus seedpod. *Advanced Functional Materials* **2017,** *27* (8), 1605446.

64. Xu, M.; Luo, X.; Davis, J. J., The label free picomolar detection of insulin in blood serum. *Biosensors and Bioelectronics* **2013,** *39* (1), 21-25.

65. Estupiц, D.; Bannwarth, M. B.; Mylon, S. E.; Landfester, K.; Muцoz-Espц, R.; Crespy, D., Multifunctional clickable and protein-repellent magnetic silica nanoparticles. *Nanoscale* **2016,** *8* (5), 3019-3030.

66. Ahmed, S. T.; Leckband, D. E., Protein Adsorption on Grafted Zwitterionic Polymers Depends on Chain Density and Molecular Weight. *Advanced Functional Materials* **2020,** *30* (30).

67. He, K.; Duan, H.; Chen, G. Y.; Liu, X.; Yang, W.; Wang, D., Cleaning of oil fouling with water enabled by zwitterionic polyelectrolyte coatings: overcoming the imperative challenge of oil–water separation membranes. *ACS nano* **2015,** *9* (9), 9188-9198.

68. Luo, X.; Xu, M.; Freeman, C.; James, T.; Davis, J. J., Ultrasensitive label free electrical detection of insulin in neat blood serum. *Analytical chemistry* **2013,** *85* (8), 4129-4134.

69. Chen, S.; Cao, Z.; Jiang, S., Ultra-low fouling peptide surfaces derived from natural amino acids. *Biomaterials* **2009,** *30* (29), 5892-6.

70. Ye, H.; Wang, L.; Huang, R.; Su, R.; Liu, B.; Qi, W.; He, Z., Superior antifouling performance of a zwitterionic peptide compared to an amphiphilic, non-ionic peptide. *ACS Applied Materials & Interfaces* **2015,** *7* (40), 22448-22457.

71. Liu, N.; Song, J.; Lu, Y.; Davis, J. J.; Gao, F.; Luo, X., Electrochemical aptasensor for ultralow fouling cancer cell quantification in complex biological media based on designed branched peptides. *Analytical chemistry* **2019,** *91* (13), 8334-8340.

72. Zhang, Y.; Liu, Y.; Liu, Y.; Zuo, P.; Miao, S.; Hu, B.; Kang, Y.; Liu, W.; Yang, Q.; Ren, H.; Yang, P., alpha-Helix-Mediated Protein Adhesion. *J Am Chem Soc* **2023,** *145* (31), 17125-17135.

73. Yang, Q.; Zhao, J.; Muhammad, A.; Tian, L.; Liu, Y.; Chen, L.; Yang, P., Biopolymer coating for particle surface engineering and their biomedical applications. *Mater Today Bio* **2022,** *16*, 100407.

74. Yang, F.; Yang, P., Protein-Based Separation Membranes: State of the Art and Future Trends. *Advanced Energy and Sustainability Research* **2021,** *2* (6).

75. Fu, C.; Wang, Z.; Gao, Y.; Zhao, J.; Liu, Y.; Zhou, X.; Qin, R.; Pang, Y.; Hu, B.; Zhang, Y.; Nan, S.; Zhang, J.; Zhang, X.; Yang, P., Sustainable polymer coating for stainproof fabrics. *Nature Sustainability* **2023,** *6* (8), 984-994.

76. Orengo, C. A.; Michie, A. D.; Jones, S.; Jones, D. T.; Swindells, M. B.; Thornton, J. M., CATH-a hierarchic classification of protein domain structures. *Structure* **1997,** *5* (8), 1093-1109.

77. Maret, W.; Li, Y., Coordination dynamics of zinc in proteins. *Chemical reviews* **2009,** *109* (10), 4682-4707.

78. Heim, M.; Rmer, L.; Scheibel, T., Hierarchical structures made of proteins. The complex architecture of spider webs and their constituent silk proteins. *Chemical Society Reviews* **2010,** *39* (1), 156-164.

79. Gray, H. B.; Malmstrm, B. G.; Williams, R., Copper coordination in blue proteins. *JBIC Journal of Biological Inorganic Chemistry* **2000,** *5*, 551-559.

80. Bhattacharjee, M.; Schultz-Thater, E.; Trella, E.; Miot, S.; Das, S.; Loparic, M.; Ray, A. R.; Martin, I.; Spagnoli, G. C.; Ghosh, S., The role of 3D structure and protein conformation on the innate and adaptive immune responses to silk-based biomaterials. *Biomaterials* **2013,** *34* (33), 8161-8171.

81. Wright, A. K.; Thompson, M., Hydrodynamic structure of bovine serum albumin determined by transient electric birefringence. *Biophysical journal* **1975,** *15* (2), 137-141.

82. Topal, T.; Bodoki, A.; Oprean, L.; Oprean, R., Bovine serum albumin interactions with metal complexes. *Clujul medical* **2014,** *87* (4), 215.

83. Majorek, K. A.; Porebski, P. J.; Dayal, A.; Zimmerman, M. D.; Jablonska, K.; Stewart, A. J.; Chruszcz, M.; Minor, W., Structural and immunologic characterization of bovine, horse, and rabbit serum albumins. *Molecular immunology* **2012,** *52* (3-4), 174-182.

84. Buchwalow, I.; Samoilova, V.; Boecker, W.; Tiemann, M., Non-specific binding of antibodies in immunohistochemistry: fallacies and facts. *Scientific reports* **2011,** *1* (1), 28.

85. Reimhult, K.; Petersson, K.; Krozer, A., QCM-D analysis of the performance of blocking agents on gold and polystyrene surfaces. *Langmuir* **2008,** *24* (16), 8695-8700.

86. Wang, R.; Zhou, X.; Zhu, X.; Yang, C.; Liu, L.; Shi, H., Isoelectric bovine serum albumin: robust blocking agent for enhanced performance in optical-fiber based DNA sensing. *ACS sensors* **2017,** *2* (2), 257-262.

87. Ma, G. J.; Ferhan, A. R.; Jackman, J. A.; Cho, N.-J., Conformational flexibility of fatty acid-free bovine serum albumin proteins enables superior antifouling coatings. *Communications Materials* **2020,** *1* (1).

88. Li, L.; Chen, G., Precise Assembly of Proteins and Carbohydrates for Next-Generation Biomaterials. *J Am Chem Soc* **2022,** *144* (36), 16232-16251.

89. Manjappa, A. S.; Chaudhari, K. R.; Venkataraju, M. P.; Dantuluri, P.; Nanda, B.; Sidda, C.; Sawant, K. K.; Murthy, R. S. R., Antibody derivatization and conjugation strategies: application in preparation of stealth immunoliposome to target chemotherapeutics to tumor. *Journal of Controlled Release* **2011,** *150* (1), 2-22.

90. Hirsch, J. D.; Eslamizar, L.; Filanoski, B. J.; Malekzadeh, N.; Haugland, R. P.; Beechem, J. M.; Haugland, R. P., Easily reversible desthiobiotin binding to streptavidin, avidin, and other biotin-binding proteins: uses for protein labeling, detection, and isolation. *Analytical biochemistry* **2002,** *308* (2), 343-357.

91. Chen, G.; Jiang, M., Cyclodextrin-based inclusion complexation bridging supramolecular chemistry and macromolecular self-assembly. *Chemical Society Reviews* **2011,** *40* (5), 2254-2266.

92. Chien, H.-W.; Tsai, C.-C.; Tsai, W.-B.; Wang, M.-J.; Kuo, W.-H.; Wei, T.-C.; Huang, S.-T., Surface conjugation of zwitterionic polymers to inhibit cell adhesion and protein adsorption. *Colloids and Surfaces B: Biointerfaces* **2013,** *107*, 152-159.

93. Melo, B. L.; Lima-Sousa, R.; Alves, C. G.; Ferreira, P.; Moreira, A. F.; Correia, I. J.; de Melo-Diogo, D., Sulfobetaine methacrylate-albumin-coated graphene oxide incorporating IR780 for enhanced breast cancer phototherapy. *Nanomedicine* **2021,** *16* (6), 453-464.

94. Ahmad Fuaad, A. A.; Azmi, F.; Skwarczynski, M.; Toth, I., Peptide conjugation via CuAAC-click-chemistry. *Molecules* **2013,** *18* (11), 13148-13174.

95. Hoyle, C. E.; Bowman, C. N., Thiol-ene click chemistry. *Angewandte Chemie International Edition* **2010,** *49* (9), 1540-1573.

96. Tang, W.; Becker, M. L., Click reactions: a versatile toolbox for the synthesis of peptide-conjugates. *Chemical Society Reviews* **2014,** *43* (20), 7013-7039.

97. Vashist, S. K., Comparison of 1-ethyl-3-(3-dimethylaminopropyl) carbodiimide based strategies to crosslink antibodies on amine-functionalized platforms for immunodiagnostic applications. *Diagnostics* **2012,** *2* (3), 23-33.

98. Parshad, B.; Yadav, P.; Kerkhoff, Y.; Mittal, A.; Achazi, K.; Haag, R.; Sharma, S. K., Dendrimer-based micelles as cyto-compatible nanocarriers. *New Journal of Chemistry* **2019,** *43* (30), 11984-11993.

99. Pan, T.; Liu, Y.; Sun, H.; Xu, J.; Liu, J., Reversible switch of a selenium-containing antioxidant system regulated by protein assembly. *ACS Catalysis* **2020,** *10* (17), 9735-9740.

100. Gorski, J. P., Acidic phosphoproteins from bone matrix: a structural rationalization of their role in biomineralization. *Calcified Tissue International* **1992,** *50*, 391-396.

101. Moradian-Oldak, J.; George, A., Biomineralization of enamel and dentin mediated by matrix proteins. *Journal of dental research* **2021,** *100* (10), 1020-1029.

102. Veis, A., A window on biomineralization. *Science* **2005,** *307* (5714), 1419-1420.

103. Yao, S.; Jin, B.; Liu, Z.; Shao, C.; Zhao, R.; Wang, X.; Tang, R., Biomineralization: from material tactics to biological strategy. *Advanced Materials* **2017,** *29* (14), 1605903.

104. Gopal, G. J.; Kumar, A., Strategies for the production of recombinant protein in Escherichia coli. *The protein journal* **2013,** *32*, 419-425.

105. Ma, C.; Sun, J.; Li, B.; Feng, Y.; Sun, Y.; Xiang, L.; Wu, B.; Xiao, L.; Liu, B.; Petrovskii, V. S.; Bin, L.; Zhang, J.; Wang, Z.; Li, H.; Zhang, L.; Li, J.; Wang, F.; Gstl, R.; Potemkin, II; Chen, D.; Zeng, H.; Zhang, H.; Liu, K.; Herrmann, A., Ultra-strong bio-glue from genetically engineered polypeptides. *Nat Commun* **2021,** *12* (1), 3613.

106. Zeng, H.; Hwang, D. S.; Israelachvili, J. N.; Waite, J. H., Strong reversible Fe^{3+}-mediated bridging between dopa-containing protein films in water. *Proc Natl Acad Sci U S A* **2010,** *107* (29), 12850-3.

107. Xiang, L.; Zhu, S.; Li, M.; Zhang, J.; Gamal El-Din, M.; Zeng, H., Probing fouling mechanism of naphthenic acids on forward osmosis polymer membranes in oil sands process water treatment. *Journal of Membrane Science* **2019,** *576*, 161-170.

108. Xiang, L.; Zhang, J.; Gong, L.; Zeng, H., Surface forces and interaction mechanisms of soft thin films under confinement: a short review. *Soft Matter* **2020,** *16* (29), 6697-6719.

109. Xie, L.; Cui, X.; Liu, J.; Lu, Q.; Huang, J.; Mao, X.; Yang, D.; Tan, J.; Zhang, H.; Zeng, H., Nanomechanical Insights into Versatile Polydopamine Wet Adhesive Interacting with Liquid-Infused and Solid Slippery Surfaces. *ACS Appl Mater Interfaces* **2021,** *13* (5), 6941-6950.

110. Xie, L.; Liu, F.; Liu, J.; Zeng, H., A Nanomechanical Study on Deciphering the Stickiness of SARS-CoV-2 on Inanimate Surfaces. *ACS Appl Mater Interfaces* **2020,** *12* (52), 58360-58368.

111. Yang, D.; Peng, X.; Peng, Q.; Wang, T.; Qiao, C.; Zhao, Z.; Gong, L.; Liu, Y.; Zhang, H.; Zeng, H., Probing the interfacial forces and surface interaction mechanisms in petroleum production processes. *Engineering* **2022**.

112. Xie, L.; Cui, X.; Liu, J.; Lu, Q.; Huang, J.; Mao, X.; Yang, D.; Tan, J.; Zhang, H.; Zeng, H., Nanomechanical insights into versatile polydopamine wet adhesive interacting with liquid-infused and solid slippery surfaces. *ACS Applied Materials & Interfaces* **2021,** *13* (5), 6941-6950.

113. Alagha, L.; Wang, S.; Xu, Z.; Masliyah, J., Adsorption Kinetics of a Novel Organic–Inorganic Hybrid Polymer on Silica and Alumina Studied by Quartz Crystal Microbalance. *The Journal of Physical Chemistry C* **2011,** *115* (31), 15390-15402.

114. Chandrasekaran, N.; Dimartino, S.; Fee, C. J., Study of the adsorption of proteins on stainless steel surfaces using QCM-D. *Chemical Engineering Research and Design* **2013,** *91* (9), 1674-1683.

115. Dourado, A. H. B.; Silva, R. A.; Torresi, R. M.; Sumodjo, P. T. A.; Arenz, M.; Cordoba de Torresi, S. I., Kinetics, Assembling, and Conformation Control of L-Cysteine Adsorption on Pt Investigated by in situ FTIR Spectroscopy and QCM-D. *Chemphyschem* **2018,** *19* (18), 2340-2348.

116. Hampitak, P.; Melendrez, D.; Iliut, M.; Fresquet, M.; Parsons, N.; Spencer, B.; Jowitt, T. A.; Vijayaraghavan, A., Protein interactions and conformations on graphene-based materials mapped using a quartz-crystal microbalance with dissipation monitoring (QCM-D). *Carbon* **2020,** *165*, 317-327.

117. Su, Y.; Hu, X.; Tang, H.; Lu, K.; Li, H.; Liu, S.; Xing, B.; Ji, R., Steam disinfection releases micro(nano)plastics from silicone-rubber baby teats as examined by optical photothermal infrared microspectroscopy. *Nat Nanotechnol* **2022,** *17* (1), 76-85.

118. Kansiz, M.; Prater, C.; Dillon, E.; Lo, M.; Anderson, J.; Marcott, C.; Demissie, A.; Chen, Y.; Kunkel, G., Optical Photothermal Infrared Microspectroscopy with Simultaneous Raman – A New Non-Contact Failure Analysis Technique for Identification of <10 μm Organic Contamination in the Hard Drive and other Electronics Industries. *Microscopy today* **2020,** *28* (3), 26-36.

119. Lima, C.; Muhamadali, H.; Xu, Y.; Kansiz, M.; Goodacre, R., Imaging isotopically labeled bacteria at the single-cell level using high-resolution optical infrared photothermal spectroscopy. *Analytical chemistry* **2021,** *93* (6), 3082-3088.

120. Marchetti, A.; Beltran, V.; Nuyts, G.; Borondics, F.; De Meyer, S.; Van Bos, M.; Jaroszewicz, J.; Otten, E.; Debulpaep, M.; De Wael, K., Novel optical photothermal infrared (O-PTIR) spectroscopy for the noninvasive characterization of heritage glass-metal objects. *Science advances* **2022,** *8* (9), eabl6769.

121. Wang, D.; Sun, Q.; Hokkanen, M. J.; Zhang, C.; Lin, F. Y.; Liu, Q.; Zhu, S. P.; Zhou, T.; Chang, Q.; He, B.; Zhou, Q.; Chen, L.; Wang, Z.; Ras, R. H. A.; Deng, X., Design of robust superhydrophobic surfaces. *Nature* **2020,** *582* (7810), 55-59.

122. Zheng, N.; Xu, Y.; Zhao, Q.; Xie, T., Dynamic Covalent Polymer Networks: A Molecular Platform for Designing Functions beyond Chemical Recycling and Self-Healing. *Chem Rev* **2021**.

123. Cheng, W.; Zeng, X.; Chen, H.; Li, Z.; Zeng, W.; Mei, L.; Zhao, Y., Versatile polydopamine platforms: synthesis and promising applications for surface modification and advanced nanomedicine. *ACS nano* **2019,** *13* (8), 8537-8565.

124. Zhao, Z.; Pan, M.; Qiao, C.; Xiang, L.; Liu, X.; Yang, W.; Chen, X. Z.; Zeng, H., Bionic Engineered Protein Coating Boosting Anti-Biofouling in Complex Biological Fluids. *Adv Mater* **2022**, e2208824.

125. He, K.; Duan, H.; Chen, G. Y.; Liu, X.; Yang, W.; Wang, D., Cleaning of oil fouling with water enabled by zwitterionic polyelectrolyte coatings: overcoming the imperative challenge of oil-water separation membranes. *ACS nano* **2015,** *9* (9), 9188-9198.

126. Niu, W.; Chen, G. Y.; Xu, H.; Liu, X.; Sun, J., Highly Transparent and Self-Healable Solar Thermal Anti-/Deicing Surfaces: When Ultrathin MXene Multilayers Marry a Solid Slippery Self-Cleaning Coating. *Advanced Materials* **2022,** *34* (10), 2108232.

127. Blacklow, S.; Li, J.; Freedman, B.; Zeidi, M.; Chen, C.; Mooney, D., Bioinspired mechanically active adhesive dressings to accelerate wound closure. *Science advances* **2019,** *5* (7), eaaw3963.

128. Inkpen, M. S.; Liu, Z. F.; Li, H.; Campos, L. M.; Neaton, J. B.; Venkataraman, L., Non-chemisorbed gold-sulfur binding prevails in self-assembled monolayers. *Nature chemistry* **2019,** *11* (4), 351-358.

129. Du, T.; Li, B.; Wang, X.; Yu, B.; Pei, X.; Huck, W. T.; Zhou, F., Bio-inspired renewable surface-initiated polymerization from permanently embedded initiators. *Angewandte Chemie International Edition* **2016,** *55* (13), 4260-4264.

130. Zeng, H., *Polymer adhesion, friction, and lubrication*. John Wiley & Sons: 2013.

131. Wang, Z.; Yang, H.-C.; He, F.; Peng, S.; Li, Y.; Shao, L.; Darling, S. B., Mussel-Inspired Surface Engineering for Water-Remediation Materials. *Matter* **2019,** *1* (1), 115-155.

132. Qi, H.; Zheng, W.; Zhang, C.; Zhou, X.; Zhang, L., Novel Mussel-Inspired Universal Surface Functionalization Strategy: Protein-Based Coating with Residue-Specific Post-Translational Modification in Vivo. *ACS Appl Mater Interfaces* **2019,** *11* (13), 12846-12853.

133. Song, S.; Yang, H.; Cui, Y.; Tang, Y.; Chen, Y.; Yang, B.; Yuan, J.; Huang, J., Mussel-inspired, self-healing polymer blends. *Polymer* **2020,** *198*, 122528.

134. Li, S.; Chen, J.; Wang, J.; Zeng, H., Anti-biofouling materials and surfaces based on mussel-inspired chemistry. *Materials Advances* **2021,** *2* (7), 2216-2230.

135. Li, L.; Yan, B.; Zhang, L.; Tian, Y.; Zeng, H., Mussel-inspired antifouling coatings bearing polymer loops. *Chem Commun (Camb)* **2015,** *51* (87), 15780-3.

136. Li, L.; Yan, B.; Yang, J.; Chen, L.; Zeng, H., Novel mussel-inspired injectable self-healing hydrogel with anti-biofouling property. *Adv Mater* **2015,** *27* (7), 1294-9.

137. Li, L.; Smitthipong, W.; Zeng, H., Mussel-inspired hydrogels for biomedical and environmental applications. *Polymer Chemistry* **2015,** *6* (3), 353-358.

138. Lee, B. P.; Messersmith, P. B.; Israelachvili, J. N.; Waite, J. H., Mussel-Inspired Adhesives and Coatings. *Annu Rev Mater Res* **2011,** *41*, 99-132.

139. Han, L.; Gong, L.; Chen, J.; Zhang, J.; Xiang, L.; Zhang, L.; Wang, Q.; Yan, B.; Zeng, H., Universal Mussel-Inspired Ultrastable Surface-Anchoring Strategy via Adaptive Synergy of Catechol and Cations. *ACS Appl Mater Interfaces* **2018,** *10* (2), 2166-2173.

140. Yang, W.; Hu, W.; Zhang, J.; Wang, W.; Cai, R.; Pan, M.; Huang, C.; Chen, X.; Yan, B.; Zeng, H., Tannic acid/Fe^{3+} functionalized magnetic graphene oxide nanocomposite with high loading of silver nanoparticles as ultra-efficient catalyst and disinfectant for wastewater treatment. *Chemical Engineering Journal* **2021,** *405*, 126629.

141. Pan, M.; Nguyen, K.-C. T.; Yang, W.; Liu, X.; Chen, X.-Z.; Major, P. W.; Le, L. H.; Zeng, H., Soft armour-like layer-protected hydrogels for wet tissue adhesion and biological imaging. *Chemical Engineering Journal* **2022,** *434*, 134418.

142. Pan, M.; Gong, L.; Xiang, L.; Yang, W.; Wang, W.; Zhang, L.; Hu, W.; Han, L.; Zeng, H., Modulating surface interactions for regenerable separation of oil-in-water emulsions. *Journal of Membrane Science* **2021,** *625*, 119140.

143. Park, J. H.; Jackman, J. A.; Ferhan, A. R.; Ma, G. J.; Yoon, B. K.; Cho, N. J., Temperature-Induced Denaturation of BSA Protein Molecules for Improved Surface Passivation Coatings. *ACS Appl Mater Interfaces* **2018,** *10* (38), 32047-32057.

144. Guin, D.; Gruebele, M., Weak Chemical Interactions That Drive Protein Evolution: Crowding, Sticking, and Quinary Structure in Folding and Function. *Chem Rev* **2019,** *119* (18), 10691-10717.

145. Chen, M.; Yang, F.; Chen, X.; Qin, R.; Pi, H.; Zhou, G.; Yang, P., Crack Suppression in Conductive Film by Amyloid-Like Protein Aggregation toward Flexible Device. *Adv Mater* **2021,** *33* (44), e2104187.

146. Masliyah, J. H.; Czarnecki, J.; Xu, Z., Handbook on Theory and Practice on Bitumen Recovery from Athabasca Oil Sands. **2011**.

147. Song, M. T.; Wang, W. Z.; Lu, Y.; Han, R. M.; Skibsted, L. H.; Zhang, J. P., Double-Site Binding and Anti-/Pro-oxidation of Luteolin on Bovine Serum Albumin Mediated by Copper(II) Coordination. *ACS Omega* **2022,** *7* (23), 19521-19534.

148. Jing, P. P.; Li, Y. X.; Su, Y. H.; Liang, W. L.; Leng, Y. X., The role of metal ions in the behavior of bovine serum albumin molecules under physiological environment. *Spectrochim Acta A Mol Biomol Spectrosc* **2022,** *267* (Pt 2), 120604.

149. Raja, S. T.; Thiruselvi, T.; Mandal, A. B.; Gnanamani, A., pH and redox sensitive albumin hydrogel: A self-derived biomaterial. *Sci Rep* **2015,** *5*, 15977.

150. Chen, J.; Peng, Q.; Peng, X.; Zhang, H.; Zeng, H., Probing and Manipulating Noncovalent Interactions in Functional Polymeric Systems. *Chem Rev* **2022**.

151. Li, L.; Yan, B.; Zhang, L.; Tian, Y.; Zeng, H., Mussel-inspired antifouling coatings bearing polymer loops. *Chemical Communications* **2015,** *51* (87), 15780-15783.

152. Mao, X.; Zhao, Z.; Yang, D.; Qiao, C.; Tan, J.; Liu, Q.; Tang, T.; Zhang, H.; Zeng, H., Facile and scalable surface functionalization approach with small silane molecules for

oil/water separation and demulsification of surfactant/asphaltenes-stabilized emulsions. *Separation and Purification Technology* **2022,** *285*, 120382.

153. Cacace, M.; Landau, E.; Ramsden, J., The Hofmeister series: salt and solvent effects on interfacial phenomena. *Quarterly reviews of biophysics* **1997,** *30* (3), 241-277.

154. Medda, L.; Barse, B.; Cugia, F.; Bostrom, M.; Parsons, D. F.; Ninham, B. W.; Monduzzi, M.; Salis, A., Hofmeister challenges: ion binding and charge of the BSA protein as explicit examples. *Langmuir* **2012,** *28* (47), 16355-16363.

155. Shimizu, S.; McLaren, W. M.; Matubayasi, N., The Hofmeister series and protein-salt interactions. *The Journal of chemical physics* **2006,** *124* (23), 234905.

156. Vlachy, N.; Jagoda-Cwiklik, B.; Vacha, R.; Touraud, D.; Jungwirth, P.; Kunz, W., Hofmeister series and specific interactions of charged headgroups with aqueous ions. *Advances in colloid and interface science* **2009,** *146* (1-2), 42-47.

157. Singh, A.; Datta, P.; Pandey, L. M., Deciphering the mechanistic insight into the stoichiometric ratio dependent behavior of Cu(II) on BSA fibrillation. *Int J Biol Macromol* **2017,** *97*, 662-670.

158. Kalab, M., Factors affecting the Ellman determination of sulfhydryl groups in skimmilk powder and gels. *Journal of Dairy Science* **1970,** *53* (6), 711-718.

159. Yang, W.; Zhao, Z.; Pan, M.; Gong, L.; Wu, F.; Huang, C.; Wang, X.; Wang, J.; Zeng, H., Mussel-inspired polyethylene glycol coating for constructing antifouling membrane for water purification. *J Colloid Interface Sci* **2022,** *625*, 628-639.

160. Pang, X.; Jiang, Y.; Xiao, Q.; Leung, A. W.; Hua, H.; Xu, C., pH-responsive polymer-drug conjugates: design and progress. *Journal of controlled release* **2016,** *222*, 116-129.

161. Fenton, O. S.; Olafson, K. N.; Pillai, P. S.; Mitchell, M. J.; Langer, R., Advances in biomaterials for drug delivery. *Advanced Materials* **2018,** *30* (29), 1705328.

162. Wong, P. T.; Choi, S. K., Mechanisms of drug release in nanotherapeutic delivery systems. *Chemical reviews* **2015,** *115* (9), 3388-3432.

163. Ping, Y.; Guo, J.; Ejima, H.; Chen, X.; Richardson, J. J.; Sun, H.; Caruso, F., pH-responsive capsules engineered from metal-phenolic networks for anticancer drug delivery. *Small* **2015,** *11* (17), 2032-2036.

164. Yang, W.; Pan, M.; Zhang, J.; Zhang, L.; Lin, F.; Liu, X.; Huang, C.; Chen, X. Z.; Wang, J.; Yan, B.; Zeng, H., A Universal Strategy for Constructing Robust and Antifouling Cellulose Nanocrystal Coating. *Advanced Functional Materials* **2021**.

165. IMARC *Implantable Medical Devices Market: Global Industry Trends, Share, Size, Growth, Opportunity and Forecast 2022-2027*; 2022.

166. Faustino, C. M. C.; Lemos, S. M. C.; Monge, N.; Ribeiro, I. A. C., A scope at antifouling strategies to prevent catheter-associated infections. *Adv Colloid Interface Sci* **2020,** *284*, 102230.

167. Leslie, D. C.; Waterhouse, A.; Berthet, J. B.; Valentin, T. M.; Watters, A. L.; Jain, A.; Kim, P.; Hatton, B. D.; Nedder, A.; Donovan, K.; Super, E. H.; Howell, C.; Johnson, C. P.; Vu, T. L.; Bolgen, D. E.; Rifai, S.; Hansen, A. R.; Aizenberg, M.; Super, M.; Aizenberg, J.; Ingber, D. E., A bioinspired omniphobic surface coating on medical devices prevents thrombosis and biofouling. *Nat Biotechnol* **2014,** *32* (11), 1134-40.

168. Joung, Y.-H., Development of implantable medical devices: from an engineering perspective. *International neurourology journal* **2013,** *17* (3), 98.

169. Zhang, C.; Lv, Y.; Qiu, W. Z.; He, A.; Xu, Z. K., Polydopamine Coatings with Nanopores for Versatile Molecular Separation. *ACS Appl Mater Interfaces* **2017,** *9* (16), 14437-14444.

170. Zhang, J.; Zhang, L.; Cui, X.; Gong, L.; Xiang, L.; Shi, C.; Hu, W.; Zeng, H., Scalable polyzwitterion–polydopamine coating for regenerable oil/water separation and underwater self-cleaning of stubborn heavy oil fouling without pre-hydration. *Chemical Communications* **2018,** *54* (70), 9734-9737.

171. Meng, J.; Wang, S., Advanced antiscaling interfacial materials toward highly efficient heat energy transfer. *Advanced Functional Materials* **2020,** *30* (8), 1904796.

172. He, K.; Duan, H.; Chen, G. Y.; Liu, X.; Yang, W.; Wang, D., Cleaning of oil fouling with water enabled by zwitterionic polyelectrolyte coatings: overcoming the imperative challenge of oil-water separation membranes. *ACS nano* **2015,** *9* (9), 9188-9198.

173. Medina Jimenez, C.; Neitzel, A.; De Hoe, G.; Tirrell, M., Probing the physical origin of the anti-biofouling performance of synthetic polyzwitterions. *Bulletin of the American Physical Society* **2022**.

174. Higaki, Y.; Takahara, A., Anti-(bio) Fouling. *Stimuli-Responsive Dewetting/Wetting Smart Surfaces and Interfaces* **2018**, 239-257.

175. Ostuni, E.; Chapman, R. G.; Holmlin, R. E.; Takayama, S.; Whitesides, G. M., A survey of structure-property relationships of surfaces that resist the adsorption of protein. *Langmuir* **2001,** *17* (18), 5605-5620.

176. Castiello, F. R.; Tabrizian, M., Multiplex surface plasmon resonance imaging-based biosensor for human pancreatic islets hormones quantification. *Analytical chemistry* **2018,** *90* (5), 3132-3139.

177. Zhang, C.; Li, H. N.; Du, Y.; Ma, M. Q.; Xu, Z. K., CuSO4/H2O2-Triggered Polydopamine/Poly(sulfobetaine methacrylate) Coatings for Antifouling Membrane Surfaces. *Langmuir* **2017,** *33* (5), 1210-1216.

178. Chen, W.; Kretzschmann, A.; Tian, W.; Wu, S., Nonlinear supramolecular polymers for therapeutic applications. *Advanced Therapeutics* **2019,** *2* (2), 1800103.

179. Wang, Z.; Gu, X.; Li, B.; Li, J.; Wang, F.; Sun, J.; Zhang, H.; Liu, K.; Guo, W., Molecularly Engineered Protein Glues with Superior Adhesion Performance. *Advanced Materials* **2022**, 2204590.

180. Fang, B.; Ling, Q.; Zhao, W.; Ma, Y.; Bai, P.; Wei, Q.; Li, H.; Zhao, C., Modification of polyethersulfone membrane by grafting bovine serum albumin on the surface of polyethersulfone/poly (acrylonitrile-co-acrylic acid) blended membrane. *Journal of Membrane Science* **2009,** *329* (1-2), 46-55.

181. Komatsu, T.; Hamamatsu, K.; Tsuchida, E., Cross-linked human serum albumin dimer incorporating sixteen (tetraphenylporphinato) iron (II) derivatives: synthesis, characterization, and O2-binding property. *Macromolecules* **1999,** *32* (25), 8388-8391.

182. Park, J. H.; Jackman, J. A.; Ferhan, A. R.; Ma, G. J.; Yoon, B. K.; Cho, N.-J., Temperature-induced denaturation of BSA protein molecules for improved surface passivation coatings. *ACS applied materials & interfaces* **2018,** *10* (38), 32047-32057.

183. Steinitz, M., Quantitation of the blocking effect of tween 20 and bovine serum albumin in ELISA microwells. *Analytical biochemistry* **2000,** *282* (2), 232-238.

184. Sweryda-Krawiec, B.; Devaraj, H.; Jacob, G.; Hickman, J. J., A new interpretation of serum albumin surface passivation. *Langmuir* **2004,** *20* (6), 2054-2056.

185. Huber, M. C.; Schreiber, A.; Von Olshausen, P.; Varga, B. z. R.; Kretz, O.; Joch, B.; Barnert, S.; Schubert, R.; Eimer, S.; Kele, P. t., Designer amphiphilic proteins as building blocks for the intracellular formation of organelle-like compartments. *Nature materials* **2015,** *14* (1), 125-132.

186. Kaiser, E.; Kezdy, F., Secondary structures of proteins and peptides in amphiphilic environments.(A review). *Proceedings of the National Academy of Sciences* **1983,** *80* (4), 1137-1143.

187. Peng, X.; Xia, X.; Xu, X.; Yang, X.; Yang, B.; Zhao, P.; Yuan, W.; Chiu, P. W. Y.; Bian, L., Ultrafast self-gelling powder mediates robust wet adhesion to promote healing of gastrointestinal perforations. *Science Advances* **2021,** *7* (23), eabe8739.

188. Yuk, H.; Wu, J.; Sarrafian, T. L.; Mao, X.; Varela, C. E.; Roche, E. T.; Griffiths, L. G.; Nabzdyk, C. S.; Zhao, X., Rapid and coagulation-independent haemostatic sealing by a paste inspired by barnacle glue. *Nature Biomedical Engineering* **2021**.

189. Tiwary, P.; Limongelli, V.; Salvalaglio, M.; Parrinello, M., Kinetics of protein-ligand unbinding: Predicting pathways, rates, and rate-limiting steps. *Proceedings of the National Academy of Sciences* **2015,** *112* (5), E386-E391.

190. Rego, N. B.; Xi, E.; Patel, A. J., Protein hydration waters are susceptible to unfavorable perturbations. *Journal of the American Chemical Society* **2019,** *141* (5), 2080-2086.

191. Hoyle, C. E.; Bowman, C. N., Thiol-ene click chemistry. *Angew Chem Int Ed Engl* **2010,** *49* (9), 1540-73.

192. Liu, Q.; Zhang, Q.; Chen, S.; Zhou, J.; Lei, X., Progress in Thiol-Ene/Yne Click Chemistry. *Chinese Journal of Organic Chemistry* **2012,** *32* (10).

193. Zhang, C.; Ma, M. Q.; Chen, T. T.; Zhang, H.; Hu, D. F.; Wu, B. H.; Ji, J.; Xu, Z. K., Dopamine-Triggered One-Step Polymerization and Codeposition of Acrylate Monomers for Functional Coatings. *ACS Appl Mater Interfaces* **2017,** *9* (39), 34356-34366.

194. Riddles, P. W.; Blakeley, R. L.; Zerner, B., Ellman's reagent: 5, 5-dithiobis (2-nitrobenzoic acid) a reexamination. *Analytical biochemistry* **1979,** *94* (1), 75-81.

195. Mekaru, H.; Yoshigoe, A.; Nakamura, M.; Doura, T.; Tamanoi, F., Biodegradability of Disulfide-Organosilica Nanoparticles Evaluated by Soft X-ray Photoelectron Spectroscopy: Cancer Therapy Implications. *ACS Applied Nano Materials* **2018,** *2* (1), 479-488.

196. Castner, D. G.; Hinds, K.; Grainger, D. W., X-ray photoelectron spectroscopy sulfur 2p study of organic thiol and disulfide binding interactions with gold surfaces. *Langmuir* **1996,** *12* (21), 5083-5086.

197. Yang, W. J.; Neoh, K.-G.; Kang, E.-T.; Lay-Ming Teo, S.; Rittschof, D., Stainless steel surfaces with thiol-terminated hyperbranched polymers for functionalization via thiol-based chemistry. *Polymer Chemistry* **2013,** *4* (10).

198. Eom, T.; Khan, A., Disulfides as mercapto-precursors in nucleophilic ring opening reaction of polymeric epoxides: establishing equimolar stoichiometric conditions in a thiol-epoxy 'click' reaction. *Chem Commun (Camb)* **2020,** *56* (54), 7419-7422.

199. Du, T.; Li, B.; Wang, X.; Yu, B.; Pei, X.; Huck, W. T.; Zhou, F., Bioinspired renewable surface initiated polymerization from permanently embedded initiators. *Angewandte Chemie International Edition* **2016,** *55* (13), 4260-4264.

200. Liu, Y.; Li, R.; Xu, R.; Liu, Y.; Wu, Y.; Ma, S.; Ma, Z.; Pei, X.; Zhou, F., Repeatedly Regenerating Mechanically Robust Polymer Brushes from Persistent Initiator Coating (PIC). *Angewandte Chemie International Edition* **2022**, e202204410.

201. Yu, B.; Hu, H.; Wang, D.; Huck, W. T.; Zhou, F.; Liu, W., Electrolyte-modulated electrochemistry and electrocatalysis on ferrocene-terminated polyelectrolyte brushes. *Journal of Materials Chemistry* **2009,** *19* (43), 8129-8134.

202. Rouxhet, P. G.; Misselyn-Bauduin, A. M.; Ahimou, F.; Genet, M. J.; Adriaensen, Y.; Desille, T.; Bodson, P.; Deroanne, C., XPS analysis of food products: toward chemical functions and molecular compounds. *Surface and Interface Analysis* **2008,** *40* (3-4), 718-724.

203. Rouxhet, P. G.; Genet, M. J., XPS analysis of bio-organic systems. *Surface and Interface Analysis* **2011,** *43* (12), 1453-1470.

204. Fan, Y.; Migliore, N.; Raffa, P.; Bose, R. K.; Picchioni, F., Synthesis of Zwitterionic Copolymers via Copper-Mediated Aqueous Living Radical Grafting Polymerization on Starch. *Polymers (Basel)* **2019,** *11* (2).

205. Alexander, T. E.; Lozeau, L. D.; Camesano, T. A., QCM-D characterization of time-dependence of bacterial adhesion. *Cell Surf* **2019,** *5*, 100024.

206. Gong, L.; Xiang, L.; Zhang, J.; Han, L.; Wang, J.; Wang, X.; Liu, J.; Yan, B.; Zeng, H., Interaction Mechanisms of Zwitterions with Opposite Dipoles in Aqueous Solutions. *Langmuir* **2019,** *35* (7), 2842-2853.

207. Qian, P. Y.; Chen, L.; Xu, Y., Mini-review: Molecular mechanisms of antifouling compounds. *Biofouling* **2013,** *29* (4), 381-400.

208. Su, Y.; Hu, X.; Tang, H.; Lu, K.; Li, H.; Liu, S.; Xing, B.; Ji, R., Steam disinfection releases micro (nano) plastics from silicone-rubber baby teats as examined by optical photothermal infrared microspectroscopy. *Nature nanotechnology* **2022,** *17* (1), 76-85.

209. Steinel, T.; Asbury, J. B.; Zheng, J.; Fayer, M., Watching hydrogen bonds break: A transient absorption study of water. *The Journal of Physical Chemistry A* **2004,** *108* (50), 10957-10964.

210. Rapaport, D., Hydrogen bonds in water: Network organization and lifetimes. *Molecular Physics* **1983,** *50* (5), 1151-1162.

211. Gale, G.; Gallot, G.; Hache, F.; Lascoux, N.; Bratos, S.; Leicknam, J.-C., Femtosecond dynamics of hydrogen bonds in liquid water: A real time study. *Physical review letters* **1999,** *82* (5), 1068.

212. Xiao, S.; Ren, B.; Huang, L.; Shen, M.; Zhang, Y.; Zhong, M.; Yang, J.; Zheng, J., Salt-responsive zwitterionic polymer brushes with anti-polyelectrolyte property. *Current opinion in chemical engineering* **2018,** *19*, 86-93.

213. Wang, F.; Yang, J.; Zhao, J., Understanding anti polyelectrolyte behavior of a well defined polyzwitterion at the single chain level. *Polymer international* **2015,** *64* (8), 999-1005.

214. Gao, H.; Mao, J.; Cai, Y.; Li, S.; Fu, Y.; Liu, X.; Liang, H.; Zhao, T.; Liu, M.; Jiang, L., Euryhaline Hydrogel with Constant Swelling and Salinity Enhanced Mechanical Strength in a Wide Salinity Range. *Advanced Functional Materials* **2021,** *31* (4), 2007664.

215. Zhang, Y.; Cremer, P. S., Interactions between macromolecules and ions: the Hofmeister series. *Current opinion in chemical biology* **2006,** *10* (6), 658-663.

216. Mu, D.; Wang, W.; Li, J.; Lv, P.; Liu, R.; Tan, Y.; Zhong, C.; Qi, Y.; Sun, X.; Liu, Y., Ultrasmall Fe (III)-Tannic Acid Nanoparticles To Prevent Progression of Atherosclerotic Plaques. *ACS Applied Materials & Interfaces* **2021,** *13* (29), 33915-33925.

217. Gunawan, S. T.; Kempe, K.; Bonnard, T.; Cui, J.; Alt, K.; Law, L. S.; Wang, X.; Westein, E.; Such, G. K.; Peter, K., Multifunctional thrombin activatable polymer capsules for specific targeting to activated platelets. *Advanced Materials* **2015,** *27* (35), 5153-5157.

218. Qiao, C.; Wang, D.; Zhao, Z.; Yang, W.; Wu, F.; Chen, H.; Yin, T.; Zhang, L.; Liu, Q.; Yang, D., Bench-scale oil fouling/antifouling tests under high temperature and high pressure conditions and the underlying interfacial interaction mechanisms. *Fuel* **2022,** *314*, 122720.

219. Rutkowski, J. L., Aspiring to a Future of Near-Zero Dental Implant Complications. The American Academy of Implant Dentistry: 2021; Vol. 47, pp 91-91.

220. Pal, S.; Pal, S., The medical device market and ethical issues of implants. *Design of Artificial Human Joints & Organs* **2014**, 377-394.

221. Mantripragada, V. P.; Lecka-Czernik, B.; Ebraheim, N. A.; Jayasuriya, A. C., An overview of recent advances in designing orthopedic and craniofacial implants. *Journal of biomedical materials research Part A* **2013,** *101* (11), 3349-3364.

222. Chaya, A.; Yoshizawa, S.; Verdelis, K.; Myers, N.; Costello, B. J.; Chou, D.-T.; Pal, S.; Maiti, S.; Kumta, P. N.; Sfeir, C., In vivo study of magnesium plate and screw degradation and bone fracture healing. *Acta biomaterialia* **2015,** *18*, 262-269.

223. Yan, Z.-Y.; Zhu, J.-H.; Liu, G.-Q.; Liu, Z.-C.; Guo, C.-B.; Cui, N.-H.; Han, J.-M., Feasibility and efficacy of a degradable magnesium-alloy GBR membrane for bone augmentation in a distal bone-defect model in Beagle dogs. *Bioinorganic Chemistry and Applications* **2022,** *2022*.

224. Wang, Y.; Liu, B.; Zhao, X.; Zhang, X.; Miao, Y.; Yang, N.; Yang, B.; Zhang, L.; Kuang, W.; Li, J., Turning a native or corroded Mg alloy surface into an anti-corrosion coating in excited CO_2. *Nature communications* **2018,** *9* (1), 4058.

225. Li, L.-Y.; Yang, Z.; Pan, X.-X.; Feng, B.-X.; Yue, R.; Yu, B.; Zheng, Y.-F.; Tan, J.-Y.; Yuan, G.-Y.; Pei, J., Incorporating Copper to Biodegradable Magnesium Alloy Vascular Stents via a Cu (II) - Eluting Coating for Synergistic Enhancement in Prolonged Durability and Rapid Re-Endothelialization. *Advanced Functional Materials* **2022,** *32* (47), 2205634.

226. Xu, W.; Birbilis, N.; Sha, G.; Wang, Y.; Daniels, J. E.; Xiao, Y.; Ferry, M., A high-specific-strength and corrosion-resistant magnesium alloy. *Nature materials* **2015,** *14* (12), 1229-1235.

227. Esmaily, M.; Svensson, J.; Fajardo, S.; Birbilis, N.; Frankel, G.; Virtanen, S.; Arrabal, R.; Thomas, S.; Johansson, L., Fundamentals and advances in magnesium alloy corrosion. *Progress in Materials Science* **2017,** *89*, 92-193.

228. Cihova, M.; Schmutz, P.; Schäublin, R.; Löffler, J. F., Biocorrosion zoomed in: evidence for dealloying of nanometric intermetallic particles in magnesium alloys. *Advanced Materials* **2019,** *31* (42), 1903080.

229. Witte, F., The history of biodegradable magnesium implants: a review. *Acta biomaterialia* **2010,** *6* (5), 1680-1692.

230. Zheng, Y.; Gu, X.; Witte, F., Biodegradable metals. *Materials Science and Engineering: R: Reports* **2014,** *77*, 1-34.

231. Uppal, G.; Thakur, A.; Chauhan, A.; Bala, S., Magnesium based implants for functional bone tissue regeneration – A review. *Journal of Magnesium and Alloys* **2022,** *10* (2), 356-386.

232. Tong, P.; Sheng, Y.; Hou, R.; Iqbal, M.; Chen, L.; Li, J., Recent progress on coatings of biomedical magnesium alloy. *Smart Materials in Medicine* **2022,** *3*, 104-116.

233. Hornberger, H.; Virtanen, S.; Boccaccini, A. R., Biomedical coatings on magnesium alloys-a review. *Acta biomaterialia* **2012,** *8* (7), 2442-2455.

234. Amukarimi, S.; Mozafari, M., Biodegradable magnesium-based biomaterials: an overview of challenges and opportunities. *MedComm* **2021,** *2* (2), 123-144.

235. Yimyai, T.; Crespy, D.; Rohwerder, M., Corrosion-Responsive Self-Healing Coatings. *Advanced Materials* **2023**, 2300101.

236. Hu, R.-G.; Zhang, S.; Bu, J.-F.; Lin, C.-J.; Song, G.-L., Recent progress in corrosion protection of magnesium alloys by organic coatings. *Progress in Organic Coatings* **2012,** *73* (2-3), 129-141.

237. Toorani, M.; Aliofkhazraei, M.; Mahdavian, M.; Naderi, R., Superior corrosion protection and adhesion strength of epoxy coating applied on AZ31 magnesium alloy pre-treated by PEO/Silane with inorganic and organic corrosion inhibitors. *Corrosion Science* **2021,** *178*, 109065.

238. Liao, S.; Yu, B.; Zhang, X.; Lu, X.; Zhou, P.; Zhang, C.; Chen, X.; Zhang, T.; Wang, F., New design principles for the bath towards chromate-and crack-free conversion coatings on magnesium alloys. *Journal of Magnesium and Alloys* **2021,** *9* (2), 505-519.

239. Hagans, P. L.; Haas, C., Chromate conversion coatings. *ASM Handbook* **1994,** *5*, 405-411.

240. Qiu, Y.; Tu, X.; Lu, X.; Yang, J., A novel insight into synergistic corrosion inhibition of fluoride and DL-malate as a green hybrid inhibitor for magnesium alloy. *Corrosion Science* **2022,** *199*, 110177.

241. Zheng, H.; Li, Z.; Chen, M.; You, C.; Wang, J., Enhanced Corrosion Resistance and Biocompatibility of $NaMgF_3$ Coating on Mg-Zn-Ca Alloy: An In Vivo and In Vitro Study. *Advanced Engineering Materials* **2023,** *25* (8), 2201364.

242. Lou, J.; Sun, Y.; Chen, Y.; Zan, R.; Peng, H.; Yang, S.; Kang, X.; Peng, Z.; Wang, W.; Zhang, X., Effects of MgF_2 coating on the biodegradation and biological properties of magnesium. *Surface and Coatings Technology* **2021,** *422*.

243. Saji, V. S., Review of rare-earth-based conversion coatings for magnesium and its alloys. *Journal of Materials Research and Technology* **2019,** *8* (5), 5012-5035.

244. Yimyai, T.; Thiramanas, R.; Phakkeeree, T.; Iamsaard, S.; Crespy, D., Adaptive Coatings with Anticorrosion and Antibiofouling Properties. *Advanced Functional Materials* **2021,** *31* (37).

245. Zhao, H.; Liu, S.; Wei, Y.; Yue, Y.; Gao, M.; Li, Y.; Zeng, X.; Deng, X.; Kotov, N. A.; Guo, L., Multiscale engineered artificial tooth enamel. *Science* **2022,** *375* (6580), 551-556.

246. Ali, S.; Farooq, I., A Review of the role of amelogenin protein in enamel formation and novel experimental techniques to study its function. *Protein and Peptide Letters* **2019,** *26* (12), 880-886.

247. Fincham, A. G.; Simmer, J. P. In *Amelogenin proteins of developing dental enamel*, Ciba Foundation Symposium 205-Dental Enamel: Dental Enamel: Ciba Foundation Symposium 205, Wiley Online Library: 2007; pp 118-134.

248. Harding, J. H.; Duffy, D. M.; Sushko, M. L.; Rodger, P. M.; Quigley, D.; Elliott, J. A., Computational techniques at the organic-inorganic interface in biomineralization. *Chemical reviews* **2008,** *108* (11), 4823-4854.

249. Mann, S., Biomineralization: principles and concepts in bioinorganic materials chemistry. **2001**.

250. Navrotsky, A., Energetic clues to pathways to biomineralization: Precursors, clusters, and nanoparticles. *Proceedings of the National Academy of Sciences* **2004,** *101* (33), 12096-12101.

251. Qiu, S. R.; Orme, C. A., Dynamics of biomineral formation at the near-molecular level. *Chemical reviews* **2008,** *108* (11), 4784-4822.

252. Shi, S.; Fan, W.; Tao, R.; Xu, H.; Lu, Y.; Han, F.; Yang, S.; Zhou, X.; Zhou, Z.; Wan, F., Natural Biomineralization-Inspired Magnesium Silicate Composite Coating Upregulates Osteogenesis, Enabling Strong Anterior Cruciate Ligament Graft-Bone Healing In Vivo. *ACS Biomaterials Science & Engineering* **2020,** *7* (1), 133-143.

253. Song, Y.; Zhang, S.; Li, J.; Zhao, C.; Zhang, X., Electrodeposition of Ca-P coatings on biodegradable Mg alloy: in vitro biomineralization behavior. *Acta Biomaterialia* **2010,** *6* (5), 1736-1742.

254. Su, Y.; Li, D.; Su, Y.; Lu, C.; Niu, L.; Lian, J.; Li, G., Improvement of the biodegradation property and biomineralization ability of magnesium-hydroxyapatite composites with dicalcium phosphate dihydrate and hydroxyapatite coatings. *ACS Biomaterials Science & Engineering* **2016,** *2* (5), 818-828.

255. Yu, Z.; Li, X.; Li, X.; Zheng, B.; Li, D.; Xu, D.; Wang, F., Nacre-Inspired Metal-Organic Framework Coatings Reinforced by Multiscale Hierarchical Cross-linking for

Integrated Antifouling and Anti-Microbial Corrosion. *Advanced Functional Materials* **2023**.

256. Zhao, Z.; Pan, M.; Yang, W.; Huang, C.; Qiao, C.; Yang, H.; Wang, J.; Wang, X.; Liu, J.; Zeng, H., Bioinspired engineered proteins enable universal anchoring strategy for surface functionalization. *Journal of Colloid and Interface Science* **2023,** *650*, 1525-1535.

257. Ryan, M.; Barbour, H., Magnesium measurement in routine clinical practice. *Annals of clinical biochemistry* **1998,** *35* (4), 449-459.

258. Yappert, M. C.; DuPre, D. B., Complexometric titrations: competition of complexing agents in the determination of water hardness with EDTA. *Journal of Chemical Education* **1997,** *74* (12), 1422.

259. Duskey, J. T.; da Ros, F.; Ottonelli, I.; Zambelli, B.; Vandelli, M. A.; Tosi, G.; Ruozi, B., Enzyme Stability in Nanoparticle Preparations Part 1: Bovine Serum Albumin Improves Enzyme Function. *Molecules* **2020,** *25* (20).

260. Archer, W. R.; Schulz, M. D., Isothermal titration calorimetry: practical approaches and current applications in soft matter. *Soft Matter* **2020,** *16* (38), 8760-8774.

261. Dill, E. D.; Folmer, J. C.; Martin, J. D., Crystal growth simulations to establish physically relevant kinetic parameters from the empirical Kolmogorov-Johnson-Mehl-Avrami model. *Chemistry of Materials* **2013,** *25* (20), 3941-3951.

262. Elabbar, A., On the application of the KJMA equation on the analysis of isothermal crystallization kinetics. *Materials Chemistry and Physics* **2019,** *238*, 121896.

263. Allnér, O.; Nilsson, L.; Villa, A., Magnesium ion-water coordination and exchange in biomolecular simulations. *Journal of chemical theory and computation* **2012,** *8* (4), 1493-1502.

264. Bellarosa, L.; Calero, S.; López, N., Early stages in the degradation of metal-organic frameworks in liquid water from first-principles molecular dynamics. *Physical Chemistry Chemical Physics* **2012,** *14* (20), 7240-7245.

265. Dudev, T.; Cowan, J.; Lim, C., Competitive binding in magnesium coordination chemistry: water versus ligands of biological interest. *Journal of the American Chemical Society* **1999,** *121* (33), 7665-7673.

266. Guo, Y.; Yu, Y.; Han, L.; Ma, S.; Zhao, J.; Chen, H.; Yang, Z.; Zhang, F.; Xia, Y.; Zhou, Y., Biocompatibility and osteogenic activity of guided bone regeneration membrane based on chitosan-coated magnesium alloy. *Materials Science and Engineering: C* **2019,** *100*, 226-235.